Maryann C. Wythers
EDITOR

ADVANCES IN Materials Science Research

VOLUME 65

Advances in Materials Science Research

This is a numbered series focused on materials science research.

Advances in Materials Science Research

Advances in Materials Science Research. Volume 65
Maryann C. Wythers (Editor)
2023. ISBN: 979-8-89113-090-6 (Hardcover)
2023. ISBN: 979-8-89113-112-5 (eBook)

Advances in Materials Science Research. Volume 64
Maryann C. Wythers (Editor)
2023. ISBN: 979-8-88697-935-0 (Hardcover)
2023. ISBN: 979-8-88697-992-3 (eBook)

Advances in Materials Science Research. Volume 63
Maryann C. Wythers (Editor)
2023. ISBN: 979-8-88697-791-2 (Hardcover)
2023. ISBN: 979-8-88697-926-8 (eBook)

Advances in Materials Science Research. Volume 62
Maryann C. Wythers (Editor)
2023. ISBN: 979-8-88697-777-6 (Hardcover)
2023. ISBN: 979-8-88697-925-1 (eBook)

Advances in Materials Science Research. Volume 61
Maryann C. Wythers (Editor)
2023. ISBN: 979-8-88697-689-2 (Hardcover)
2023. ISBN: 979-8-88697-900-8 (eBook)

Advances in Materials Science Research. Volume 60
Maryann C. Wythers (Editor)
2023. ISBN: 979-8-88697-543-7 (Hardcover)
2023. ISBN: 979-8-88697-631-1 (eBook)

More information about this series can be found at
https://novapublishers.com/product-category/series/advances-in-materials-science-research/

Maryann C. Wythers
Editor

Advances in Materials Science Research

Volume 65

nova
science publishers
www.novapublishers.com

Library of Congress Cataloging-in-Publication Data

ISBN: 979-8-89113-112-5(eBook)
ISSN: 2159-1997

Published by Nova Science Publishers, Inc. † New York

Contents

Preface

This volume contains eight chapters that detail advances in materials science research. Chapter One provides a comprehensive overview of modern materials utilized in various components of supercapacitors, including electrode materials, electrolyte materials, current collectors, binders, and separators. Chapter Two reports on the electrochemical deposition of corrosion-resistant and protective coatings from a recently developed new generation of ionic liquids, the so-called deep eutectic solvents (DES). Chapter Three discusses a study that aims to diminish the raw material from petroleum in plastic production. Chapter Four presents recent advances in Fourier Transform Infrared (FTIR) studies of Co-MOFs. Chapter Five aims to explain how to characterize the structure of the organic metal cobalt framework-74 (Co-MOF-74) material using scanning electron microscopy (SEM). Chapter Six provides an in-depth explanation of the thermal characterization of pure and modified Co-MOF-74 materials (Mn, TTF, NDHPI, and Ni) using Thermogravimetric Analysis (TGA). Chapter Seven gives an in-depth explanation of how to characterize the structure of currently prepared Co-MOF materials using a Transmission Electron Microscope (TEM). Lastly, Chapter Eight details the phase states and surface electrical activity of the low-temperature synthesized fine PbZr1−xTixO3 powders.

Chapter 1

Electrochemical Supercapacitors: Promising Energy Storage Devices for Sustainable Power Supply and Agricultural Applications

Huda. F. Khalil[1,*]
Sara Gad[1]
Merna Fahmy[2]
Noura M. Ahmed[2]
Mai I. Mohamed[3]
Hana Elmoatsem Bellah[4]
Rania Emara[4]
and Mohamed Hafez[5,†]

[1]Electronic Materials Department, advanced Technology and New Material Institute (ATNMI), City of Scientific Research and Technological Applications (SRTA-City), Alexandria, Egypt
[2]Physics Department, Faculty of Science, Alexandria University, Alexandria, Egypt
[3]Biotechnology Department, Faculty of Science, Alexandria University, Alexandria, Egypt
[4]Chemistry Department, Faculty of Science, Alexandria University, Alexandria, Egypt
[5]Land and Water Technologies Department, Arid Lands Cultivation Research Institute, City of Scientific Research and Technological Applications, New Borg El-Arab, Egypt

[*] Corresponding Author's Email: Hfarid@srtacity.sci.eg .
[†] Corresponding Author's Email mhafez290@yahoo.com.

In: Advances in Materials Science Research. Volume 65
Editor: Maryann C. Wythers
ISBN: 979-8-89113-090-6

Abstract

As a result of the growing demand for clean, sustainable energy, as well as the benefits of high-power density, efficiency, and long-life expectancy, electrochemical supercapacitors have emerged as promising devices for energy storage and power supply. Perovskite anode materials have gained attention due to their charge storage process of oxygen-anion intercalation. This chapter provides a comprehensive overview of modern materials utilized in various components of supercapacitors, including electrode materials, electrolyte materials, current collectors, binders, and separators. It discusses a variety of electrode materials, such as carbon-based options, perovskites, conducting polymers, metal oxides, and composite materials. Green binder materials are compared to standard binders, and the chapter highlights the hybrid, asymmetric, and future aspects of supercapacitors. Furthermore, the chapter sheds light on the various ways supercapacitors can contribute to agricultural practices, offering sustainable and efficient power solutions. It explores their role in soil moisture management, precision agriculture, sensor networks, and other relevant areas. By harnessing the power of electrochemical supercapacitors, advancements in soil science and agricultural practices can be achieved.

Keywords: supercapacitor, perovskites, carbon electrode, agriculture, hybrid supercapacitors

Abbreviations

AC	Activated Carbon
ACA	Active Carbon Aerogel
ACC	Active Carbon fiber Cloth
AG	Activated Graphene
ASCs	Asymmetric Supercapacitors
BCN	Boron and Nitrogen-doped Carbon
BET	Brunaver, Emmett and Teller
CA	Carbon Aerogel
CBFFs	Carbon-Based Fibre Fabrics
CCO	Composite Cotton Carbon
CMC	Carboxymethylcellulose Codium
CNFs	Carbon Nanofibers
CNM	Co-Ni-Mn

CNTFF	Carbon Nanotube Fibre Fabric
CNTs	Carbon Nano Tubes
Co_3O_4	Cobalt Oxide
CPF	Carbonized Phenol Formaldehyde
CPs	Conducting Polymers
CV	Cyclic Voltammetry
DMF	Dimethylformamide
DWNTs	Double Wall Nano Tubes
EDLC	Electric Double Layer Capacitive
EES	Electrochemical Energy Storage
ES	Energy Source
ESPW	Electrochemically Stable Potential Window
ESs	Electrode Supercapacitors
FSCs	Fiber Supercapacitors
FSSCs	Fiber-Shaped Supercapacitors
Gd_2O_3	Gadolinium Oxide
GG	Guar Gum
GNW	Graphene Nanowalls
GO	Graphene Oxide
GONRs	Graphene Oxide Nanoribbons
GPEs	Gel Polymer Electrolytes
HFP	Hexafluoro Propylene
HSCs	Hybrid Supercapacitors
IHP	Inner Helmholtz Plane
ketone	Polyetheretherketone
$LaCoO_3$	Lanthanum Cobalt
$LaFeO_3$	Lanthanum Ferrite
$LaMnO_3$	Lanthanum Manganite
$LaNiO_3$	Lanthanum Nickel Oxide
$LaSrMnO_3$	Lanthanum Strontium Manganite
LDH	Layered Double Hydroxides
LIBs	Lithium Ion Batteries
MACA	Modified Activated Carbon Aerogel
MOF	Metal Organic Framework
MWCNT	Multi Wall Carbon Nano Tubes
MWNTs	Multi Wall Nano Tubes
Na_2SO_4	Sodium Sulfate
NACs	Nitrogen-doped Activated Carbon
NEC	Japanese multinational Information Technology provider

NF	Nickel Form
NiV	Nickel-Vanadium
ODA	Oxydianiline
OHP	Outer Helmholtz Plane
PAA	Polyacrylic Acid
PAN	Polyacrylonitrile
PANI	Polyaniline
PBI	Polybenzimidazole
PBM	$PrBaMn_2O_6$
PDA	Polydiacetylene
PEDOT	Poly-(3,4)-ethylenedioxythiophene
PEG	Polyethyleneglycol
PEO	Poly Ethyl Oxide
PF5	Penta Fluoride
PMDA	Pyromellitic Dianhydride
PMMA	Polymethylmethacrylate
PP	Polypropylene
PPA	Polyamic Acid
PPY	Polypyrrole
PS	Potato Starch
PTFE	Polytetrafluoroethylene
PVA	Polyvinylalcohol
PVDC	Polyvinylidene Chloride
PVDF	Polyvinylidene Fluoride
PVP/PVB	Polyvinylpyrrolidone/polyvinyl butyral poly ether
RF	Resorcinol Formaldehyde
rGO	reduced Graphene Oxide
SCs	Supercapacitors
SG	Small-size Graphene
SOHIO	Standard oil company of Cleveland Ohio
SPEEK	Sulfonated Polyetheretherketone
SrTiO3	Strontium Titanate
SSA	Specific Surface Area
SWNTs	Single Wall Nano Tubes
WS	Wheat Starch
ZnO	Zinc Oxide

Introduction

Nowadays everything depends on energy such as mobile phones, homes, cities, and the world. Huge amounts of energy are produced every day around the world using traditional methods such as the combustion of fossil fuels or through more advanced modern and sustainable technologies such as wind turbines and solar panels [1, 2]. This energy must be stored by using batteries or capacitors. A capacitor is a device that stores electrical energy in an electric field. It is a passive electronic component with two terminals, it consists of two conducting plates separated by a distance. But the energy density of batteries is higher than that of capacitors [3]. Therefore, research directed to develop the capacitor to obtain a larger capacity, which led to the discovery of the supercapacitor [4]. Supercapacitor, ultra-capacitors, electrochemical capacitors (EDLCs), or electrochemical capacitors are devices that store electrochemical energy and may be charged or discharged by connecting or removing a DC power source, respectively [5, 6]. The capacitance of supercapacitors is extremely high, ranging from a few to hundreds of Farads. Supercapacitors have a higher power density, virtually infinite cycle life, and higher charge/discharge efficiency when compared to current battery technologies [7, 8]. Supercapacitors are improved electric energy devices with substantially larger capacitance in very tiny packaging. They operate on a concept that is essentially the same as ordinary capacitors. Both of them have a dielectric between two electrodes (plates), but supercapacitors have a thinner dielectric and electrodes with a larger surface area, allowing for higher energy densities [9]. There are three types of supercapacitor shown in Figure 1 according to the mechanism of charge storage. Figure 1a shows the mechanism of energy storage in electric double-layer supercapacitors; Figure 1b shows the mechanism of energy storage in pseudo supercapacitors employing charge transfer reactions, i.e., by Faradaic reactions; Figure 1c shows the mechanism of energy storage in hybrid supercapacitors through a combination of electric double-layer formations and pseudo-Faraday reactions [10].

Because of the global energy crisis and increasing pollution, there has been a significant increase in research on new ways to make energy and make it go further in the past few years [11]. Much research has been committed to producing devices with numerous advantages, such as high efficiency, sustainability, environmental friendliness, and long service life. However, it could be more beneficial because it has less energy per unit volume than a battery. Several scientists are trying to solve this problem by making high-

energy-density supercapacitors with electrodes of suitable materials [12]. Carbon-based materials [13], conducting polymers [14], transition metal oxides and hydroxides [15, 16], and transition metal oxides are the four types of electrode materials utilized in supercapacitors.

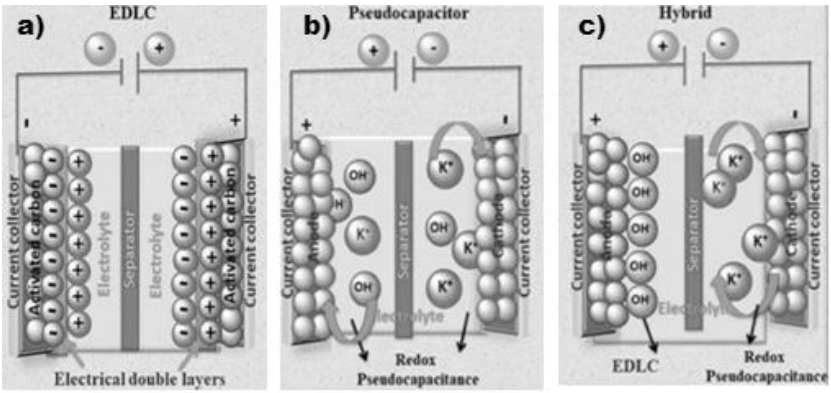

Figure 1. Mechanism of energy storage in a) electric double layer supercapacitors, b) pseudo supercapacitors, and c) hybrid supercapacitors [10]. Adapted with permission from Ref. [10] (Copyright 2019, RCS).

Carbon-based materials have a low energy density, are not chemically or thermally stable, and conduct electricity well [17]. Transition metal oxides and hydroxides have a higher energy density and electrochemical stability. Electrical double-layer capacitor (EDLC) electrode materials [18] and pseudocapacitance electrode materials [19] are used in supercapacitors. In EDLC electrode materials, charge accumulates at the interface between the electrolyte and the electrode surface. Hence, there is no electrochemical reaction involved in the charge storage process. As illustrated in Figure 2 (a), they have rectangular cyclic voltammetry (CV) curves and a linear connection between voltage and discharge duration (c). Chemical reactions happen at the interfaces between the electrolyte and the electrode surface or subsurface. These reactions store charge through ion intercalation or Faradaic redox reactions. Unlike battery electrode materials, pseudocapacitance materials do not require a phase transition [20]. The galvanostatic discharge curves of pseudocapacitive electrode materials are shown in Figure 2(c), while their CV curves are shown in Figure 2(b), (d), and (e). Figure 2(h) and (i) show the galvanostatic discharge and a typical CV curve for a battery electrode material. Because of this, the electrode materials of pseudocapacitance charge and discharge faster than batteries but slower than EDLC. Furthermore,

pseudocapacitance electrode materials are widely employed during the charge storage process with the EDLC behavior, demonstrating that pseudocapacitance has a greater specific capacitance [21]. Systematic research has been devoted to cation-intercalation-based electrode materials for pseudocapacitors because cation sizes are smaller than anions, implying that cations can be more easily intercalated into electrodes from electrolytes to produce efficient charge storage [22, 23].

Electrochemical supercapacitors have shown great potential in managing soil moisture levels in agricultural fields. By utilizing their high-power density and rapid charge-discharge capabilities, supercapacitors can efficiently control irrigation systems, optimizing water usage and reducing water waste [188]. This technology enables precise and automated irrigation, ensuring that plants receive the right amount of water at the right time, leading to improved water efficiency and enhanced crop productivity.

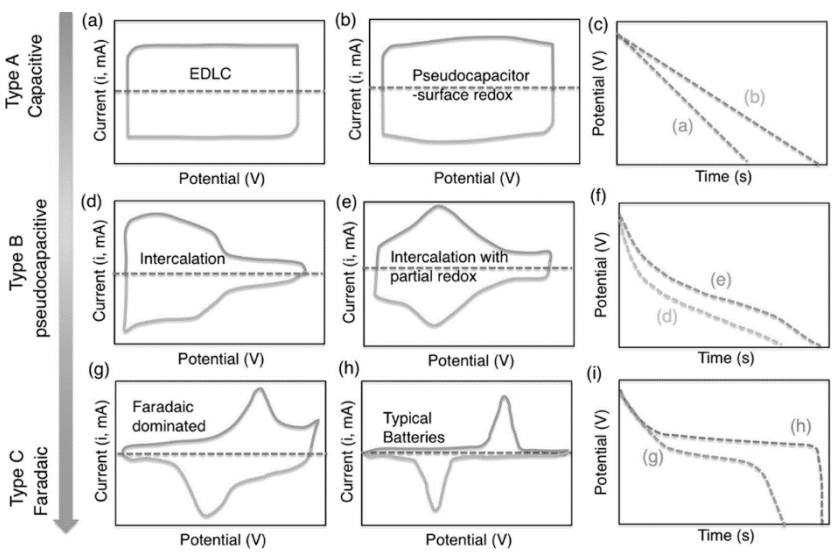

Figure 2. The CV curves of (a) EDLC materials, (b, d, e) pseudo capacitor materials, (g) battery-like materials, and (h) battery materials, as well as the related galvanostatic discharge curves for several types of energy-storage materials [23]. Adapted with permission from Ref. [23] (Copyright 2018, ACS).

Electrochemical supercapacitors play a crucial role in precision agriculture, which involves the use of advanced technologies for site-specific crop management. Supercapacitors can power sensors and monitoring devices deployed in agricultural fields, providing real-time data on soil conditions,

nutrient levels, and crop health. This information enables farmers to make informed decisions regarding irrigation, fertilization, and pest control, leading to optimized resource allocation and improved agricultural practices [189].

Supercapacitors offer reliable and sustainable power supply solutions for sensor networks used in soil sciences. These networks consist of numerous sensors deployed in the field to collect data on soil properties, temperature, humidity, and other relevant parameters. By incorporating supercapacitors, which can store and deliver energy efficiently, sensor networks can operate autonomously and continuously without the need for frequent battery replacements or external power sources [190]. This enhances the scalability and longevity of sensor networks, enabling comprehensive monitoring and analysis of soil conditions.

Historical Background and Present Status of the Supercapacitors

H. I. Becker of General Electric patented the first electrochemical capacitor device in 1957. Although double-layer charge storage was used with this device, it was impracticable due to the requirement to immerse it in the electrolyte [24]. Robert A. Rightmire, a Standard Oil Corporation of Ohio chemist, designed the conventional EC design used today (SOHIO). SOHIO could not identify a purpose for the application, but the design was patented to the Japanese company Nippon Electric Corporation (NEC). NEC introduced the first commercially effective EC, the “Supercapacitor,” in 1975. ECs are often called supercapacitors or ultracapacitors, but the only actual supercapacitor is NEC’s brand of ECs of the same name [25]. After NEC commercialized its idea, many other firms began designing their ECs. For example, the PSCap, an EC, is manufactured by ECOND and is used as a starter for diesel locomotive engines. The PSCap can be nine inches in diameter and two feet tall, with energy up to 45 kJ, voltages up to 200 V, and an RC time constant of less than a second. PSCap research began in 1978 but was completed in the mid-1990s. One Goldcap EC was developed to replace coin-cell batteries and was a massive hit in the market for solar-powered wristwatches. The second concept was a spirally coiled configuration aimed toward electric automobiles and hybrid electric vehicles. The spiral-wound capacitor, known as the UpCap, is rated at 2,000 F and has a voltage of 2.3V. It is also inexpensive, has low series resistance, and dissipates internally

generated heat, making it excellent for hybrid car applications [26]. Today, most electronic companies, including Maxwell, Tecate Group and Murata manufacture ECs. Most of the time, their product is used in transportation and energy systems. The automotive industry, hybrid transportation systems, grid stability, utility vehicles, and railway traction system are all current applications [24].

Battery vs. Supercapacitor

To store energy, batteries conduct chemical processes. These chemical reactions cause various resistive losses due to the flow of slow electrons. This generates heat when operating at high power, posing major safety concerns [27]. Although it is often used and has a high energy density, it lacks power density. This restricts its use in situations where an instant power explosion is necessary. The supercapacitor can supplement or even replace batteries in various applications. It can deliver quick charging, high power density, and long cycle life when combined with batteries. Because the charges are stored electrostatically, supercapacitors provide high power density. Because it does not experience any chemical changes during charge/discharge processes, supercapacitors have substantially higher cyclic stability than batteries. On the other hand, little energy density is provided because charge storage processes are constrained by the availability of the electrode surface [28].

Supercapacitors vs. Fuel Cells

The primary method for converting energy into electricity that is constantly used to create power is the fuel cell. It has a high energy density and produces no environmentally good byproducts. It is safe and needs little maintenance [29]. The high cost and complexity of fuel cell operation pose a significant barrier. It is susceptible to contamination, which shortens cell life. Also, the power density per unit volume could be higher, resulting in better efficiency. A supercapacitor, on the other hand, stores energy through physical adsorption. In general, carbon-based electrode materials are employed, which are environmentally friendly. Compared to fuel cells, the device's construction is simpler and less expensive. Since there are no chemical processes taking place during the charge/discharge operation, supercapacitors offer a long cycle life and high power density [30].

Conventional Capacitors vs. Supercapacitors

The conventional capacitor also called electrostatic capacitor has been limited to low-power application or short-term memory backup supply due to their low capacitance value. An electrostatic capacitor is made up of two conducting metal electrodes separated by non-conducting material, which acts as a dielectric medium [31] The operating voltage depends on the strength of the dielectric material, and the capacitance of the assembly is expressed as follows [32]:

$$C = {}^{Q}/_{V} \quad (1)$$

where C is the capacitance of the device, Q is the amount of charge stored, and V is the operating voltage. Also, the capacitance depends upon the area, A of conducting electrodes separated by distance d, and ε is the relative permittivity. Equation (2) can be expressed as follows [33]:

$$C = \varepsilon\left({}^{A}/_{d}\right) \quad (2)$$

Equation (2) suggests that capacitance increases by increasing the area of the electrode and decreasing the distance of charge separation [33]. The electric double-layer capacitor shares a similar charge storage mechanism with a dielectric capacitor. On the application of voltage, the polarization of electrolytic ions occurs, which acts as dielectric material in a supercapacitor. Supercapacitors show greater capacitance as compared to electrostatic capacitors. This is due to the porous behavior of electrode material, which allows a large number of electrolyte ions to get adsorbed at the surfaces [34]. The compact bilayer is called the Helmholtz layer and has a thickness ~1 nm. At the macroscopic level, according to (1.2), high surface area (A) of the electrode material and atomic range separation d between electronic and electrolyte ion charge at the electrode surface deliver higher capacitance value than the conventional electrostatic capacitor. The high surface area enables a large amount of charge to get stored, which increases its energy density over the electrostatic capacitor. The charge and discharge process are purely electrostatic, no chemical reactions are involved, and it delivers high-power density [34].

Classification of Supercapacitors Based on the Charge Storage Mechanism

Electric Double-Layer Capacitor (EDLC) (Capacitive Mechanism)

The electric double layer is a capacitive mechanism, which is seen in a device due to the application of electrostatic force. This bilayer formation is observed when the electronic conducting electrode material is immersed in an ion-conductive electrolyte. The arrangement of charges is noticed at the electrode–electrolyte interfaces, which is also called bilayer formation. The capacitance arises from the electrode potential-dependent accumulation of electrostatic charges at the interface. The most significant feature of EDLC is that no charge transfers occur between electrode and electrolyte interfaces [35]. Since a pure EDLC's charge storage process is non-Faradaic, no charge or mass is transported across the electrode-electrolyte interface during charging or discharging, leaving only electrostatic energy to be stored. In contrast to the Faradaic processes commonly found in battery electrodes, electrostatic interactions do not harm the structure and stability of the electrodes, so EDLCs can withstand 1,000 000 cycles of charge-discharge in organic electrolytes with less than 10% degradation. However, compared to rechargeable batteries, these devices' energy density is an order of magnitude smaller [36]. High power density and extended cycle life are two characteristics of EDLC. However, owing to the limited surface area, its energy density and specific capacitance are unsatisfactory [37].

During the discharge process, the reverse process takes place. No charge transfer occurs during charging and discharging. This shows that the electrolytic ion concentration remains constant [38], as shown in Figure 3. The capacitance arises from the physical adsorption of electrolyte ions at the electrode surface [39]. The whole charging and discharging mechanism of EDLC electrode material can be expressed by the following equations.

On the positive electrode,

$$S_1 + A^- \xrightarrow{charging} S_1{}^+ \parallel A^- + e^- \xrightarrow{discharging} S_1 + A^- \quad (3)$$

On the negative electrode,

$$S_2 + C^+ + e^- \xrightarrow{charging} S_2{}^- \parallel C^+ \xrightarrow{discharging} S_2 + C^+ + e^- \quad (4)$$

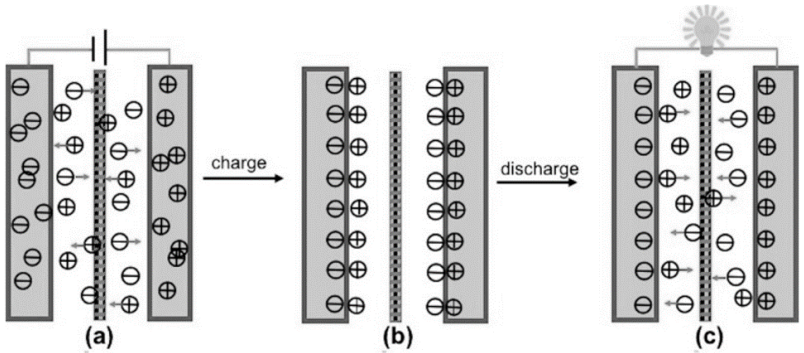

Figure 2. Schematic illustration of charge/discharge process in EDLC. (a) The charging process, (b) EDLC after charging, and (c) the discharging process [38]. Adapted with permission from Ref. [38] (Copyright 2018, MPDI).

The two electrode surfaces are expressed as S_1 and S_2, anions are expressed as A^-, cations are expressed as C^+, and electrode–electrolyte interface is depicted as follows [40]. The formation of the bilayer at the interface and the interaction of electrolytic ions at the electrode surface are explained by several theories and models [41].

Helmholtz Model

This model explains the simplest theory for the spatial distribution of charges at the bilayer interfaces. The theory considers a rigid layer of charges, which is formed to counterbalance the charges from the electrode surface. The distance d is the distance between the layer of two opposite charges. Although this model is the simplest, it does not explain the other phenomena of double-layer formation [42].

Gouy–Chapman or Diffuse Model

This model explains that ionic charges are present in the electrolyte surrounding the charged particles but they are not rigidly attached to the charged surface. This theory contradicts the Helmholtz theory, which explains that electrolytic ions are rigidly attached to a charged surface at distance d. The electrolytic ions diffuse over a distance into the liquid phase forming a

diffuse layer. The kinetic energy of the ions partially determines the thickness of the diffuse layer. Gouy–Chapman's theory for double-layer formation follows Boltzmann distribution for ions, where ion concentration plays an important role to explain the thickness of the diffuse layer. For a highly charged double layer, this model fails to explain the charge accumulation [42].

Stern Modification of Diffuse Double Layer

The Gouy–Chapman model assumes that the ions are point charged and an approach to the charged surface with no limits. Stern modified this assumption by assuming that ions possess finite sizes. So, ions can approach the charged surface having some distance. The Stern model depicts that there is a surface adsorbed ion in the plane having distance δ, where δ is the distance of the first layer of ions from the surface. This layer is called the Stern layer. This layer consists of electrolytic ions, which strongly get adsorbed at the electrode surface resulting in the formation of a compact layer called the inner Helmholtz plane (IHP). After this layer, poorly adsorbed counter ions form the outer Helmholtz plane (OHP), ψ denotes the potential, and ψo is the electrode potential. The Stern model explains a better approach to reality than the other two models. The above model provides a satisfactory explanation for the double-layer formation on the plane surfaces. These models have a major shortcoming to describe real charge distribution in a hierarchical pore structure containing pores of multiple sizes and shapes. The pore size greatly influences the mobility of ions, where a very small pore size makes it inaccessible for ions to get adsorbed, hence not contributing to the double-layer formation [42]. This suggests that there is no linear relation between the capacitance of the material and its specific surface area. Generally, the surface area of the electrode material is measured by the small gas molecules such as nitrogen, argon, and helium, whose size is smaller than electrolytic ions. So, the process of charge/discharge in an electric double-layer capacitor involves the rearrangement of ions at the electrode surface, without undergoing any Faradaic reaction. This makes it highly reversible having extremely large cyclic stability [42].

Component of Supercapacitor

The supercapacitors' parts and structure resemble those of batteries. A supercapacitor device's parts are made from [43]:

1. Electrode material
2. Electrolyte material
3. Current collector
4. Binders
5. Separators

Electrode Material

Since the sort of electrode-active materials utilized determines how much charge can be stored inside a supercapacitor, the electrode is part of the supercapacitor that is active. Good electrical conductivity, a high surface area, a strong porous structure, and good redox activity are all qualities that electrodes should possess. There are many types of an electrode material such as [44]:

1. Carbon-based electrode material
2. Perovskites
3. Metal oxides
4. Conducting polymers
5. Composite materials

Carbon-Based Electrode Material

Because the performance of these devices depends greatly on the electrode materials, carbon-based nanomaterials have emerged as incredibly promising components [44]. In this item, the different forms of carbon and their performance in the manufacture of supercapacitors were discussed.

Activated carbon: was the first material chosen for EDLC electrodes [44]. Even though its electrical conductivity is approximately 0.003% that of metals (1,250 to 2,000 S/m), it is sufficient for supercapacitors, it is derived from biomass have become one of the most promising electrode materials for supercapacitors due to their reproducibility and low cost, it has abundant pore structure and high specific surface area, which is the ideal material for

supercapacitor electrodes. The conductivity of the material is also affected by the particle size of activated carbon and the density of its active layer, it can often achieve capacitances as high as 100 to 200 F. in aqueous electrolyte systems and 50 to 150 F in organic media [45]. Activated carbon can be produced in two steps and involves either chemical or physical activation from various types of carbon-rich organic precursors such as fossil fuels, coke or synthetic polymers, wood, and coconut shells. In this section, the manufacture of activated carbon from many different sources and its electrochemical properties were discussed [45, 46]. Table 1 shows some different sources of activated carbon.

Carbon Aerogel: a type of high-surface-area material produced via sol-gel chemistry. Because of their high mass-specific surface area, electrical conductivity, environmental compatibility, and chemical inertness, they are particularly promising materials for a wide range of energy-related applications [54]. Aerogels are an open-cell foam category that contains materials with unusual properties such as low mass densities, continuous porosities, and huge surface areas. These unique properties are due to the aerogel microstructure, which is typically composed of three-dimensional networks of connected primary particles the size of a nanometer. Sol-gel chemistry is used to transform molecular precursors into strongly cross-linked inorganic or organic gels, which can subsequently be dried using specialized processes (such as supercritical drying, freeze drying, etc.) to maintain the fragile solid network. Polymerization of multiple-functional organic species into three-dimensional polymer networks for organic and carbon aerogels is involved in this process [55]. Brunaver, Emmett, and Teller (BET) surface measurement, constant-current charge-discharge [56]. Table 2 illustrates the attributes of several aerogel production methods.

Graphene: is a novel advanced carbon material with a distinctive shape [44], and it is expected to be a strong conductor due to its improved conductivity, due to graphene's large specific surface area, which can reach 2630 m^2/g [57]. Table. 3 displays the features of various graphene manufacturing processes. The highest capacitance was discovered in graphene oxide, which was attributed to oxygen functional groups, which also caused pseudo-capacitance [58].

Carbon nanotubes: They are cylindrical nanostructures with near-1-dimensional structures. The cylinders are made up of graphitic carbon walls that come in single, double, and multiwall varieties (MWNTs) [44].

Table 1. Different sources of activated carbon

Carbon Source	Electrolyte	Specific capacitance	Surface Area	Energy Density	Power density	Ref
Sweet-Lime-Peels	aqueous electrolyte	421.67 F/g (at 1 A/g)	667.87m^2/g	45.52 Wh/kg	-	[47]
Rice Husk	KOH	147 F/g	2696 m^2/g	5 Wh/kg	25 w/kg	[48]
Willow Wood	Na_2SO_4	197 F/g	2800 m^2/g	32 Wh/kg	10000 w/kg	[49]
Pineapple Crown.	Solution of H_2SO_4	150 F/g	700 m^2/g	5.2 wh/kg	42 w/kg	[50]
Banana Leaves	Na_2SO_4	55 F/g	1469 m^2/g	2.75 wh/kg	300 W/kg	[51]
	$TEABF_4$/AN	114 F/g		22.5 wh/kg	600 W/kg	
	$[BMIM][PF_6]$	190 F/g		59 wh/kg	750 W/kg	
Oak seeds-650ºC	H_2SO_4	552 F/g	2896 m^2/g	34 wh/kg	336 W/kg	[52]
Syzygium oleana leaves	H_2SO_4	188 F/g At 1mV/s	216 to 1218 m^2/g	26 wh/kg	96 W/kg	[53]

Table 2. Different methods for carbon aerogel synthesis and their physical properties

Carbon aerogel method	Specific Surface area (m^2/g)	Current density (mA/cm^2)	Specific capacitance (F/g)	Energy delivered (wh/kg)	Ref
Pyrolysis of resorcinol formaldehyde (RF) (CA)	661	~3	~48	~13	[56]
		~6	~46	~11	
		~12	~43	~9	
		~24	~40	~6	
		~50	~34	~3	
Pyrolysis of resorcinol formaldehyde (RF) followed by activation under CO2 flow at 1000 C for 1 h (ACA)	1408	~3	~101	~26	[56]
		~6	~95	~22	
		~12	~82	~16	
		~24	~71	~8	
		~50	~53	~2	
Pyrolysis of resorcinol formaldehyde (RF) followed by modification with a surfactant sodium oleate solution (MACA)	1342	~3	~110	~29	[56]
		~6	~104	~25	
		~12	~97	~20	
		~24	~87	~13	
		~50	~76	~5	

Table 3. The properties of the different production processes of graphene

Material	Electrolyte	Specific capacitance (F/g)	Ref
Graphene oxide	6 M KOH	154 (at 0.5A/g)	[58]
Anodic electrochemically exfoliated graphene	-	44	[58]
Graphene nano-spheres	6 M KOH	529 (at 1A/g)	[59]

CNTs have a distinct structure, a narrow size distribution in the nanometer range, a large amount of easily accessible surface area, low resistance, and excellent stability [60], functionalized MWCNTs had a specific area of 430 m^2/g, a gravimetric capacitance of 102 F/g, and an energy density of 0.5 Wh/kg obtained at 1 Hz on a single cell device [61].

Perovskites Are a Type of Energy-Storage Molecule Known as a "Halide"

Although oxygen-anion intercalation has been proposed as a charge storage method for perovskites, and numerous perovskites have been described as pseudocapacitance materials, many researchers are still confused to which category of energy-storage material perovskites belong. Perovskites retain their crystal structure during charge and discharge due to the oxygen-anion intercalation mechanism that explains how they store charge. This hypothesis proposes a way for intercalating pseudo-capacitors. However, lithium-ion battery behavior in terms of lithium-ion intercalation has been explained, and phase transitions exist. Concurrently with the publication of this method, the $LaMnO_3$ used in the study demonstrated pseudo-capacitor behavior and transmitted an easily confused signal, implying that perovskites were pseudocapacitance materials. Another misunderstanding is that all perovskites are pseudocapacitance materials, which results from a long-standing misunderstanding of the terms "pseudo-capacitor" and "battery." Perovskites' electrochemical properties are investigated in order to classify them as either pseudocapacitance or battery-like materials [62].

The CV curves of $La_{0.75}Sr_{0.15}MnO_3$ [63], $LaNiO_3$ [64], and $SrCoO_3$ [65] electrolytes in KOH were previously discussed. Every perovskite of them, with the exception of $La_{0.75}Sr_{0.15}MnO_3$, has a pair of redox peaks. The $La_{0.75}Sr_{0.15}MnO_3$ curve is structured like a raked rectangle, with nearly continuous anodic and cathodic redox peaks. As a result, $La_{0.75}Sr_{0.15}MnO_3$is a pseudo-capacitor material that can be used as a perovskite electrode [63], however the redox peaks of $LaNiO_3$ [64] and $SrCoO_3$ [65] are very different. These should be regarded as pseudo-capacitor material. In that situation, their integral area should be as small as possible inside a section of the potential window, and their capacitance should be independent of it. As the potential window spanned from 0.2 to 0.45 V, the integral area of $LaNiO_3$ became significantly larger. However, it was insignificant when the window ranged from 0 to 0.2 V, showing that minerals such as $LaNiO_3$ are insignificant [64].

Table 4 summarizes some of the results from the previous studies [66-74] on perovskite electrode materials for anion-intercalation supercapacitors. The research on anode perovskite materials grows to include diverse perovskites such as A site element-doped $A_{1-x}A'_xMnO_3$ perovskites, B site element-doped $AB_{1-x}B'_xO_3$ perovskites, and perovskite composites such as $LaMnO_3/SiO_2$.

Metal Oxides

As electrode materials for pseudo-capacitors, transition metal oxides, such as ruthenium oxide (RuO_2), cobalt oxide (Co_3O_4) and manganese dioxide (MnO_2) and nickel oxides (NiO) have received extensive research [75], Transitional metal oxide materials have been identified as promising candidates to be used as electrodes of energy storage devices because of their accessibility, abundant reserves, environmental friendliness, and other intriguing qualities like their large surface area, varied constituents and morphologies, and high theoretical specific capacitance [76]. Table 5 displays how various metal oxide electrodes behave [77-81].

Conducting Polymers

Conducting polymers (CPs), which have a unique combination of features including tunable electrical conductivity, ease of fabrication, light weight, and ease of processing, have recently attracted the interest of the research community. These distinctive properties enable the usage of CPs in a wide range of exciting applications, including contemporary electrochemical devices. Two popular synthesis strategies for the creation of CPs are chemical and electrochemical polymerization methods. It is easy to customize the electrical conductivity of CPs by adjusting the doping kinds and concentrations [82], CPs are another class of pseudocapacitive materials. Among the most popular varieties (PEDOT) are polypyrrole (PPy), polyaniline (PANI), and poly-(3,4)-ethylenedioxythiophene, which have theoretical maximum specific capacitances of 1000 F/g, or nearly twice as high as EDLC[83], The intrinsic conductivity of CPs is a result of this sort of bonding because the basic polymer chain of CPs contains both single and double bonds[82]. Physical proprieties of some conducting polymers are collected in Table 6 [83-88].

Table 4. Behaviour of some perovskite material for supercapacitor electrode

Perovskite material		Synthesis method	Capacitance (F/g)	Scan rate/ Current density	Electrolyte	Energy density (Wh /kg)	Power density (W/kg)	Potential window	Ref
$LaNiO_3$ (nanoparticles) 700ºC		Co-precipitation	206.37	2 mV/s	1 M KOH aqueous solution	-	-	-	[66]
			212.86	2 A/g					
La_2CoMnO_6 (Hollow sphere)		Impregnating carbon sphere template	376	1 A/g	1 M Na_2SO_4	65.8	20000	2 V	[67]
$SrTiO_3$ (Film thickness 1µm)		Sol-gel technique	592	5 mV/s	3 M KOH	27.8	1921	-	[68]
$LaMO_3$ (nanofibers)	M = Fe	Electro-spinning approach coupled with calcination process	183.6	1 A/g	6 M KOH	-	-	-	[69]
			110.16	2 A/g		-	-	-	
			102.31	3 A/g		-	-	-	
			97.87	4 A/g		-	-	-	
			92.98	5 A/g		-	-	-	
	M = Co		95.8	1 A/g		-	-	-	
			90.4	2 A/g		-	-	-	
			85.7	3 A/g		-	-	-	
			81.8	4 A/g		-	-	-	
			78.2	5 A/g		-	-	-	
	M = Ni		116.3	1 A/g		-	-	-	
			110.6	2 A/g		-	-	-	
			106.1	3 A/g		-	-	-	
			101.7	4 A/g		-	-	-	
			78.2	5 A/g		-	-	-	

Perovskite material		Synthesis method	Capacitance (F/g)	Scan rate/ Current density	Electrolyte	Energy density (Wh /kg)	Power density (W/kg)	Potential window	Ref
$La_{0.85}$ $Sr_{0.15}MnO_3$		Sol-gel	102	1 A/g	1 M KOH	3.6	120	-	[70]
$CoTiO_3$ (nanoparticle-embedded mesoporous)		Sol-gel	608.4	-	2 M OH	9.77	4835.7		[71]
$CeMO_3$	M = Co	Electro-spinning	128	0.5 A/g	6 M KOH	-	-	-	[72]
	M = Ni		189	0.5 A/g		-	-	-	
	M = Cu		117	0.5 A/g		-	-	-	
$LaFeO_3$		Calcining the MOF (metal organic framework) gel template	241.3	1 A/g		34	900	1.8	[73]
Honeycomb $LaMnO_3$ (600^oC)		Sol-gel	535	1 A/g	3 M KOH	74.3	500	-	[74]
			278	2 A/g		38.6	500		
			157	4 A/g		21.8	500		
			101	8 A/g		14	499		
			89	16 A/g		12.4	510.6		

Table 5. The behavior of different metal oxides electrode

Material	Structure	Surface area (m^2/g)	Specific capacitance (F/g)	Pore radius (nm)	Mean particle size (nm)	Scan rate /current density	Ref
Co_3O_4	solid	28.57	102.5 (Nano wire)	1.64	218	1A/g	[77]
	hollow	98.80	146	1.59	202	3 A/g	
Fe_2O_3	solid	69.48	40 (Bulk)	1.82	426	1A/g	[77, 78]
	hollow	125.40	81	1.95	215	10 mV/s	
SnO_2	solid	10.35	34.85 (Nano particle)	2.39	179	100 mV/s	[77, 79]
	hollow	30.91	109	1.70	390	1 A/g	
Mn_3O_4	solid	30.63	91.8 (Nano particle)	1.71	310	1 A/g	[77, 80]
	hollow	40.17	72	1.59	250	1 A/g	
Cu_2O	solid	4.13	144 (micro-structure)	1.71	274	0.1 A/g	[77, 81]
	hollow	10.35	154	2.39	160	1 A/g	

Table 6. Behavior of some conducting polymers

Electrode material	Electrolyte	Specific capacitance (F/g)	Scan rate/current density	Reference
PAn NW/CC	1M H_2SO_4	1079	1.73A/g	[83]
CNT/PPy/MnO_2 sponge	2M KCl	305.9	2mV/s	[84]
PPy/VGCF	6M KOH	588	30mV/s	[85]
G-PEDOT	2M HCl	304	10 mV/s	[86]
	2M H_2SO_4	261	10 mV/s	
Polyaniline/graphene/Fe_2O_3 hydrogel	1M H_2SO_4	1124	0.25A/g	[87]
Polythiophene-graphite graphene oxide	1M KOH	971	1A/g	[88]
Carbonized ron/polyaniline/graphene Ni foam	1M $NaNO_3$	69.9	1A/g	[89]

Composite Materials

A macroscopic blend of two or more distinct materials with a finite interface is referred to as a composite material. Due to their superior bending, stretching, and compression capabilities compared to single-component materials, composite materials with particular components and distinctive architectures have recently attracted a lot of interest as flexible EES devices [90].

ZnO Based Composite Material

Due to their benefits like low-cost, high-energy density, good electrochemical reversibility, environmental protection, high specific capacitance, good cycling stability, high power density and simplicity of preparation, composite materials based on zinc oxide are promising materials for advanced supercapacitors. ZnO composites with a variety of other materials have been attempted by researchers, as shown in Figure 3 [91].

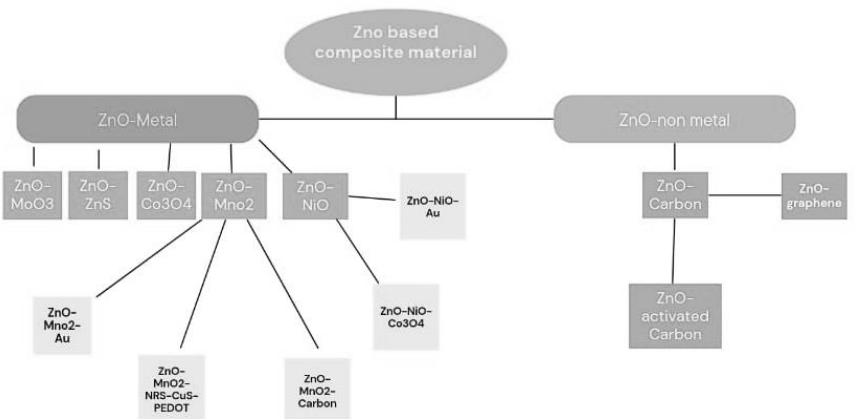

Figure 3. Some of ZnO based composite materials for advanced SCs.

The ideal porous electrode composite materials for supercapacitor electrodes have a large surface area, a suitable pore size, and a short electrolyte ion diffusion distance in the pore channels. Porous silicon composite zinc oxide nanoparticles with exceptional cycle performance and stability have been produced by combining vacuum filtration, homogenizing, and hydrothermal methods. The composite material of the specific capacitance is 40 times greater than pure porous silicon, measuring at 3.9 mFg^{-1} [92]. The combination of increased electrical conductivity and high-performance electron and ion transport channels has attracted the most interest in research

for high-performance supercapacitor applications in binary metal oxides with well-morphologically optimized electrode materials. A straightforward coprecipitation method produces $ZnCo_2O_4$ nanoparticles using NaOH and urea as precipitation ingredients. A composite material has been made to increase electrical conductivity by adding the proper carbon material, such as carbon nanotubes (CNT). The three-electrode method was used to calculate the generated material's specific capacitance, and the most efficient $ZnCo_2O_4$/CNT electrode produced a moderate 888 Fg^{-1} capacitance at 1 Ag^{-1} in 3M KOH with 94.72% cycling stability still present after 5000 charge-discharge cycles [93].

Carbon-Based Composite Materials

Carbon-based composite materials have received interest as supercapacitor electrode materials because of their extensive surface area and solid electrochemical conductivity. Many scientists have created carbon-based composite supercapacitors with high specific capacitance and outstanding cycle stability. Hence, carbon composites are a material that shows the highest promise for supercapacitor electrodes [94].

Zhou et al. reported a supercapacitor made of graphene nanowalls (GNW) on nickel foam with a capacitance of 0.053 F/cm^3 using a three-electrode configuration with a scan rate of 50 mV/s. After 800 rounds of charging and discharging, the electrode only slightly deteriorated (10%) [95]. An all-solid-state bendable supercapacitor was created using MWCNTs/PEDOT as the electrode material and PVA-H_3PO_4 gel as the electrolyte. The device illustrated wearable electronics' potential and showed an accurate capacitance of 32.06 mF/cm^2 [96]. Multiwalled carbon nanotube graphene oxide, nanoribbon@graphitic carbon nitride/NiCo layered double hydroxide/nickel foam (MWCNTs-GONRs@g-C_3N_4 /Ni single bond Co-LDH/NF), also known as MW-CN-LDH, is prepared by a single step microwave-assisted method using MWCNTs-GONRs@g-C_3N_4 as a novel carbon composite material. Adhesives and electrode impedance are both prevented. Consequently, the MW-CN-LDH electrode exhibits outstanding efficacy (75.81% capacitance retention at 20 Ag) and high specific capacitance (2532.80 Fg^{-1} at 1 Ag^{-1}). With a high capacitance of 193.36 Fg^{-1} and a high cycle life of 91.92% capacitance retention after 10,000 cycles, the MW-CN-LDH/AC (active carbon) supercapacitor is an excellent choice. The greatest energy density is also attained (77.61 Wh kg^{-1} at 0.85 kW kg^{-1}). With this synthetic technique, high-performance supercapacitors can be produced rapidly, paving the way for their widespread use in the future [97]. The solvothermal method and

calcination successfully manufacture a composite cotton carbon/Co-Ni-Mn LDH (CCO/CNM) material that combines cotton carbon with the metal-organic framework (ZIF-67). Concurrently, the effect of load on the sacrificial template CCO/ZIF-67 and the electrochemical performance of CCO/CNM are investigated further, and it is discovered that the optimized CCO/Co-Ni-Mn LDH-2 (CCO/CNM-2) composite electrode has outstanding electrochemical characteristics. CCO/CNM-2 electrode materials with high specific capacitance may be computed with a current density of 1 A g^{-1} as 2995.56 F g^{-1}. Moreover, when the current density is adjusted to 10 A g^{-1}, the capacitance value retains 91.8% of its original capacitance after 5000 charging and discharging cycles [98].

Perovskite Oxides: Selecting the Appropriate Ones for Their Desirable Electrical Properties

The electrical properties of perovskites are influenced by their structural makeup. When the B element is replaced by the B′ element, a larger 180° angle and a shorter bond length are produced, which essentially decide the (B-O-B) angle and the B-O bond length of the material [99]. The B sites are displaced, and the A ion's radius is reduced when other B′ elements are doped. The B′ and B degeneracy thus becomes better. The perovskites become silverier [100]. Another change and potential growth are in the number of oxygen vacancies. Diffusion resistance decreases as the quantity increases [101]. Even more intriguingly, the temperature can affect the (electrical properties). Due to their structure's high stability and high oxygen diffusion rate, distinguishing them from metals, most perovskites can achieve high conductivity at high temperatures [102]. The perovskite structure affects additional characteristics like catalytic activity [103], Magnetism [104], and thermoelectricity [105].

The oxygen vacancy significantly impacts the conductivity and ionic movement of electrode materials. The electrical characteristics of $PrBaMn_2O_{6-\delta}$ (f-PBM) and its reduction to $PrBaMn_2O_{6-\delta}$ were studied by Liu et al. [106]. The specific capacity of r-PBM is considerably higher than that of f-BPM, which is 64.21 mA h g^{-1}, at the same current density of 1 A g^{-1} (462.3 F g^{-1}). The overall density of states for both materials and the oxygen diffusion rate were measured to comprehend this occurrence better. Compared to f-PBM, r-PBM has a considerably higher oxygen diffusion rate. Additionally, until the decrease time reaches (45 min), the oxygen diffusion rate of r-PBM rises, suggesting a suitable oxygen vacancy concentration that will increase the oxygen diffusion rate. Perovskite structure may be destroyed by a rise in oxygen vacancy concentration, which would lower the oxygen diffusion rate.

r- PBM with a single cubic phase shows the orbital crossing of the fermi level in terms of the total density of states, proving its metallic property in the ground state by density functional theory. The hexagonal phase of f-PBM, in contrast to the cubic phase, has a tiny band gap of 1.39 eV, indicating poor electronic conductivity. The electrochemical performance of perovskite electrodes may be improved by increasing the oxygen diffusion rate and conductivity at the right oxygen vacancy content. Element doping, as covered in the chapter after this one, could modify the oxygen vacancy content in perovskites. Calcium doping was used by Mo et al. [107] to regulate the oxygen vacancy concentration of $LaMnO_3$. $La_{1-x}Ca_xMnO_3$ plates' electrical properties were studied using electrochemical impedance spectroscopy. (EIS). The electrode materials $La_{0.8}Ca_{0.2}MnO_3$, $La_{0.67}Ca_{0.33}MnO_3$, $La_{0.5}Ca_{0.5}MnO_3$, and $La_{0.25}Ca_{0.75}MnO_3$ had internal resistances (Rs) of 2.22, 2.17, 2.13, and 2.36, respectively. These electrodes' charge transfer resistance (Rct) calculated values were 4.58, 1.21, 2.16, and 16.58, respectively. Rct and Rs were correlated with the charge transfer rate in electrode materials and the conductivity of the electrode material, respectively. Similar conclusions were made by Lang et al. [108] and Cao et al. [109] regarding the relationship between the oxygen passage rate in perovskites and the charge transfer rate in electrode materials. The oxygen vacancy concentration of perovskites rises with adequate element doping, which raises conductivity and oxygen diffusion rate. The fourth period and the transition metals of the VII B and VIII groups, particularly manganese, iron, cobalt, and nickel, have received the most attention in studies on perovskite electrode materials for anion-intercalation energy storage devices up to this point, with other transition metals being infrequently investigated. B site elements should be selected from the subset IV B to VIII because A site elements have bivalent or trivalent valence. Most of the B site elements' valences are +2 and +3 when the oxygen in perovskite is sub-stoichiometric; otherwise, some of the B site elements' valences are +4. As was already mentioned, the valence shift of the components in the B site primarily controls the charge storage of perovskite. The ionization energy of B site elements is influenced by both the stored charge and the reversibility of faradic redox. Similar to the valence change ionization energy differential of Mn, Ti, Zr, V, and Nb also have high ionization energies. In addition to those previously mentioned, Mn, Fe, Ni, and Co these elements may have promise as perovskite electrode B site components.

For cation-intercalation-based supercapacitors, significant research has been done on materials like Nb_2O_5 [110] and TiO_2 [111]. However, both exhibit poor conductivity and limited specific capacitance [112]. Additionally,

Nb and Ti have valences of +5 and +4, respectively. Nb_2O_5 and TiO_2 have few uses for anion-intercalation supercapacitors because they are infrequently subjected to further oxidation. $La_{0.33}NbO_3$ [113] with a perovskite-like structure is used in all-solid-state lithium-ion electrolytes because lacking the A site promotes lithium-ion transfer. Nb is primarily found in the +4 and +5 valence states concerning oxygen gaps. La0.33NbO3 can be used as an anode in a supercapacitor that uses anion intercalation. After hydrogen treatment, Pb (Zr, Ti)O_3 exhibits the same reduction in resistivity as a traditional piezoelectric ceramic [114]. Because of the low resistivity created after appropriate hydrogen treatment due to the increased Ti^{3+} and Zr^{3+} acquisition due to this phenomenon, decreased Pb (Zr, Ti)O_3 can function as an anode for an anion-intercalation supercapacitor. Further oxidation of these valence-low elements may produce a cathode with a high specific capacitance. The oxygen vacancy content can be controlled in a variety of ways to enhance the electrochemical performance of perovskites. Many (perovskite oxides) should be investigated further as anodes for anion-intercalation supercapacitors.

Other Composite Material

Due to their high electronic conductivity, variable oxidation states, large surface area, and porous structure, transition metal dichalcogenides-based composite materials have recently gained popularity as supercapacitor electrode materials. A composite material based on $MoSe_2$ as electrode is prepared using a conventional one-step hydrothermal strategy, and M@AC 1:5 electrode displays the highest specific capacity of all prepared composite electrodes (514 F g^{-1} for voltage window 1 V at a scan rate of 10 mV s^{-1} in KOH electrolyte solution) [115]. Composite materials made of Fe_3O_4 and poly pyrrole (Fe_3O_4@PPy) could be synthesized selectively to improve the conductivity of hybrid materials. When used as an electrode material for supercapacitors, the resulting Fe_3O_4@PPy composite material displays a high specific capacitance of 290.2 F g^{-1} at a current density of 1 A g^{-1}. To further improve energy density, the asymmetric coin supercapacitor (Fe_3O_4@PPy/ MoO_3) has been developed. It exhibits a high energy density of 26.6 W h Kg^{-1} as well as a power density of 700 W Kg^{-1} [116]. A composite material electrode composed of $NiCo_2O_4$ and MnO_2 was produced by using a hydrothermal method, electrodeposition, annealing, and simple drying. A number of electrochemical experiments were then used to measure the electrochemical properties. The final electrode displays a pleasing cycling stability of 87.5% (3000 cycles) and a noteworthy specific capacitance of 1485.24 F.g^{-1} (2 A g^{-1}) in contrast to the starting electrode [117].

The simple hydrothermal method used to create the SnS_2/g-C_3N_4 composite has shown it to be a viable option for the electrode materials used in supercapacitor uses. Even at a relatively high current density of 10 A g^{-1}, the SnS_2/g-C_3N_4 composite shows good cycling stability with capacitance retention of 95.8% after 15000 cycles. Additionally, it exhibits a reasonable specific capacitance of 552 F.g^{-1} at 0.5 A g^{-1} current density in 3 M KOH [118]. Using a straightforward chemical process, core-shell nanostructured $NiCo_2S_4$@NiV-LDH/NF composite material was produced. $NiCo_2S_4$@NiV-LDH/NF-1, $NiCo_2S_4$@NiV-LDH/NF-2, and $NiCo_2S_4$@NiV-LDH/NF-3 were also created by changing the concentration of sulphur. Due to the components' synergistic reactivity, the $NiCo_2S_4$@NiV-LDH/NF-2 composite material shows good electrochemical performance. The specific volume is 1778.8 C g^{-1} at 1 A g^{-1}. (3557.6 F g^{-1}). Furthermore, a conventional hybrid supercapacitor was constructed using biochar (BC) as the negative electrode and a mixture of $NiCo_2S_4$@NiV-LDH/NF-2 as the positive electrode. It is noteworthy that the $NiCo_2S_4$@NiV-LDH/NF-2//BC gadget has a power density of 749.98 W kg^{-1} and an energy density of 120.81 Wh Kg^{-1} [119].

A composite of graphene with MnO_2 nanorods is created and evaluated as an electrode material for supercapacitor devices using hydrothermal oxidation of Mn-precursor on a graphene surface. The performance of the composite electrode in a symmetric device creation using galvanostatic charge-discharge revealed a high energy density of 42.7 Wh kg^{-1}, which is equal to a specific capacitance of 759 F.g^{-1} [120]. In a hydrothermal process, polydopamine-modified graphene sheets were used to absorb metal ions. After being pyrolyzed, graphene-supported $NiMoO_4$ nanorod composite materials were created. $NiMoO_4$ nanorods were equally dispersed across the surface of a thinned-out graphene oxide layer under vigorous electrostatic adsorption. A 73% capacitance retention rate was achieved after 5000 charging and discharging cycles in an asymmetric supercapacitor made of activated carbon that had an energy density of 48 Wh kg^{-1} at a power density of 800 W kg^{-1}. The specific capacitance of the composite material was measured at a current density of 1 A g^{-1} to be 856 F.g^{-1} (514 C g^{-1}). As a result, hybrid materials made of PDA-rGO@$NiMoO_4$ offer great potential as supercapacitor electrode materials [121].

On nickel foam, a composite material composed of reduced graphene oxide (rGO) and $RuCo_2O_4$ was produced using a one-step hydrothermal method and an annealing process. (Which serves as a conductive substrate to support the composite). The created electrodes ($RuCo_2O_4$/rGO@NF) exhibit remarkable electrochemical performance at 2283 F.g^{-1} at 1 A.g^{-1}. At 10 A.g^{-1}

of current density, the electrodes' specific capacitance is 1850 $F.g^{-1}$, retaining 81% of the initial specific capacitance. The created electrodes also have an extended cycling life with capacitance retention of 92.60% after 3000 cycles under a current density of 10 A g^{-1}. So, the composite material is a potential electrode material for high-performance supercapacitors [122]. On a nickel foam (NF) substrate, a porous flower-like microsphere structure composite made of gadolinium oxide (Gd_2O_3), tricobalt tetraoxide (Co_3O_4), and reduced graphene oxide (rGO) was created using the hydrothermal synthesis method and annealing process. This material can be used as an electrode material for supercapacitors without the need for a conductive adhesive or binder. The Gd_2O_3/Co_3O_4/rGO/NF composite electrode has a specific capacitance of 3616 $F.g^{-1}$ at a current density of 1 $A.g^{-1}$. The impact of temperature on the charge storage capacity of SCs has also been extensively researched for usage in real-world applications, with a specific capacitance of up to 442.5 F g^{-1} and capacitance retention of 93.3% (40,000 cycles). The supercapacitor maintains good performance up to 60°C (368.3 Fg^{-1}). When cooled to 0°C, it can provide a specific capacitance of 415 $F.g^{-1}$ [123]. The physical characteristics of some composite material are listed in Table7.

Electrolyte Materials

Supercapacitor performance depends heavily on electrolyte, which is one of the components and the most important one in determining the performance of any electrochemical energy device. It is crucial to think about any potential interactions and compatibilities between the improved electrolytes being developed for any electrochemical device and the electrode materials and other electrode components [124]. Wide voltage window, high electrochemical stability, high ionic concentration and conductivity, low viscosity, and low toxicity are all characteristics of an excellent electrolyte [125].

The choose of the electrolytes is based on the ions' types and sizes, concentrations, electrode materials, interactions between the solvent and the ions, and more. It's crucial to note that the pore size of the electrode material must be less than or equal to the size of the ions in the electrolyte [126]. Common electrolytes come in three different varieties: aqueous, organic liquid, and ionic liquid, Water-soluble aqueous electrolytes with strong ionic conductivity and low internal resistance include KOH and H_2SO_4 [125].

Table 7. The electrochemical performances of the composite electrode

Electrode materials	Specific capacitance	Cycling performance	Energy density at power density	Ref.
$ZnCo_2O_4$/CNT	888 Fg^{-1}at 1 Ag^{-1}	94.72% after 5000 charge discharge cycles		[93]
MW-CN-LDH	2532.80 $F.g^{-1}$at 1 $A.g^{-1}$	75.81%		[97]
MW-CN-LDH//AC	193.36 $F{\cdot}g^{-1}$	91.92% (10 000 cycles)	77.61$Wh{\cdot}kg^{-1}$at 0.85 $kW{\cdot}kg^{-1}$	[97]
CCO/CNM-2	2995.56 $F.g^{-1}$	79.3% at current density 10 A g^{-1} after 10,000 charge–discharge cycles	104.98Wh Kg^{-1} at 800 kW Kg^{-1}	[98]
MnO_2/$NiCo_2O_4$	1485.24 F g^{-1} (2 A g^{-1})	87.5% (3000 cycles)		[118]
PDA-rGO@$NiMoO_4$	856 F g^{-1} (514 C g^{-1})	73% after 5000 cycles of charging and discharging,	48 Wh kg^{-1} at 800 W kg^{-1}	[121]
$RuCo_2O_4$/rGO@NF	2283 $F.g^{-1}$ at 1 $A.g^{-1}$	92.6% (3000 cycles) at 10 A g^{-1}		[122]
Gd_2O_3/Co_3O_4/rGO/NF	3616 $F.g^{-1}$ at 1 $A.g^{-1}$	93.3% (40000 cycles)	88.5 $Whkg^{-1}$ at 300 W kg^{-1}	[123]

So, compared to capacitors having organic electrolytes, supercapacitors using an aqueous electrolyte solution may have a greater capacitance and more power. Aqueous electrolytes also have a significant advantage over organic electrolytes in that they can be created and used with less severe production process control, whereas organic electrolytes need exact preparation methods in order to produce pure electrolytes [127].

The design concepts for perovskite electrode materials, which may be broken down into the following categories, can be elucidated based on the charge storage mechanism of perovskite oxide electrodes. A Create perovskite oxide elements with high oxygen vacancy concentration, low valence state of B site elements, BOB bond angle close to 180°, and BO bond length shorter by replacing A and B sites with other elements [128]. Low A-site valence substitution may raise the valence of B-site elements or increase the concentration of oxygen vacancies, according to the structural theory of perovskite oxides [129]. Yet, while the oxygen vacancy concentration is unaffected, substitution with high A-site valence can lower the valence of B-site or A-site elements. More hydroxide anions are intercalated via the electrode surface as a result of the increased concentration of oxygen vacancies, which promotes the diffusion of hydroxide anions from the electrolyte to the electrode. More hydroxide anion intercalation via the electrode surface is caused by increased hydroxide anion diffusion from electrolyte to electrode at higher oxygen vacancy concentrations. On the other hand, the potential specific capacitance is constrained by increases in the valence of the B site element. Hence, replacing a high valence A site is a faulty method for enhancing the electrochemical efficiency of perovskite. Although theoretical specific capacitance is challenging to accomplish, the method can be utilized to enhance electrochemical performance in a variety of ways. Hence, replacing a high valence A site is a faulty method for enhancing the electrochemical efficiency of perovskite. Due to the difficulty in achieving theoretical specific capacitance, the method can be utilized to enhance electrochemical performance by helping diffusion and intercalation as well as somewhat lowering internal resistance [129].

Types of Electrolytes

When dissolved in water, chemical molecules called electrolytes can separate into ions. This aqueous solution can carry electricity thanks to these ions. The electrolyte must be an ionic composition to disintegrate into its ions. Cations and anions are the building blocks of ionic compounds [130]. These ions are evenly distributed across the entire solution. In that case, the solution has no

electrical charge. The ions in this solution begin to migrate when an external electrical current is applied. Cations travel to the electrode's area with the highest electron density. Anions frequently shift to the other electrode. An electric current flow through the solution as a result of the ion mobility [131]. Electrolytes in supercapacitors are divided into three categories:

1. Liqid electrolytes.
2. Solid- or quasi-solid-state electrolytes for Ess.

Liquid Electrolytes: (Aqueous Electrolytes)

Generally, in attention of power density, aqueous electrolytes are a low desire for industrial ES merchandise because of their slim voltage windows. This may also be One of the essential motives why maximum business Ess use natural electrolytes instead of (aqueous electrolytes) [132]. Normally, aqueous electrolytes show off excessive conductivity (for example, approximately zero S cm^{-2} for 1 M H_2SO_4 at 25°C), that is at the least one order of significance better than That of natural and ionic liquid electrolytes. This is useful for decreasing the ESR, leading to a higher energy shipping of Ess. The choice standards for aqueous electrolytes Commonly considers the sizes of naked and hydrated cations and anions and the mobility of ions, which influences now no longer most effective the ionic conductivity however additionally the specific [133]. Capacitance value. an electrolyte's ESPW and the corrosive diploma should be taken into account. In general, aqueous electrolytes may be grouped into acid, alkaline, and impartial Answers wherein H_2SO_4, KOH and Na_2SO_4 are representatives and additionally the most Often used electrolytes [134].

Enormously slim ESPW, limited through the decomposition of water. For example: (hydrogen evolution) happens at a bad electrode capacity of ≈ zero V vs. SHE, and oxygen evolution at a high-quality electrode capacity of round 1.23 V), the ensuing ES has a mobile lar voltage approximately 1.23 V. The fuel line Evolution could doubtlessly reason the rupture of the ES cells, threatening the safety. The lowering the performance keep away from the fuel line evolution, the mobiliary voltage of Ess with aqueous electrolytes is usually limited to approximately 1.to zero V [135].

Strong Acid Electrolytes

Because of its extremely high ionic conductivity (0.8 S cm^{-1} for 1 M H_2SO_4 at 25°C), H_2SO_4 is the acid electrolyte that is most frequently utilized for aqueous-based EESs. A significant factor influencing its conductivity is the

H_2SO_4 concentration. Regarding this, some recommended concentrations to reach the H_2SO_4 electrolytes' maximal ionic conductivities at specific *Numerous* studies have been done on temperatures. The ionic conductivity of the water is typically. If the concentration is too high or too low, electrolyte levels can be lowered *Because* the H_2SO_4 electrolyte's maximum ionic conductivity is attained at 1.0 M concentration. Most investigations at 25°C employ (1.0) M H_2SO_4 electrolyte solution, especially for those ESs that employ electrode materials based on carbon [136].

Acid Electrolytes for Electrical Double-Layer Capacitors

The majority of comparative studies found that the EDLCs' individual capacitances, obtained in the H_2SO_4 electrolyte, are superior to those obtained in the neutral electrolytes. The ESR of Ess with H_2SO_4 as the electrolyte is typically lower than that with the impartial electrolytes because of the higher ionic conductivity of H_2SO_4 [137]. Previous research has also found a relationship between the specific capacitance of the activated carbons and the electrolyte conductivity, with the unique capacitance multiplying with increasing the electrolyte conductivity. Considering about the ion mobility, which is closely related to the electrolyte conductivity, will help you understand this. The H_2SO_4 electrolyte-based EDLCs have higher specific capacitances than other types of EDLCs, as is typically found. Even while employing the same electrode materials. This could imitate the unique interactions between the electrode materials and the electrolytes that are brought about by particular electrolytes [138].

Acid Electrolytes for Pseudocapacitors

Due to the low power density of EDLCs, significant efforts had been made to growth the price of the strength density with the aid of using exploring different kind of Ess, like pseudocapacitor, for carbon-primarily based totally electrode substances, it became observed that the specific Capacitance in aqueous H_2SO_4 electrolyte additionally covered a few pseudocapacitance Contributions except the electrostatic EDL capacitance [139]. Fast redox reactions that occurred at particular floor functions, including oxygenated carbon species, are what are responsible for this. By adding heteroatoms or sure-floor beneficial groups (such as anthraquinone) to the carbon material surfaces, this pseudo capacitance may be made much greater. It must be stressed that the electrolyte's characteristics have a significant impact on the pseudocapacitive properties of carbon-based materials since the surface functionalities respond differently with different electrolytes [140].

Strong Alkaline Electrolytes

Among of the most often utilized types of aqueous electrolytes in literature. As contrast to more acidic electrolytes, some commercially available metal materials, including Ni, can be used as the current collectors for ESs. Due to its high ionic conductivity (maximum value of 0.6 Scm^{-1} for 6 M at 25°C) [141], KOH has been the most commonly utilized alkaline electrolyte, but alternative base electrolytes like NaOH and LiOH have also been studied. These alkaline electrolytes can be used in carbon-based EDLCs as well as pseudo capacitors constructed of $Ni(OH)_2$ and Co_3O_4., and carbon-based EDLCs can all use these alkaline electrolytes.

Alkaline Electrolytes for Double-Layer Electrical Capacity

The values of aqueous KOH electrolyte-based EDLC specific capacitances and energy densities published in the literature are frequently comparable to those of H_2SO_4 electrolyte-based values. Strong acid electrolytes have attracted a lot of attention, along with efforts to boost the energy densities of ESs using base electrolytes by raising capacitance and enlarging the operating voltage window [142]. Improving the capacitance of carbon-based electrode materials, Pseudo-capacity contribution is introduced. The creation of materials with high specific capacitance for pseudo-capacity [142]. In general, the positive electrode is different from the positive electrode in these asymmetric Ess. negative electrode. The positive electrode is a battery type (Ex: $Ni(OH)_2$). Also, Pseudo The Faraday reaction stores charge in a capacitance (EX: RuO_2) [143]. And the (negative electrode), where electric charge is stored EDL, is primarily an electrode made of carbon. According to [145], KOH electrolyte effectively increases the operating cell voltages for these asymmetric Materials, which are 1.7 V for carbon /$Ni(OH)_2$ and V for carbon/$Co(OH)_2$.

Neutral Electrolytes

Together with acidic and alkaline electrolytes, neutral electrolytes have also been thoroughly investigated for ESs [144]. This is due to their advantages, which include (higher safety, smaller corrosion, and larger operating potential windows). The typical conducting salts in the neutral electrolytes include Li (like LiCl, Li_2SO_4, and $LiClO_4$), Na (like NaCl, Na_2SO_4, and $NaNO_3$), K (like KCl, K_2SO_4, and KNO_3), Ca (like Ca $(NO_3)_2$), and Mg (like $MgSO_4$). Na_2SO_4 is the most commonly used neutral electrolyte among them and has been discovered to be a promising electrolyte for several pseudo capacitive materials (especially MnO_2-based materials). Even though some studies have

concentrated on EDLCs, the majority of these neutral electrolytes are used in hybrid ESs and pseudocapacitors [146].

Ionic Liquid-Based ES Electrolytes

According to standard definitions, ionic liquids (ILs), also known as low temperature or room temperature molten salts) are salts that are formed solely of ions (cations and anions) and have melting points below 100°C. Ionic liquid electrolytes' overall composition, properties, and ES performance [147]. An IL is often composed of a large, asymmetric organic cation and either an inorganic or organic anion; this unusual combination of a particular cation and anion contributes to the low melting point of an IL. Due to their unique structures and characteristics, ILs have recently gained a lot of interest as potential substitute electrolytes for ESs because of their distinctive structures and features. High thermal, chemical, and electrochemical stability, minimal volatility, and non-flammability are only a few of the possible benefits of ILs in typical conditions depending on the combination of cations and anions. ILs' physical and chemical properties are also Optimized or modified to satisfy specific ES performance parameters, including operative cell voltage, operating temperature range, ESR (related to ionic conductivity), and others.

Solvent-Free Ionic Liquids

The main challenge in creating or choosing solvent-free ionic liquids with strong ionic conductivity, big ESPW, and wide temperature range is to build ILs for EDLCs [148]. It has taken a lot of effort to develop different alternative ILs based on the tunable properties of ILs to adjust the structure of the anion, the cation, or both as well as the IL composition itself in order to get around these shortcomings.

Solid- or Quasi-Solid-State Electrolytes for Ess

Solid electrolyte-based electrochemical energy devices have gained a lot of attention recently due to the constantly expanding need for wearable electronics, wearable electronics, microelectronics, printable electronics, and notably flexible electronics devices. There are other solid electrolytes as well [149] not only as an ion-conducting medium, but also as an electrode separator. Great advantages simplify manufacturing and packaging when a solid electrolyte is used, No liquid leakage as a result of ES processing. The principal categories of solids to date Polymer electrolytes are the foundation of the electrolytes created for ES. Only a small amount of research has been done on inorganic solids (e.g., ceramics).

Design and Synthesis of QSE Films

The (porous PI NF film skeleton) had a low ionic conductivity, but its high porosity could store enough (gel state) PDOL/$LiPF_6$/LiTFSI/DME, which were components of a particular type of (commercial liquid electrolytes) and, as a result, displayed a high ionic conductivity [150]. The following is a description of the specific fabrication processes.

1. The porous PI NF films were fabricated with a sol-gel electrospinning technique followed by a step-heating treatment, that is one of the most popular techniques for (fabricating ultrafine NF films) with controllable thicknesses and porosity. Polyamic acid PAA was chosen as the Pi precursor.
2. The PAA sol was prepared by mixing the same molar quantity of pyromellitic dianhydride PMDA and (4,4 -Oxydianiline) (ODA) in N.N-dimethylformamide (DMF) solution in a (low humidity environment).
3. At room temperature, the PMDA and ODA readily polymerized to create PAA. White PAA NF films were electrospun from the (stable PAA sol). To create yellow PI NF films, the (PAA NF film) was heated using a step heating mode. The amide groups in PAA underwent reaction of (thermal aided immunization or closed-loop intramolecular dehydration), resulting in the formation of imide rings (cycloaddition and polycondensation dehydration).
4. The PAA then changed into (PI). Tensile strengths of PI NF films heated for 0.5 hours at various temperatures (160, 200, 250, 300, and 350°C) were compared because the heating temperature had a significant impact on the mechanical properties of the PI NF films. The PI NF films had a thickness of 37 micro m. As the temperature was fixed to 300°C, the analysis found that the PI NF film had the highest tensile strength of 12.35 MPa since the temperature was set to be 300°C. The step heating mode was set as follows:
    - After heating the PAA NF films at 100°C for 1 hour to remove the organic solvents and water, the films were subsequently heated at 160°C, 250°C, and 300°C for 0.5 hours each
    - The yellow PI NF films were produced after it was heated and allowed to naturally cool to room temperature.

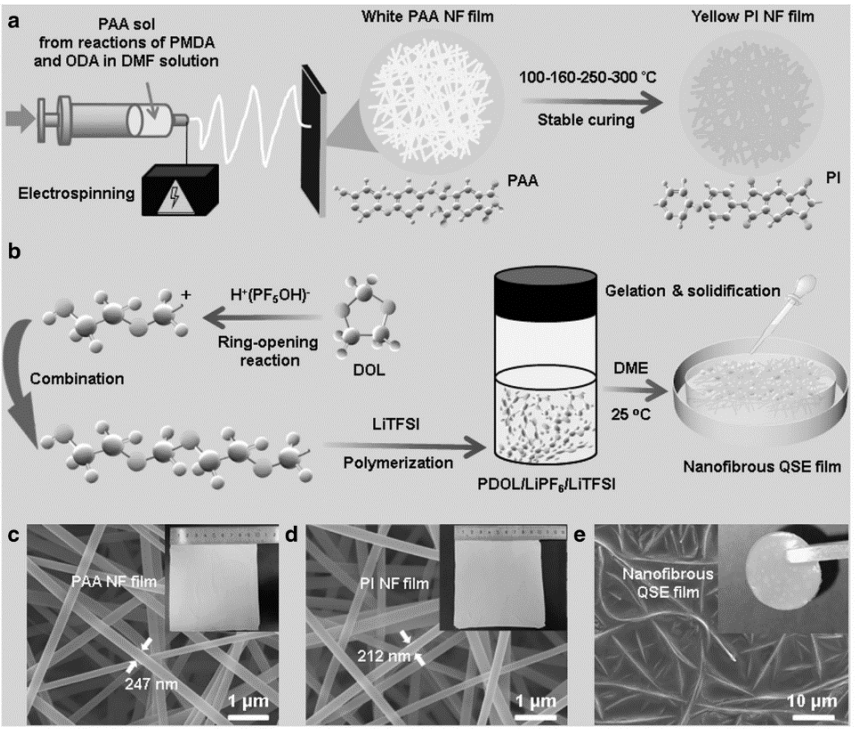

Figure 4. Synthesis of QSE films; 1- Controllable fabrication of (PI NF films) with a sol- gel electrospinning followed by a step of heating. 2-Self-polymerization of (DOL) within the porous PI NF film at the room temperature and fabrication of (nano fibrous QSE films). 3- Surface morphology and digital photos of the (PAA NF film), PI NF film, and nano fibrous QSE film [151] Adapted with permission from Ref. [151] (Copyright 2022, Wiley).

- The next stage was to create dense QSE films by producing the highly ionic conductive (quasi-solid gel) within the porous PI NF films. The quasi-solid gel was created in a glovebox filled with argon where the concentrations of (H_2O) and (O_2) were both less than 0.1. ppm. Specifically; 1 M $LiPF_6$ were firstly dissolved into a mixed solution of (DOL and LiTFSI) and then DME were added into the system to form a mixed sol. After which dropped the mixed sol into the PI NF film and waited for one hour until the formation of quasi-solid gel within the NF film. Also, Figure 4 shows the steps of fabrication of QSE film [151].

Gel Polymer Electrolytes (GPEs)

Due to their strong ionic conductivity, GPEs are currently the electrolytes for solid-state ESs that have received the most research. A liquid electrolyte, such as an aqueous electrolyte, organic solvent containing conducting salt, and IL, make up a gel polymer electrolyte in most cases. Many polymer matrices have been investigated for creating GPEs that use the host polymer, including [152] Poly vinyl alcohol {PVA}, poly (-acrylic acid) {PAA}, potassium polyacrylate (PAAK), poly (ethyl oxide) {PEO}, poly(methylmethacrylate) [PMMA], poly (ether ketone) {PEEK}, poly(acrylonitrile)-block-poly (ethyleneglycol)-block-poly(acrylonitrile) PAN-b-PEG-b-PAN and poly (vinylidene fluoride-co-hexafluoro propylene) {PVDF-HFP}. The resulting Gel polymer electrolytes are known as hydrogel polymer electrolytes because water is used as a plasticizer. These electrolytes have some 3-dimensional polymeric networks that can tap water in the polymer matrices primarily through surface tension. Other than water, organic solvents like PC and (DMF) or combinations of them such as PC-EC, PC-EC-DMC, and PC-EC have also been commonly used as the plasticizers in Gel polymer electrolytes. The degree of plasticization, which affects the glass-transition temperature of Gel polymer electrolytes, is often greatly influenced by the composition ratio between polymer and plasticizer. One of the most significant advantages of employing solid-state electrolytes, such as Gel polymer electrolytes in ESs, is that they allow for the construction of a wide range of flexible and adjustable geometries for a wide range of desired applications [152].

Hydrogel Polymer Electrolyte

Being a linear polymer, poly (vinyl alcohol, or PVA) has received the greatest research attention among the numerous host polymers for hydro gel electrolytes. This is due to the fact that PVA is simple to prepare, has excellent film-forming properties, is non-toxic, and is inexpensive. PVA is typically combined with other aqueous solutions to create hydrogels, such as strong acids like H_2SO_4 and H_3PO_4, strong alkaline like KOH, and neutral solutions like LiCl electrolyte [153].

Hydrogel Polymer Electrolytes for Carbon-Based Electrodes

The design of the electrode/electrolyte interface for optimal performance is crucial when gel polymer electrolytes are employed as “ES electrolytes.” According to several studies, gel polymer electrolyte-based ESs can have poor performance because of their restricted ability to diffuse ions or their high interfacial resistance at the electrode/electrolyte contact. The thickness of the

electrode layer is also found by T Ioannides et al. [154] to be crucial in achieving high capacitance for PVA/H_3PO_3-based ESs [155]. Since using (PVA/H_3PO_3) hydrogel as the electrolyte, a saturation of the capacitance value could be seen. In an aqueous electrolyte, the capacitance increases linearly with increase in thickness of the electrode layer. This was believed to be brought on by the ion penetration into the tissue being limited (porous electrodes). For applications requiring a high capacity for charge storage, the hydrogel electrolyte used in this instance might be the best option.

Organogel Electrolytes

Gel polymer electrolytes based on organic solvents mixed with carbonaceous components to increase the working cell voltage (hybrid composites). In general, hydrogel electrolyte has the same drawbacks as (an aqueous Electrolyte). Due to the hydrogel electrolytes' narrow ESPW of the aqueous component, symmetric ESs using them may experience poor energy density and limited operating cell voltage (hydrogel). To increase the operative cell voltage, hydrogel electrolyte-based asymmetric ESs using the two different electrodes with potential complementary windows have recently been explored. It was determined that compared to the symmetric (PVA hydrogel-based ESs), the operating cell voltage of asymmetric ESs could be greatly improved to a high value, such as 1.8 V [155].

Structural Electrolytes

The development of load-bearing solid-state electrolytes, also known as structural electrolytes, for some vibration devices, such as electric vehicles, has received attention. [155]. M Monne et al. [155] prepared some {IL-epoxy resin composites} as structural electrolytes for ESs. The morphology ionic conductivity and mechanical properties It was discovered that the weight ratio between IL and the epoxy resin affected different types of electrolytes. A chamber might be provided by the optimal electrolyte, which contains 70% Il and 30% resin.

Compatibility Current Collector

It has a significant impact on the supercapacitor's electrochemical performance and cycle stability. They support the electrode material and collect electrons. The power density and capacitance of a supercapacitor are directly impacted by (conductivity and contact resistance with the electrode material of the current collector). High mechanical strength/modulus, low weight, high thermal stability, high electrochemical stability, and high

electrical conductivity should all be present in a current collector. Metal foam and metal foil-type current collectors are used in which metal foam provides the highest performance. For flexible supercapacitors, carbon fibers are generally used as the (current collector) [156].

Metal Foil and Metal Foam-Based Current Collector

A supercapacitor's charge transfer resistance and power delivery rate are significantly influenced by the interaction between the electrode and the current collector. Above the current collector, electrode materials are deposited, and binders are utilized to reduce contact resistance [156]. The electrode and current collector are sandwiched together. Polytetrafluoroethylene (PTFE), polybenzimidazole (PBI), polyvinylidene fluoride (PVDF), and bitumen paint are just a few examples of the various types of binders. Their classification is heavily influenced by the underlined (physical and chemical properties). The material for the current collector should be chosen so that, throughout the charging and discharging processes, it won't react with the electrode and electrolyte. For two electrode cells, the family of materials known as metal foil and metal plates is frequently utilized as current collectors. The metal foil should have a lower thickness and low contact resistance to obtain high power performance [156].

Charge transfer occurs at the intersection of the current collector, metal frame, and electrode material under improved conditions thanks to the metal foil's high contact area with the electrode material. Because they have high mechanical adhesion and electronic connectivity with the nickel foam current collector, several electrode materials can be employed directly with it (current collector). When the porosity of metal foam serves as a quick transport mechanism for electrodes, the average diffusion distance of electron transfer lowers. The contact area at the electrode and current collector interface is reduced since the metal foil current collector is only present on the back side of the electrode material. Metal foam and foil impedance analyses. Metal foam has a considerably lower charge transfer resistance than metal foil. Although there is no discernible difference in internal resistance, the metal foil has a charge transfer resistance that is 7 times greater than metal foams. It is obvious that the metal foam's porous structure allows for a uniform distribution of electrode material inside the current collector, increasing the contact surface and lowering charge transfer resistance. The relatively small area of contact between the metal foil and the electrode material raises the charge transfer resistance [156]. It is clear which superconducting magnets have a high charge transfer resistance.

Current Collector for Flexible Supercapacitors

The use of storage devices in flexible and portable devices is constrained by their rigidity. For the production of flexible and wearable electronics, flexibility is crucial. The development of flexible current collectors is crucial. The development of current collectors with outstanding mechanical qualities, such as high bendability and compressibility, high electrical conductivity, and ultrathin, lightweight design, are crucial difficulties [156]. There is a severe lack of current collector materials for flexible supercapacitor applications. The current collector for flexible, super capacitors frequently used is (carbon fiber-derived carbon fabrics). Carbon fabrics suffer from limited electrical conductivity despite having strong mechanical strength and good flexibility. Polymer film with a conducting layer and metal foil are additional materials for flexible current collectors.

Current Collector Materials

The most popular materials for supercapacitor devices are carbon fiber-based metal foil, polymer film, metal foam, paper-coated metal substrates, and current collectors. Most usually used as current collectors are metals, including gold, copper, titanium, platinum, steel, aluminum, and nickel. The most popular current collector for supercapacitor devices is nickel-based. It offers low contact resistance with an electrode material, good electrical conductivity, strong mechanical strength, and inexpensive cost. Foil and foam versions of nickel are both used [156, 157]. Aluminum-based products are less expensive, light in weight, highly electrically conductive, and low contact resistive (current collector). High contact resistance is the result of the electrode material peeling off of the aluminum foil even when the working conditions are poor. Stainless steel is frequently utilized as the current collector in supercapacitor and battery applications because it is inexpensive and chemically stable. High mechanical strength, good ductility, acceptable electrical conductivity, and electrochemical stability are all characteristics of stainless steel. In addition to its superior (physical features), it is a material that is easily available. Stainless steel's chemical and electrochemical stability as a (current collector) depends on the electrolyte employed [158]. Copper is a reddish-orange ductile current collector with strong thermal and electrical conductivity. High electrical conductivity is provided via 3D porous structured copper foams, a novel type of current collector. The pores in the copper foams range in size from micrometers to millimeters. The current collector (surface area) for high-performance super capacitors should have a high surface area and porosity in addition to strong electrical conductivity. Ultrasonic methods

are also used to enhance the surface area of the current copper collector by generating mesoporous and microporous structures on the surface [156, 157].

Binders

Electrode materials are incorporated using binders in lithium-ion batteries or supercapacitor applications. In order to maintain the layer's structural integrity and to ensure that active particles adhere well to the current collector, binder ingredients bind conductive agents and active materials together [158]. Fluorinated polymeric materials, such as polyvinylidene fluoride (PVDF), polytetrafluoroethylene (PTFE) [159], and nafion, are frequently used as electrode supercapacitors (ESs) binder materials. Polyvinylpyrrolidone/ polyvinyl butyral (PVP/PVB), Carboxymethylcellulose sodium (CMC), polyvinylidene chloride, and sulfonated polyetheretherketone (SPEEK) are examples of the nonfluorinated ESs binders (PVDC). It is typically noticed that the characteristics and composition of the binders can have a significant impact on the performance of electrodes and the associated ESs [160].

Graphene Oxide Binder

On the other hand, the binder materials have not received much attention. Insulating fluorinated polymer binders, which are used for the fabrication of carbon electrodes in supercapacitors, reduce electrode conductivity, rate performance, and capacitance [161]. Given its large specific surface area (SSA) and affordable price, activated carbon (AC) is the most widely utilized electrode material for commercial electric double-layer capacitors (EDLC). However, as AC is typically employed in powder form, creating continuous fibers from AC powders remains a significant difficulty. In order to meet the rapid development of flexible electronics, supercapacitors (SCs) and AC powders may be scaled up if they can be converted into the fiber. The fabrication of AC fiber was done using a bottom-up approach with graphene oxide (GO) as both a dispersion and a binder. The fiber has remarkable mechanical flexibility, a high specific surface area (1476.5 m^2 g^{-1}) and strong electrical conductivity (185 S m^{-1}), and after chemical reduction. Using the produced fiber as the electrode, which is free of binder, conducting additives, and extra current collectors, an all-solid-state flexible SC was built. The fiber-shaped SC exhibits excellent cyclability (90.4% retention after 10,000 cycles), good bendability (96.8% retention after 1000 bends), and high capacitance (27.6 F cm-3 or 43.8 F g^{-1}, standardized to the two-electrode volume) [162].

A generic method was employed to create flexible, freestanding, high-performance supercapacitor electrodes from diverse micron-sized porous carbons using reduced graphene oxide (rGO), The effective electronic conductivity, two-dimensional structure and high specific surface area of rGO enable us to eliminate the addition of insulating binder, current collector and conductive additive. The synergistic effect of rGO and carbon materials in both aqueous and non-aqueous electrolytes makes a 3D conductive network and widens the electrode/electrolyte interface, which improves electrode capacitance and rate performance [163]. Highly porous activated graphene (AG) is inserted into graphene fibres to increase the electrochemical performance of (Fiber supercapacitors) FSCs based on electric double-layer capacitance (EDLC). The creation of continuous and conductive graphene fibers is made possible by wet spinning AG combined with graphene oxide (GO) and then chemically reducing GO to reduced graphene oxide (rGO). The FSCs' electrochemical performance is considerably enhanced by the AG powders with extraordinarily high surface areas, with a PVA/LiCl gel electrolyte, the rGO/AG fiber in particular achieves a specific areal capacitance of 145.1 mF/cm2 at a current density of 0.8 mA/cm^2. This is equivalent to areal energy and power densities for the FSCs of 5.04 μWh/cm2 and 0.50 mW/cm^2, respectively. Moreover, flexible FSCs made of rGO/AG fibers exhibit respectable cycling performance, with 91.5% capacitance retention after 10,000 cycles [164].

As flexible electrodes for flexible solid-state supercapacitors, carbon-based fiber fabrics (CBFFs) are highly sought-after because to their outstanding mechanical flexibility, high conductivity, and light weight (SCs). The realized areal capacitance of the majority of CBFFs is still insufficient. Unusual CBFF known as carbon nanotube fiber fabric (CNTFF) might provide a high-performance flexible electrode replacement. The activated CNTFF demonstrates a remarkable combination of high areal capacitance (1988 mF cm^{-2} at 2 mA cm^{-2}), excellent rate performance (45% capacitance reservation at 100 mA cm^{-2}), and amazing cycle longevity (only 3% capacitance decay after 10,000 cycles). The built-in solid-state SC has a maximum power density of 30,600 W cm-2 and an energy density of 143 Wh cm^{-2} at 1000 W cm^{-2}[165]. With their high-power density, quick charge/discharge rate, incredibly long cycling life, and secure working conditions, all-carbon fiber-shaped supercapacitors (FSSCs) hold a lot of potential for powering wearable technology. However, their low energy density precludes their employment in practical applications due to the lack of efficient methods for highly electrically conductive fiber electrodes with high specific capacitance. Simple

carbonized phenol formaldehyde (CPF) resin that contains small-size (156 nm in diameter) graphene (SG) is used to decorate graphene fiber to create a hierarchical structure. The combination of CPF and SG produces ultrahigh micro-porosity with narrowed micro-/meso-PSDs and enhanced electrical conductivity, which makes it easier to store and transport ions. In a two-electrode cell with a polyvinyl alcohol/H_2SO_4 electrolyte, the constructed FSSCs exhibit an ultrahigh specific areal capacitance of 391.2 mF cm^2, which is 17 times that of graphene fibers. The overall device energy density Ecell, A is 8.7 W h cm^2 for aqueous electrolytes and 66.4 W h cm^2 for organic electrolytes at an aerial power density of 0.54 mW cm^2. The FSSCs also exhibit excellent flexibility and an extremely long cycling life (98.9% capacitance retention after 7000 cycles) [166].

Boron and nitrogen-doped carbon (BCN) anchored on active carbon fiber cloth (ACC) are specially designed and manufactured by immersing ACC in a mixed solution of urea, boric acid and polyethylene oxide-propylene oxide (P123) and then calcining, which can be used to assemble high-performance FSSCs as electrodes. The three-dimensional (3D) cross-linked network of BCN grown on the carbon fibers improves the transmission rate of electrons and provides abundant electrochemical reaction sites, which are conducive to the performance of supercapacitors. The ACC@BCN electrode exhibits an area specific capacitance of 1018 mF cm^{-2} and a volume specific capacitance of 535.8 F g^{-1} at a current of 1 mA cm^{-2}. Furthermore, the symmetric FSSCs based on ACC@BCN show high energy density of 1.573 mWh cm^{-3} and power density of 128.7 mW cm^{-3}, and the capacitance retention can still keep 89.5% even after 10,000 cycles [167].

Green Binders

The term “green” is widely used to express the environmental friendliness of materials and processes. However, its meaning can significantly vary depending on the context of use. When talking about polymeric binders, green alternatives could be identified according to (i) processability, (ii) chemical composition and (iii) natural availability (Figure 5). According to the first criterion, binders soluble or dispersible in environmentally benign solvents, such as water or ethanol, could be classified as green alternatives. Poly(tetrafluoroethylene) (PTFE), also known as Teflons (Dupont), is highly hydrophobic with strong C–C and C–F bonds providing high chemical and mechanical stability, rendering it very suitable for highly resistant coatings and membranes [168].

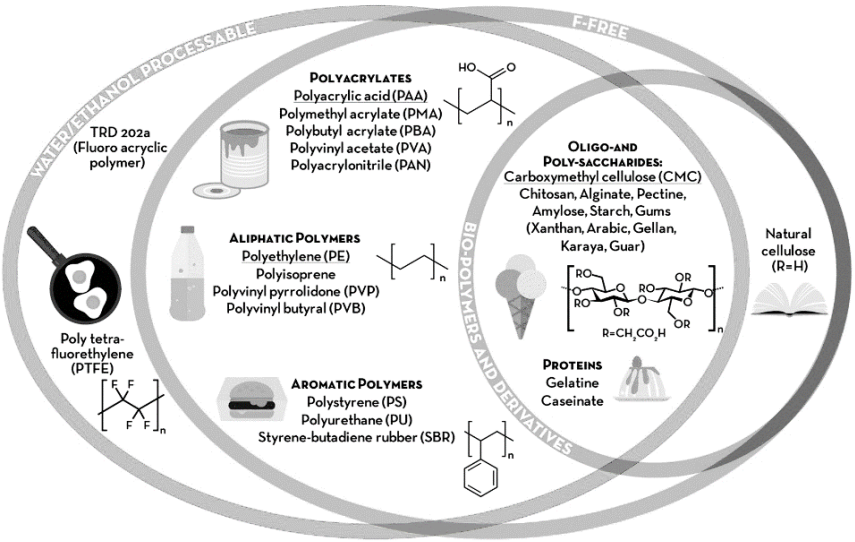

Figure 5. Overview of the different classes of binders. Adapted with permission from Ref. [168] (Copyright 2018, RCS).

Polysaccharide cellulose, which makes up the skeleton of plants, is a crucial raw element for polymers. Pyranose D-glucose molecules make up cellulose, which also has a flexible, semi-crystalline fibrous morphological structure. These molecules are connected linearly by -(1,4) connections. Using lignocellulosic raw materials, cellulose nanocrystals are rod-shaped particles with exceptional crystallinity [169]. Several levels of conformation and polymerization of cellulose macromolecules can be produced by microbes and plants. Materials derived from Cladophora algae, bacteria, or wood, for instance, can have various degrees of crystallinity and crystallographic forms. The most sophisticated aqueous binder for supercapacitors is carboxymethyl cellulose (CMC) [170]. The bulk loading of the coatings is nevertheless constrained by shrinkage after drying. In order to find alternatives, natural polymers like guar gum (GG), wheat starch (WS), and potato starch (PS) were researched. The 75:25 (w/w) PS/GG ratio combination behaved nicely as shown in Figure 6. The electrodes were examined using a SEM, heat, adhesion, and bending tests. By permitting mass loadings larger than CMC (7.0 mg cm^2) while keeping the same specific capacitance (26 F g^{-1}) and power performance, the PS/GG blend complied with industrial production requirements (20 F g^{-1} at 10 A g^{-1}). The specific energy at the electrode level

increases by +45% when the mass of the current collector is taken into consideration [171].

Figure 6. The bending test of CMC and potato starch [171]. Adapted with permission from Ref. [171] (Copyright 2020, Wiley).

The production of highly efficient and durable supercapacitors using sustainable materials remains a challenge. So the production of *thin film* binder electrodes is very significant for *electric double layer capacitors* (EDLCs) based on onion-like carbon. The active material obtained by high temperature treated detonation nanodiamond offers a specific surface area of 527 m^2 g^{-1} after an additional activation step. The key to facilitate the electrode manufacturing for this active material was the introduction of an agglomeration step of the carbon nano-onions which qualified them for the usage of plant-based carboxymethyl cellulose (CMC) as binder. The new types of electrodes were successfully tested in a *supercapacitor* full cell setup and benchmarked against electrodes relying on conventional *fluorinated polymer* (PVDF) as binder. The green electrodes provide about 22% higher specific capacitance of 56 F g^{-1} at a similar durability over more than 5000 cycles, combining sustainable production with excellent performance [172].

Although they typically have a low energy density, flexible supercapacitors are an appealing technology for the next generation of wearable consumer devices. A complex design of binder is disclosed by a biosynthetic process to produce flexible electrodes with outstanding mechanical properties and electrochemical performance, inspired by the natural structure of the spider web. With this method, an active electrode

material can have a significant amount of ion-accessible surface area, a high packing density, and effective ion transport channels thanks to a 3D structural binder that is inspired by spider webs. The composite electrodes and symmetric supercapacitors are thus able to achieve high areal capacitance of 4.62 F cm^{-2} and high areal energy density of 0.18 $mW.h.cm^{-2}$, respectively, demonstrating a promising potential to construct flexible energy storage devices for various practical applications [173].

Separators

The separator in an ES cell is placed between the two electrodes to avoid contact and electron transport between the negative and positive electrodes. The separators must meet a number of critical criteria, including: (1) low ion transfer resistance within the electrolyte while having a strong electronic insulating capability; (2) high chemical and electrochemical stabilities in the electrolyte; and (3) adequate mechanical strength to ensure device durability. ES separators are often made using thin, highly porous membranes or films based on these parameters. As separator materials, glass fibers, polymer membranes, and cellulose are frequently used. As is well known, the kind of electrode, working temperature, and ES cell voltage all have an impact on separator material selection [174]. The most often used dense separator membranes are nafion and sulfonated Poly (ether ether ketone) (SPEEK). Separators from these membranes are made by immersing them in sulfuric acid solutions. The majority of nafion is made up of the hydrophobic Teflon backbone and the hydrophilic sulfonic acid groups. However, the high cost of these membranes, as well as the scarcity of fundamental chemicals required for their manufacturing, is a considerable disadvantage. Figure 7 depicts the developments gained in the materials and manufacturing techniques used to construct separators [175].

When metal oxide fibers are used as separators, they must have exceptional mechanical pliability, high temperature tolerance, and superior wettability. High-performance energy systems rely largely on metal oxide-based nanofiber separators because they have a large specific surface area, good ion mobility, and a high rate of electrolyte retention [176]. Aluminum silicate nanofibers are therefore a possibility for use in high performance supercapacitor separators [177]. PVdF membrane that has been electrospun serves as a separator in supercapacitor uses. The polymer separator membranes were made using the electrospinning method and PVdF in various

weight percentages (5, 10, 15, 20, and 25 wt%) suspended in 50:50 wt% THF and DMAc solvents, respectively. As a result, it was discovered that PVdF polymer membrane with a 20-weight percent content showed superior structural and thermal characteristics to other membranes, making it a trust worthy separator membrane for supercapacitors [178].

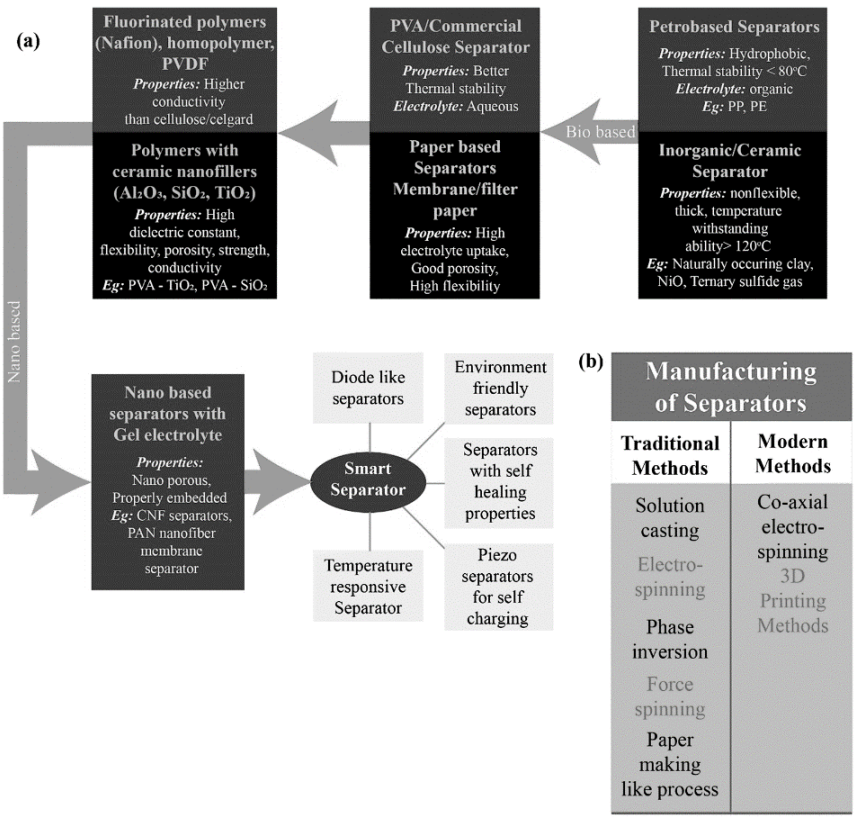

Figure 7. The gradual growth of separator a) materials and b) manufacturing techniques [175]. Adapted with permission from Ref. [175] (Copyright 2022, RCS)

Asymmetric and Hybrid Supercapacitor

Electrochemical devices called hybrid supercapacitors (HSCs) blend the qualities of batteries and supercapacitors into a single asymmetric cell. Supercapacitors (SCs) and lithium-ion batteries (LIBs) are at opposite

extremes of the power and energy density spectrum. On one end of the Ragone plot spectrum, LIBs use faradaic reactions to produce high energy densities (150–250 Wh kg^{-1}); however, the power density of LIBs is limited to about 1000 W kg^{-1} due to this comparatively slow reaction process. Lithium is intercalated and de-intercalated into the active material by the faradic mechanism, changing the molecular phase and raising the possibility of material deterioration, which results in a short cycle life. (500-300 cycles). Contrarily, SCs, which are based on electrostatic charge collection, involve the quick, reversible adsorption and desorption of ions on the surface of the active substance without phase change or chemical reactions. Asymmetric supercapacitors (ASCs) hold tremendous promise as a substitute power source for hybrid cars and portable electronics. The development of high-performance anodes is an important research area because the disparity in anode and cathode material development for ASCs continues to be a major problem. The most recent developments in the design and production of innovative ASC anodes, which are classified as carbon-based, metal oxides-based, metal nitrides-based, and other anodes. Based on the findings that have been recently released in the literature, the advantages and disadvantages of these anodes are examined and discussed. The methods used to get around certain problems with different anode materials are described in detail. Further analysis and comparison of the electrochemical capabilities of ASC devices built with these anodes is done [179].

Asymmetric Supercapacitor

Recently, some asymmetric hybrid supercapacitors with the negative electrode based on an EDLC activated carbon electrode and the positive electrode based on a real pseudocapacitive metal oxide electrode (not a composite electrode) were created. Due to their extensive operating potential, which can significantly improve the capacitive behavior, asymmetric supercapacitors (ASC) have emerged as a great potential option for high-performance supercapacitors. The greater voltage and consequently higher specific energy of these supercapacitors (up to 10–20 Wh/kg (36-72 kJ/kg)) are advantages. Additionally, they possess excellent cycling stability. For instance, to create an asymmetric supercapacitor, researchers used innovative skutterudite Ni-CoP3 nanosheets as positive electrodes and activated carbon (AC) as negative electrodes. (ASC). It has a high energy density of 89.6 Wh/kg at 796 W/kg and stability of 93% after 10000 cycles, making it a strong choice for a next-

generation electrode. Additionally, AC was employed as the negative electrode and carbon nanofibers/poly(3,4-ethylenedioxythiophene)/ manganese oxide (f-CNFs/PEDOT/MnO_2) as the positive electrode. It has excellent cycling stability (81.06 percent after 8000 cycles) and a high specific energy of 49.4 Wh/kg [180].

Hybrid Supercapacitor

Due to their advantageous power and energy densities, hybrid supercapacitor devices—built with both capacitive and electrodes resembling batteries—have been accepted as promising energy storage technologies. To enhance the total energy storage performances of hybrid supercapacitors, the design and fabrication of capacitive and battery-like electrode materials with high specific capacitances, high-rate performance, and acceptable durability is essential. In order to achieve the desired energy storage performances of hybrid supercapacitors, metal-organic frameworks with advantageous porous properties, tunable chemical compositions, and changeable morphologies are developing porous crystalline materials. It was elaborated on the most current developments of pure metal-organic frameworks, metal-organic framework composites, and materials derived from metal-organic frameworks used in hybrid supercapacitors. The difficulties and prospects of metal-organic framework-based materials for hybrid supercapacitor application were also compiled based on prior efforts [180].

Nitrogen-Doped Activated Carbon for a High Energy Hybrid Supercapacitor

In a one-step process, nitrogen-doped activated carbons (NACs) were created. The obtained NACs have high surface areas of up to 2900 m^2 g^{-1} and a relatively low N concentration of up to 4 wt%. The NACs exhibit outstanding rate capability and cycling stability as well as a high specific capacity of 129 mA h g1 (185 F g^{-1}) in an organic electrolyte at a current density of 0.4 A g^{-1}. With 230 W h kg^{-1} at 1747 W kg^{-1}, the hybrid-type supercapacitor built with NACs and a Si/C anode has a high material level energy density. After 8000 tests at 1.6 A g^{-1}, the hybrid device obtained 76.3% capacity retention [180]. It was possible to create novel N-doped activated carbons in just one process. With a specific capacity of up to 129 mA h g^{-1} and capacity retention of 86% after 500 cycles, the obtained NAC materials demonstrated outstanding electrochemical performance. It was discovered that the N-doping of the

NACs enhanced efficiency. NAC and Si/C nanocomposites were used to further assemble and test the hybrid-type supercapacitor. The hybrid system demonstrated high energy densities of 230 - 141 W h kg^{-1} at power densities of 1747 to 30127 W kg^{-1}, which are among the highest figures recorded for hybrid-type systems, with the optimized N/P ratio. For the hybrid-type supercapacitor, a satisfactory long cycling stability was also attained with a capacity retention of 76.3% after 8000 cycles [181].

Trend and Scope Beyond Traditional Supercapacitors

The development of wearable and adaptable zero-pollution technologies is being hampered by limitations in the size reduction of electrical components, which affect charge storage devices like batteries and supercapacitors. Due to their power density, quick charge-discharge cycles, and intrinsic extended cycle life, supercapacitors perform better than other energy storage technologies. The modern market for zero-pollution energy gadgets is presently favored by the lightweight formula and shape adaptability to meet the demand for wearables. This prerequisite can be satisfied by carbon nanoparticles, which are the primary component of active electrode materials for supercapacitors and are texturally created to exhibit flexible and stretchable qualities [182]. In this context, the most current research on novel materials is discussed, ranging from conventional carbons to recently developed and nanomaterials towards light, stretchable active compounds for flexible, wearable supercapacitors. The difficulties and constraints of using wearable energy storage devices as well as the potential of nanomaterials to improve wearable technology are also covered. The topic of commercially feasible wearable materials is also covered. This could spur scientists to continue developing flexible, affordable nanostructures for energy storage, which would lead to a variety of material-based uses. The two electrodes of a traditional capacitor are typically parallel metal slabs that are spaced apart by a dielectric medium. Although they have distinct parts, modern super-capacitors perform similarly to conventional capacitors [182]. Due to the large surface area of the carbon electrode (specific surface areas can vary from 1000 to 2000 m^2/g), supercapacitors perform better than conventional capacitors [183]. Supercapacitors composed of pure carbon or materials derived from carbon have undergone rapid change over the past few decades. There is little possibility that the potential working window will increase because the majority of these traditional supercapacitors have two electrodes made of the

same material [184]. New electronic and optoelectronic gadgets are currently being produced all over the globe. This indicates the need for more durable power sources with greater energy densities. Supercapacitors are currently one of the most promising energy-storage technologies due to their many benefits, such as high-power density, quick charging and discharging, and extended cyclic stability. However, traditional supercapacitors are difficult to use due to their low energy density, so researchers have been developing novel kinds of supercapacitors [185]. A wide operational voltage window is a distinct benefit of asymmetric supercapacitors (ASCs) assembled with two different electrode materials, which greatly improves energy density. An exhaustive survey of the materials created for ASC electrodes, as well as the advancements made in the fabrication of ASC devices over the past few decades, are covered in this critical review of recent developments in the field of ASCs. The subject of ASCs was discussed, including its current issues and prospects for the future. contrasting the energy and power densities of different cutting-edge batteries and supercapacitors with ASCs [185].

A few critical considerations must be made in order to produce a high performance asymmetric and/or hybrid storage device (supercapacitor) [184]. Maximizing an ASC's operating voltage will result in a high energy density. The selection of electrode materials has a big impact on the device's voltage range. Fundamental understanding of the various methods for widening the voltage range in supercapacitors is lacking. However, the work function of the metal oxides used as electrode materials is closely linked to the oxidation reduction reaction [186]. Current collector is being created. It ought to be incredibly resilient to any physical or toxic threats. It is preferable to use a sturdy, long-lasting, non-corrosive, and flexible substance as the current collector, such as metal foam or foil. Generally, supercapacitors use electrolytes that are usually classified into three types; aqueous, i.e., ions in water; organic, salts in organic solvents; ionic liquid; pure liquid salts [187].

Supercapacitors Application in Agriculture

The application of supercapacitors in agriculture has gained significant attention as a promising solution for advancing sustainable power systems in agricultural practices. This chapter delves into the various aspects of utilizing supercapacitors in the agricultural sector, highlighting their potential to revolutionize energy storage and power supply in farming operations.

Soil Moisture Management

Proper management of soil moisture is crucial for optimizing crop growth and reducing water usage in agriculture. Electrochemical supercapacitors offer significant potential in this area. With their high-power density and fast charge-discharge characteristics, supercapacitors can efficiently control irrigation systems in agricultural fields [190] developed an energy management system based on supercapacitors for efficient irrigation in precision agriculture. The system integrated supercapacitors with sensors and actuators to monitor soil moisture levels and deliver precise amounts of water to the crops. This approach not only optimizes water usage but also minimizes water wastage, leading to improved water efficiency and enhanced crop productivity.

Precision Agriculture

Precision agriculture involves the use of advanced technologies to manage crops and maximize yields based on real-time data and site-specific conditions. Electrochemical supercapacitors have a crucial role to play in powering sensors and monitoring devices used in precision agriculture [191-197] developed an autonomous supercapacitor-powered wireless sensor network for precision agriculture. The supercapacitors stored energy during the day and provided a reliable power supply for sensors deployed in the field. These sensors collected data on soil conditions, nutrient levels, and crop health, enabling farmers to make informed decisions regarding irrigation, fertilization, and pest control. The integration of supercapacitors in precision agriculture improves resource allocation, enhances crop management, and promotes sustainable agricultural practices [198-209].

Sensor Networks

In soil sciences, sensor networks are widely used to monitor and analyze soil properties and environmental conditions. However, the reliable and sustainable power supply for these networks remains a challenge. Electrochemical supercapacitors offer a viable solution by storing and delivering energy efficiently [192-198] proposed an energy harvesting and power management scheme for long-term environmental monitoring with wireless sensor networks. The scheme utilized supercapacitors to store harvested energy from solar panels or other sources and deliver it to the sensor nodes. By incorporating supercapacitors, the sensor networks can operate autonomously and continuously, reducing the dependence on batteries and

external power sources. This improves the scalability and longevity of the sensor networks, allowing comprehensive monitoring and analysis of soil conditions and facilitating research in soil sciences [193-200].

These applications demonstrate the potential of electrochemical supercapacitors in revolutionizing soil sciences and agricultural practices. With their clean and sustainable energy storage capabilities, high-power density, and long-life expectancy, supercapacitors offer promising solutions for efficient soil moisture management, precision agriculture, and reliable power supply for sensor networks in soil sciences.

Conclusion

Electrochemical supercapacitors look to be promising and one of the primary new devices for energy storage and power supply, with the advantages of high-power density, high efficiency, and long-life expectancy, to fulfil the increasing demand for clean, sustainable energy. To address this issue, research and development efforts must be encouraged in order to identify or seek for new electrode materials with high capacitance and a broad potential window. ES electrode materials should have the following properties: (1) a high specific surface area, resulting in more active sites, (2) a suitable pore-size distribution, pore network, and pore length for facilitating high-rate ion diffusion, (3) a low internal electrical resistance for efficient charge transport in the composite electrode, and (4) better electrochemical and mechanical stability for good cycling performance. In regards of ES material porosity, nano micropores are required to achieve larger specific surface area, and these micropores must be electrochemically accessible for ions. This chapter discussed the most recent materials used in supercapacitor components such as electrode materials, electrolyte materials, current collectors, binders, and separators. A number of electrode materials were also discussed, including carbon-based electrode materials, perovskites, conducting polymers, metal oxides, and composite materials diverse applications of supercapacitors in agriculture, particularly in soil moisture management, precision agriculture, sensor networks, and other relevant areas. In a summary, the chapter describes the principles that encourage the development and application of perovskite oxide electrode materials and other developed materials in supercapacitors.

References

[1] Liu PY, Zhao JJ, Dong ZP, Liu ZL, Wang YQ. (2021). Interwoving polyaniline and a metal-organic framework grown in situ for enhanced supercapacitor behavior. *J Alloys Compd* 854:157181.

[2] Zan G, Wu T, Chen H, Dong F, Wu Q. (2021). $BiVO_4$ nanocoral superstructures and their excellent electrical/optical dual-functions. *J. Alloys Compd* 852: 157035.

[3] Kar KK (2020). *Handbook of nanocomposite supercapacitor materials II*. Cham: Springer International Publishing 302.

[4] Kumar S, Saeed G, Zhu L, Hui KN, Kim NH, Lee JH (2021). 0D to 3D carbon-based networks combined with pseudocapacitive electrode material for high energy density supercapacitor: A review. *Chem Eng J* 403: 126352.

[5] Wu ZS, Parvez K, Feng X, Müllen K (2013). Graphene-based in-plane micro-supercapacitors with high power and energy densities. *Nat Commun* 4(1): 1-8.

[6] Simon P, Gogotsi Y (2008). Materials for electrochemical capacitors. *Nat Mater* 7(11): 845-854.

[7] Inagaki M, Konno H, Tanaike O (2010) Carbon materials for electrochemical capacitors. *J Power Sources* 195:7880–903.

[8] Yu Z, Tetard L, Zhai L, Thomas J (2015) Thomas Supercapacitor electrode materials: nanostructures from 0 to 3 dimensions, *Energy Environ. Sci.* 8 (3) 702–730.

[9] Zhang Y, Feng H, Wu X, Wang L, Zhang A, Xia T, Dong H, Li X, Zhang Li (2009). Progress of electrochemical capacitor electrode materials: A review. *Int J Hydrogen Energy*, 34 (11): 4889- 4899.

[10] Pal B, Yang S, Ramesh S, Thangadurai V, Jose R (2019). Electrolyte selection for supercapacitive devices: a critical review. *Nanoscale Adv* 1(10): 3807-3835.

[11] Liu X, Zhao J, Cao Y, Li W, Sun Y, Lu J, Men Y, Hu J (2015). Facile synthesis of 3D flower-like porous NiO architectures with an excellent capacitance performance. *RSC Advances* 5(59): 47506-47510.

[12] Jiang H, Lee PS, Li C (2013). 3D carbon-based nanostructures for advanced supercapacitors. *Energy Environ. Sci* 6(1): 41-53.

[13] Snook G A, Kao P, Best A. S. (2011). Conducting-polymer-based supercapacitor devices and electrodes. *J Power Sources* 196(1): 1-12.

[14] Yuan C, Yang L, Hou L, Shen L, Zhang X, Lou XW (2012). Growth of ultrathin mesoporous Co_3O_4 nanosheet arrays on Ni foam for high-performance electrochemical capacitors. *Energy Environ.* Sci 5(7): 7883-7887.

[15] Deng T, Zhang W, Arcelus O, Kim JG, Carrasco J, Yoo SJ, Rojo T (2017). Atomic-level energy storage mechanism of cobalt hydroxide electrode for pseudocapacitors. *Nat Commun* 8(1): 15194.

[16] Hu L, Deng Y, Liang K, Liu X, Hu W (2015). $LaNiO_3$/NiO hollow nanofibers with mesoporous wall: a significant improvement in NiO electrodes for supercapacitors. *J Solid State Electrochem* 19: 629-637.

[17] Xu Y, Hennig I, Freyberg D, Strudwick AJ, Schwab MG, Weitz T, Cha KCP (2014). Inkjet-printed energy storage device using graphene/polyaniline inks. *J Power Sources* 248: 483-488.

[18] Duan BR, Cao Q (2012). Hierarchically porous Co3O4 film prepared by hydrothermal synthesis method based on colloidal crystal template for supercapacitor application. *Electrochimica acta* 64: 154-161.

[19] Yan D, Guo Z, Zhu G, Yu Z, Xu H, Yu A. (2012). MnO2 film with three-dimensional structure prepared by hydrothermal process for supercapacitor. *J Power Source* 199: 409-412.

[20] Augustyn V, Simon P, Dunn B (2014). Pseudocapacitive oxide materials for high-rate electrochemical energy storage. *Energy Environ Sci* 7(5): 1597-1614.

[21] Wang G, Zhang L, Zhang J (2012). A review of electrode materials for electrochemical supercapacitors. *Chem. Soc. Rev* 41(2): 797-828.

[22] Hahn BP, Long JW, Rolison DR (2013). Something from nothing: enhancing electrochemical charge storage with cation vacancies. *Acc Chem Res* 46(5): 1181-1191.

[23] Gogotsi Y, Penner RM (2018). Energy storage in nanomaterials–capacitive, pseudocapacitive, or battery-like? *ACS nano* 12(3): 2081-2083.

[24] Miller J R. (2018). Perspective on electrochemical capacitor energy storage. *Appl. Surf. Sci.* 460, 3-7.

[25] Khorate A, Kadam A V. (2022). An overview of patents and recent development in flexible supercapacitors. *J. Energy Storage*. 52, 104887.

[26] Chen D, Wang Q, Wang R, Shen G (2015). Ternary oxide nanostructured materials for supercapacitors: a review. *J. Mater. Chem.* A 3(19): 10158-10173.

[27] Sudhakar YN, Selvakumar M, Bhat DK (2018). *Biopolymer electrolytes: fundamentals and applications in energy storage*. Elsevier.

[28] Sharma K, Arora A, Tripathi SK (2019). Review of supercapacitors: Materials and devices. *J Energy Storage* 21: 801-825.

[29] Ho MY, Khiew PS, Isa D, Tan TK, Chiu WS, Chia CH (2014). A review of metal oxide composite electrode materials for electrochemical capacitors. *Nano* 9(06): 1430002.

[30] Obreja VV (2008). On the performance of supercapacitors with electrodes based on carbon nanotubes and carbon activated material A review. *Physica E: Low-dimensional Systems and Nanostructures*, 40(7): 2596-2605.

[31] Gidwani M, Bhagwani A, Rohra N (2014). Supercapacitors: the near future of batteries. *Int J Eng Inventions* 4(5): 22-27.

[32] Cherusseri J, Kar KK (2015). Hierarchically mesoporous carbon nanopetal based electrodes for flexible supercapacitors with super-long cyclic stability. *J Mater Chem A* 3(43): 21586-21598.

[33] Emara R, Masoud M. S, Abboudy, S. (2022). Optical, electrical, thermal and kinetic studies for some pyrimidine ligands and their complexes. *J. Non-Cryst.* Solids 597, 121873.

[34] Cherusseri J, Sharma R, Kar KK (2016). Helically coiled carbon nanotube electrodes for flexible supercapacitors. *Carbon*, 105: 113-125.

[35] Frackowiak E, Béguin F (2013). *Supercapacitors: Materials, Systems and Applications*. Wiley-VCH Germany 207 233.

[36] Wei L, Yushin G (2012). Nanostructured activated carbons from natural precursors for electrical double layer capacitors. *Nano Energy* 1(4): 552-565.

[37] You B, Wang L, Yao L, Yang J (2013). Three-dimensional N-doped graphene–CNT networks for supercapacitor. *Chem Commun* 49(44): 5016-5018.

[38] Lin Y, Zhao H, Yu F, Yang J (2018). Design of an extended experiment with electrical double layer capacitors: Electrochemical energy storage devices in green chemistry. *Sustainability*, 10(10), 3630.

[39] Tang W, Zhang Y, Zhong Y, Shen T, Wang X, Xia X, Tu J (2017). Natural biomass-derived carbons for electrochemical energy storage. *Mater Res Bull* 88: 234-241.

[40] Hu B, Wang K, Wu L, Yu SH, Antonietti M, Titirici MM (2010) Engineering carbon materials from the hydrothermal carbonization process of biomass. *Adv Mater* 22(7): 813-828.

[41] Fic K, Frackowiak E, Béguin F (2012). Unusual energy enhancement in carbon-based electrochemical capacitors. *J Mater Chem* 22(46): 24213-24223.

[42] Singh SK, Prakash H, Akhtar MJ, Kar KK (2018). Lightweight and high-performance microwave absorbing heteroatom-doped carbon derived from chicken feather fibers. *ACS Sustainable Chem. Eng*. 6(4), 5381-5393.

[43] Kar KK, Rana S, Pandey J (2015). *Handbook of polymer nanocomposites processing, performance and application* (pp. 283-297). Berlin/Heidelberg, Germany: Springer.

[44] Yu A, Chabot V, Zhang J (2013). *Electrochemical supercapacitors for energy storage and delivery: fundamentals and applications*. Taylor, Francis.

[45] Lu H, Zhao XS (2017). Biomass-derived carbon electrode materials for supercapacitors. *Sustainable Energy Fuels* 1(6), 1265-1281.

[46] Zhang L, Liu Z, Cui G, Chen L (2015). Biomass-derived materials for electrochemical energy storages. *Prog. Polym. Sci*. 43, 136-164.

[47] Ahirrao DJ, Tambat S, Pandit AB, Jha N (2019). Sweet-Lime-Peels-Derived Activated-Carbon-Based Electrode for Highly Efficient Supercapacitor and Flow-Through Water Desalination. *Chemistry Select*, 4(9), 2610-2625.

[48] Teo EYL, Muniandy L, Ng EP, Adam F, Mohamed AR, Jose R, Chong KF (2016). High surface area activated carbon from rice husk as a high-performance supercapacitor electrode. *Electrochim. Acta* 192, 110-119.

[49] Phiri J, Dou J, Vuorinen T, Gane PA, Maloney TC (2019). Highly porous willow wood-derived activated carbon for high-performance supercapacitor electrodes. *ACS omega*, 4(19), 18108-18117.

[50] Taer E, Apriwandi A, Ningsih YS, Taslim R, Agustino A (2019). Preparation of activated carbon electrode from pineapple crown waste for supercapacitor application. *Int. J. Electrochem. Sci*, 14, 2462-2475.

[51] Roy CK, Shah SS, Reaz AH, Sultana S, Chowdhury AN, Firoz SH, Aziz MA (2021). Preparation of hierarchical porous activated carbon from banana leaves for high-performance supercapacitor: effect of type of electrolytes on performance. *Chem. Asian J*. 16(4), 296-308.

[52] Borghei SA, Zare MH, Ahmadi M, Sadeghi MH, Marjani A, Shirazian S, Ghadiri M (2021). Synthesis of multi-application activated carbon from oak seeds by KOH activation for methylene blue adsorption and electrochemical supercapacitor electrode. *Arabian J. Chem.* 14(2), 102958.

[53] Taer E, Apriwandi A, Taslim R, Agutino A, Yusra DA (2020). Conversion Syzygium oleana leaves biomass waste to porous activated carbon nanosheet for boosting supercapacitor performances. *J. Mater. Res. Technol*. 9(6), 13332-13340.

[54] Biener J, Stadermann M, Suss M, Worsley M A, Biener MM., Rose KA, Baumann TF (2011). Advanced carbon aerogels for energy applications. *Energy Environ. Sci*., 4(3), 656-667.

[55] Kistler SS (1931). Coherent expanded aerogels and jellies. *Nat.* 127(3211), 741-741.

[56] Fang B, Wei YZ, Maruyama K, Kumagai M (2005). High-capacity supercapacitors based on modified activated carbon aerogel. *J. Appl. Electrochem.* 35, 229-233.

[57] Cossutta M, Vretenar V, Centeno TA, Kotrusz P, McKechnie J, Pickering SJ (2020). A comparative life cycle assessment of graphene and activated carbon in a supercapacitor application. *J. Cleaner Prod*. 242, 118468.

[58] Le Fevre LW, Cao J, Kinloch IA, Forsyth AJ, Dryfe RA (2019). Systematic comparison of graphene materials for supercapacitor electrodes. *Chemistry Open*, 8(4), 418-428.

[59] Yan Z, Gao Z, Zhang Z, Dai C, Wei W, Shen PK (2021). Graphene nanosphere as advanced electrode material to promote high performance symmetrical supercapacitor. *Small,* 17(18), 2007915.

[60] Ebbesen TW, Lezec HJ, Hiura H, Bennett JW, Ghaemi HF, Thio T (1996). Electrical conductivity of individual carbon nanotubes. *Nat.* 382(6586), 54-56.

[61] Pan H, Li J, Feng Y (2010). Carbon nanotubes for supercapacitor. *Nanoscale Res. Lett.* 5(3), 654-668.

[62] Nan HS, Hu XY, Tian HW (2019). Recent advances in perovskite oxides for anion-intercalation supercapacitor: a review. *Mater. Sci. Semicond. Process*. 94, 35-50.

[63] Lang X, Mo H, Hu X, Tian H (2017). Supercapacitor performance of perovskite La_{1-x} Sr_x MnO_3. *Dalton Trans*. 46(40), 13720-13730.

[64] Shao T, You H, Zhai Z, Liu T, Li M, Zhang L (2017). Hollow spherical $LaNiO_3$ supercapacitor electrode synthesized by a facile template-free method. *Mater. Lett*. 201, 122-124.

[65] Liu Y, Dinh J, Tade MO, Shao Z (2016). Design of perovskite oxides as anion-intercalation-type electrodes for supercapacitors: cation leaching effect. *ACS Appl. Mater. Interfaces* 8(36), 23774-23783.

[66] Harikrishnan MP, Bose AC (2019, July). LaNiO3 perovskite oxides by co-precipitation method as electrode for high performance supercapacitor. *AIP Conf. Proc.* (Vol. 2115, No. 1, p. 030129). AIP Publishing LLC.

[67] Meng Z, Xu J, Yu P, Hu X, Wu Y, Zhang Q, Tian H (2020). Double perovskite La2CoMnO6 hollow spheres prepared by template impregnation for high-performance supercapacitors. *Chem. Eng. J*. 400, 125966.

[68] Tomar AK, Singh G, Sharma RK (2019). Charge storage characteristics of mesoporous strontium titanate perovskite aqueous as well as flexible solid-state supercapacitor cell. *J. Power Sources* 426, 223-232.

[69] Hu Q, Yue B, Shao H, Yang F, Wang J, Wang Y, Liu J (2021). Facile syntheses of perovskite type $LaMO_3$ (M=Fe, Co, Ni) nanofibers for high performance

supercapacitor electrodes and lithium-ion battery anodes. *J. Alloys Compd*. 852, 157002.

[70] Lang X, Mo H, Hu X, Tian H (2017). Supercapacitor performance of perovskite La $_{1-x}$ Sr_xMnO_3. *Dalton Trans*. 46(40), 13720-13730.

[71] Kitchamsetti N, Choudhary RJ, Phase DM, Devan RS (2020). Structural correlation of a nanoparticle-embedded mesoporous $CoTiO_3$ perovskite for an efficient electrochemical supercapacitor. *RSC advances* 10(39), 23446-23456.

[72] Hu Q, Yue B, Shao H, Yang F, Wang J, Wang Y, Liu J (2020). Facile syntheses of cerium-based $CeMO_3$ (M=Co, Ni, Cu) perovskite nanomaterials for high-performance supercapacitor electrodes. *J. Mater. Sci.* 55, 8421-8434.

[73] Zhang Y, Ding J, Xu W, Wang M, Shao R, Sun Y, Lin B (2020). Mesoporous $LaFeO_3$ perovskite derived from MOF gel for all-solid-state symmetric supercapacitors. *Chem. Eng. J.* 386, 124030.

[74] Zhang C, Zhang W, Li X, Zhu Z, Wang Q, Luo S, Xie A (2021). Honeycomb $LaMnO_3$ perovskite synthesized by a carbon sphere as a self-sacrificing template for supercapacitors. *Energy Fuels* 35(16), 13457-13465.

[75] Wang Y, Guo J, Wang T, Shao J, Wang D, Yang YW. (2015). Mesoporous transition metal oxides for supercapacitors. *Nanomater*. 5(4), 1667-1689.

[76] Wang G, Zhang L, Zhang J. (2012). A review of electrode materials for electrochemical supercapacitors. *Chem. Soc. Rev*. 41(2), 797-828.

[77] Biswas S, Sharma V, Mandal D, Chowdhury A, Chakravarty M, Priya S, Chandra A. (2020). Hollow nanostructures of metal oxides as emerging electrode materials for high performance supercapacitors. *Cryst Eng Comm*, 22(9), 1633-1644.

[78] Shivakumara S, Penki TR, Munichandraiah N (2014). High specific surface area α-Fe_2O_3 nanostructures as high-performance electrode material for supercapacitors. *Mater. Lett.* 131, 100-103.

[79] Jayalakshmi M, Venugopal N, Raja KP, Rao MM. (2006). Nano SnO_2–Al_2O_3 mixed oxide and SnO_2–Al_2O_3–carbon composite oxides as new and novel electrodes for supercapacitor applications. *J. Power Sources* 158(2), 1538-1543.

[80] Jin G, Xiao X, Li S, Zhao K, Wu Y, Sun D, Wang F. (2015). Strongly coupled graphene/Mn_3O_4 composite with enhanced electrochemical performance for supercapacitor electrode. *Electrochim. Acta* 178, 689-698.

[81] Chen L, Zhang Y, Zhu P, Zhou F, Zeng W, Lu DD, Wong C. (2015). Copper salts mediated morphological transformation of Cu_2O from cubes to hierarchical flower-like or microspheres and their supercapacitors performances. *Sci. Rep.* 5(1), 1-7.

[82] Pal T, Banerjee S, Manna PK, Kar KK. (2020). Characteristics of conducting polymers. *Handbook of Nanocomposite Supercapacitor Materials I: Characteristics*, 247-268.

[83] He S, Chen W (2015). 3D graphene nanomaterials for binder-free supercapacitors: scientific design for enhanced performance. *Nanoscale*, 7(16), 6957-6990.

[84] Li P, Yang Y, Shi E, Shen Q, Shang Y, Wu S, Wu D. (2014). Core-double-shell, carbon nanotube@ polypyrrole@ MnO_2 sponge as freestanding, compressible supercapacitor electrode. *ACS Appl. Mater. Interfaces 6*(7), 5228-5234.

[85] Kim JH, Sharma AK, Lee YS. (2006). Synthesis of polypyrrole and carbon nano-fiber composite for the electrode of electrochemical capacitors. *Mater. Lett.* 60(13-14), 1697-1701.

[86] Alvi F, Ram MK, Basnayaka PA, Stefanakos E, Goswami Y, Kumar A (2011). Graphene–polyethylenedioxythiophene conducting polymer nanocomposite-based supercapacitor. *Electrochim. Acta*, 56(25), 9406-9412.

[87] Gupta A, Sardana S, Dalal J, Lather S, Maan AS, Tripathi R, Ohlan A (2020). Nanostructured polyaniline/graphene/Fe2O3 composites hydrogel as a high-performance flexible supercapacitor electrode material. *ACS Appl. Energy Mater*., 3(7), 6434-6446.

[88] Li Y, Zhou M, Wang Y, Pan Q, Gong Q, Xia Z, Li Y. (2019). Remarkably enhanced performances of novel polythiophene-grafting-graphene oxide composite via long alkoxy linkage for supercapacitor application. *Carbon*, 147, 519-531.

[89] Rantho MN, Madito MJ, Manyala N (2020). High-performance symmetric supercapacitor device based on carbonized iron-polyaniline/nickel graphene foam. *J. Alloys Compd*., 819, 152993.

[90] Lin L, Ning H, Song S, Xu C, Hu N. (2020). Flexible electrochemical energy storage: the role of composite materials. *Compos. Sci. Technol*, 192, 108102.

[91] Wang Y, Xiao X, Xue H, Pang H (2018). Zinc oxide based composite materials for advanced supercapacitors. *Chemistry Select*, 3(2), 550-565.

[92] Ge D, Wang Y, Hu Z, Babangida AA, Zhang L. (2022). Porous silicon composite ZnO nanoparticles as supercapacitor electrodes. *J. Electron. Mater.* 51(6), 2964-2970.

[93] Isacfranklin M, Daphine S, Yuvakkumar R, Kungumadevi L, Ravi G, Al-Sehemi AG, Velauthapillai D. (2022). $ZnCo_2O_4$/CNT composite for efficient supercapacitor electrodes. *Ceram. Int.*, 48(17), 24745-24750.

[94] Jasna M, Manoj MP, Jayaraj MKE. (2022). Carbon Based Composites for Supercapacitor Applications. In *Energy Harvesting and Storage: Fundam. Mater.* 259-284.

[95] Zhou H, Liu D, Luo F, Luo B, Tian Y, Chen D, Shen C (2018). Preparation of graphene nanowalls on nickel foam as supercapacitor electrodes. *Micro Nano Lett* 13(6) 842-844.

[96] Chen Y, Yang W, Yang D, Wangyang P, Li X (2019). Facile synthesis and electrochemical performances of multi-walled carbon nanotubes/poly (3, 4-ethylenedioxythiophene) composite films as electrodes for fabric supercapacitors. *J Mater Sci : Mater Electron.* 30, 6350-6357.

[97] Qiu H, Ma Q, Sun X, Han X, Jia G, Zhang Y, He W (2022). Construction of orderly self-growing nanosheet arrays on nickel foam by introducing novel carbon composite materials for high-performance supercapacitors. *Appl Surf Sci* 578, 152019.

[98] Hao C, Wang X, Wu X, Guo Y, Zhu L, Wang X (2022). Composite material CCO/Co-Ni-Mn LDH made from sacrifice template CCO/ZIF-67 for high-performance supercapacitor. *Appl Surf Sci*., 572, 151373.

[99] Radaelli PG, Iannone G, Marezio M, Hwang HY, Cheong SW, Jorgensen JD, Argyriou DN (1997). Structural effects on the magnetic and transport properties of perovskite $A_{1-x}A_{x'}MnO_3$ (x=0.25, 0.30). *Phys Rev B* 56(13) 8265.

[100] Zhang L, Zhou Q, He Q, He T (2010). Double-perovskites $A_2FeMoO_{6-\delta}$ (A=Ca, Sr, Ba) as anodes for solid oxide fuel cells. *J Power Sources* 195(19): 6356-6366.

[101] Kim G, Wang S, Jacobson AJ, Reimus L, Brodersen P, Mims CA (2007). Rapid oxygen ion diffusion and surface exchange kinetics in $PrBaCo_2O_{5+x}$ with a perovskite related structure and ordered A cations. *J Mater Chem* 17(24) 2500-2505.

[102] Lu K, Shen F (2014). Long term behaviors of $La_{0.8}Sr_{0.2}MnO_3$ and $La_{0.6}Sr_{0.4}Co_{0.2}Fe_{0.8}O_3$ as cathodes for solid oxide fuel cells. *Int J Hydrogen Energy* 39(15) 7963-7971.

[103] Suntivich J, May KJ, Gasteiger HA, Goodenough JB, Shao-Horn Y (2011). A perovskite oxide optimized for oxygen evolution catalysis from molecular orbital principles. *Science* 334(6061): 1383-1385.

[104] Dhahri J, Zemni S, Cherif K, Dhahri J, Oumezzine M, Ghedira M, Vincent H (2005). The effect of deficit of strontium on structural, magnetic and electrical properties of $La_{0.8}Sr_{0.2-x}M_xMnO_3$ manganites. *J Alloys Compd* 394(1-2) 51-57.

[105] Kim JH, Lee KT, Kim YN, Manthiram A (2011). Crystal chemistry and electrochemical properties of $Ln(Sr, Ca)_3(Fe, Co)_3O_{10}$ intergrowth oxide cathodes for solid oxide fuel cells. *J. Mater. Chem*, 21(8) 2482-2488.

[106] Liu Y, Wang Z, Veder JPM, Xu Z, Zhong Y, Zhou W, Shao Z (2018). Highly defective layered double perovskite oxide for efficient energy storage via reversible pseudocapacitive oxygen-anion intercalation. *Adv. Energy Mater* 8(11) 1702604.

[107] Mo H, Nan H, Lang X, Liu S, Qiao L, Hu X, Tian H (2018). Influence of calcium doping on performance of $LaMnO_3$ supercapacitors. *Ceram Int* 44(8): 9733-9741.

[108] Lang X, Mo H, Hu X, Tian H (2017). Supercapacitor performance of perovskite $La_{1-x}Sr_xMnO_3$. *Dalton Trans* 46(40): 13720-13730.

[109] Cao Y, Lin B, Sun Y, Yang H, Zhang X (2015). Sr-doped lanthanum nickelate nanofibers for high energy density supercapacitors. *Electrochim Acta* 174, 41-50.

[110] Wang X. Li G, Chen Z, Augustyn V, Ma X, Wang G, Lu Y (2011). High-performance supercapacitors based on nanocomposites of Nb_2O_5 nanocrystals and carbon nanotubes. *Adv. Energy Mater* 1(6) 1089-1093.

[111] Lu X, Wang G, Zhai T, Yu M, Gan J, Tong Y, Li Y. (2012). Hydrogenated TiO_2 nanotube arrays for supercapacitors. *Nano Lett* 12(3) 1690-1696.

[112] Kim H, Cho MY, Kim MH, Park KY, Gwon H, Lee Y, Kang K (2013). A novel high-energy hybrid supercapacitor with an anatase TiO_2–reduced graphene oxide anode and an activated carbon cathode. *Adv Energy Mater*, 3(11) 1500-1506.

[113] Zheng JQ, Li YF, Yang R, Li G, Ding XK. (2017). Lithium ion conductivity in the solid electrolytes $(Li_{0.25}La_{0.25})_{1-x}M_{0.5x}NbO_3$ (M=Sr, Ba, Ca, x=0.125) with perovskite-type structure. *Ceram Int* 43(2): 1716-1721.

[114] Shafiei A, Oprea C, Alfantazi A, Troczynski T (2011). In situ monitoring of the effects of hydrogen on Pb (Zr, Ti)O_3 structure. *J Appl Phys* 109(11) 114108.

[115] Tanwar S, Singh N, Sharma AL. (2022). Structural and electrochemical performance of carbon coated molybdenum selenide nanocomposite for supercapacitor applications. *J Energy Storage*, 45, 103797.

[116] Li S, Zhang L, Guo Y, Chen X, Holze R, Tang T (2021). Preparation of Fe_3O_4@ polypyrrole composite materials for asymmetric supercapacitor applications. *New J Chem* 45(35) 16011-16018.

[117] Tao B, He J, Miao F, Zhang Y (2022). MnO_2/$NiCo_2O_4$ loaded on nickel foam as a high-performance electrode for advanced asymmetric supercapacitor. *Vacuum* 195, 110668.

[118] Xu Y, Zhou Y, Guo J, Zhang S, Lu Y (2019). Preparation of SnS_2/g-C_3N_4 composite as the electrode material for Supercapacitor. *J Alloys Compd*, 806, 343-349.

[119] Pan J, Li S, Li F, Zhang W, Guo D, Zhang L, Ruan Y (2022). Design and construction of core-shell heterostructure of Ni-V layered double hydroxide composite electrode materials for high-performance hybrid supercapacitor and L-Tryptophan sensor. *J Alloys Compd*, 890, 161781.

[120] Jadhav S, Kalubarme RS, Terashima C, Kale BB, Godbole V, Fujishima A, Gosavi SW (2019). Manganese dioxide/reduced graphene oxide composite an electrode material for high-performance solid state supercapacitor. *Electrochim Acta*, 299, 34-44.

[121] Li J, Zou Y, Jin L, Xu F, Sun L, Xiang C (2022). Polydopamine-assisted $NiMoO_4$ nanorods anchored on graphene as an electrode material for supercapacitor applications. *J Energy Storage* 50, 104639.

[122] Meng J, Lu S, Xu W, Li S, Dong X (2022). Fabrication of composite material of $RuCo_2O_4$ and graphene on nickel foam for supercapacitor electrodes. *RSC advances* 12(24) 15508-15516.

[123] Meng J, Lu, S., Xu, W, Li, S, Dong X (2022). Fabrication of composite material of $RuCo_2O_4$ and graphene on nickel foam for supercapacitor electrodes. *RSC advances*, 12(24) 15508-15516.

[124] Xin, Y, Lu, S, Xu, W, Wang S (2023). Fabrication of honeycomb-structured composite material of $Pr_2O_3Co_3O_4$ and graphene on nickel foam for high-stability supercapacitors. *New Journal of Chemistry* 47(1) 211-219.

[125] Scibioh MA, Viswanathan B (2020). *Materials for Supercapacitor Applications*. Elsevier.

[126] Wang Q, Chen S, Zhang D (2020). CNT yarn-based supercapacitors. In *Carbon nanotube fibers and yarns*, 243-270. Woodhead Publishing.

[127] Zhou L, Li, C, Liu, X., Zhu, Y, Wu, Y, Van Ree T (2018). Metal oxides in supercapacitors. In *Metal Oxides in Energy Technologies* (pp. 169-203). Elsevier.

[128] Zhong C, Deng Y, Hu, W, Qiao J, Zhang L, Zhang J (2015). A review of electrolyte materials and compositions for electrochemical supercapacitors. *Chemical Society Reviews* 44(21), 7484-7539.

[129] Mefford JT, Hardin WG, Dai S, Johnston KP, Stevenson KJ (2014). Anion charge storage through oxygen intercalation in $LaMnO_3$ perovskite pseudocapacitor electrodes. *Nature materials* 13(7) 726-732.

[130] Pena MA, Fierro JLG. (2001). Chemical structures and performance of perovskite oxides. *Chemical reviews*, 101(7) 1981-2018.
[131] Mehetre SS, Ameta RK, Behere SS, Inwati GK (2023). Supercapacitors—new developments. In *Smart Supercapacitors*, 39-64. Elsevier.
[132] Wu, Q. Wang, W. Zhang, Y. Wang, W. Chen (2020). Preparation of all-solid-state su-percapacitor integrated with energy level indicating functionality, *Synth. Met.* 220, 494-501
[133] Wang PH, Tseng LH, Li WC, Lin CH, Wen TC. (2021). Zwitterionic polymer coupled with high concentrated electrolytes to achieve high ionic conductivity and wide electrochemical window for supreme specific energy aqueous supercapacitors. *J. Energy Storage*, 42, 103060.
[134] Liu M, Yang X, Wu X, Wang X, Li Y, Ma F, Zhou J. (2022). Understanding the pore-structure dependence of supercapacitive performance for microporous carbon in aqueous KOH and H_2SO_4 electrolytes. *Electrochim. Acta*, 401, 139422.
[135] Srinivasan KP, Muthuramalingam T. (2021). Fabrication and performance evolution of AgNP interdigitated electrode touch sensor for automotive infotainment. *Sensors*, 21(23), 7961.
[136] Wu X, Yang X, Feng W, Wang X, Miao Z, Zhou P, Zhao J, Zhou J, Zhuo S. (2021). Enhanced Energy Density for P-Doped Hierarchically Porous Carbon-Based Symmetric Supercapacitor with High Operation Potential in Aqueous H_2SO_4 Electrolyte. *Nanomaterials*, 11(11) 2838.
[137] Chen X, Put B, Sagara A, Gandrud K, Murata M, Steele J, Yabe H, Hantschel T, Roeffaers M, Tomiyama M, Arase H, Kaneko Y, Shimada M, Mees M, Vereecken P, (2020). Silica gel solid nanocomposite electrolytes with interfacial conductivity promotion exceeding the bulk Li-ion conductivity of the ionic liquid electrolyte filler. *Science Advances*, 6(2) 340.
[138] Hirata K, Kawase T, Sumida Y. (2020). Electrode/Electrolyte Interface Study of LiCoO2/Graphite Cell Using Carbonate-Free Electrolytes Based on Lithium Bis (fluorosulfonyl) imide and Sulfolane. *J. Electrochem. Soc.* 167(2), 020518.
[139] Jorn-am T, Praneerad J, Attajak R, Sirisit N, Manyam J, Paoprasert P. (2021). Quasi-solid, bio-renewable supercapacitor with high specific capacitance and energy density based on rice electrolytes and rice straw-derived carbon dots as novel electrolyte additives. *Colloids Surf.*, A. 628, 127239.
[140] Ni Q, Kim B, Wu C, Kang K. (2022). Non-electrode components for rechargeable aqueous zinc batteries: Electrolytes, solid-electrolyte-interphase, current collectors, binders, and separators. *Advanced Materials*, 34(20) 2108206.
[141] Massey RS, Prakash R. (2021). Modeling the double layer capacitance effect in electrolyte gated FETs with gel and aqueous electrolytes. *Micromachines*, 12(12) 1569.
[142] Dong X, Hou L. (2021). Electrochemical oxidation of 2D B, N-doped carbon nanosheets for pseudocapacitance property [J]. *New Carbon Mater.* 36(6) 1109-1117.
[143] Leistenschneider D, Heß LH, Balducci A, Borchardt L. (2020). Solid-state transformation of aqueous to organic electrolyte–Enhancing the operating voltage

window of ‘in situ electrolyte’supercapacitors. *Sustain. Energy Fuels*, 4(5) 2438-2447.

[144] Kaipannan S, Marappan S. (2019). Fabrication of 9.6 V high-performance asymmetric supercapacitors stack based on nickel hexacyanoferrate-derived Ni (OH) 2 nanosheets and bio-derived activated carbon. *Sci. Rep.* 9(1), 1104.

[145] Murugesan RA, Raja KCN. (2023). Capacitance Performance of $Ti_3C_2T_x$ Mxene Nanosheets on Alkaline and Neutral Electrolytes. *Mater. Res. Bull*, 112217.

[146] Lisik Z. (1981). *Heat generation in semiconductor devices*. Solid State Electron., 24(1), 85-87.

[147] Shi M, Lin T, Wang Y, Hu Y, Peng J, Li J, Zhai M. (2020). One-step radiation synthesis of novel star-shaped polymeric ionic liquid–POSS gel electrolytes with high ionic conductivity and mechanical properties for supercapacitor. *J. Mater. Sci*, 55, 16347-16359.

[148] Xie ZW, Su KY. (2011). Macro-TG Reactor and Thermogravimetric Analysis for Cooking Oil Tar Samples. *Adv. Mat. Res*, 199, 1569-1573.

[149] Yue L, Zhang X, Li W, Tang Y, Bai Y. (2019). Quickly self-healing hydrogel at room temperature with high conductivity synthesized through simple free radical polymerization. *J. Appl. Polym. Sci.* 136(18), 47379.

[150] Mindemark J, Lacey MJ, BowdenT, Brandell D. (2018). Beyond PEO—Alternative host materials for Li+-conducting solid polymer electrolytes. *Prog. Polym. Sci*, 81, 114-143.

[151] Huang Y, Liu S, Chen Q, Jiao K, Ding B, Yan J. (2022). Constructing Highly Conductive and Thermomechanical Stable Quasi-Solid Electrolytes by Self-Polymerization of Liquid Electrolytes within Porous Polyimide Nanofiber Films. *Adv. Funct. Mater*, 32(31), 2201496.

[152] Kundu S, Kraytsberg A, Ein-Eli Y. (2022). Recent development in the field of ceramics solid-state electrolytes: I—oxide ceramic solid-state electrolytes. *J Solid State Electrochem*, 26(9), 1809-1838.

[153] Hua Y, Xu Z, Zhao B, Zhang Z. (2022). Efficient separation of electrode active materials and current collector metal foils from spent lithium-ion batteries by a green deep eutectic solvent. *Green Chem.* 24(20), 8131-8141.

[154] Ioannides T, Verykios X E. (1996). Charge transfer in metal catalysts supported on doped TiO2: a theoretical approach based on metal–semiconductor contact theory. *J. Catal.* 161(2), 560-569.

[155] Monne M A, Chen Y M. (2022). High Current On–Off Ratio Inkjet-Printed Flexible Microelectromechanical System Switch. *IEEE J-FLEX*, 1(3), 167-173.

[156] Swamy M K, Pinto R. (2022). Study on thermal contact resistance of low melting alloy used as thermal interface material. *Mater. Today: Proc*, 66, 2508-2512.

[157] Zhao Z, Wang Z, Li K, Zhang D. (2022). Cathode diffusion layer and current collector with slotted foam stainless steel for a micro direct methanol fuel cell. *RSC Adv.* 12(44), 28738-28745.

[158] Bizot C, Blin MA, Guichard P, Soudan P, Gaubicher J, Poizot P. (2021). Aluminum current collector for high voltage Li-ion battery. Part II: Benefit of the En’Safe® primed current collector technology. *Electrochem. Commun*. 126, 107008.

[159] How Y Y, Numan A, Mustafa MN, Walvekar R, Khalid M, Mubarak NM. (2022). A review on the binder-free electrode fabrication for electrochemical energy storage devices. *J. Energy Storage*, 51, 104324.

[160] Gerard O, Numan A, Krishnan S, Khalid M, Subramaniam R, Kasi R (2022). A review on the recent advances in binder-free electrodes for electrochemical energy storage application. *J. Energy Storage*, 50, 104283.

[161] Zhu Z, Tang S, Yuan J, Qin X, Deng Y, Qu R, Haarberg GM. (2016). Effects of various binders on supercapacitor performances. *Int. J. Electrochem. Sci*, 11(10), 8270-8279.

[162] Xu B, Wang H, Zhu Q, Sun N, Anasori B, Hu L, Gogotsi Y. (2018). Reduced graphene oxide as a multi-functional conductive binder for supercapacitor electrodes. *Energy Storage Mater.*, 12, 128-136.

[163] Ma W, Chen S, Yang S, Chen W, Weng W, Zhu M. (2016). Bottom-up fabrication of activated carbon fiber for all-solid-state supercapacitor with excellent electrochemical performance. *ACS Appl. Mater. Interfaces*, 8(23), 14622-14627.

[164] Ho BT, Lim T, Jeong MH, Suk JW. (2021). Graphene fibers containing activated graphene for high-performance solid-state flexible supercapacitors. *ACS Appl. Energy Mater.* 4(9), 8883-8890.

[165] Liang Y, Luo X, Weng W, Hu Z, Zhang Y, Xu W, Zhu M. (2021). Activated carbon nanotube fiber fabric as a high-performance flexible electrode for solid-state supercapacitors. *ACS Appl. Mater. Interfaces*, 13(24), 28433-28441.

[166] Zheng X, Zhang K, Yao L, Qiu Y, Wang S. (2018). Hierarchically porous sheath–core graphene-based fiber-shaped supercapacitors with high energy density. *J. Mater. Chem. A*, 6(3), 896-907.

[167] Shi L, Ye J, Lu H, Wang G, Lv J, Ning G. (2021). Flexible all-solid-state supercapacitors based on boron and nitrogen-doped carbon network anchored on carbon fiber cloth. *Chem. Eng. J*, 410, 128365.

[168] Bresser D, Buchholz D, Moretti A, Varzi A, Passerine S (2018). Alternative binders for sustainable electrochemical energy storage–the transition to aqueous electrode processing and bio-derived polymers. *Energy Environ. Sci*. 11(11) 3096-3127.

[169] Taskin OS., Hubble D, Zhu T, Liu G (2021). Biomass-derived polymeric binders in silicon anodes for battery energy storage applications. *Green Chem*. 23(20) 7890-7901.

[170] Zhou S, Nyholm L, Strømme M, Wang Z (2019). Cladophora cellulose: unique biopolymer nanofibrils for emerging energy environmental and life science applications. *Acc. Chem. Res.* 52(8) 2232-2243.

[171] Ruschhaupt P, Varzi A, Passerini S (2020). Natural Polymers as Green Binders for High-Loading Supercapacitor Electrodes. *Chem Sus Chem* 13(4) 763-770.

[172] Bauer C, Bilican A, Braxmeier S, Reichenauer G, Krueger A (2022). Sustainable supercapacitor electrodes based on preagglomerated carbon onions and a green binder. *Carbon*, 197 555-562.

[173] Guan QF, Ling ZC, Han ZM, Luo TT, Yang HB, Yang KP, Yu SH (2021). Sustainable 3D Structural Binder for High-Performance Supercapacitor by Biosynthesis Process. *Adv. Funct. Mater*. 31(42) 2105070.

[174] Bittner AM, Zhu, M., Yang Y, Waibel HF, Konuma M, Starke U, Weber CJ (2012). Ageing of electrochemical double layer capacitors. *J. Power Sources*. 203 262-273.
[175] Ahankari S, Lasrado D, Subramaniam R (2022). Advances in materials and fabrication of separators in supercapacitors. *Materials Advances* 3(3) 1472-1496.
[176] Jing P, Liu M, Wang P, Yang J, Tang M, He C, Liu M (2020). Flexible nonwoven ZrO_2 ceramic membrane as an electrochemically stable and flame-resistant separator for high-power rechargeable batteries. *Chem. Eng. J.* 388 124259.
[177] Wen J, Xu K, Li R, Lv D, Cui Y, Chen Y, Wei Y, Yu Y, Yu Y, Wei, H. (2022). Electrospun flexible aluminum silicate nanofibers as a flame-resistant separator for the high-performance supercapacitor. *Ionics*, 28(1), 433-442.
[178] Arthi R, Jaikumar V, Muralidharan P. (2022). Development of electrospun PVdF polymer membrane as separator for supercapacitor applications. Energy Sources A: Recovery Util. *Environ. Eff.* 44(1), 2294-2308.
[179] Fisher RA., Watt MR, Ready WJ. (2013). Functionalized carbon nanotube supercapacitor electrodes: a review on pseudocapacitive materials ECS. *J Solid State Sci. Technol.* 2(10):M3170.
[180] Iniewski K. (Ed.). (2010). *Devices, Circuits, and Systems*. CRC press.
[181] Samantara AK, Ratha S, Samantara AK, Ratha S. (2018). Trend and Scope Beyond Traditional Supercapacitors. *Materials Development for Active/Passive Components of a Supercapacitor: Background, Present Status and Future Perspective*, 47-48.
[182] Choudhary N, Li C, Moore J, Nagaiah N, Zhai L, Jung Y, Thomas J. (2017). Asymmetric supercapacitor electrodes and devices. *Adv Mater*, 29(21): 1605336.
[183] Singh A, Chandra A. (2015). Significant performance enhancement in asymmetric supercapacitors based on metal oxides, carbon nanotubes and neutral aqueous electrolyte. *Sci Rep*, 5(1): 15551.
[184] Zhong C, Deng Y, Hu W, Qiao J, Zhang L, Zhang J. (2015). A review of electrolyte materials and compositions for electrochemical supercapacitors. *Chem. Soc Rev*, 44(21): 7484-7539.
[185] Shao Y, El-Kady MF, Sun J, Li Y, Zhang Q, Zhu M, Kaner RB. (2018). Design and mechanisms of asymmetric supercapacitors. *Chem Rev*, 118(18): 9233-9280.
[186] Pal B, Yang S, Ramesh S, Thangadurai V, Jose R. (2019). Electrolyte selection for supercapacitive devices: a critical review. *Nanoscale Adv*, 1(10): 3807-3835.
[187] Penke YK, Yadav AK, Sinha P, Malik l, Ramkumar J, Kar KK. (2020). Arsenic remediation onto redox and photo-catalytic/electrocatalytic Mn-Al-Fe impregnated rGO: sustainable aspects of sludge as supercapacitor. *Chem Eng J*, 390, 124000.
[188] Simon, P., & Gogotsi, Y. (2008). Materials for electrochemical capacitors. *Nature Materials*, 7(11), 845-854.
[189] Pandolfo, A. G., & Hollenkamp, A. F. (2006). Carbon properties and their role in supercapacitors. *Journal of Power Sources*, 157(1), 11-27.
[190] Naskar, P., & Hota, G. (2020). Oxygen intercalation in perovskite materials: a novel approach to achieve high-performance supercapacitors. *Materials Chemistry Frontiers*, 4(5), 1444-1464.

[191] Li, X., Gu, Z., Wang, C., Zhang, Y., & Li, Z. (2018). An energy management system based on supercapacitors for efficient irrigation in precision agriculture. *Computers and Electronics in Agriculture, 152*, 48-55.

[192] Dong, H., & Yeo, K. S. (2017). Autonomous supercapacitor-powered wireless sensor network for precision agriculture. *IEEE Transactions on Industrial Electronics*, 64(6), 4981-4989.

[193] Ji, Y., Li, B., Xiao, G., Wang, L., & Zhang, Y. (2014). An energy harvesting and power management scheme for long-term environmental monitoring with wireless sensor networks. *Sensors*, 14(2), 2175-2191.

[194] Mohamed Hafez, Alexander I. Popov, Tatiana Minkina, Vishnu D. Rajput, Song Ge, Kseniya I. Tsivka, Ahmed M. Abdallah, and Mohamed Rashad (2022). The Hollow Magic of Humic Substances as an Essential Environmental Component for Human Life. The Debatable Points: Humification Process and Humic Substance's Properties. Book "*Advances in Environmental Research*." Volume 91. BISAC : SCI026000 https://novapublishers.com/shop/advances-in-environmental-research-volume-91/.

[195] Wafaa Fathi Zohir, Promita Deb, Santhosh Kumar Kookal, Mohamed Hafez, Ashok Ganesan, Ahmed M. Abdallah, and Shashi Kumar (2022). Engineered Microalgae in Bioremediation. "*Advances in Environmental Research*." Volume 91. BISAC: SCI026000 https://novapublishers.com/shop/advances-in-environmental-research-volume-91/.

[196] Hafez, M., Sally, F., Abo El-Ezz., Popov, A. I., and Rashad, M. (2021) Organic Amendments Combined with Plant Growth-Promoting Rhizobacteria (*Azospirillum brasilense*) as an Eco-Friendly By-Product to Remediate and Enhance the Fertility of Saline Sodic-Soils in Egypt. *Communications in Soil Science and Plant Analysis*, 2021, Volume 52, 2021 pp 1416-1433. https://doi.org/10.1080/00103624.2021.1885687.

[197] M. Rashad, M. Hafez, Popov, A.I. (2022) Humic substances composition, properties as an environmentally sustainable system : A review and way forward to soil conservation. *Journal of Plant Nutrition*, 2022, Vol. 45, NO. 7, 1072–1122.

[198] Hafez, M., Rashad, M., Popov, A.I. The Biological Correction Using Humic Substances, Vermicompost, and Azospirillum as an Optimum Way of Optimizing Plant Production and Enhance Soil Micronutrients in Arid Regions // *Open Agriculture journal*. 2022, 16(1), e187433152204180.

[199] Hafez, M., Abdulla. A. Ahmed, Abdulla E. Mohamed, M., Rashad (2022). Influence of environmental-friendly bio-organic ameliorants on abiotic stress to sustainable agriculture in arid regions: A long term greenhouse study in northwestern Egypt, *Journal of King saud university-sciencs*. 2022, 34(6), 102212.

[200] Mohamed Rashad, Alexander Popov, Hesham Gaber, Mohamed Hafez (2022). Toward sustainable agriculture using extracts of natural materials for transferring organic wastes to environmental-friendly ameliorants in Egypt, *International Journal of Environmental Science and Technology*. 2022. https://link.springer.com/article/10.1007/s13762-022-04438-8.

[201] Hafez, M., Popov, A.I., Rashad, M. (2022) Enhancing calcareous and saline soils fertility by. increasing organic matter decomposition and enzyme activities: An

incubation study// *Communications in Soil Science and Plant Analysis*. 2022, VOL. 53, NO. 18, 2447-2459. https://doi.org/10.1080/00103624.2022.2071930.

[202] Ahmed Mohamed Mahdy, Nieven O. Fathi & Mohamed Hafez (2022) Yield Productivity and Nitrogen Uptake of Wheat Crop Are Highly Dependent on Irrigation Water Availability and Quality under Water-Limited Conditions. *Communications in Soil Science and Plant Analysis*. https://doi.org/10.1080/00103624.2022.2130936.

[203] Mohamed K El-ghannam, Fatma Wassar, Sabah Morsy, Mohamed Hafez, Chiter M Parihar, Kent O Burkey, Ahmed M Abdallah. (2023). Controlled drainage in the Nile River delta of Egypt : A promising approach for decreasing drainage off-site effects and enhancing yield and water use efficiency of wheat. *Journal of Arid Land*, https://doi.org/10.1007/s40333-023-0095-3.

[204] Hafez, M., and Popov, A.I., (2020) Influence of N-Fertigation Stress and Agro-Organic Wastes (Biochar) io Improve Yield and Water Productivity of Sweet Pepper Under Sandy Soils Conditions, *Plant Archievs*, 20(Jan), pp. 3165–3172. http://www.plantarchives.org/SPECIAL%20ISSUE%2020-1/214__3208-3217_ pdf.

[205] Mohamed Hafez., Rashad, M., Popov, A.I. (2020). The Biological Correction of Agro- Photosynthesis of Soil Plant Productivity. *Journal of Plant Nutrition*, Volume (43): 17, 2020. https://doi.org/10.1080/01904167.2020.1799008.

[206] Mohamed Hafez., Rashad, M., Popov, A.I. (2020). Evaluation of the Effects of New Environmental Additives Compared to Mineral Fertilizers on the Leaching Characteristics of Some Anions and Cations under Greenhouse Plant Growth of Saline-Sodic Soil. *Open Agriculture Journal*, 14(1), pp. 246–256, 2020. DOI : 10.2174/1874331502014010246, 2020, 14, 246-256.

[207] Rashad, M., Kenawy, E.-R., Hosny, A., Hafez, M., Elbana, M. (2021). An environmental friendly superabsorbent composite based on rice husk as soil amendment to improve plant growth and water productivity under deficit irrigation conditions. *Journal of Plant Nutrition*, vol. 44, NO. 7, 1010–1022, 2021. https://doi.org/10.1080/01904167.2020.1849293.

[208] Mohamed Hafez., Popov, A.I., Rashad, M. (2021) Integrated use of bio-organic fertilizers for enhancing soil fertility–plant nutrition, germination status and initial growth of corn (Zea Mays L.), *Environmental Technology & Innovation*, Volume 21, February 2021, 101329. https://doi.org/10.1016/j.eti.2020.101329.

[209] Hafez, M., E.A. Mohamed., Rashad, M., Popov, A.I. (2021) The efficiency of application of bacterial and humic preparations to enhance of wheat (Triticum aestivum L.) plant productivity in the arid regions of Egypt. *Biotechnology Reports*, Volume 29, March 2021. 2021, 29, e00584. DOI:10.1016/j.btre.2020. e00584.

Chapter 2

Electrochemical Corrosion Behavior and Protective Properties of Coatings Deposited from Deep Eutectic Solvents-Assisted Plating Baths

Vyacheslav Protsenko*, ScD
Ukrainian State University of Chemical Technology, Dnipro, Ukraine

Abstract

Electrochemical deposition of various types of coatings is widely used in modern industry to modify the physicochemical properties of product surfaces and increase corrosion resistance when operating in corrosive-aggressive environments. Corrosion-resistant and protective coatings based on metals, their alloys and composites can be produced using both traditional aqueous electrolytes and electrolytes containing non-aqueous organic solvents and ionic liquids. Expanding the range of types of plating baths used for electrochemical deposition of coatings opens up additional opportunities for flexible control of microstructure, chemical composition, morphology, and therefore electrochemical corrosion and protective properties. This chapter reports on the electrochemical deposition of corrosion-resistant and protective coatings from a recently developed new generation of ionic liquids, the so-called deep eutectic solvents (DES). Electrodeposition from DESs offers some environmental, technological and economic advantages over traditional aqueous and organic solvent-assisted electrolytes. The processes of electrodeposition of coatings based on zinc, nickel and chromium from plating baths of this type are described. The patterns of corrosion-

* Corresponding Author's Email: Vprotsenko7@gmail.com.

In: Advances in Materials Science Research. Volume 65
Editor: Maryann C. Wythers
ISBN: 979-8-89113-090-6

electrochemical behavior and protective properties of the manufactured coatings are characterized. The potential opportunities and prospects for further development of electrochemical deposition of anti-corrosion and protective coatings from DES-assisted electroplating baths are also considered.

Keywords: corrosion resistance, protective properties, electrodeposition, deep eutectic solvents, coating, zinc, nickel, chromium, alloy, composite

Introduction

Metal-based coatings are widely used for corrosion protection of metal substrates due to their excellent corrosion resistance properties [1]. Among various types of metal coatings, electrodeposited metal-based coatings are extensively employed in industries because of their ease of application, high adhesion, and low cost. Electrodeposited coatings are applied by the electroplating process where the coating material is deposited on the substrate surface by electrolysis. Electrodeposition offers advantages such as uniformity, thickness control, and ease of application [2, 3]. In addition, electrodeposition allows the production of nanocrystalline coatings, which usually exhibit increased corrosion resistance and protective properties. [4, 5]. The electrochemical corrosion behavior of electrodeposited coatings is a significant factor that determines their protective properties. Both the corrosion characteristics of the deposited coatings themselves and their protective properties in relation to the substrate metal can be flexibly varied by changing the chemical composition of electroplating baths and the electrolysis conditions.

Several factors can influence the corrosion behavior of electrodeposited coatings, such as the composition of the coating material, the deposition conditions, and the substrate surface preparation [1, 2]. The coating composition can influence the corrosion behavior by affecting the anodic and cathodic polarization behavior of the coating material. The deposition conditions can also influence the corrosion behavior by affecting the coating thickness, morphology, and crystal structure. The substrate surface preparation can affect the coating adhesion and barrier properties by removing contaminants and providing a clean and rough surface for coating deposition. Electrochemical deposition can be carried out using pulse and pulse reverse electrolysis, which opens up additional opportunities for adjusting the

microstructure, composition, and corrosion and protective properties of the resulting coatings [6].

Electrodeposited coatings can provide a barrier to the metal substrate by preventing corrosive species from reaching the substrate surface. The barrier properties of coatings can be affected by factors such as coating thickness, surface roughness, and the presence of defects. Electrodeposited coatings can also provide sacrificial anodic protection to the metal substrate, where the coating material corrodes instead of the substrate material. The sacrificial anode behavior of coatings is influenced by the anodic polarization behavior of the coating material.

The protective properties of electrodeposited coatings can be enhanced by modifying the coating composition, morphology, and crystal structure. The composition of the coating material can be modified by adding different alloying elements to improve the coating's corrosion resistance. The morphology of the coating can be influenced by changing the deposition conditions, such as current density, temperature, and pH. These modifications can lead to the formation of nanocrystalline coatings, which generally exhibit improved corrosion resistance and protective properties due to their unique structure and properties.

The formation of a "foreign" metal coating on the surface of the metal-substrate creates a barrier that prevents contact of the substrate with an aggressive environment. Therefore, at first glance, the patterns of corrosion behavior of coated samples should be determined exclusively by the features of corrosion of the deposited metal. However, a specific feature of the electrochemical corrosion of electrodeposited coatings, which largely determines their protective properties, is the presence of pores and cracks, which in the presence of an aggressive environment leads to the appearance of galvanic corrosion couples. In such galvanic microcells, depending on the ratio of electrode potentials, the metal of the coating and the metal of the substrate can be either the anode or the cathode. Depending on this, electrodeposited coatings based on metals and their alloys are classified into two groups [7]: (a) anodic coatings and (b) cathodic coatings.

Anodic coatings are formed from a metal that is more anodic (i.e., more electronegative) than the metal substrate. Such coatings are often called sacrificial coatings. A typical coating of this type is zinc on a steel surface. The standard electrode potentials of the electrochemical couples Zn(II)/Zn and Fe(II)/Fe are –0.76 and –0.44 V, respectively. Therefore, if pores are formed in the zinc coating, the zinc coating will perform the function of a sacrificial anode, and the steel (iron) substrate will be polarized cathodically, preventing

electrochemical corrosion destruction of the steel from a thermodynamic point of view.

Cathodic coatings are formed from a metal that is more electropositive in relation to the metal of the substrate. An example can be a copper coating (the standard electrode potential of the Cu(II)/Cu couple is +0.34 V) on steel. In this case, the protection of the substrate is possible only due to the barrier action of the coating. If there are pores in the coating, then in the formed galvanic couple, the metal substrate will be anodically dissolved during electrochemical corrosion. However, sometimes it is advisable to intentionally create a large number of very small pores in the coating as it contributes to the flow of uniform (rather than local) corrosion of the base metal. This can be acceptable for ensuring the long-term operation of products.

Electrochemical deposition of multilayer coatings is a technique used to enhance the corrosion resistance and protective properties of coatings [8]. In this process, an intermediate layer is often deposited between the substrate and the noble coating, such as nickel-chromium coatings. Typically, a layer of bright nickel with high sulfur content is applied on top of the dull nickel layer, making it nobler than the steel substrate. A finish layer of bright chromium is then deposited on the bright nickel layer. Such systems offer excellent protection against corrosion [7]. An electrodeposition procedure for a three-layer zinc-iron-chromium coating was reported in which an intermediate iron layer was used to ensure adhesion of chromium to zinc, resulting in a coating with good protective properties [9].

Electrodeposition from deep eutectic solvents (DESs) has gained increasing attention as an alternative to traditional aqueous and organic solvents for the electrodeposition of metal-based coatings. Deep eutectic solvents (DESs) are a new class of ionic liquids that have attracted significant attention in recent years due to their unique properties. DESs are composed of a hydrogen bond donor and acceptor, which form a eutectic mixture at a lower melting point than the individual components [10, 11]. Typical examples of DESs include "*ethaline*" (a eutectic mixture of choline chloride and ethylene glycol, in a 1:2 (mol.) ratio, respectively) and "*reline*" (a eutectic mixture of choline chloride and urea, in a 1:2 (mol.) ratio, respectively) [10]. The melting temperatures of these eutectic ionic liquids and their individual components are listed in Table 1. It can be observed that these DESs remain in a liquid state at temperatures close to room temperature.

DESs have several advantages over traditional solvents, such as low toxicity, low flammability, and high biodegradability [10, 11]. DESs can also dissolve a wide range of compounds, including inorganic salts and organic

molecules, making them a versatile solvent for various applications, including electrodeposition of metal-based coatings.

Table 1. Melting points of *ethaline* and *reline* and their individual constituents

Substance or eutectic mixture	Melting point, °C
ethylene glycol	–12.9
urea	134
choline chloride	303
ethaline (ethylene glycol + choline chloride, a DES)	–66
reline (urea + choline chloride, a DES)	12

Electrodeposition from DESs offers advantages such as low toxicity, high conductivity, and the ability to deposit metals at lower temperatures than traditional solvents [12–14]. The properties of DESs, such as high viscosity and low conductivity, can affect the electrodeposition process, including the nucleation and growth of the coating material.

In recent years, the electrochemical corrosion behavior and protective properties of metal-based coatings electrodeposited from DESs have been investigated in several works. This review aims to discuss the main features and peculiarities of the electrochemical corrosion behavior and protective properties of some types of metal-based coatings electrodeposited from DES-assisted electroplating baths. Specifically, we will focus on the characterization of electrodeposition and corrosion properties of coatings based on zinc, nickel, and chromium, since these are the most important and widespread types of corrosion-resistant and protective galvanic coatings used in industry.

Electrochemical Corrosion Behavior and Protective Properties of Coatings

Zinc-Based Coatings

Zinc and its alloys are an extremely common type of galvanic coatings used in industry to protect steel surfaces from corrosion in the engineering, automotive, and aerospace industries [15]. Usually, electrochemical deposition of zinc and its alloys is carried out from aqueous cyanide baths, alkaline cyanide-free baths, and acid chloride baths; all of them are, to a

greater or lesser degree, toxic and corrosive-aggressive environments. Despite the prevalence and availability of such industrial processes, they have a number of disadvantages, among which hydrogen embrittlement, low current efficiency and complications associated with wastewater treatment should be mentioned [16]. These and a number of other disadvantages of aqueous zinc plating electrolytes stimulate the development of new types of non-aqueous electrolytes, in particular those based on the use of DESs [17].

The electrochemical deposition of zinc has been studied using electrolytes based on both a eutectic mixture of choline chloride and ethylene glycol (ethaline) [18–20] and a eutectic mixture of choline chloride and urea (reline) [21, 22]. However, not all of the aforementioned published works investigated the corrosion and protective behavior of the obtained zinc coatings. The exception is the study [22], in which zinc coatings were electrochemically deposited from an electrolyte containing 0.4 M zinc chloride and 0.1 M thiourea dissolved in reline. Electrolysis was carried out at a temperature of 80°C using the following pulsed current regime: a pulse current density of 2.5 mA cm^{-2}, a frequency of 1000 Hz, and a duty cycle of 50%. The resulting zinc deposits were then modified by forming a polypropylene film on their surface by immersing the coating in a solution of polypropylene in dimethylbenzene at 130°C for 30 minutes, followed by washing and drying. In this way, superhydrophobic composite layers were fabricated. The wetting angle of the zinc coating at the interface with a drop of water before treatment was 120°, but it increased to 170° after applying the polypropylene film. The superhydrophobicity of the surface is a result of the cooperative effect of the hydrophobicity of polypropylene and the porous structure of the zinc electrodeposit. It has been shown that the formation of a superhydrophobic deposit of zinc leads to a significant increase in the corrosion resistance of coatings. In particular, the results of polarization measurements showed [22] that zinc coatings without modification have a corrosion potential E_{corr} = –1.072 V and a corrosion current density $i_{corr} = 2.53\times10^{-4}$ A cm^{-2}. Coatings modified with polypropylene, on the other hand, exhibit improved corrosion resistance, with corrosion potential E_{corr} = –0.934 V and corrosion current density $i_{corr} = 6.92\times10^{-5}$ A cm^{-2}.

The influence of inorganic and organic additives on the electrodeposition of zinc from deep eutectic solvents has been researched in several publications [23, 24]. Abbott et al., [23] studied the effect of acetonitrile, ammonia (aqueous solution), and ethylenediamine additives on zinc electrodeposition from electrolytes based on a mixture of choline chloride with ethylene glycol

or urea. It was shown that ammonia and ethylenediamine act as efficient levelers and brighteners, significantly affecting the morphology of the zinc deposit surface. These effects contribute to the improvement of the corrosion resistance of coatings in aqueous plating baths. Alesary et al., [24] investigated the influence of nicotinic acid, boric acid, and benzoquinone on the deposition of Zn from an ethaline-based solution. The additives were found to be effective brighteners that produced highly uniform and smooth Zn coatings.

Based on the current literature, it is clear that the corrosion behavior of "pure" zinc deposits obtained from DES-assisted plating baths is not well studied. It is known that zinc coatings are not highly resistant in aggressive environments, but electroplating technologies traditionally use alloying with other metal components to increase their corrosion resistance [17].

The electrodeposition of a Zn–Ni alloy from electrolytes based on DESs has been investigated in various publications [25-29]. Fashu et al., [25] examined the electrodeposition of a Zn–Ni alloy from a reline-based electrolyte with different concentrations of metal ions. The metal ions were introduced in the form of chlorides at the following concentrations: 0.4 M Zn(II) and 0.1 M Ni(II); 0.45 M Zn(II) and 0.05 M Ni(II); and 0.475 M Zn(II) and 0.025 M Ni(II). It was found that the relatively small difference in reduction potential between Ni(II) and Zn(II) ions leads to the codeposition of both components in the alloy. The coatings contained from 10 to 50% zinc, depending on the deposition conditions. The zinc content increased with a decrease in Ni(II) concentration, an increase in temperature, and an increase in cathodic polarization. The corrosion resistance of the coatings depended on their composition and morphology. An increase in the nickel content contributed to the improvement of corrosion resistance (Figure 1). The highest corrosion resistance was achieved for the Zn–Ni alloy deposited at 55 °C and a cathodic potential of –0.8 V from an electrolyte containing 0.45 M Zn(II) and 0.05 M Ni(II), which resulted from an even, dense and defect-free surface morphology due to an optimal content of components in the coating.

Li et al., [26] studied the deposition of a Zn–Ni alloy from a reline solution with varying water concentrations (0, 1, 3, 5, and 7 wt.%). The introduction of a certain amount of water is a method for controlling the coating composition. By adjusting the water concentration and deposition potential, the nickel content in the alloy could be varied from 4 to 96 wt.%. All coatings exhibited lower corrosion currents and more positive corrosion potentials than the steel substrate in 3.5 wt.% NaCl solution. Corrosion resistance was increased with increasing the nickel content. Notably, coatings with higher nickel content showed more positive corrosion potentials than steel when the water content

in the electrolyte was less than 3 wt.%. When the water content in the electrolyte exceeded 3 wt.%, the Zn–Ni coatings with increased zinc content were deposited; they showed slightly negative corrosion potentials than steel and exhibited protective properties. The coating with a content of ~14 wt.% Ni (γ-phase) exhibited the highest protective properties against steel in 3.5% NaCl.

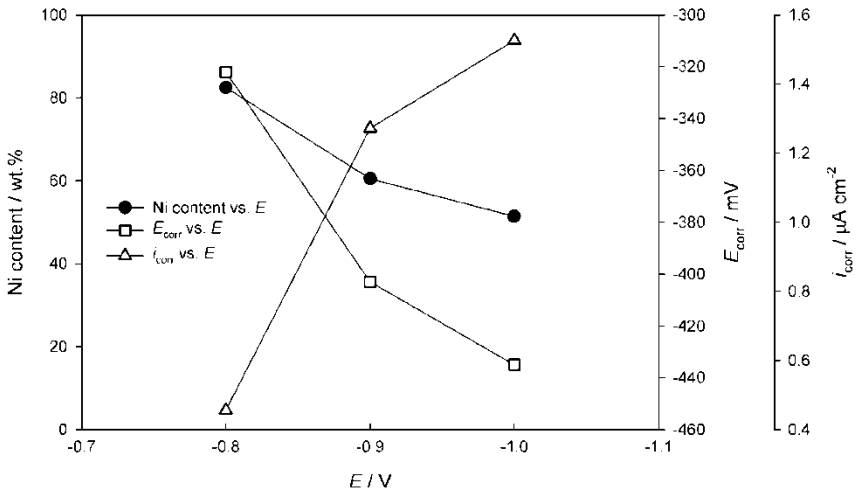

Figure 1. Corrosion potential E_{corr} and corrosion current density i_{corr} in 0.35 M NaCl solution for the Zn–Ni coatings deposited at different electrode potentials (0.45 M Zn(II), 0.05 M Ni(II) at 70°C). The figure is plotted based on data from reference [25].

Lei et al., [27] deposited a Zn–Ni alloy coating from an ethaline-based electrolyte, modified by adding propylene carbonate to reduce the liquid's viscosity. Boric acid was also added to improve the surface morphology and adhesion of coatings. The proposed electrolyte composition can be used for the production of electrodeposited zinc-nickel alloy coatings (γ-phase) with a Zn content of approximately 81–85%, using either potentiostatic or pulse electrolysis modes. The obtained coatings exhibit high protective properties against corrosion of the steel substrate in an aggressive 3.5% NaCl environment (Figure 2).

A comparative analysis was conducted on the deposition processes of Zn–Ni alloy from electrolytes in which the solvent was either a eutectic mixture of choline chloride and ethylene glycol (ethaline) or pure ethylene glycol as the solvent [28]. It was found that an increase in the concentration of ethylene

glycol shifts the deposition potentials of both nickel and zinc in the negative direction, which indicates the formation of the corresponding complexes of nickel and zinc. Increasing the concentration of ethylene glycol (when going from ethaline to pure ethylene glycol) reduces the difference between the deposition potentials of the alloy components. The electrodeposition of the Zn–Ni alloy in electrolytes of both types obeys the laws of anomalous codeposition, where the more electronegative component (zinc) is preferentially deposited in the alloy. From both studied of electrolytes, it is possible to obtain coatings with the nickel content in the range from 10 to 20 wt.%, which is of great interest for industrial use in corrosion protection. At the same time, a metastable γ-phase is formed on the cathode, built of nanocrystallites with an average size of approximately 17.4 nm and 11.06 nm for electrolytes based on ethaline and pure ethylene glycol, respectively. Table 2 shows the systematized results obtained from corrosion measurements. The corrosion potential of the Zn–Ni alloy is more negative than that of steel and slightly higher than that of pure zinc. This indicates that during the electrochemical corrosion of the zinc-nickel alloy, the zinc component disintegrates mainly, forming a surface layer enriched with nickel. This layer is a physical barrier that prevents further corrosion [28].

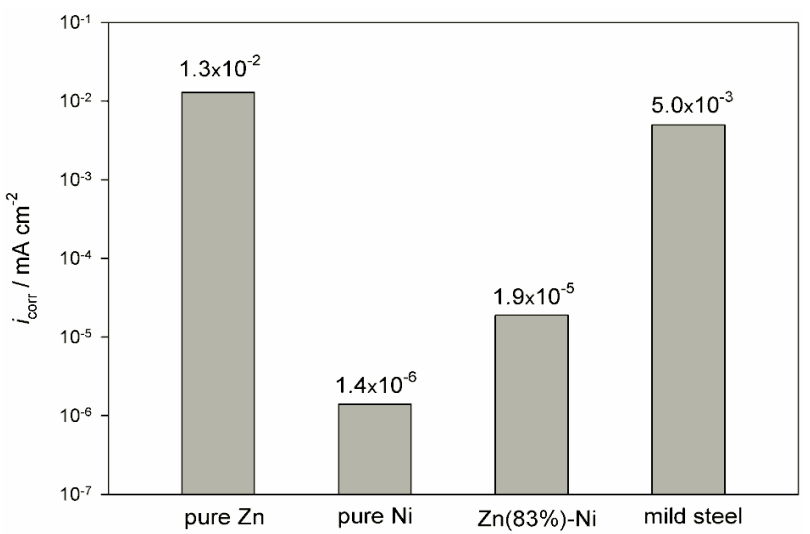

Figure 2. Corrosion current density of Zn, Ni, Zn–Ni coatings and mild steel in 3.5% NaCl. The figure is plotted based on data from reference [27].

Table 2. Corrosion data for Zn–Ni alloys and Fe substrate in 3.5% NaCl solution

Sample	E_{corr} (mV vs. Ag/AgCl)	i_{corr} (μA cm^{-2})
Fe substrate	–402	7.5
20% Ni deposited from ChCl/EG 1:2	–902	1.6
20% Ni deposited from ChCl/EG 1:4.5	–859	4.3
15% Ni deposited from ChCl/EG 1:4.5	–774	3.7
12% Ni deposited from ChCl/EG 1:4.5	–853	7.9
18% Ni deposited from pure EG	–852	18.1
15% Ni deposited from commercial ZnNi plating bath	–826	11.8

Reprinted from [28].

Alesary et al., [30] investigated the effects of boric acid, ammonium chloride, and nicotinic acid additives on the electrochemical deposition of Zn–Sn alloy from an ethaline-assisted plating bath. Without additives, dark gray coatings of unsatisfactory quality are formed. However, the introduction of boric and nicotinic acids produces uniform and bright deposits due to their adsorption on the cathode, which inhibits the processes of zinc and tin deposition. The addition of ammonium chloride promotes the formation of complexes with zinc ions, inhibiting the partial process of zinc deposition. The presence of additives enhances the morphology, microstructure, and corrosion resistance of coatings. The experimentally determined corrosion rates (mm year^{-1}) are 0.0117, 0.00369, 0.095, 0.0609, 0.0305, and 0.0875 for pure zinc, pure tin, zinc-tin alloy without additives, zinc-tin alloy with boric acid addition, zinc-tin alloy with ammonium chloride addition, and zinc-tin alloy with nicotinic acid addition, respectively.

Bučko et al., [31] studied the electrochemical deposition of a zinc-manganese alloy from ethaline. They demonstrated the formation of electrodeposited Zn–Mn coatings that exhibit good corrosion resistance in a 3% NaCl solution.

From electrolytes based on DESs, it is possible to produce not only corrosion-resistant alloys based on zinc, but also composite coatings, which are an electrodeposited metal matrix with embedded particles of a solid dispersed phase [32]. For example, Marín-Sánchez et al., [33] reported electrodeposition of Zn/Ce_2O_3–CeO_2 composite coatings using an electrolyte containing 0.3 M $ZnCl_2$ and 0.3 M $CeCl_3{\cdot}7H_2O$ in reline. When the cathode deposition density varied in the range from 1.13 to 0.75 A dm^{-2}, coatings were formed with a total cerium content of 8.30 to 1.36 at.% in the form of cerium

oxides with different degrees of Ce oxidation (≈50.6% Ce_2O_3 + 49.4% CeO_2). The introduction of Ce_2O_3 and CeO_2 particles into the zinc matrix helps to increase the corrosion resistance of coatings. In particular, the corrosion rate of a zinc coating in an aggressive environment of 0.05 M NaCl is 2.29×10^{-5} A cm^{-2}, while when cerium oxide particles are included in the coating, it is in the range of $(1.62–1.78)\times10^{-5}$ A cm^{-2}.

It is worth noting that the literature reports on the electrodeposition of other zinc alloys from electrolytes based on DESs, such as Zn–Co [34] and Zn–Ti [35]. It could be argued *a priori* that these coatings may exhibit increased corrosion resistance and protective properties, but corresponding experimental studies have not yet been conducted.

Thus, the use of DESs enables the expansion of the chemical compositions available for various types of zinc alloys when compared to traditional aqueous electrolytes. However, currently, there is a lack of research on the corrosion behavior of these coatings, which highlights the need for further investigation in this area as an urgent task for future studies.

Nickel-Based Coatings

The electrochemical deposition of nickel and coatings based on its alloys and composites is one of the oldest and most widespread types of electroplating [36–39]. Nickel coatings are used to provide corrosion protection and decorative properties. Although nickel is a highly electronegative metal (with a standard potential of –0.25 V for the Ni(II)/Ni electrochemical couple), due to its tendency to passivate, it acquires a sufficiently positive potential and exhibits considerable resistance to atmospheric exposure, alkaline solutions, and some acids. Nevertheless, nickel corrodes rapidly in many mineral acids. In the nickel-iron galvanic corrosion couple, nickel acts as the cathode and protects steel surfaces from corrosion only if the coating has no through pores or cracks. Nickel is often applied to steel with an intermediate copper layer. Electrodepositing several successive layers of nickel containing sulfur is a common practice. Electrodeposition of nickel alloys can improve not only corrosion resistance, but also other functional properties such as hardness, wear resistance, magnetic properties, and electrocatalytic properties [39–41].

In industry, nickel coatings are primarily deposited from aqueous electrolytes. However, recent research has explored the electrodeposition of nickel, its alloys and composites from DES-based solutions [40–49]. It can

also be noted that a significant number of published scientific works in this field are focused on the electrodeposition of nickel-based coatings. Below, we will describe only those works that have characterized the corrosion behavior and protective properties of the deposited coatings.

Nanocrystalline nickel coatings were electrodeposited on a brass substrate using an electrolyte based on ethaline at room temperature under potentiostatic conditions [43]. The coatings were composed of Ni nanocrystals with a face-centered cubic lattice and an average crystallite size of approximately 6 nm. Results showed that these electrodeposits had increased microhardness and high corrosion resistance in an aggressive environment containing 3% NaCl. Specifically, the corrosion potential was found to be about –220 mV and the corrosion current density was 4.92×10^{-4} mA cm^{-2} for the brass substrate, while the corresponding values for the deposited nanocrystalline nickel coating were approximately –690 mV and 11.02×10^{-2} mA cm^{-2}. As a result, the nickel layers acted as sacrificial anode protection for the brass substrate in a 3 wt.% NaCl aqueous solution at room temperature.

The use of an ethaline-based electrolyte offers broad possibilities for manipulating the micro/nanoarchitecture of electrodeposited nickel deposits through programmed electrolysis techniques [44]. For instance, during stationary potentiostatic electrolysis, nanoplates with sizes of 10–50 nm can be formed on the surface, the edges of which resemble arrowheads. In pulsed mode, depending on the duty cycle, coatings with surface morphology similar to fingerprints are produced, lined up in a row of narrow strips and nanoplates. When using the reverse pulse mode, flower-like clusters with a hierarchical structure on the surface are formed. Nanostructuring of the surface leads to the formation of superhydrophobic surfaces in the electrodeposited nickel layers, which exhibit increased corrosion resistance in a 3 wt.% NaCl aqueous solution. For example, the corrosion potential of the brass substrate was approximately –0.225 V (vs. the saturated calomel electrode), whereas the corrosion potential of the superhydrophobic nickel layer was –0.710 V, which is significantly more negative than that of the substrate. Hence, the nickel coating deposited from the DES-based electrolyte provides an efficient protection of the brass surface against corrosion.

Bernasconi and Magagnin [46] investigated the electrodeposition of nickel on an aluminum surface using a deep eutectic solvent. Interestingly, the deposits obtained from DESs showed reduced corrosion resistance, making them unsuitable for industrial use. However, depositing a nickel intermediate layer from the DES-based electrolyte on the aluminum surface, followed by the deposition of a final layer from an aqueous nickel-plating electrolyte,

significantly improved corrosion resistance. It is suggested that the DES-assisted plating electrolyte helps to form a well-bonded layer on the surface of the aluminum alloy without passivating the substrate. Subsequently, depositing nickel from water plating baths on this intermediate layer is advisable.

It has been found that by adding water to electrolytes based on deep eutectic solvents, several physicochemical and operational parameters of the nickel electrodeposition process can be significantly improved [47, 48]. However, water should not be regarded as an additional solvent, but rather as an additional source of hydrogen bonds during the formation of the deep eutectic solvent [48]. At certain concentrations, not exceeding a certain level, the electrolyte based on a DES retains a specific hole mechanism of mass and charge transfer, and remains essentially an ionic liquid, without turning into a highly concentrated aqueous solution.

The introduction of additional water into the nickel-plating electrolyte based on DESs leads to a decrease in viscosity and an increase in electrical conductivity, which is important and favorable from the point of view of the potential practical application of these systems [48]. In addition, the introduction of water into the composition of electrolytes allows controlling the microstructure and various properties of the obtained coatings [47]. Nanocrystalline coatings with a face-centered cubic lattice are deposited from nickel plating electrolytes based on ethaline with water additives. The average crystallite sizes, estimated according to the Scherrer equation, ranged from 3.1 to 7.2 nm. The introduction of additional water into the DES-based nickel-plating electrolytes resulted in an increase in the deposit microhardness and an improvement in corrosion resistance. Figure 3 shows Nyquist diagrams for corrosion of Ni coatings in a 0.05 M H_2SO_4 solution. These diagrams (impedance hodographs) have the form of compressed semicircles with the center located below the real axis. This indicates that the corrosion rate of nickel coatings is determined by the charge transfer on the heterogeneous electrode surface, which can be described by the so-called constant phase element (CPE) [50]. To interpret the results of electrochemical impedance measurement, the equivalent circuit shown in Figure 4 was used. This equivalent circuit contains the polarization resistance of the electrode reaction (R_{ct}), the constant phase element (characterized by two parameters Q and n) and the ohmic resistance of the solution (R_s). The calculated kinetic parameters are summarized in Table 3.

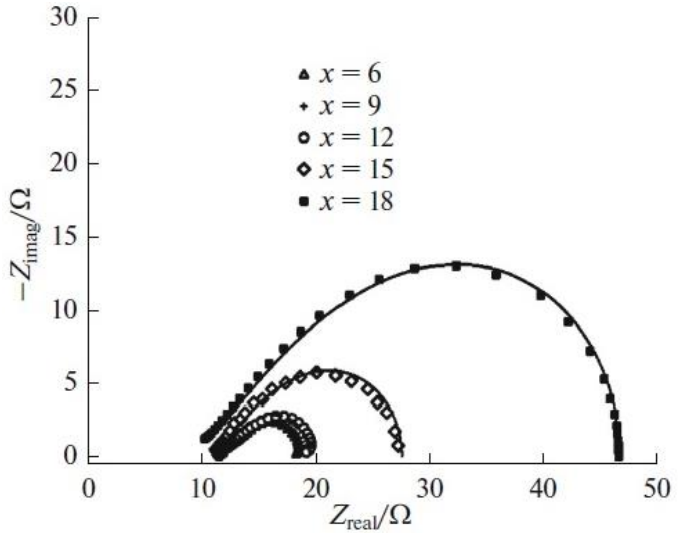

Reprinted from [47] by permission of Springer Nature, Copyright 2017.

Figure 3. Nyquist diagrams of nickel coatings electrodeposited from electrolytes containing ethaline+$NiCl_2$+xH_2O. Symbols represent experimental values and solid lines reflect calculated results.

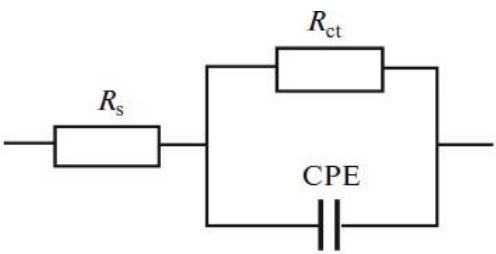

Reprinted from [47] by permission of Springer Nature, Copyright 2017.

Figure 4. Equivalent circuit simulating the electrochemical impedance of the corroding electrode/solution surface.

An increase in the polarization resistance R_{ct} with an increase in the water content in the nickel plating electrolyte indicates an increase in the corrosion resistance of nickel deposits. Simultaneously, the value of Q decreases and the parameter n increases. Analysis of the obtained data allows us to conclude that the introduction of additional water into the solution of $NiCl_2 \cdot 6H_2O$ in ethaline leads to a decrease in the degree of roughness and heterogeneity of Ni coatings and an increase in their corrosion resistance in a 0.05 M H_2SO_4 solution [47]. It was suggested that water molecules from the nickel-plating electrolyte are

captured by the coating and absorbed on the active centers (crystal defects) of the metal, blocking them. As a result, a continuous and stable nickel hydroxide passivating film is quickly formed. In addition, the corrosion resistance of coatings increases due to the leveling of the surface, which is indicated by higher values of the parameter *n*.

Table 3. Calculated parameters of the equivalent circuit that simulates the corrosion of nickel coatings in a solution of 0.05 M H_2SO_4 at the corrosion potential

System*	R_s, Ω	R_{ct}, Ω	Q, Ω^{-1} s^n	n
Ethaline + $NiCl_2{\cdot}6H_2O$	11.37	8.45	78.81×10^{-3}	0.526
Ethaline + $NiCl_2{\cdot}9H_2O$	11.22	8.81	68.24×10^{-3}	0.530
Ethaline + $NiCl_2{\cdot}12H_2O$	11.49	8.85	51.04×10^{-3}	0.629
Ethaline + $NiCl_2{\cdot}15H_2O$	11.05	16.32	1.24×10^{-3}	0.985
Ethaline + $NiCl_2{\cdot}18H_2O$	10.61	22.83	84.61×10^{-6}	0.991

Note: * – The numbers before H_2O in the first column indicate the molar amount of water.
Reprinted from [47] by permission of Springer Nature, Copyright 2017.

The addition of a second component can improve the corrosion and protective properties of coatings by forming an alloy with nickel [37, 39]. Wang et al., [51] reported the formation of a binary nickel-copper alloy from a reline-based solution containing 0.6 M $NiCl_2{\cdot}6H_2O$ and 0.01 M $CuCl_2{\cdot}H_2O$. Unlike aqueous electrolytes, the deposition potentials for copper and nickel in DESs are very close to each other, allowing the alloy to be deposited without the use of special additives. By increasing the cathode current density, the copper content in the alloy can be enriched, and alloys with copper content ranging from 5 to 40 at.% can be formed. Polarization measurements in a 3.5 wt.% NaCl solution showed that Ni–Cu alloy coatings (~17.6 at.% Cu) deposited from the reline-assisted plating electrolyte demonstrate greater corrosion resistance than commercial Monel-400 alloy (~28 at.% Cu) or an alloy with a higher copper content (~33.6 at.%), but deposited from an aqueous electrolyte. The corrosion current densities of the coatings were found to be 3.17×10^{-7}, 2.24×10^{-6} and 1.27×10^{-6} A cm^{-2}, respectively [51].

Yang et al., [52] described the electrolytic deposition of a Ni–Zn alloy from an electrolyte in which 0.1 M $NiCl_2$ and 0.4 M $ZnCl_2$ were dissolved in reline. It was shown that nickel, as a more electropositive metal, is deposited preferentially compared to zinc. Deposition of the Zn component occurs only at sufficiently negative potentials, therefore its content in the coating is always less than 50 at.% (Figure 5, a). The resulting Ni–Zn alloy was a solid solution.

Coatings with a Ni content of 87 at.% and above showed increased corrosion resistance (Figure 5, b) due to the dense and nonporous microstructure.

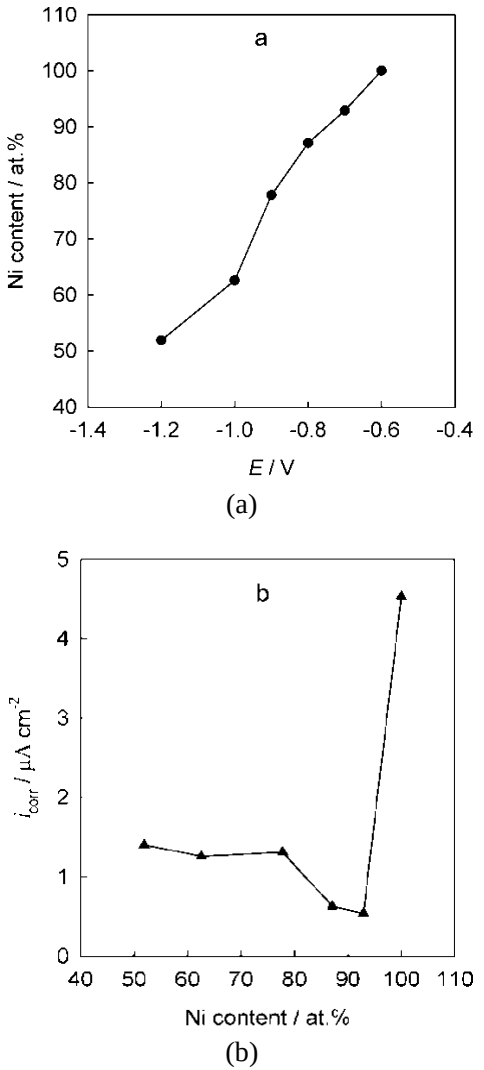

Figure 5. Dependences of the nickel content in the Ni–Zn coating on the electrodeposition potential (a) and the corrosion current density in 0.1 M NaCl on the nickel content in the coating (b) for Ni–Zn coatings deposited from an electrolyte containing 0.1 M $NiCl_2$ and 0.4 M $ZnCl_2$ in reline, at 70 °C. The figure is plotted based on data from reference [52].

You et al., [53] demonstrated the possibility of electrodepostion of a nickel–cobalt alloy from solutions based on ethaline. An increase in the concentration of cobalt ions in the electrolyte allows obtaining alloys with the cobalt content of 4% to 40%. However, introducing cobalt increases the corrosion currents of the coating in an aggressive environment of 3% NaCl. For example, the corrosion current densities are equal to 2.5, 3.7, 5.8 and 6.1 μA cm^{-2} when the cobalt content in the coating is 0, 4, 18 and 40 wt.%, respectively. On the contrary, Li et al., [54] studied the electrodeposition of a Ni–Co alloy from an ethaline-based electrolyte and showed that an increase in the cobalt content leads to a certain decrease in the corrosion current density in an aggressive environment of 3.5% NaCl. It is obvious that the data on the corrosion behavior of this kind of electrodeposited alloy is contradictory and require further research.

The study by Vijayakumar et al., [55] focused on the electrodeposition of a ternary Ni–Co–Sn alloy from an electrolyte based on ethaline. The authors also prepared Ni–Sn and Co–Sn binary alloys from the same electrolyte for comparison. The results showed that the Ni–Co–Sn ternary alloy has potential as an electrocatalyst for hydrogen production in an aqueous alkaline medium, with higher current density of the hydrogen evolution reaction and greater corrosion resistance compared to the Ni–Sn and Co–Sn binary alloys in a 1 M KOH solution. The corrosion current densities of Ni–Sn, Co–Sn, and Ni–Co–Sn alloys were determined to be 1.167×10^{-3}, 1.472×10^{-3}, and 5.340×10^{-4} A cm^{-2}, respectively.

Nanocrystalline nickel-molybdenum alloys have been successfully deposited from an electrolyte based on a reline solvent [56]. The composition of the obtained coatings varied from 2 to 35 wt.% molybdenum, depending on the electrolysis conditions and the electrolyte composition. The introduction of molybdenum into nickel led to a significant increase in the corrosion resistance of the coating, with the corrosion current density for the nickel coating in a 0.5 M NaCl solution being 169 μA cm^{-2}, compared to only 3.94 μA cm^{-2} for the nickel-molybdenum alloy (8–9 wt.% Mo). Notably, Ni–Mo alloys deposited from DESs exhibited higher corrosion resistance than similar coatings obtained from conventional aqueous electrolytes. This behavior was attributed to the unique surface morphology of coatings fabricated from DESs, which featured more uniform and low-defect patterns, as well as their nanocrystalline structure. High corrosion resistance in an aggressive environment was also observed for nickel-molybdenum coatings deposited

from electrolytes based on a eutectic mixture of choline chloride and propylene glycol [57].

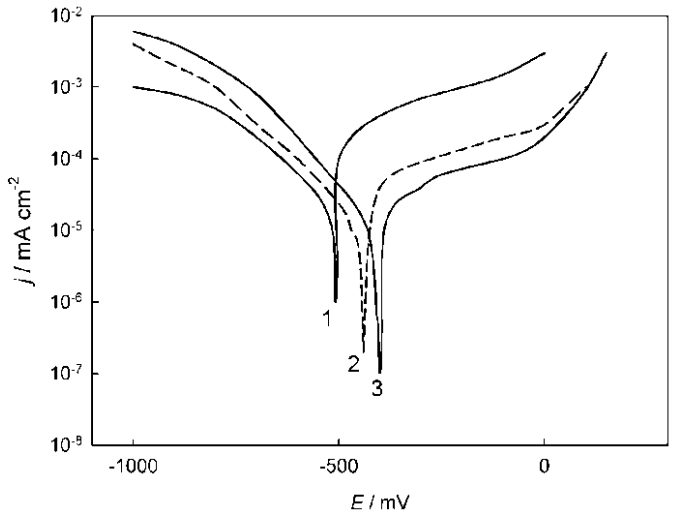

Reprinted with modification from [60].

Figure 6. Polarization curves of nickel (1), nickel-titania (5% TiO_2) (2) and nickel-titania (10% TiO_2) (3) electrodeposits in 3% NaCl. Sweep rate was 0.001 V s^{-1}.

Electrolytes based on deep eutectic solvents can also be used for the electrochemical deposition of composite coatings with a nickel matrix. It has been established that the inclusion of a dispersed phase into the nickel matrix contributes to a significant increase in the coating's corrosion resistance [58–60]. For illustration, Figure 6 shows the polarization curves characterizing the electrochemical corrosion behavior of Ni and Ni–TiO_2 coatings in a corrosive medium of 3% NaCl, and the calculated corrosion parameters are summarized in Table 4 [60]. It can be seen that the inclusion of titanium dioxide nanoparticles in the nickel matrix and the increase in their concentration lead to a shift in the corrosion potential towards positive values and a decrease in the corrosion current density. This behavior is explained by the presence of a barrier effect, which partially prevents the contact of the metal matrix with an aggressive environment, the formation of a large number of corrosion microcells, which contributes to the inhibition of local corrosion, and the growth of the length of current paths during electrochemical corrosion [61].

Table 4. Corrosion potential and corrosion current density of Ni and Ni–TiO_2 coatings in a 3% NaCl water solution extracted from Tafel analysis

Coating	E_{corr} (mV)	j_{corr} (mA cm^{-2})
Ni	–508	9.31×10^{-6}
Ni–TiO_2 (5%)	–451	3.45×10^{-6}
Ni–TiO_2 (10%)	–408	1.28×10^{-6}

Reprinted with modification from [60].

Thus, the use of DES-assisted plating baths makes it possible to expand the range of various nickel alloys and composites and controllably adjust the composition of coatings by changing the electrolysis conditions. This opens up additional opportunities for increased corrosion resistance compared to water systems.

Chromium-Based Coatings

As is known, electrochemical chromium plating is an extremely widespread type of coating electrodeposition [36, 62]. The wide use of chromium coatings is due to a number of their unique multifunctional properties. In particular, although the standard potential of the electrochemical couple Cr(III)/Cr = –0.74 V is quite negative, due to the ability of chromium to passivate, its surface is covered with a thin dense protective oxide film that inhibits corrosion in many types of aggressive environments. Chromium coatings exhibit an attractive surface appearance, which is maintained for a very long time. Chromium deposition is widely used for applying hard, wear-resistant and anti-friction coatings [63].

A major disadvantage of conventional chromium plating processes is the use of concentrated solutions of hexavalent chromium compounds, which are extremely toxic and harmful. It is well known that the use of hexavalent chromium is currently very limited [64]. An alternative to chromium plating electrolytes based on Cr(VI) could be environmentally friendly chromium plating baths based on Cr(III) salts [65]. However, progress in this direction is not yet fast enough due to the peculiarities of the chemistry and electrochemistry of trivalent chromium compounds in aqueous solutions [66, 67].

The use of DES-assisted trivalent chromium plating baths could offer a promising alternative to conventional water electrolytes for chromium plating [68–75]. They have several advantages over water-based analogues, including environmental safety, a smaller volume of wastewater generated, stability of

the chemical composition, ability to deposit various chromium-based alloys and composites, and increased current efficiency. Chromium coatings deposited from electrolytes based on DESs exhibit increased electrocatalytic activity [76], attributed to their unique electrochemical properties and specific corrosion behavior, which has been the subject of research in several publications.

Protsenko et al., [72] described the electrodeposition of coatings from a DES composed of $1CrCl_3 + 2.5ChCl + 15H_2O$ (where the numbers before the chemical formulae indicate molar ratios). The coatings exhibited amorphous-type microstructures and contained chromium, carbon, oxygen, and chlorine. It is obvious that the source of metalloids in the coating is the corresponding components of the electrolyte. Carbon incorporation into coatings produced from Cr(III) electroplating baths is a typical phenomenon, occurring by a chemical or electrochemical mechanism [77]. The modified chemical composition due to the introduction of metalloids and the formation of an amorphous structure significantly changed the electrochemical corrosion behavior of coatings. For example, the polarization curve of the anodic dissolution of "ordinary" chromium in an acidic medium includes the classic sections of active dissolution, passive state, and transpassive dissolution (Figure 7, curve 1). However, coatings produced from a DES-based electrolyte did not show a section of active dissolution, and the segment corresponding to cathodic hydrogen evolution shifted towards more positive potentials (Figure 7, curve 2) [72]. This behavior suggests high corrosion resistance of coatings produced from DES, attributed to the formation of a special surface protective film enriched with carbon [78]. Carbon and its compounds with chromium, such as chromium carbides, act as specific "cathodic agents" that shift the corrosion potential to the area of the passive state, thereby significantly reducing the rate of corrosion destruction.

A study was conducted to determine the corrosion resistance and protective properties of coatings deposited from a liquid mixture containing choline chloride, chromium (III) chloride, and water (at a molar ratio of 2.5:1:12, respectively) [74]. Coatings with a thickness of 2.5, 5, 10, 15, and 20 μm were deposited on a steel substrate. A 0.1 N Na_2SO_4 solution was used as an aggressive medium with a pH of 3.0. In such an environment, chromium is in a passive state and does not dissolve in an active state (Figure 8). Therefore, by neglecting the dissolution rate of chromium compared to iron (steel, which dissolves through pores and cracks in the coating), the degree of protection (*DP*) can be calculated using the following equation:

$$DP = \frac{j_s - j}{j_s} \cdot 100\%$$

where j is the maximum current density of anodic dissolution of steel with Cr deposit; and j_s is the maximum current density of anodic dissolution of steel without Cr deposit.

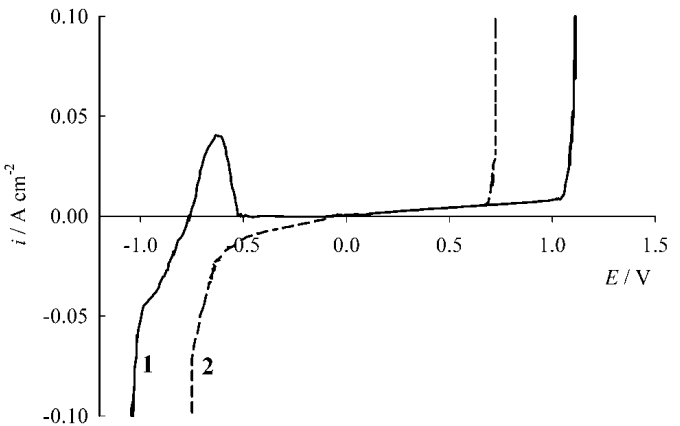

Reprinted with modification from [72].

Figure 7. Polarization dependences of deposits in 0.5 M H_2SO_4 solution at 25°C: (**1**) coatings from hexavalent chromium bath (250 g dm^{-3} CrO_3 + 2.5 g dm^{-3} H_2SO_4) at 40 A dm^{-2} and 45°C; (**2**) coatings from electrolyte containing $CrCl_3$ + 2.5ChCl + 15H_2O at 5 A dm^{-2} and 40°C. Scan rate is 50 mV s^{-1}.

The results presented in Table 5 show that the degree of protection reaches its maximum value of 97.5% when the coating thickness increases to 5 μm. However, further thickness increase leads to a gradual decrease in the protective properties, probably due to the cracking of the coatings and an increase in their defectiveness [74].

Table 5. The effect of coating thickness on the degree of protection

Chromium deposits thickness (μm)	*DP* (%)
2.5	55.8
5	97.5
10	94.1
15	86.4
20	78.3

Reprinted from [74].

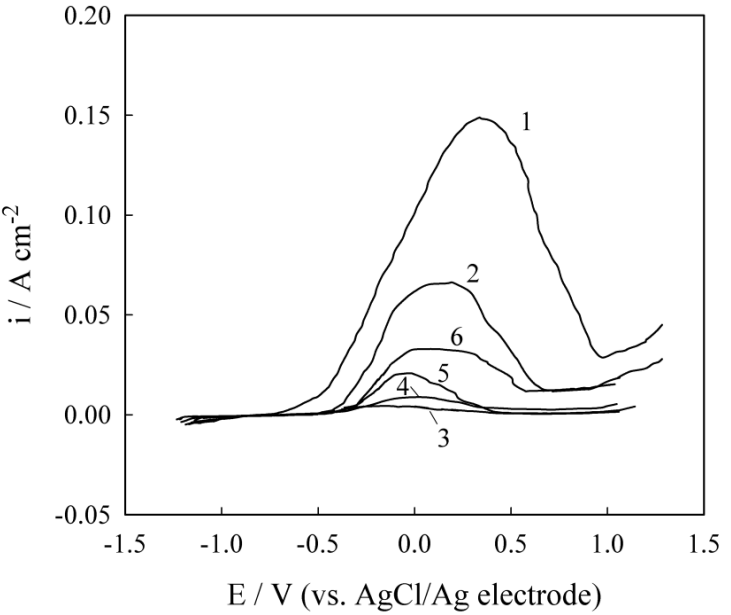

Reprinted from [74].

Figure 8. Polarization curves of a steel sample (1) and steel samples coated with chromium layers with a thickness of 2.5 μm (2), 5 μm (3), 10 μm (4), 15 μm (5) and 20 μm (6) recorded in 0.1 N aqueous Na_2SO_4 solution (pH 3.0).

The electrochemical impedance spectroscopy method was used to conduct a detailed study of the corrosion and protective properties of chromium coatings. The results showed that the coating thickness of 5 μm corresponded to the highest polarization resistances of the electrode reaction and the smallest values of capacitive components and dimensionless index in the constant phase element, indicating the best protective and corrosion characteristics (Figure 9, Table 6). This contradicts the commonly accepted notion that thicker chromium coatings provide better protection against corrosion. These findings are significant for the practical application of chromium coatings deposited from DESs.

There are several published works devoted to the electrochemical deposition of chromium alloys with other metals and metalloids from deep eutectic solvents, where the corrosion characteristics of the deposits were studied [79–83].

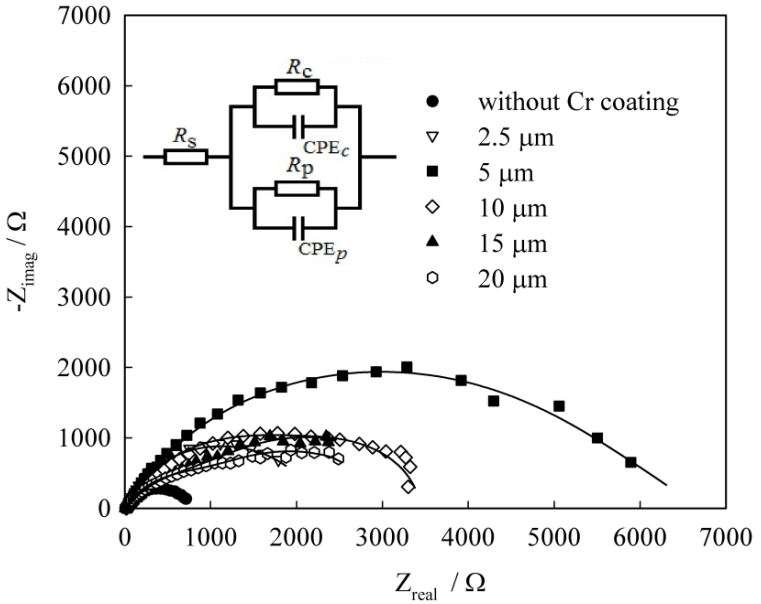

Reprinted from [74].

Figure 9. Nyquist plots of mild steel (1) and Cr deposits on mild steel substrate (2–6) in 0.1 N Na_2SO_4 (pH 3.0) at open circuit potential. The thickness of chromium deposits (μm): 2.5 (2), 5 (3), 10 (4), 15 (5) and 20 (6). The inset shows the equivalent circuit used to interpret the impedance of electrode/solution interface.

Chromium–phosphorus coatings were deposited from an electrolyte based on ethaline, which contained 0.3 M $CrCl_3 \cdot 6H_2O$, 0.2 M NaCl, and 0.05 M $NH_4H_2PO_2$ [79]. The resulting coatings contained approximately 6 wt.% phosphorus, as well as impurities of Cr_2O_3 and $Cr(OH)_3$ in addition to the dominant metal component. It was found that the corrosion resistance of Cr–P alloy coatings is higher than that of "pure" chromium in an aggressive environment of 0.1 M H_2SO_4, but lower in an aggressive environment of 3.5 wt.% NaCl.

Nanocrystalline coatings of Fe–Cr alloy were electrodeposited from the ethaline-based DES without adding other organic components [80]. The resulting coating has high corrosion resistance in an aqueous solution of 5 wt.% NaCl. This is due to the nanocrystalline structure of the coating (an average particle size of about 1.53 nm) and the formation of a very compact protective passive film of Cr_2O_3 and Fe_2O_3 oxides. Similar results are described in study [81].

Table 6. The calculated electrochemical impedance parameters of the corrosion of chromium coatings and steel substrate

Thickness of deposit (μm)	R_s (Ω)	Characteristics of corrosion of Cr deposits			Characteristics of corrosion of steel substrate through pores		
		R_c (Ω cm^2)	$Q_c \times 10^6$ (Ω^{-1} s^n cm^{-2})	n_c	R_p (Ω cm^2)	$Q_p \times 10^3$ (Ω^{-1} s^n cm^{-2})	n_p
– (steel substrate)	10.5	–	–	–	748	2010	0.650
2.5	10.5	940	1180	0.675	2199	4.09	0.700
5	10.0	5050	39	0.959	3595	0.73	0.998
10	10.3	2310	200	0.807	3100	2.5	0.997
15	10.4	1010	680	0.795	2500	2.9	0.800
20	10.2	950	780	0.755	2200	3.9	0.500

Reprinted from [74].

Saravanan and Mohan [82] demonstrated the possibility of electrodeposition of a ternary chromium-nickel-iron alloy (with 4–15% Cr, 34–41% Ni, and 53–61% Fe) from an ethaline-based electrolyte. Thick coatings of this composition can compete with highly corrosion-resistant stainless steels. Potentiodynamic polarization tests and electrochemical impedance spectroscopy showed that the deposited $Fe_{54.62}Ni_{30.87}Cr_{14.5}$ alloy exhibits superior corrosion resistance in an aggressive environment of 3.5% NaCl, surpassing the resistance of mild steel substrate. It should be noted that deposition of Fe–Cr–Ni ternary alloys from conventional aqueous solutions is an extremely difficult task [83], and therefore, the use of electrolytes based on DESs presents excellent prospects in this direction.

The use of DES-assisted plating baths for the electrochemical deposition of corrosion-resistant chromium-based composite coatings remains largely unexplored in the literature. However, there is one study [84] that reports the production of Cr–single walled carbon nanotube (SWCNT) composite coatings from an ethaline-based solution using pulse electrolysis. The addition of single-walled carbon nanotube particles resulted in a significant increase in microhardness and corrosion resistance of the coatings in an environment of 3.5 wt.% NaCl. The corrosion current densities for the chromium coating and the Cr–SWCNT composite were 312.7 and 180.9 μA cm^{-2}, respectively.

Conclusion

The literature analysis reveals that deep eutectic solvents-based electrolytes can be effectively utilized for the electroplating of protective and corrosion-resistant coatings. Compared to conventional water-based plating solutions, the advantages of DES-based systems include improved environmental, economic, and technological factors, as well as the capability for flexible tuning of the coatings' chemical composition and microstructure, resulting in improved physicochemical properties such as increased resistance to corrosion in aggressive environments and enhanced protective characteristics. DES-assisted electrodeposition processes can produce nanocrystalline structured alloys based on nickel, zinc, and chromium with other metals and metalloids, where the chemical composition and properties of the coatings can be varied within a broad range. Additionally, the production of composite coatings from DESs is a promising direction, as these systems provide enhanced stability

against aggregation and sedimentation, leading to the stable formation of composites with a high content of dispersed phase in the metal matrix.

The lack of systematic and comprehensive studies on the electrochemical deposition of DES-based coatings and their corrosion behavior and protective properties makes it difficult to draw clear conclusions about the potential of these systems for practical applications. Therefore, further research in this area is needed to establish reliable correlations between the composition, structure, and properties of the coatings obtained, as well as to optimize the conditions of their synthesis and application. This will help to expand the range of technological solutions based on DES-assisted electrodeposition and to create new materials with tailored properties and improved performance in various fields of industry and technology.

Disclaimer

None.

References

[1] Chung, P. P., Wang, J. and Durandet, Y. (2019). Deposition processes and properties of coatings on steel fasteners – A review. *Friction*, 7 (5): 389-416.

[2] Haseeb, A., Blanpain, B., Wouters, G., Celis, J. P. and Roos, J. (1993). Electrochemical deposition: a method for the production of artificially structured materials. *Mater. Sci. Eng. A*, 168: 137-140.

[3] Fotovvati, B., Namdari, N. and Dehghanghadikolaei, A. (2019). On coating techniques for surface protection: a review. *J. Manuf. Mater. Process*, 3: 28.

[4] Herrasti, P., Ponce de León, C. and Walsh, F. C. (2012). The corrosion behaviour of nanograined metals and alloys. *Rev. Metal.*, 48 (5): 377-394.

[5] Gurrappa, I. and Binder, L. (2008). Electrodeposition of nanostructured coatings and their characterization – a review. *Sci. Technol. Adv. Mater.*, 9: 043001.

[6] Chandrasekar, M. S. and Pushpavanam, M. (2008). Pulse and pulse reverse plating – Conceptual, advantages and applications. *Electrochim. Acta*, 53: 3313-3322.

[7] Ahmad, Z. (2006), Chapter 7 – Coatings. In: *Principles of Corrosion Engineering and Corrosion Control*. Elsevier, p. 382-437.

[8] Aliofkhazraei, M., Walsh, F. C., Zangari, G., Köçkar, H., Alper, M., Rizal, C., Magagnin, L., Protsenko, V., Arunachalam, R., Rezvanian, A., Moein, A., Assareh, S. and Allahyarzadeh, M. H. (2021). Development of electrodeposited multilayer coatings: A review of fabrication, microstructure, properties and applications. *Appl. Surf. Sci. Adv.*, 6: 100141.

[9] Protsenko, V. S. and Danilov, F. I. (2010). The corrosion-protective traits of electroplated multilayer zinc-iron-chromium deposits. *Metal Finish.*, 108: 28-32.
[10] Smith, E. L., Abbott, A. P. and Ryder, K. S. (2014). Deep eutectic solvents (DESs) and their applications. *Chem. Rev*., 114: 11060-11082.
[11] Hansen, B. B., Spittle, S., Chen, B., Poe, D., Zhang, Y., Klein, J. M., Horton, A., Adhikari, L., Zelovich, T., Doherty, B. W., Gurkan, B., Maginn, E. J., Ragauskas, A., Dadmun, M., Zawodzinski, T. A., Baker, G.A., Tuckerman, M. E., Savinell, R. F. and Sangoro, J. R. (2021). Deep eutectic solvents: a review of fundamentals and applications. *Chem. Rev*., 121: 1232-1285.
[12] Tome, L. I. N., Baiao, V., da Silva, W., Brett, C. M. A. (2018). Deep eutectic solvents for the production and application of new materials. *Appl. Mater. Today*, 10: 30-50.
[13] Abbott, A. P., Ryder, K. S. and König, U. (2008). Electrofinishing of metals using eutectic based ionic liquids. *Trans. Inst. Met. Finish*., 86: 196-204.
[14] Costa, J. G. d. R. d., Costa, J. M. and Almeida Neto, A. F. d. (2022). Progress on electrodeposition of metals and alloys using ionic liquids as electrolytes. *Metals*, 12: 2095.
[15] Fashu, S. and Khan, R. (2019). Recent work on electrochemical deposition of Zn-Ni(-X) alloys for corrosion protection of steel. *Anti-Corros. Methods Mater.*, 66: 45-60.
[16] Lotfi, N., Aliofkhazraei, M., Rahmani, H. and Darband, G. B. (2018). Zinc–nickel alloy electrodeposition: characterization, properties, multilayers and composites. *Prot. Met. Phys. Chem. Surf*., 54: 1102-1140.
[17] Maniam, K. K. and Paul, S. (2020). Progress in electrodeposition of zinc and zinc nickel alloys using ionic liquids. *Appl. Sci*. 10: 5321.
[18] Whitehead, A. H., Pölzler, M. and Gollas, B. (2010). Zinc electrodeposition from a deep eutectic system containing choline chloride and ethylene glycol. *J. Electrochem. Soc*., 157: D328-D334.
[19] Starykevich, M., Salak A. N., Ivanou, D. K., Lisenkov, A. D., Zheludkevich, M. L., Ferreira, M. G. S. (2015). Electrochemical deposition of zinc from deep eutectic solvent on barrier alumina layers. *Electrochim. Acta*, 170: 284-291.
[20] Vieira, L., Schennach, R. and Gollas, B. (2016). The effect of the electrode material on the electrodeposition of zinc from deep eutectic solvents. *Electrochim. Acta*, 197: 344-352.
[21] Yang, H. and Reddy, R. G. (2014). Electrochemical deposition of zinc from zinc oxide in 2:1 urea/choline chloride ionic liquid. *Electrochim. Acta*, 147: 513-519.
[22] Zhang, X., Liang, J., Liu, B. and Peng, Z. (2014). Preparation of superhydrophobic zinc coating for corrosion protection. *Colloids Surf. A*, 454: 113-118.
[23] Abbott, A. P., Barron, J. C., Frisch, G., Ryder, K. S. and Silva, A. F. (2011). The effect of additives on zinc electrodeposition from deep eutectic solvents. *Electrochim. Acta*, 56: 5272-5279.
[24] Alesary, H. F., Cihangir, S., Ballantyne, A. D., Harris, R. C., Weston, D. P., Abbott, A. P. and Ryder, K. S. (2019). Influence of additives on the electrodeposition of zinc from a deep eutectic solvent. *Electrochim. Acta*, 304: 118-130.

[25] Fashu, S., Gu, C. D., Wang, X. L. and Tu, J. P. (2014). Influence of electrodeposition conditions on the microstructure and corrosion resistance of Zn–Ni alloy coatings from a deep eutectic solvent. *Surf. Coat. Technol*., 242: 34-41.

[26] Li, R., Dong, Q., Xia, J., Luo, C., Sheng, L., Cheng, F. and Liang, J. (2019). Electrodeposition of composition controllable Zn–Ni coating from water modified deep eutectic solvent. *Surf. Coat. Technol*., 366: 138-145.

[27] Lei, C., Alesary, H. F., Khan, F., Abbott, A. P. and Ryder, K. S. (2020). Gamma-phase Zn-Ni alloy deposition by pulse-electroplating from a modified deep eutectic solution. *Surf. Coat. Technol*., 403: 126434.

[28] Bernasconi, R., Panzeri, G., Firtin, G., Kahyaoglu, B., Nobili, L. and Magagnin, L. (2020). Electrodeposition of ZnNi alloys from choline chloride/ethylene glycol deep eutectic solvent and pure ethylene glycol for corrosion protection. *J. Phys. Chem. B*, 124: 10739-10751.

[29] Lei, C., Skouby, H., Kellner, R., Goosey, E., Goosey, M., Sellars, J., Elliott, D. and Ryder, K. S. (2022). Barrel electroplating of Zn-Ni alloy coatings from a modified deep eutectic solvent. *Trans. Inst. Met. Finish*., 100: 63-71.

[30] Alesary, H. F., Ismail, H. K., Shiltagh, N. M., Alattar, R. A., Ahmed, L. M., Watkins, M. J. and Ryder, K. S. (2020). Effects of additives on the electrodeposition of ZnSn alloys from choline chloride/ethylene glycol-based deep eutectic solvent. *J. Electroanal. Chem*., 874: 114517.

[31] Bučko, M., Tomić, M. V., Maksimović, M., Bajat, J. B. (2019). The importance of using hydrogen evolution inhibitor during the Zn and Zn–Mn electrodeposition from ethaline. *J. Serb. Chem. Soc*., 84 (11): 1221-1234.

[32] Walsh, F. C. and Larson, C. (2020). Towards improved electroplating of metal-particle composite coatings. *Trans. Inst. Met. Finish*., 98: 288-299.

[33] Marín-Sánchez, M., Gracia-Escosa, E., Conde, A., Palacio, C. and García, I. (2018). Deposition of zinc–cerium coatings from deep eutectic ionic liquids. *Materials*, 11: 2035.

[34] Chu, Q., Liang, J. and Hao, J. (2014). Electrodeposition of zinc-cobalt alloys from choline chloride–ureaionic liquid. *Electrochim. Acta*, 115: 499-503.

[35] Xu, C., Wu, Q., Hua, Y. and Li J. (2014). The electrodeposition of Zn-Ti alloys from $ZnCl_2$-urea deep eutectic solvent. *J. Solid State Electrochem*., 18: 2149-2155.

[36] Okonkwo, B. O., Jeong, C. and Jang, C. (2022). Advances on Cr and Ni electrodeposition for industrial applications – a review. *Coatings*, 12: 1555.

[37] Oriňáková, R., Turoňová, A., Kladeková, D., Gálová, M. and Smith, R. M. (2006). Recent developments in the electrodeposition of nickel and some nickel-based alloys. *J. Appl. Electrochem*., 36: 957-972.

[38] Mohanty, U. S., Tripathy, B. C., Singh, P., Keshavarz, A. and Iglauer, S. (2019). Roles of organic and inorganic additives on the surface quality, morphology, and polarization behavior during nickel electrodeposition from various baths: a review. *J. Appl. Electrochem*., 49: 847-870.

[39] Torabinejad, V., Aliofkhazraei, M., Assareh, S., Allahyarzadeh, M. H. and Rouhaghdam, A. S. (2017). Electrodeposition of Ni-Fe alloys, composites, and nano coatings – a review. *J. Alloys Compd*., 691: 841-859.

[40] Niciejewska, A., Ajmal, A., Pawlyta, M., Marczewski, M. and Winiarski, J. (2022). Electrodeposition of Ni–Mo alloy coatings from choline chloride and propylene glycol deep eutectic solvent plating bath. *Sci. Rep*., 12: 18531.

[41] Danilov, F. I., Bogdanov, D. A., Smyrnova, O. V., Korniy, S. A. and Protsenko, V. S. (2022). Electrodeposition of Ni–Fe alloy from a choline chloride-containing ionic liquid. *J. Solid State Electrochem*., 26: 939-957.

[42] Abbott, A. P., El Ttaib, K., Ryder, K. S. and Smith, E. L. (2008). Electrodeposition of nickel using eutectic based ionic liquids. *Trans. Inst. Met. Finish*., 86: 234-240.

[43] Gu, C. D., You, Y. H., Yu, Y. L., Qu, S. X. and Tu, J. P. (2011). Microstructure, nanoindentation, and electrochemical properties of the nanocrystalline nickel film electrodeposited from choline chloride–ethylene glycol. *Surf. Coat. Technol*., 205: 4928-4933.

[44] Gu, C. and Tu, J. (2011). One-step fabrication of nanostructured Ni film with Lotus effect from deep eutectic solvent. *Langmuir*, 27: 10132-10140.

[45] Abbott, A. P., Ballantyne, A., Harris, R. C., Juma, J. A., Ryder, K. S. and Forrest G. (2015). A comparative study of nickel electrodeposition using deep eutectic solvents and aqueous solutions. *Electrochim. Acta*, 176: 718-726.

[46] Bernasconi, R. and Magagnin, L. (2017). Electrodeposition of nickel from DES on aluminium for corrosion protection. *Surf. Eng*., 33: 131-135.

[47] Danilov, F. I., Protsenko, V. S., Kityk, A. A., Shaiderov, D. A., Vasil'eva, E. A., Pramod Kumar, U. and Joseph Kennady, C. (2017). Electrodeposition of nanocrystalline nickel coatings from a deep eutectic solvent with water addition. *Prot. Met. Phys. Chem. Surf*., 53: 1131-1138.

[48] Protsenko, V. S., Kityk, A. A., Shaiderov, D. A. and Danilov, F. I. (2015). Effect of water content on physicochemical properties and electrochemical behavior of ionic liquids containing choline chloride, ethylene glycol and hydrated nickel chloride. *J. Mol. Liq*., 212: 716-722.

[49] Yang, H., Guo, X., Birbilis, N., Wu, G. and Ding, W. (2011). Tailoring nickel coatings via electrodeposition from a eutectic-based ionic liquid doped with nicotinic acid. *Appl. Surf. Sci*., 257: 9094-9102.

[50] Mulder, W. H. and Sluyters, J. H. (1998). An explanation of depressed semi-circular arcs in impedance plots for irreversible electrode reactions. *Electrochim. Acta*, 33: 303-310.

[51] Wang, S., Guo, X., Yang, H., Dai, J. C., Zhu, R., Gong, J., Peng, L. and Ding, W. (2014). Electrodeposition mechanism and characterization of Ni–Cu alloy coatings from a eutectic-based ionic liquid. *Appl. Surf. Sci*., 288: 530-536.

[52] Yang, H. Y., Guo, X. W., Chen, X. B., Wang, S. H., Wu, G. H., Ding, W. J. and Birbilis, N. (2012). On the electrodeposition of nickel–zinc alloys from a eutectic-based ionic liquid. *Electrochim. Acta*, 63: 131-138.

[53] You, Y. H., Gu, C. D., Wang, X. L. and Tu, J. P. (2012). Electrodeposition of Ni–Co alloys from a deep eutectic solvent. *Surf. Coat. Technol*., 206: 3632-3638.

[54] Li, W., Hao, J., Mu, S. and Liu, W. (2020). Electrochemical behavior and electrodeposition of Ni–Co alloy from choline chloride-ethylene glycol deep eutectic solvent. *Appl. Surf. Sci*., 507: 144889.

[55] Vijayakumar, J., Mohan, S., Kumar, S. A., Suseendiran, S. R. and Pavithra, S. (2013). Electrodeposition of Ni–Co–Sn alloy from choline chloride-based deep eutectic solvent and characterization as cathode for hydrogen evolution in alkaline solution. *Int. J. Hydrogen Energy*, 38: 10208-10214.

[56] Costovici, S., Manea, A. C., Visan, T. and Anicai, L. (2016). Investigation of Ni-Mo and Co-Mo alloys electrodeposition involving choline chloride based ionic liquids. *Electrochim. Acta*, 207: 97-111.

[57] Niciejewska, A., Ajmal, A., Pawlyta, M., Marczewski, M. and Winiarski, J. (2022). Electrodeposition of Ni–Mo alloy coatings from choline chloride and propylene glycol deep eutectic solvent plating bath. *Sci. Rep*., 12: 18531.

[58] Hou, Y., Peng, Z., Liang, J. and Fu, S. (2020). Ni–Ti nanocomposite coatings electro-codeposited from deep eutectic solvent containing Ti nanoparticles. *J. Electrochem. Soc*., 167: 042502.

[59] Danilov, F. I., Kityk, A. A., Shaiderov, D. A., Bogdanov, D. A., Korniy, S. A. and Protsenko, V. S. (2019). Electrodeposition of Ni–TiO_2 composite coatings using electrolyte based on a deep eutectic solvent. *Surf. Eng. Appl. Electrochem*., 55: 138-149.

[60] Protsenko, V. S., Butyrina, T. E., Bobrova, L. S., Korniy, S. A. and Danilov, F. I. (2022). Electrochemical corrosion behavior of Ni–TiO_2 composite coatings electrodeposited from a deep eutectic solvent-based electrolyte. *Coatings*, 12: 800.

[61] Shao, W., Nabb, D., Renevier, N., Sherrington, I., Fu, Y. and Luo J. (2012). Mechanical and anti-corrosion properties of TiO_2 nanoparticle reinforced Ni coating by electrodeposition. *J. Electrochem. Soc*., 159: D671-D676.

[62] Dennis, J. K. and Such, T. E. (1993). *Nickel and chromium plating*. 3rd edition. Woodhead Publishing. 385 p.

[63] Fedrizzi, L., Rossi, S., Bellei, F. and Deflorian, F. (2002). Wear-corrosion mechanism of hard chromium coatings. *Wear*, 253(11–12): 1173-1181.

[64] Vaiopoulou, E. and Gikas, P. (2020). Regulations for chromium emissions to the aquatic environment in Europe and elsewhere. *Chemosphere*, 254, 126876.

[65] Protsenko, V. S. and Danilov, F. I. (2014). Chromium electroplating from trivalent chromium baths as an environmentally friendly alternative to hazardous hexavalent chromium baths: comparative study on advantages and disadvantages. *Clean Technol. Environ. Policy*, 16: 1201-1206.

[66] Survilienė, S., Nivinskienė, O., Češunienė, A. and Selskis, A. (2006). Effect of Cr(III) solution chemistry on electrodeposition of chromium. *J. Appl. Electrochem*., 36: 649-654.

[67] Protsenko, V. and Danilov, F. (2009). Kinetics and mechanism of chromium electrodeposition from formate and oxalate solutions of Cr(III) compounds. *Electrochim. Acta*, 54: 5666-5672.

[68] Abbott, A. P., Capper, G., Davies, D. L. and Rasheed, R. K. (2004). Ionic liquid analogues formed from hydrated metal salts. *Chem. Eur. J*., 10: 3769-3774.

[69] Abbott, A. P., Al-Barzinjy, A. A., Abbott, P. D., Frish, G., Harris, R. C., Hartley, J. and Ryder, K. S. (2014). Speciation, physical and electrolytic properties of eutectic mixtures based on $CrCl_3{\cdot}6H_2O$ and urea. *Phys. Chem. Chem. Phys*., 16: 9047-9055.

[70] Ferreira, E. S. C., Pereira, C. M. and Silva, A. F. (2013). Electrochemical studies of metallic chromium electrodeposition from a Cr(III) bath. *J. Electroanal. Chem*., 707: 52-58.

[71] Mejía-Caballero, I., Aldana-González, J., Manh, T. L., Romero-Romo, M., Arce-Estrada, E. M., Campos-Silva, I., Ramírez-Silva, M. T. and Palomar-Pardavé, M. (2018). Mechanism and kinetics of chromium electrochemical nucleation and growth from a choline chloride/ethylene glycol deep eutectic solvent. *J. Electrochem. Soc*., 165: D393-D401.

[72] Protsenko, V., Bobrova, L. and Danilov, F. (2018). Trivalent chromium electrodeposition using a deep eutectic solvent. *Anti-Corros. Methods Mater*., 65: 499-505.

[73] Protsenko, V. S., Bobrova, L. S., Baskevich, A. S., Korniy, S. A. and Danilov, F. I. (2018). Electrodeposition of chromium coatings from a choline chloride based ionic liquid with the addition of water. *J. Chem. Technol. Metall*., 53(5): 906-915.

[74] Protsenko, V. S., Bobrova, L. S., Korniy, S. A., Kityk, A. A. and Danilov, F. I. (2018). Corrosion resistance and protective properties of chromium coatings electrodeposited from an electrolyte based on deep eutectic solvent. *Funct. Mater*., 25: 539-545.

[75] Protsenko, V. S., Bobrova, L. S., Kityk, A. A. and Danilov, F. I. (2020). Kinetics of Cr(III) ions discharge in solutions based on a deep eutectic solvent (ethaline): effect of water addition. *J. Electroanal. Chem*., 864: 114086.

[76] Protsenko, V. S., Bobrova, L. S., Korniy, S. A. and Danilov, F. I. (2022). Electrochemical synthesis and characterization of electrocatalytic materials for hydrogen production using Cr(III) baths based on a deep eutectic solvent. *Mater. Lett*., 313: 131800.

[77] Protsenko, V. S., Gordiienko, V. O. and Danilov, F. I. (2012). Unusual "chemical" mechanism of carbon co-deposition in Cr-C alloy electrodeposition process from trivalent chromium bath. *Electrochem. Commun*., 17: 85-87.

[78] Danilov, F. I., Protsenko, V. S., Gordiienko, V. O., Kwon, S. C., Lee, J. Y. and Kim, M. (2011). Nanocrystalline hard chromium electrodeposition from trivalent chromium bath containing carbamide and formic acid: Structure, composition, electrochemical corrosion behavior, hardness and wear characteristics of deposits. *Appl. Surf. Sci*., 257: 8048-8053.

[79] Zhang, J., Gu, C., Tong, Y., Gou, J., Wang, X. and Tu, J. (2015). Microstructure and corrosion behavior of Cr and Cr–P alloy coatings electrodeposited from a Cr(III) deep eutectic solvent. *RSC Adv*., 5: 71268-71277.

[80] Wang, Z., Wu, T., Ru, J., Hua, Y., Bu, J. and Wang, D. (2021). Eco-friendly preparation of nanocrystalline Fe-Cr alloy coating by electrodeposition in deep eutectic solvent without any additives for anti-corrosion. *Surf. Coat. Technol*., 406: 126636.

[81] Wang, Z., Wu, T., Geng, X., Ru, J., Hua, Y., Bu, J., Xue, Y. and Wang, D. (2022). The role of electrolyte ratio in electrodeposition of nanoscale Fe–Cr alloy from choline chloride-ethylene glycol ionic liquid: A suitable layer for corrosion resistance. *J. Mol. Liq*., 346: 117059.

[82] Saravanan, G. and Mohan, S. (2011). Electrodeposition of Fe-Ni-Cr alloy from deep eutectic system containing choline chloride and ethylene glycol. *Int. J. Electrochem. Sci*., 6: 1468-1478.
[83] Meinhold, V., Höhlich, D., Mehner, T. and Lampke, T. (2022). Electrodeposition of thick and crack-free Fe-Cr-Ni coatings from a Cr (III) electrolyte. *Coatings*, 12: 56.
[84] Maharaja, J., Raja, M. and Mohan, S. (2014). Pulse electrodeposition of Cr–SWCNT composite from choline chloride-based electrolyte. *Surf. Eng*., 30: 722-727.

Chapter 3

Tapioca Starch: Xylan Derived Bioplastics

Siti Roshayu Hassan[1,2,*], PhD
Ahmad Zaid Azri bin Zakaria[1], BSc
and Mohamad Johari Abu[1], PhD

[1]Faculty of Bioengineering and Technology, Universiti Malaysia Kelantan Campus Jeli, Jeli, Kelantan, Malaysia
[2]Advance Industrial Biotechnology Cluster, Universiti Malaysia Kelantan, Malaysia

Abstract

Abundance of plastic by non-biodegradable petrochemical-based plastic packaging materials has caused an interest in developing biodegradable plastic using waste derived polysaccharides or starch. Therefore, this study aims to diminish the raw material from petroleum in plastic production besides mitigating the pollution due to nonbiodegradable petroleum-based plastics. In this study, tapioca starch – *Nicotiana tabacum* xylan composite films were successfully prepared. The influence of *Nicotiana tabacum*-xylan content on the functional properties of tapioca starch film was studied. This study used xylan-tapioca starch to produce bioplastic films. Xylan was extracted from the tobacco plant. The purpose of this study is to study the effect of different ratios of sorbitol and glycerol as plasticizers on physical and chemical properties and to investigate the optimum formulation to produce a good quality tobacco derived bioplastic. Different ratios of sorbitol and glycerol (wt %) (0.15S:0.85G, 0.25S:0.75G, 0.5S:0.5G, 0.75S:0.27G, 0.85S:0.15G) were formulated based on 1.0 wt % of glycerol from the previous research. 1.0 wt % glycerol was served as an experimental control. 0.3% of tobacco xylan was added into the formulation and acts

* Corresponding Author's Email: roshayu.h@umk.edu.my.

In: Advances in Materials Science Research. Volume 65
Editor: Maryann C. Wythers
ISBN: 979-8-89113-090-6

as a filler. Physical properties of all bioplastic samples were determined by conducting moisture content test, water absorption test and biodegradability test. Bioplastic samples also undergo several characterizations on thermal analysis, functional group analysis and morphological analysis. The best ratio of plasticizer was sample E with 0.85:0.15 wt % Sorbitol-Glycerol. Sample E shows better result on physical analysis with the lowest rate of moisture content, water absorption and biodegradability. Besides, sample E also shows greater heat stability and better surface morphology on thermal and morphological analysis. The result also shows that the interaction between *Nicotiana tabacum*-xylan and glycerol occurs between δC-C groups, while the other bonds are unaffected. This indicates that xylan acts as filler loads which eventually increase the mechanical and strength of the composite films without affecting the major properties of the bioplastic based. This biocomposite film has high potential to be commercially used as natural biodegradable composite film replacing petrochemical-based plastic.

Keywords: tobacco xylan, tapioca starch, bioplastic, crosslinker, formulation

Introduction

Active food packaging has drawn much attention in recent years beyond the inert passive containment which is helpful to extend shelf-life, monitor freshness, display information on quality and even improve safety of the foods and pharmaceutical products [1]. Furthermore, concern about environmental waste problems caused by nonbiodegradable petrochemical-based plastic packaging materials has generated an interest in developing biodegradable plastic using waste-derived polysaccharides or starch. Literature shows that few research works have been done on producing biocomposite films using natural biopolymers. Huq et al. [1] successfully used alginate with cellulose that gives better qualities in terms of its physical and mechanical properties. Wu et al. [2] produced edible starch-alginate-based composite as packaging for precooked ground beef patties. The result shows that edible films prepared can serve as oxygen or moisture barriers that can preserve the food quality. The aims of synthesizing bioplastics are to diminish the raw material from petroleum in plastic production besides mitigating the pollution due to the non-biodegradable petroleum-based plastics. Hence, in this study, utilizing of xylan, natural polysaccharides from *Nicotiana tabacum* stalks or known as

tobacco plant was conducted. In Kelantan, Malaysia, plantation of *Nicotiana tabacum* contributes to one of the main agricultural residues. The leaves were cut to be processed and the stalks were left as agricultural waste. In 2016, about 1,500 tonnes of *Nicotiana tabacum* stalk was abundant in Kelantan. The stalks of *Nicotiana tabacum* actually containing natural polymer which are 30% cellulose (450 tonnes), 30% hemicelluloses (450 tonnes), and also 40% lignin (600 tonnes). So, there is relevancy in utilizing the source of xylan (hemicelluloses) as biopolymer in preparing good composite film for food packaging purposes.

Xylan, are the largest group of hemicelluloses that are unutilized valuable biopolymers with broad potential applications. The structure and material properties of xylan can act as a renewable raw material for bio-based plastic production. Further studies on plasticizing xylan need to be carried out to produce more flexible films that exhibit improved strength and oxygen barrier properties. Although xylan has its own advantages, there is a drawback of xylan film in terms of its high internal cohesion, which results in fragmented and fragile films which are not suitable to be used in food packaging applications [3]. To overcome these drawbacks, a combination of xylan and tapioca starch gives high mechanical properties and high water resistance biocomposite film, which are more suitable for active food packaging. The processes involved are extraction of xylan from *Nicotiana tabacum* stalks and gelatinization of tapioca starch, as well as preparation of xylan-tapioca starch biocomposite film. This study aims to synthesis and characterizes the waste derived bioplastics as high potential to be commercially used as natural biocomposite film in active food packaging.

Preparation and Characterization of Tapioca Starch – *Nicotiana tabacum* Xylan Composite Films

Nicotiana tabacum or tobacco were collected from local farmer at Bachok, Kelantan. The stalks were cut into small pieces and dried under sunlight for three days before ground to form fine powders. Then, the stalk powders underwent xylan extraction process using dimethyl sulfoxide (DMSO) extraction. In this process, about 15 g of stalk powder was added into 210 mL of DMSO and stirred for 18 hours at room temperature. The mixture containing tobacco biomass and solution was separated by filter paper. The pH of the solution was stabilized until 5.5. About 96% (w/v) of ethanol was added into the solution and then centrifuged at 8000 rpm for 10 minutes at 4°C

to obtain suspended xylan. Finally, the suspended xylan was dried in an oven at 80°C for 24 hours to form fine powders. Meanwhile, tapioca starch (food grade; particle size of those starches ranged from 11.3 µm to 87.1 µm with an average particle size of 49.2 µm and moisture content of tapioca starch is middle of 14%) has been prior dried in an oven at 80°C for 24 hours. The development of bioplastics films was carried out according to three formulations as shown in Table 1. Firstly, tapioca starch-forming solutions were prepared by dissolving 5 g of wheat starch powder into 100 mL of distilled water. The solutions were heated in a water bath at 82°C for 30 minutes at 700 rpm, stirring to obtain solubilization and gelatinization of the starch. Then, these film-forming solutions were cooled down to 40°C. The plasticizer and tobacco xylan were added while stirring at 150 rpm. A defined volume of film-forming solution was poured into a petri dish to obtain a constant film thickness. Films were dried in laminar flow. The phase structure, morphology and elemental composition of extracted *Nicotiana tabacum* xylan were characterized by X-ray diffraction (XRD, Bruker D2 Phaser), scanning electron microscopy (SEM, JEOL; model JSM-IT100) and energy dispersive Xray spectroscopy (EDX), respectively. Besides that, the properties of prepared samples were recorded by Fourier transform infrared spectroscopy (FTIR, Nicolet Avatar 360 ESP FT-IR).

Table 1. Bioplastic formulation

Sample	Tapioca starch (wt%)	Glycerol (wt%)	Distilled water (wt%)	Tobacco Xylan (wt%)
Sample A	5	1.5	93.5	-
Sample B	5	1.5	93.2	0.3
Sample C	5	1.5	93.0	0.5

Figure 1(a) shows the XRD patterns of tobacco powder before and after treated with DMSO extraction. The result of raw tobacco powder can be indexed to xylan polysaccharides (amorphous) phase coexisted with Sb with ICSD file no. 96-901-3009. However, the XRD peaks, which belong to Sb phase were, totally disappeared after treated with DCMO extraction. Figure 1(b) shows the SEM image of extracted tobacco powder. It is clearly observed that the extracted powders were in the form of irregular shape with an average particle size of 100 µm. The elemental composition analysis (Figure 1(c)) on this extracted powder revealed that the C, O and S are dominated, whilst the other elements present in small atomic percentages. Figure 2(b) illustrates typical FTIR spectra of bioplastics samples. Sample A shows numerous characteristics of absorption bands for tapioca starch and glycerol. Three

characteristic absorption bands centered of 3284 cm−1, 2924 cm−1 and 1647 cm−1, corresponding to the motion of O-H stretching, C-H aliphatic stretching and C-C stretching vibration, respectively of tapioca starch. While, the other absorption peaks belong to glycerol [4].

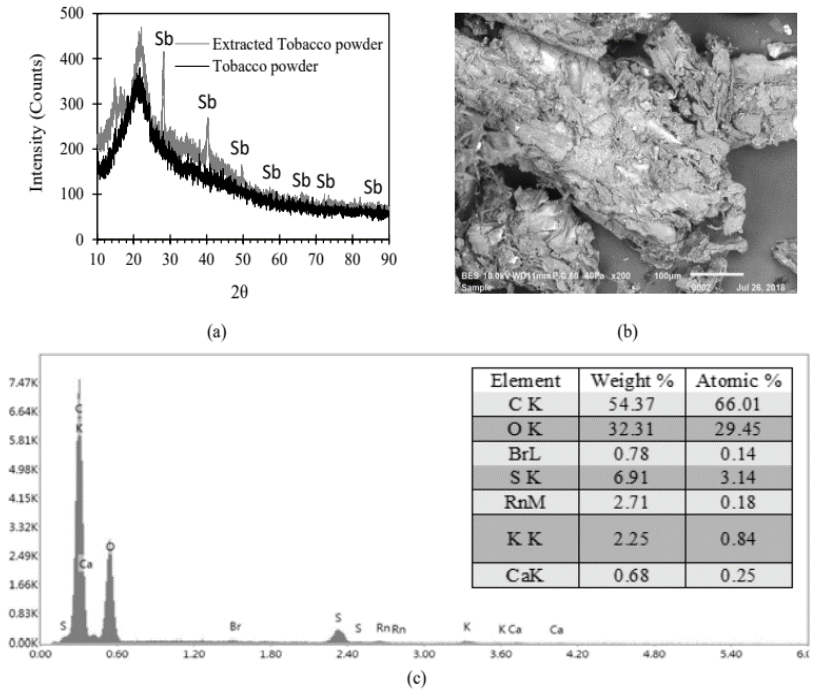

Figure 1. (a) XRD pattern of tobacco powder and extracted tobacco powder. (b) SEM image and (c) EDX result of extracted tobacco powder.

With addition of *Nicotiana tabacum*-xylan, the FTIR spectra for samples B and C displayed same pattern with sample A. However, there is one characteristic absorption band centered at 759 cm−1 (δC-C linkages) was shifted to the lower wavenumber (758 cm−1). This shifting is assigned due to the addition of *Nicotiana tabacum*-xylan promoted the carbon bonding interactions among glycerol and *Nicotiana tabacum* xylan and increases the distance of δC-C bond of glycerol. However, the other peaks are unaffected, due to the *Nicotiana tabacum* xylan atoms is not interact with other atoms from tapioca starch and glycerol.

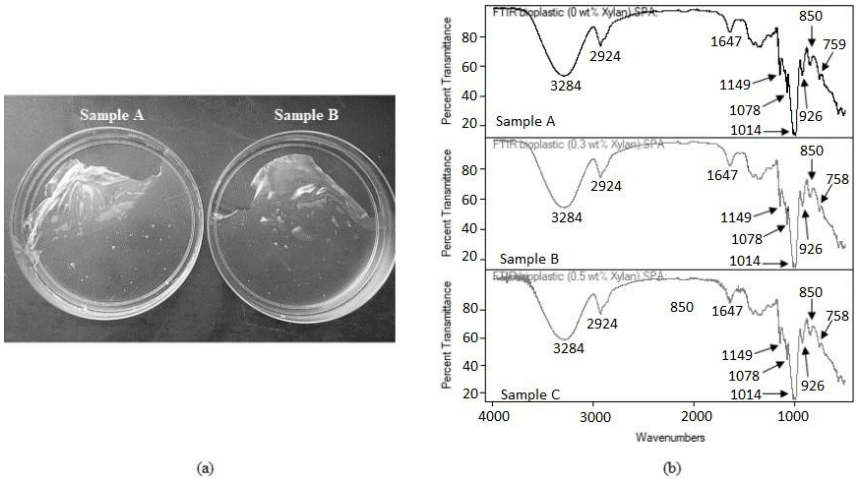

Figure 2. (a) An image and (b) FTIR spectrum of composite films.

Effect of Glycerol and Gluteraldehyde towards Performances of *Nicotiana tabacum*/Starch Derived Bioplastic

Mainly bioplastic uses native starches as its main ingredients. But bioplastics made from native starches easily crumble into bits when dried in ambient conditions. Strong intermolecular hydrogen bonding between the amylose and amylopectin macromolecular network chains [5,6] is responsible for the brittle nature of starches. Tobacco is used as raw material as it is easy to get for example this tobacco being picked in. Crosslinking has been used to improve the properties of regenerated proteins fibers. The most frequent plasticizer used in bioplastic production is glycerol, which is a small molecule which non-toxic that lessens intermolecular interactions and increases intermolecular spacing by gaining access to the polymer chains through hydrogen bonds and increasing stretch ability [7]. Glycerol can strongly affect the functional properties of starch-based coatings and films [8] (Basiak et al., 2018). This study aims to study the effect of glycerol and glutaraldehyde on the bioplastic films from Nicotiana Tobaccum. The optimum bioplastic will be known after the chemical test and characterization of the bioplastic being applied.

The powders of Tobacco stalk were mixed with DMSO solution in 14ml/g for the ratio. Then, the solution to be extracted was left overnight at room temperature for 18 hours. The extraction was then centrifuged at 5000 rpm for 20 minutes, followed by neutralization (pH 5.5) with glacial acetic acid. For

the crystallization process, 95% of ethanol was added at double the volume of the extraction. Then, the solutions were centrifuged at 8000 rpm for 10 minutes at 4°C. The xylans were produced after the sample was dried in a drying oven until a constant weight was obtained and ready to produce bioplastics.

The development of bioplastics films was carried out according to three formulations, as shown in Table 2 and Table 3. The solutions were heated on hot plate while stirring until to obtain gelatinization of the starch. The plasticizer and tobacco xylan were added while stirring. A defined volume of gelatinized solution was poured into a petri dish using syringe to obtain a constant film thickness. The films were dried in room temperature.

Table 2. The formulation for glycerol bioplastic

Sample	Tapioca starch (wt%)	Glycerol (wt%)	Distilled water (wt%)	Tobacco Xylan (wt%)
Sample A	5	0.5	93.2	0.3
Sample B	5	1.0	93.2	0.3
Sample C	5	1.5	93.2	0.3
Sample D	5	2.0	93.2	0.3
Sample E	5	2.5	93.2	0.3

After all the sample for Table 1 have been tested to get the optimum sample, test using mechanical analysis (Tensile test, water activity test, biodegradability test, and moisture content test) being applied. For characterization used Fourier – Transform Infrared Spectroscopy (FTIR). Then, the optimum sample follow the Table 2 and being tested using mechanical analysis and FTIR analysis to find a optimum sample.

Table 3. The formulation for glutaraldehyde sample

Sample	Tapioca starch (wt%)	Distilled water (wt%)	Tobacco Xylan (wt%)	GL (µL)
Sample A	5	93.2	0.3	10.0
Sample B	5	93.2	0.3	20.0
Sample C	5	93.2	0.3	30.0
Sample D	5	93.2	0.3	40.0
Sample E	5	93.2	0.3	50.0

Table 4 and Figure 4 shows the biodegradability test result for glycerol and glutaraldehyde. We can see that for Glycerol, sample D have the highest rate which is 99.28% and sample B has the lowest rate which is 46.48%. For

glutaraldehyde the degradation rates of glycerol are higher than glutaraldehyde. This is because adding the glutaraldehyde decreases the degradation rate. Hanafi & Zaaba [8] studied that when glutaraldehyde added the degradation become decrease because a higher density of chemical crosslink among polymer chains which make it a strong influence of crosslinking on the degradation.

Table 4. Percentage of biodegradability test for glycerol sample

Sample	Days					
	7	14	21	28	35	42
A	11.83%	17.86%	25.10%	32.91%	45.28%	86.17%
B	21.14%	22.95%	26.03%	30.61%	36.57%	46.48%
C	10.46%	20.65%	23.03%	37.29%	52.97%	64.73%
D	12.79%	27.57%	35.5%	45.79%	73.81%	99.28%
E	15.28%	33.44%	40.74%	50.14%	59.03%	69.27%

Table 5. Percentage of soil burial test for glutaraldehyde

Sample (µL)	Days			
	7	14	21	28
10	6.37%	12.2%	18.06%	22.67%
20	9.49%	20.10%	26.31%	36.86%
30	5.73%	13.60%	19.09%	31.23%
40	9.71%	18.16%	24.64%	31.46%
50	11.24%	18.6%	24.53%	32.01%

For the water activity test, glycerol sample B which contain 0.5 wt% Glycerol has the highest water absorption rate while Sample E, which contain 2.5 wt% glycerol have the lowest water absorption rate. For glutaraldehyde, Glutaraldehyde shows that it has lower absorption rate compared to the sample only using the Glycerol. This is because according to H. Ismail & Zaaba N. F [8] studied that heterogenous crosslinking produced more highly hydrophobic structures. The network structure prevented the water molecules from dissolving and improved the water resistances of the films.

For Moisture content in However the trend line show that while the glycerol content increase this indicates that moisture content of bioplastics also decreasing. For the Glutaraldehyde, all the samples also show the moisture content increasing. But from the result, we can see that sample using Glutaraldehyde are low moisture content rate compare to the sample that only using Glycerol.

For the tensile test, for the result of glycerol indicated that additives give effect to the mechanical properties. The elongation at break increase slowly with increase in glycerol. Adding glycerol here is to overcome the brittleness caused by strong intermolecular forces. Sample B show the highest elongation.

For FTIR spectra in glycerol samples, it shows that the spectrum for raw tobacco which is 3342.01 of wavenumber that represent medium N-H stretching for aliphatic primary amine were shifted downward and to the right for the glycerol samples, which around 3282.40 wavenumber which is strong abroad O-H stretching for carboxylic group. The spectrum of tobacco and glycerol shows to the similar functional groups of monomer units in the polymeric chains.

For FTIR Analysis for Glutaraldehyde, the functional groups for the bioplastic for Glutaraldehyde are aliphatic phosphates, aliphatic primary amides, alkynes monosubstituted, aliphatic hydrocarbons and primary aliphatic alcohols. Based on the spectrum in tobacco, there is a 3342.01 wavenumber that represent medium of N-H stretching were change shifted to the right at around 3282.52 which is strong broad O-H stretching. It is change from aliphatic primary amine to carboxylic acid. Another one was 1011.24 wavenumber from raw tobacco was shifted upwards when with the glycerol sample which are 1643.79 which is alkene. It can be identified that all the samples of glutaraldehyde have similar peaks which correspond to the similar functional groups. The strong and broad absorption band around 3550- 3200 cm-1 are the characteristics of peaks of –OH stretching, which its compound class is alcohol. Other peaks observed at around 3100 – 3000 which is medium absorption correspond to C-H stretching. Then, at around 1336 its have medium absorption of O-H bending.

From the research work, both glycerol and glutaraldehyde are suitable to use as plasticizer and crosslinker for the bioplastic from *Nicotiana tabacum* with tapioca starch. However, the mechanical of bioplastics from glycerol and glutaraldehyde show different result from different quantity.

It is shown that, the sample that use only glycerol, sample B (1.0 wt% of glycerol) is the optimum sample because it have the lowest degrade rate which is shown its have longest shelf life, low moisture content, have high elongation at break and strain at break for the tensile. But, after additional 20 µL glutaraldehyde it shown its optimum form other volume of glutaraldehyde. This is because it have lowest rate of water activity, and have highest young modulus. The degradation of bioplastic both of glycerol and glutaraldehyde shown the positive result which is shown it benefit and useful for the future study.

Characterization of Tobacco Derived Bioplastic Based on Tapioca Starch with Different Ratios of Sorbitol and Glycerol as Plasticizers

Plastic are polymers with round up of similar chemical subunits called monomer. Plastics are usually natural polymers with high molecular mass and frequently contained different substances. Plastics are typically engineered which are mostly derived from petrochemicals. However, these plastics are usually formed as non-renewable and non-degradable properties which can lead to pollution. They could be widespread across the earth, no matter whether it's on land or in the oceans because of their harmful properties which are low density, non-degradable, and commonly robust materials that can affect the environment and cause biological harm [9]. Bioplastic is types of plastic that produce from natural biopolymers includes starches, cellulose derivatives, chitosan/chitin, gums, proteins such as animal or plant-based and lipids. However, because of their low mechanical strength, the bioplastics application has been limited. In this era, high performance bioplastic should be considered to meet the higher requirements than standard or engineering plastics. This is because, high performance plastic can be varied from standard and engineered plastics in terms of stability, chemical resistance, price, quality, production quantity and mechanical properties.

In most studies, due to their strong mechanical properties, synthetic fibers, such as glass and carbon fibers are usually involved as fortifications in bioplastic production [10]. Furthermore, the synthetic fibers also cause harmful effect towards the environment which is because of their non-biodegradable characteristic towards the environment [11]. Lignocellulosic fibers are biodegradable, renewable and widely available compared to synthetic fibers. However, the fibers consist of low density, competitive specific mechanical properties, and a relatively low cost [12]. Because of their properties such as renewable and environmentally friendly, the demand of natural fibers has seen drastically increase in recent years. These natural fibers have many advantages as filler, which for example, lower cost, light weight, low density, high strength to weight ratio, biodegradability, and thermal characteristic improvement [13].

Xylan Extraction Process

The raw materials used is *Nicotiana tobacum* stalks. The tobacco stalks were cut into small pieces and were grind into fine powder before undergo drying

process until the tobacco is completely dried. Tapioca starch was purchased from local store in Jeli, Kelantan.

Extraction of xylan was conducted by dimethyl sulphoxide (DMSO) extraction which produced the water-soluble hemicellulose. Tobacco stalks powder were then mixed with DMSO solution with approximately 14mL/g ratio. The extraction process then was left overnight at room temperature for 18 hours. The extract was centrifuged at 5000 rpm for 20 minutes followed by neutralization (pH 5.50) with glacial acetic acid. Then crystallization process was taking place by addition of 95% of ethanol at double volume. The solution was then centrifuged at 8000 rpm for 10 minutes at 4 ºC. The xylan that obtained after the samples were dried in drying oven with a constant weight. Pure xylan was stored until further use.

Bioplastics Development

Six bioplastic films were prepared using casting method. It consists of 5 wt% tapioca starches. To see the effect of Glycerol, 1.0 wt% which was the optimize formulation for bioplastic from the previous research. The glycerol-based bioplastic was act as the control for this project. The glycerol formulation is as shown in Table 6.

Next, other five samples were proceeded to another formulation to see the effect of different ratio of sorbitol and glycerol as plasticizer. Five different concentration of different ratio sorbitol and glycerol were used for effects of sorbitol. The concentration of the mixture was based on optimize formulation which is 1.0 wt% from the previous research. 5 different formulations were casted on each petri dish for the effects of different ratio of glycerol and sorbitol is as shown in Table 7.

In the development of bioplastic, 0.3 wt% of tobacco xylan was used based on the optimize amount of xylan in the previous research. The most optimized samples were determined through mechanical test which are tensile strength test, texture analysis, biodegradability test and moisture content test and for characterization is using FTIR analysis, SEM analysis and TGA analysis and XRD analysis.

Table 6. The formulation for the effect of glycerol

Sample	Tapioca starch (wt%)	Glycerol (wt%)	Distilled water (wt%)	Tobacco xylan (wt%)
Sample Control	5	1.0	93.7	0.3

Table 7. The formulations for the effect of different ratio of sorbitol and glycerol

Sample	Tapioca starch (wt%)	Sorbitol (wt%)	Glycerol (wt%)	Distilled water (wt%)	Tobacco Xylan (wt%)
Sample A	5	0.15	0.85	93.7	0.3
Sample B	5	0.25	0.75	93.7	0.3
Sample C	5	0.5	0.5	93.7	0.3
Sample D	5	0.75	0.25	93.7	0.3
Sample E	5	0.85	0.15	93.7	0.3

Physical Characterization of Xylan-Tapioca Starch Bioplastic Films

Biodegradibility Test

The best bioplastic formulation undergoes biodegradable analysis. Biodegradation process were run according to soil burial test. The samples were tested by using soil burial test. In this method, samples were cut into 2.0 〖 cm〗^2. The soil was collected near the roots of plants and stored in different containers for different samples. Samples were buried inside the soil at a depth of 3 cm for 42 days under the conditions of the room. The results being recorded in every 7 days. Scanning Electron Microscopic (SEM) images of the specimen were taken before and after the testing for visual inspection. The rate of biodegradation is calculated by mass reduction calculation.

Moisture Content Test

By measuring the weight loss of films, the moisture content were estimated. The samples were cut into square pieces of 2.0 cm2. The samples then were weighed accurately. The dry film mass was recorded upon drying in an oven at 100°C until a fixed dry weight is acquired [13]. Each film treatment was used with two replications and the moisture content will be measured.

Water Absorbtion Test

By measuring the weight of films, the adsorption were estimated. The samples were cut into square pieces of 2.0 cm2. The samples then were weighed accurately. Water activity test shows the amount of water absorbed by the bioplastic film samples using different plasticizer which is glycerol, and different ratio of glycerol and sorbitol. In this method, samples were cut into 2.0 cm2 and the result be determined by immersing the samples in water for 60 minutes. The results being recorded in every 15 minutes.

Morphological Analysis (SEM)

The surface, cross section and morphologies of bioplastics were noted using SEM. The bioplastic samples were cut into smaller piece and submerged into liquid nitrogen for 1 min then were fractured. The samples were mounted vertically double-sided carbon 37 adhesion foil in order to hold the sample. SEM was used to determine the physical condition and surface morphology under several magnifications. The samples will be tested before and after biodegradability test.

Thermal Analysis (TGA)

TGA was used to measures the weight changes associated with thermal event. TGA was used to determine the compositional analysis and thermal stability. It also predicted the short-term and long-term thermal stability.

Chemical Characterization of Xylan-Tapioca Starch Bioplastic Films

Functional Group Analysis (FTIR)

FTIR spectroscopy was used by observing changes in the chemical bonding of molecules to classify the surface chemistry of the prepared membranes. FTIR spectra was computed by using FTIR Nicolet Nexus 670, USA over a wave number range of 4000-425 cm-1. The FTIR was equipped with an OMNI-sample attenuated total reflection (ATR) smart accessory and coupled to a diamond crystal operated at incidence angle of 45 º. With a resolution of 4 cm1, every spectrum that was recorded as the average of 32 scans will be taken. FTIR was used to determine the composition of functional group of xylan and bioplastic films.

Results and Discussion

Xylan-Based Bioplastic Film Development

The result for the formulation shows that the bioplastic film can be formed after being dried at room temperature for 4 days in the Petri dish. The film can be easily peeled off from the Petri dish. The bioplastic is thin and can be used for stretchable food wrapping. Bioplastic for the glycerol formulation have been taken from the optimize formulation from previous experiment and act

as a control for this experiment. Then, the formulation is improvised by combining two plasticizers which is different ratio of sorbitol and glycerol based on the previous formulation.

Bioplastic Development Based on Glycerol and Different Ratio of Glycerol and Sorbitol as Plasticizer

The formulation results show that the bioplastic film can be formed after being dried at room temperature for 4 days in the Petri dish. The film can be easily peeled off from the Petri dish. The bioplastic is thin and can be used for stretchable food wrapping. For sample D and sample E, the bioplastic shows that the surface is likely more flexible than samples A, B and C. This might be because of the higher content of glycerol in the formulation. This is because glycerol acts as a plasticizer that improves bioplastic flexibility. Apart from that, the addition of glycerol can improvise hydrogen bonds just so the distance between molecules of biopolymer appears tenuous. Moreover, the strained condition between biopolymer compounds increases the flexibility of bioplastic samples [14]. Moreover, the combination of sorbitol and glycerol as a plasticizer shows a more durable bioplastic film than the control bioplastic film, which only uses glycerol as a plasticizer. This is because, increasing the concentration of different types of plasticizers such as sorbitol and glycerol can increases the durability of bioplastic films. The low molecular size of the plasticizers allows them to move within the polymer chains of intermolecular space which reducing the strength of the intermolecular hydrogen bond, thereby the molecular mobility is increasing. Nevertheless, the change in type of plasticizers greatly impacted the durability of their subsequent bioplastic films at the same plasticizer concentration. It was observed that sorbitol-glycerol-plasticized bioplastic films exhibit greater flexibility, followed by glycerol-plasticized bioplastic films [15]. Table 8 shows six samples of bioplastic for glycerol-plasticized bioplastic film and different ratio of sorbitol and glycerol plasticized bioplastic.

Physical Characterization of Xylan-Tapioca Starch Bioplastic Films

Moisture Content Test

Moisture content is the amount of moisture in the sample given as a percentage of the sample's original (wet) weight. Dry content is the amount of solids left

after drying given as a percentage of the sample's original (wet) weight. In this method, samples were cut into 2.0 〖cm〗^2 and the result be determined by using a drying oven with 100°C in 45 minutes. The results are recorded in every 15 minutes.

Table 8. Six samples of bioplastic for glycerol plasticized bioplastic film and different ratio of sorbitol and glycerol plasticized bioplastic film

Sample	
CONTROL (1.0 wt% glycerol)	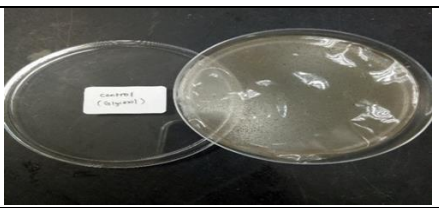
A (0.15 wt% sorbitol, 0.85 wt% glycerol)	
B (0.25 wt% sorbitol, 0.75 wt% glycerol)	
C (0.5 wt% sorbitol, 0.5 wt% glycerol)	
D (0.75 wt% sorbitol, 0.25 wt% glycerol)	
E (0.85 wt% sorbitol, 0.15 wt% glycerol)	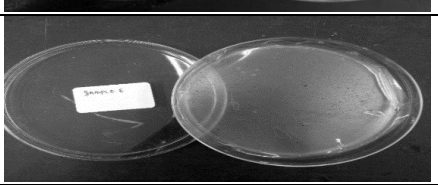

Table 9. Rate for moisture content of tobacco derived bioplastic

Sample	No. of sample	Before drying (g)	15 min	30 min	45 min	Average of moisture content rate (%)
Control	1.	0.039	0.034	0.032	0.031	
	2.	0.049	0.044	0.041	0.040	
	Average	0.044	0.039	0.037	0.036	
	Moisture content rate (%)		11.36	17.05	19.32	15.91
A	1.	0.048	0.040	0.039	0.038	
	2.	0.053	0.047	0.046	0.046	
	Average	0.051	0.044	0.043	0.042	
	Moisture content rate (%)		13.86	15.84	16.83	15.51
B	1.	0.044	0.040	0.039	0.038	
	2.	0.048	0.042	0.042	0.041	
	Average	0.046	0.041	0.041	0.040	
	Moisture content rate (%)		10.87	11.96	14.13	12.32
C	1.	0.031	0.029	0.026	0.025	
	2.	0.032	0.030	0.029	0.027	
	Average	0.032	0.030	0.028	0.026	
	Moisture content rate (%)		6.35	12.70	17.46	12.17
D	1.	0.050	0.045	0.046	0.045	
	2.	0.045	0.039	0.038	0.037	
	Average	0.048	0.043	0.042	0.041	
	Moisture content rate (%)		10.52	11.58	13.68	11.92
E	1.	0.041	0.033	0.032	0.030	
	2.	0.042	0.039	0.037	0.035	
	Average	0.039	0.036	0.035	0.033	
	Moisture content rate (%)		7.69	10.26	15.38	11.11

Table 9 shows the rate of moisture content for control which is glycerol based bioplastic. The temperature used in this test was 100ºC. This is because if the temperature is too low or the retention time is too short, all of the water might not be driven off. If the temperature value is too high, it can degrade the polymer and actually generate water in some cases. After 45 minutes of drying, all samples shows the rate of moisture content are increasing over time. The glycerol-based bioplastic which act as a control shows a highest average of moisture content rate which is 15.91%. Followed by Sample A, 0.15:0.85 Sorbitol-Glycerol (15.51%), Sample B, 0.25:0.75 Sorbitol-Glycerol (12.32%), Sample C, 0.5:0.5 Sorbitol-Glycerol (12.17%), Sample D, 0.75:0.25 Sorbitol-Glycerol (11.92%) and Sample E, 0.85:0.15 Sorbitol-Glycerol (11.11%). This is because as time passed, the increasing of moisture content rate was attributed to the loss of water from the bioplastic, creating a more rigid and brittle plastic.

Furthermore, an addition or higher amount of glycerol in the mixture caused leaching from the bioplastics and absorption of atmospheric moisture by the plastic. This caused the increase in moisture content. This may make this material unsuitable for most uses as the resultant absorption of water would change the bioplastic properties decreasing its tensile strength. Throughout the study, Sample E shows more stability in terms of moisture content. This is because the sample is maintaining a moisture content between at average of 11.11% which is the lowest rate compared to other samples. This can be due to the high molecular structure that is similar to units of glucose to the sorbitol, creating greater molecular interactions between sorbitol and the chains of intermolecular polymers. Resultantly, the chances of sorbitol reacting with water molecules is decreased [15]. Therefore, the more addition of the concentration of sorbitol, the less moisture content rate of the bioplastic films.

Water Absorption Test

Water activity test shows the amount of water absorbed by the bioplastic film samples using different plasticizers which is glycerol, and different ratios of sorbitol-glycerol bioplastic films. In this method, samples were cut into 2.0 〖cm〗^2 and the result be determined by immersing the samples in water for 60 minutes. The results being recorded in every 15 minutes.

Table 10 shows the result of water absorbtion test for glycerol (control) and different ratio of sorbitol-glycerol plasticized bioplastic. Water absorption test or hydrophobicity test is to identify water resistance of bioplastic or biofilm so that the bioplastic is suitable to be used for packaging purposes. This test was based on the percentage of weight gain of polymer following the presence of water after undergoes film swelling. Water absorption is important to know whether the production of bioplastic is already compatible with the nature of synthetic plastic as the packaging plastic used to sustain the food packaging quality is water resistant. It is observed that the biofilms produced cannot reduce the hydrophilic properties to the maximum. This might be because both sorbitol and glycerol have high hydrophilic properties.

Based on the result shows glycerol plasticized bioplastic shows the highest average of water absorption rate which is 327.12%. Followed by Sample A, 0.15:0.85 Sorbitol-Glycerol (296.40%), Sample B, 0.25:0.75 Sorbitol-Glycerol (281.70%), Sample C, 0.5:0.5 Sorbitol-Glycerol (273.66%), Sample D, 0.75:0.25 Sorbitol-Glycerol (272.70%) and Sample E, 0.85:0.15 Sorbitol-Glycerol (158.84%). Müller et al., 2008 stated that glycerol is more

hydrophilic and has a better ability of plasticizing than sorbitol. Therefore, the water absorption rate increase as the amount of glycerol added increase. Additionally, the solubility in water increased with the use of hydrophilic plasticizers. Glycerol used in the production of bioplastic provide greater solubility on starch-based bioplastic relative to sorbitol. Therefore, sample E shows better result than all samples as the lowest water absorption rate.

Table 10. Rate for water absorption of tobacco derived bioplastic

Sample	No. of sample	Before immersion (g)	15 min	30 min	45 min	60 min	Average of water absorption rate (%)
Control	1.	0.031	0.129	0.131	0.136	0.159	
	2.	0.028	0.081	0.108	0.119	0.145	
	Average	0.030	0.105	0.120	0.128	0.152	
	Water absorption rate (%)		255.93	305.08	332.20	415.25	327.12
A	1.	0.042	0.152	0.159	0.165	0.179	
	2.	0.046	0.162	0.166	0.221	0.224	
	Average	0.044	0.157	0.163	0.193	0.202	
	Water absorption rate (%)		256.82	232.18	338.64	357.95	296.40
B	1.	0.049	0.182	0.198	0.213	0.217	
	2.	0.048	0.159	0.163	0.173	0.176	
	Average	0.049	0.171	0.181	0.193	0.197	
	Water absorption rate (%)		251.55	272.16	297.94	305.15	281.70
C	1.	0.046	0.126	0.132	0.162	0.165	
	2.	0.047	0.189	0.192	0.210	0.214	
	Average	0.047	0.158	0.186	0.186	0.190	
	Water absorption rate (%)		238.71	248.39	300.00	307.53	273.66
D	1.	0.043	0.131	0.144	0.155	0.192	
	2.	0.044	0.141	0.145	0.192	0.197	
	Average	0.044	0.136	0.145	0.174	0.195	
	Water absorption rate (%)		212.64	232.18	298.85	347.13	272.70
E	1.	0.046	0.107	0.118	0.115	0.168	
	2.	0.053	0.106	0.110	0.144	0.157	
	Average	0.050	0.107	0.114	0.130	0.163	
	Water absorption rate (%)		115.15	130.30	161.62	228.28	158.84

Biodegradibility Test

The samples were tested by using soil burial test. In this method, samples were cut into 2.0cm^2. The soil was collected near the roots of plants and stored in different containers for different samples. Samples were buried inside the soil

at a depth of 3 cm for 42 days under the conditions of the room. The results being recorded in every 7 days.

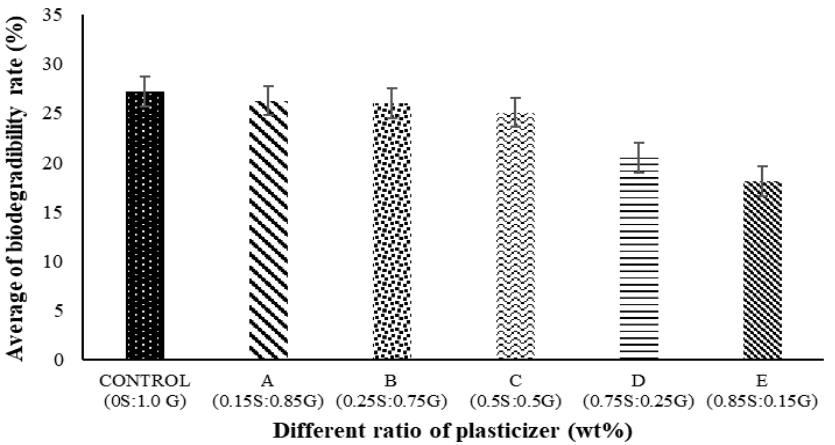

Figure 3. Rate for biodegradability of tobacco derived bioplastic.

Table 11 and Figure 3 shows the rate of biodegradability for glycerol (control) and different ratio of sorbitol-glycerol plasticized bioplastic. In order to form a good food packaging, it is best if the rate of biodegradation is not too fast. This is because, the food packaging will decompose during the food wrapping in certain surrounding condition that allows. In this study, all the six samples were buried at the same depth in the pot filled with soil. Based on the result shows no significant differences between all the samples. However, all the samples shows weight loss over time. Sample control shows the greatest average of biodegradability rate which is 27.18%.

While Sample E, 0.85:0.15 Sorbitol-Glycerol shows the least average of biodegradability rate which is 18.09%. This might be because, of samples were kept in a dry and closed location. Therefore, the samples could not absorb too much humidity from the environment. Hence, microorganisms did not show up in the sample. The difference of the rate between the six samples might be due to the addition of sorbitol in the bioplastic production. Based on this study, loss of weight (%) of the bioplastic film is caused by sorbitol added to the formulation of bioplastic. Bakry et al., [16] stated that the higher molecular weight of sorbitol leads to reduced solubility of water in the bioplastic film polymer chains compared to the film plasticized with only glycerol (control). Increased in sorbitol concentration in the bioplastic film

will generate less reaction of proteolytic enzyme, less microbial growth and reaction of hydrolysis. Thereby reducing the rate of bioplastic film biodegradation [17]. Therefore, sample E shows the best biodegradability rate among all the samples because it took a longer time to biodegrade, so it can withstand a longer time of wrapping.

Table 11. Biodegradability test for six samples of bioplastic films on 28th and 42nd days

Days	
Days 28 of biodegradability test	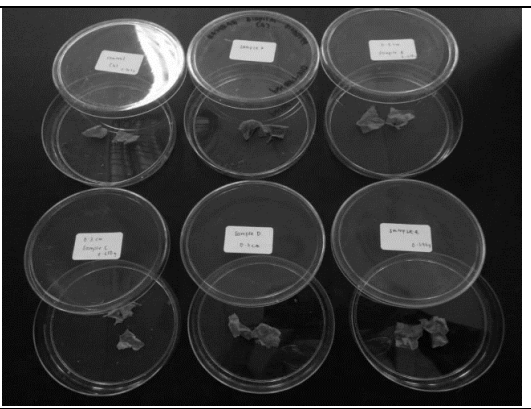
Days 42 of biodegradability test	

Morphological Analysis (SEM)

The surface, cross section and morphologies of bioplastics were noted using SEM. The bioplastic samples were cut into smaller piece and submerged into liquid nitrogen for 1 min then were fractured. The samples were mounted vertically double-sided carbon 37 adhesion foil in order to hold the sample.

SEM was used to determine the physical condition and surface morphology under several magnifications. The samples will be tested before and after biodegradability test under 1000x magnification.

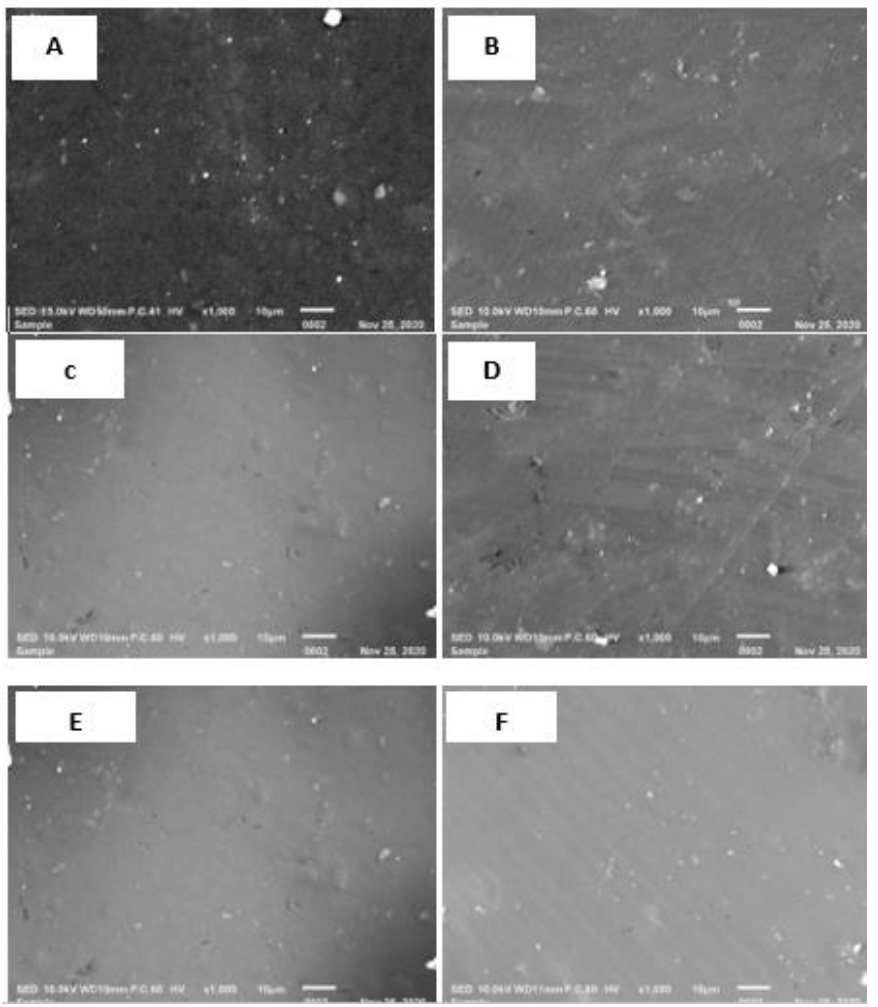

Figure 4. SEM micrograph of six samples of xylan-tapioca starch bioplastic films before biodegradability test under 1000x magnification.

The results of SEM bioplastic with different ratio of plasticizers and 0.3% of fillers (tobacco xylan) were tested. Figure 4 shows the SEM micrograph of surface morphologies of xylan-tapioca starch bioplastic. From the figure

shown, it can be seen that the all of the samples shows a smooth surface of bioplastic. However, there are some clumping that can be seen on the surface. This might be because distribution of fillers is not evenly distributed and filler clumping occurs which can result in the low mechanical properties of bioplastics produced, due to the buildup of fillers so that interactions between the filler and the matrix do not occur. Better compatibility and mixing techniques are needed such as using ultrasonic processing to increase filler distribution [18].

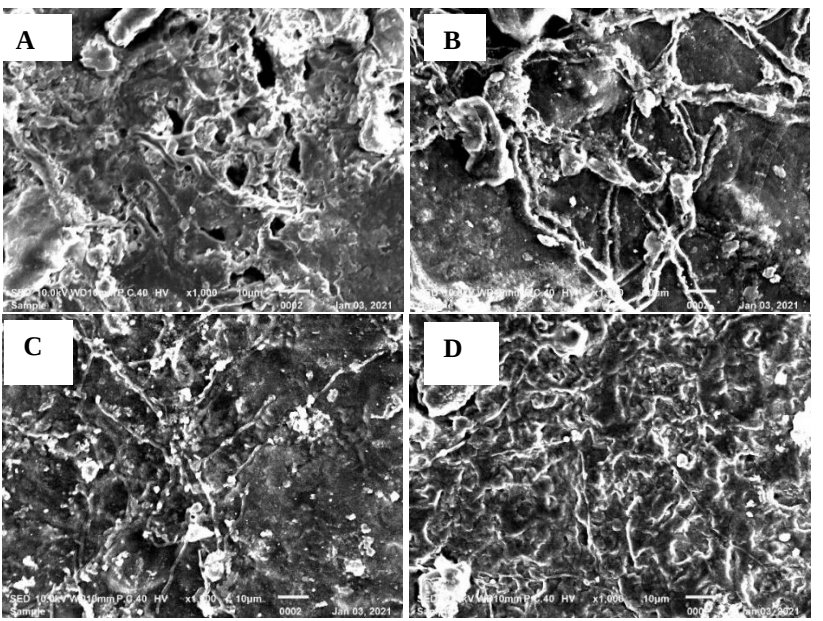

Figure 5. SEM micrograph of four samples with optimize formulation of xylan-tapioca starch bioplastic films after 42 days of biodegradability test under 1000x magnification.

Figure 5 shows SEM micrographs of four samples which is sample control (1.0 wt % Glycerol), sample A (0.15:0.85 Sorbitol-Glycerol), sample C (0.5:0.5 Sorbitol-Glycerol) and Sample E (0.85:0.15 Sorbitol-Glycerol). This is to compare the surface morphologies of bioplastic with the highest degradation rate and the lowest degradation rate. Figure shows non-homogeneous morphology structure. In the surface morphologies, it can be observed that there are voids, edges, holes and poor interfacial adhesion. Few propagations of cracks in the bioplastics surface indicates poor components bonding. The roughness of the surface of higher content of glycerol as

plasticizers increased. Therefore, sample control who has the highest glycerol content shows more cracks and holes compared to sample E which has the lowest degradation rate.

Chemical Characterization of Xylan-Tapioca Starch Bioplastic Films

Functional Group Analysis (FTIR)

FTIR spectroscopy was used by observing changes in the chemical bonding of molecules to classify the surface chemistry of the prepared membranes. FTIR was used to determine the composition of functional group of xylan and bioplastic films.

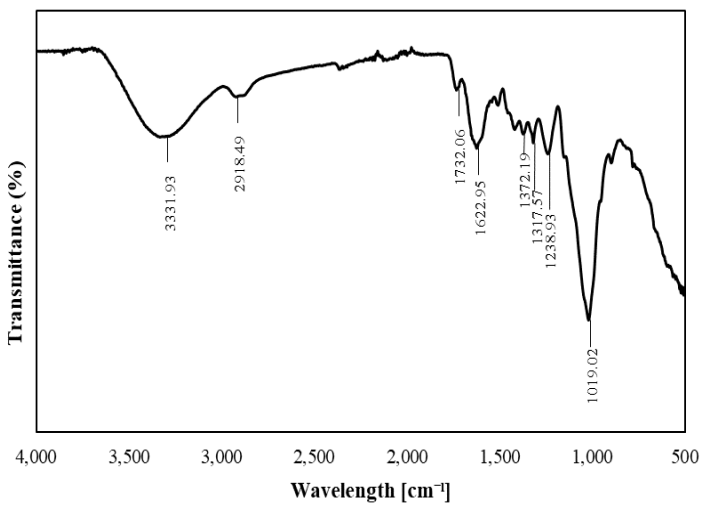

Figure 6. Functional group analysis of tobacco xylan.

Figure 6 shows the FTIR analysis of tobacco xylan. The FTIR data analysis shows that all hemicellulosic fractions clearly exhibited the standard hemicellulosic fraction of signal pattern and also had a particular maximum band in the region of 1,200-1,000 cm-1. At 1,600 cm-1, the absorption seen in all spectra is predominantly correlated with absorption of water [19]. Bands between 1,166 and 1,000 cm−1 are representative of xylans. Denise, S et al., 2008 stated that an absence of a signal around 1,720 cm-1 for carbonyl stretching in all four spectra, implied that alkali treatment did not substantially assault the glycosidic bonds and hemicellulose hydroxyl groups under the

conditions provided. The wide peak at 3332 cm-1 where the maximum is located, resulted from the OH group's fundamental stretching vibration. The prominent band around 3332 cm−1 represents the vibrations of the hemicelluloses hydroxyl stretching and involvement of water in hydrogen bonding. The absorbances at 2918, 1732, 1623, 1372, 1317, 1239, 1019 in the spectra are hemicelluloses associated. The absorbance of lignin-related around 1,500 cm−1 is rather weak and poorly resolved which shows the low level of lignin associated in the hemicelluloses.

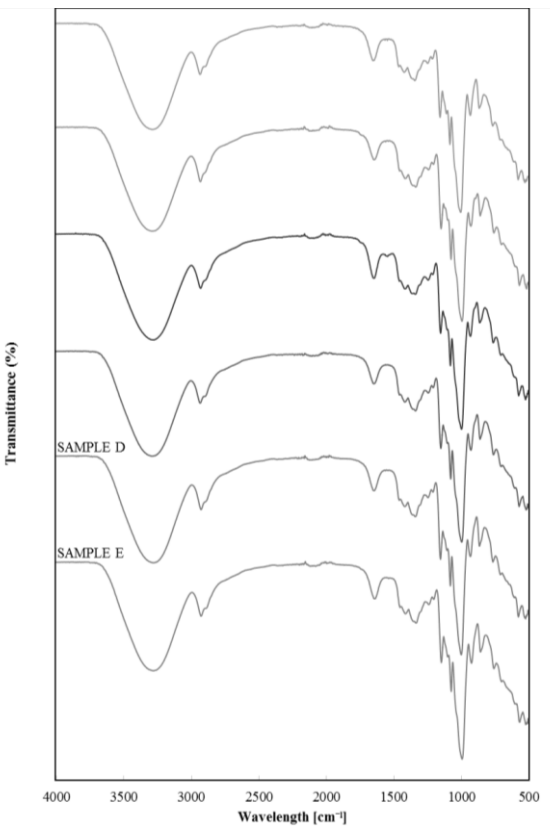

Figure 7. Functional group analysis of tobacco derived bioplastic.

Figure 7 shows FTIR analysis of six bioplastic films. The analysis is to compare the FTIR spectra of glycerol plasticized bioplastic (control) and different ratio of sorbitol-glycerol plasticized bioplastic. At 3273, 3278, 3282, 3284, 3286 cm-1, the peaks of bioplastics shows characteristic of O-H

stretching, the wavenumbers of 2927 until 2929 cm-1 shows stretching of C-H, 1644-1646 cm-1 shows a water bending δ(O-H), 1336-1338 cm-1 shows stretching of CH2, 1076-1077 cm-1 shows stretching of C-O-C bond and 994 and 997 cm-1 (pyranose ring) [20]. Most of the signature peaks occurred at the same wavenumber with the increase of sorbitol in the bioplastics. Moreover, the O-H peaks were changed to a higher wavenumber with the increase of glycerol content in the bioplastic. This is due to weakening of hydrogen bonds formation between molecules of starch due to the creation of hydrogen bonds with glycerol between certain starch molecules [21]. In comparison, when the glycerol content was increased, the C-O-H peak corresponding to the crystalline starch at 995 cm-1 displayed a higher intensity. This finding revealed that the crystalline part of starch increased after gelatinization, leading to improved mechanical properties of bioplastics [22].

Conclusion

The current study manifested that xylan-tapioca starch with different ratios of plasticizers can be used for developing optimized formulations to produce good bioplastic films in terms of physical and chemical properties. Using plasticizers helps to overcome brittleness and enhance the flexibility of bioplastic film. Different plasticizer types and concentrations were exploited to investigate their effect on xylan-tapioca starch bioplastic films' physical and chemical properties. The results demonstrated that plasticizer type and concentration influence film morphologies, moisture content, biodegradability, and water absorption. The optimized result obtained in this study was sample E (0.85:0.15 Sorbitol-Glycerol) which shows a low moisture content rate, water absorption, and biodegradability suitable for food packaging application. Sample E also shows better heat stability and morphology. However, further research regarding the mechanical, thermal, and barrier properties of xylan-tapioca starch bioplastic films should be conducted to select the most suitable film for food packaging applications.

Disclaimer

None.

References

[1] Huq, T., S. Salmieri, A. Khan, R. A. Khan, C. Le Tien, B. Riedl, C. Fraschini, J. Bouchard, J. Uribe Calderon, and M. R. Kamal, *Carbohydr. Polym.* 90, 1757–1763 (2012).

[2] Wu, Y., C. L. Weller, F. Hamouz, S. Cuppett, and M. Schnepf, E. Basiak, A. Lenart, F. Debeaufort, *Polym. (Basel)*. 10, 412 (2018). 66, 486–493 (2001).

[3] Atef, M., M. Rezaei, and R. Behrooz, *Food Hydrocoll.* 45, 150–157 (2015).

[4] Basiak, E., A. Lenart, and F. Debeaufort, *Polymers* 10, 412 (2018).

[5] Ma, X., & Yu, J. (2004). The plastcizers containing amide groups for thermoplastic starch. *Carbohydrate Polymers*, 57(2), 197-203.

[6] Zhang, Y., Rempel, C., & Liu, Q. (2014). Thermoplastic starch processing and characteristics—a review. *Critical reviews in food science and nutrition*, 54(10), 1353-137

[7] Abdullah, A. H. D., Pudjiraharti, S., Karina, M., Putri, O. D., & Fauziyyah, R. H. (2019). Fabrication and Characterization of Sweet Potato Starch-based Bioplastics Plasticized with Glycerol. *Journal of Biological Sciences*, 19(1), 57-64.

[8] Ismail, H., & Zaaba, N. F. (2014). Effects of poly (vinyl alcohol) on the performance of sago starch plastic films. *Journal of Vinyl and Additive Technology*, 20(2), 72-79.

[9] Zalasiewicz, J., Gabbott, S., & Waters, C. (2019). Plastic Waste: How Plastics Have Become Part of the Earth's Geological Cycle. *Waste*, 443-452.

[10] Yong, K., Ching, Y., Afzan, M., Lim, Z., & Chong, K. (2015). Mechanical and Thermal Properties of Chemical Treated Oil Palm Empty Fruit Bunches Fiber Reinforced Polyvinyl Alcohol Composite. *J. Biobased Mater. Bioenergy*, 9, 231-235.

[11] Ershad, M., Yong, K., Ching, Y., Chuah, C., & Liou, N. (2015). Effect of Single and Double Stage Chemically Treated Kenaf Fibers on Mechanical Properties of Plyvinyl Alcohol Film. *BioResource*, 10, 822-838.

[12] Ching, Y., Ershad, A., C. A., L., Choo, K., Yong, C., Sabariah, J., ... Liou, N. (2016). Rheological Properties of Cellulose Nanocrystal-embedded Polymer Composites: A review. *Cellulose*, 23, 1011-1030.

[13] Kim., B.-J., Yao., F., Han., G., & Wu, Q. (2012). Performance of bamboo plastic composites with hybrid bamboo and precipitated calcium carbonate fillers. *Polymer Composites*, vol. 33, no.1, pp, 68-78.

[14] Lestari, R. A., Kasmiyatun, M., Dermawan, K., Aini, A. N., Riyati, N., & Putri, F. R. (2020). Bioplastic from Jackfruit Seeds and Rice. *IOP Conf.Series: Materials Science and Engineering*, 835.

[15] Sanyang, M. L., Sapuan, S., Jawaid, M., Ishak, M., & Sahari, J. (2016). Effect of plasticizer type and concentration on physical properties of biodegradable films based on sugar palm (arenga pinnata) starch for food packaging. *Journal of Food Science and Technology*, 53(1), 326-336.

[16] Ching, Y., Ershad, A., C. A., L., Choo, K., Yong, C., Sabariah, J., Chuah, C. H. & Liou, N. (2016). Rheological Properties of Cellulose Nanocrystal-embedded Polymer Composites: A review. *Cellulose*, 23, 1011-1030.

[17] Alvarez-Chavez, C., Edwards, S., Moure-Eraso, R., & Geiser, K. (2011). Sustainability of Bio-based Plastics: General Comparative Analysis and Recommendations for Improvement. *Journal of Cleaner Production* 23 (1), 46-7.

[18] Pajak, P., Przetaczek-Roznowska, I., & Juszczak, L. (2019). Development and physicochemical, thermal and mechanical properties of edible films based on pumpkin, lentil and quinoa starches. *Int. J. Biol. Macromol*, 138, 441-449.

[19] Sarasa, J., Gracia, J., & Javierre, C. (2008). Study of the Biodisintegration of a Bioplastic Material Waste. *Bioresource Technology* 100, 3764-8.

[20] Sahari, J., Sapuan, S., Zainudin, E., & Maleque, M. (2014). Physico-chemical and Thermal Properties of Starch Derived from Sugar Palm Tree (Arenga pinnata). *Asian Journal of Chemistry*, vol. 26, no.4, 955-959.

[21] Dang, K. M., & Yoksan, R. (2015). Development of thermoplastic starch blown film by incorporating plasticized chitosan. *Carbohydrate Polymers*, vol. 115, 575-581.

[22] Abdullah, A. H., Pudjiraharti, S., Karina, M., Putri, O. D., & Fauziyyah, R. H. (2019). Fabrication and Characterization of Sweet Potato Starch based Bioplastics Plasticized with Glycerol. *Journal of Biological Sciences*, vol. 19, no. 1, 57-64.

Chapter 4

The Structural Characterization of Cobalt-Based Metal-Organic Framework (Co-MOF) Using Fourier Transform Infrared (FTIR)

Ni Putu Yunika Arindita
and Asep Bayu Dani Nandiyanto*
Department of Chemistry Education, Indonesian University of Education, Bandung, West Java, Indonesia

Abstract

Cobalt-based Metal–Organic frameworks (Co-MOF) are promising materials with many practical applications. This study aims to present recent advances in Fourier Transform Infrared (FTIR) studies of Co-MOFs, including the identification of characteristic vibrational bands, the detection of guest molecules, and the investigation of changes in the infrared spectrum that are influenced by temperature. The research approach utilized is a Systematic Literature Study (SLR). As a result, FTIR spectroscopy is known to be very useful for identifying the typical structure of functional groups in Co-MOF, such as peaks at around 595 cm^{-1} (Co−O vibration), 1162 cm^{-1} (N–C stretching of the imidazolium ring), and 1580 cm^{-1} (C=N vibration are attributed to the presence of the triazine ring). Overall, FTIR spectroscopy is a valuable technique for the characterization and understanding of Co-MOF, and its combination with other analytical methods can provide comprehensive insights into their properties and applications.

Keywords: Co-MOF, characterization, FTIR, IR spectra

* Corresponding Author's Email: nandiyanto@upi.edu.

In: Advances in Materials Science Research. Volume 65
Editor: Maryann C. Wythers
ISBN: 979-8-89113-090-6

Introduction

Metal-organic frameworks (MOFs) are a versatile class of porous and crystalline hybrid materials, composed of both organic and inorganic components. MOF is one of the popular subjects that has been well-studied and reviewed (Nandiyanto, 2019; Shidiq, 2023; Nordin et al., 2018). MOFs, also referred to as porous coordination polymers (PCPs), are gaining increasing attention due to their potential for functional applications in various research fields. These materials consist of metal ions or clusters, which are linked together by organic ligands, creating a unique and tunable porous structure (Jiao et al., 2019; Ren et al., 2020).

MOFs possess remarkable features, including large surface areas that typically range from 1000 to 10,000 m^2/g, high porosity, and tunable structures. In comparison to traditional porous materials like zeolites and activated carbons, MOFs offer greater flexibility in customization (Zhou et al., 2012). As the result of their interesting structural properties, such as low density, large surface area, customizable pore functionality, and structural flexibility make MOFs highly useful across a broad spectrum of potential applications, including gas sorption, heterogeneous catalysis, separation, drug delivery (Wu & Yang, 2017), sensing, and proton conductivity (Pettinari et al., 2017). Despite their numerous advantages, MOFs are typically bulky materials with large sizes, and they exhibit certain weaknesses in terms of their chemical stability (Xiao et al., 2020). To fulfill the practical application of MOFs materials, considerable attention has been given to strategies aimed at modifying MOFs materials.

Numerous research groups have extensively studied transition-metal-based MOFs, particularly Co-MOF, due to their favorable properties. In practical applications, derivatives of Co-MOF are more commonly used than the pure form or its composites (Zheng et al., 2017). Co-MOF are often used as precursors, which are then synthesized into various forms, such as Co-related oxides and sulfides, with differing morphologies. Co-MOF and their composites often act as templates for other active components to enhance the overall properties of the materials (Hua et al., 2019). A study by Zhang et al. (2020) revealed that Co-MOF with nano block microspheres form give the highest specific capacitance, indicating that the nanonization of Co-MOF can significantly enhance their energy storage performance. Based on the previous study, it can be inferred that the structure of the Co-MOF is a crucial role in its performance for these applications. To gain a deeper understanding of the structural and surface properties of Co-MOF, an FTIR study can be conducted.

FTIR works by measuring the absorption of infrared radiation by the sample. The absorption occurs at specific wavelengths corresponding to the vibrational frequencies of the chemical bonds in the sample. By analyzing the resulting spectrum, it is possible to identify the functional groups present in the sample and their vibrational modes (Baudot et al., 2010; Eid, 2021; Y. Jiang et al., 2011). In Co-MOF, the FTIR spectrum can be used to identify the functional groups of the organic ligands, such as carboxylic acids, amines, and imines, and confirm their coordination with the cobalt ions. The presence of characteristic absorption bands at specific wavenumbers indicates the formation of specific chemical bonds and coordination modes. For example, the presence of a peak at around 1600 cm^{-1} is indicative of the carboxylate group in the organic ligand, while the presence of peaks at around 3400 cm^{-1} and 1620 cm^{-1} indicates the presence of amino groups (Sahoo et al., 2020; Sargazi et al., 2014). Unfortunately, the characterization of intermolecular interactions in Co-MOF using FTIR can be challenging since the infrared spectrum of the material can be complex and difficult to interpret (Ovchinnikov et al., 2016; Rakipov et al., 2022; Tatulian, 2019).

However, several methods can be used to extract information about its intermolecular interaction. One common approach is to analyze the changes in the infrared spectrum upon different types of stimuli, such as changes in temperature, pressure, or gas exposure (Śmiechowski, 2021; Tatulian, 2019). These changes can provide information on the interactions between the organic ligands, cobalt ions, and guest molecules within the MOFs structure. For instance, if the Co-MOF contains guest molecules that can be adsorbed and desorbed, such as gases or solvents, FTIR can be used to monitor the changes in the vibrational modes of the guest molecules as they are adsorbed or desorbed from the MOFs. By comparing the spectrum of the guest molecules in the MOFs to that of the pure guest molecules, it is possible to determine the strength and nature of the interactions between the guest molecules and the MOFs structure. Hence, this chapter provided the characterization of Co-MOF by FTIR spectroscopy analysis by the Systematic Literature Study (SLR) method of several journal articles. Also, this study presents a comprehensive and in-depth review of Co-MOF characterization by FTIR regarding its intramolecular and intermolecular interaction.

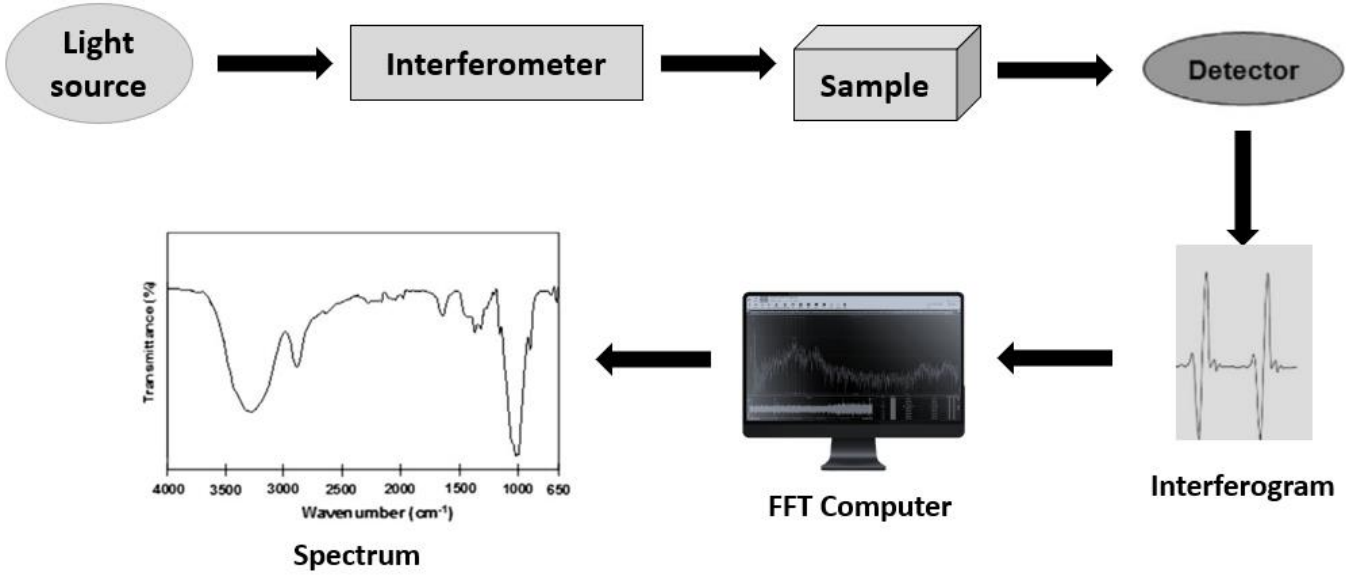

Figure 1. FTIR instrumentation schematic. (Figure was adopted from Mohamed et al., 2017).

Literature Review

Co-MOFs Characterized by FTIR Spectroscopy

Fourier transform infrared (FTIR) spectroscopy is a widely used technique for the molecular-level characterization of materials through their infrared absorption spectra. The instrument used to obtain the absorption spectrum of a compound is called a spectrophotometer, with the Fourier transform spectrophotometer being a faster alternative to the traditional method. This technique involves the absorption of infrared radiation by the functional groups of the sample, which causes a change in their electric dipole moment. In this case, the FTIR technique is used to identify molecules based on the absorption pattern of infrared radiation generated by the functional groups within the molecule. FTIR spectroscopy has several advantages, one of which is its ability to identify functional groups such as C=O, C-H, or N-H. Another advantage is FTIR can measure all types of samples including solids, liquids, and gases (Mohamed et al., 2017).

Figure 1 shows a schematic of the FTIR instrumentation. There are three main components of the FTIR spectrometer including the interferometer, the sample compartment, and the detector. The instrument operates by emitting infrared radiation from a light source, which passes through the interferometer and reaches the detector after interacting with the sample. The signal is amplified and converted to a digital signal using an analog-to-digital converter. The interferogram is then transformed into a spectrum through a fast Fourier transform algorithm. Currently, the Michelson interferometer is the most widely used type of interferometer in FTIR. The Michelson interferometer is the central component of the FTIR spectrometer, which consists of a beam splitter, a fixed mirror, and a movable mirror. The beam splitter is designed to split the incoming light into two beams, one of which is transmitted to the fixed mirror while the other is reflected to the movable mirror. The two beams are then recombined at the beam splitter, and the resulting beam interacts with the sample before reaching the detector (Khan et al., 2018; Rosas-Casarez et al., 2014). When the two beams are in phase, the resulting interference is constructive, which means that the amplitude of the combined beam is greater than that of the individual beams. When the two beams are out of phase, the resulting interference is destructive, which means that the amplitude of the combined beam is less than that of the individual beams. The interference pattern can be observed by detecting variations in the

intensity of the combined beam as the position of the moving mirror is varied. By analyzing this interference pattern, information about the sample being studied can be obtained (Escobar-Barrios et al., 2012).

In Fourier transform infrared (FTIR) spectroscopy, the IR range is typically divided into three smaller regions. The near-IR region (NIR) spans from approximately 4000-10,000 cm^{-1}, while the mid-IR region (MIR) ranges from 4000-400 cm^{-1}. The far-IR region (FIR) extends from 400-10 cm^{-1}. When IR photons interact with molecules, it can cause groups of atoms to vibrate relative to the bonds between them. Similar to electronic transitions, these vibrational transitions correspond to specific energies, and molecules absorb IR radiation only at certain frequencies and wavelengths. The MIR region includes the frequencies corresponding to the fundamental vibrations of nearly all functional groups and a diverse array of bonds, including those found in metals, within both organic and inorganic compounds. While the MIR spectrum is frequently employed for sample analysis, both FIR and NIR spectra can also offer valuable insights into the characteristics of the samples being studied (Shabanian et al., 2020).

FTIR spectroscopy can provide valuable information about compounds like MOFs that have OH groups in their structure. Using FTIR, the analysis of modifier molecules in the surfaces of MOFs can be done. MOFs are structured porous materials made up of metal ions or clusters that are linked together by organic compounds to form coordination networks with one, two, or three dimensions (Hu et al., 2015). The Co-MOF, which is a common type of MOF, has gained considerable interest due to its outstanding characteristics that show potential for significant applications. FTIR analysis of Co-MOF can provide valuable information about the nature and strength of the chemical bonds between cobalt ions and organic ligands that make up the framework. Carboxylic acids are one of the most common functional groups in Co-MOF. These groups are formed when a carboxyl group (-COOH) is attached to an organic ligand. Carboxylic acids are acidic and can form hydrogen bonds with other molecules, making them important for the stability and reactivity of Co-MOF (Bhadra et al., 2022).

Amides are another functional group that can be identified in Co-MOF using FTIR. Amides are formed when a carbonyl group (-C=O) is attached to an amino group ($-NH_2$) in an organic ligand. Amides are important for the mechanical strength and stability of Co-MOF, as they can form hydrogen bonds and other interactions with neighboring ligands. Imines are a less common but still present functional group in Co-MOF. Imines are formed when a nitrogen atom (-N) is double-bonded to a carbon atom (-C) in an

organic ligand. These groups are important for the electronic properties of Co-MOF, as they can participate in electron transfer reactions and other chemical processes.

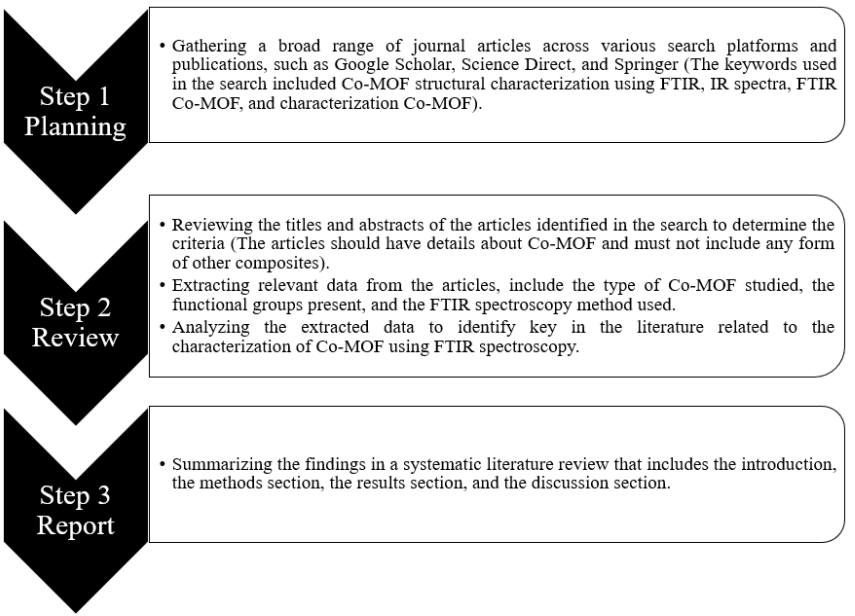

Figure 2. Method for conducting an SLR on the characterization of Co-MOF using FTIR spectroscopy.

Method

The present study employed a Systematic Literature Review (SLR) approach to investigate the structural characterization of Co-MOF using FTIR (Figure 2). SLR is a methodical approach to reviewing literature that involves a structured and transparent process to identify, evaluate, and synthesize all available evidence on a specific research question. Its objective is to minimize bias by conducting comprehensive literature searches and considering the transparency, transferability, and replicability of the reviewed journal (Mengist et al., 2020). Detailed information for the use of FTIR is explained in previous studies (Nandiyanto et al., 2019; Nandiyanto et al., 2023; Sukamto & Rahmat, 2023; Obinna, 2022).

Table 1. The spectral interpretations of Co-MOF

Peak	Assignment	FTIR Instrumentation	Reference
3432 cm^{-1}	O–H stretching vibration.	FTIR Jasco-680 spectrometer	(Rahmati & Rafiee, 2021)
1638 cm^{-1}	Asymmetrical stretching vibrations of C=O bond (COO^-).	FTIR – 4100 type A, JASCO Inc.	(Naseem et al., 2022)
1475 cm^{-1}	Symmetrical stretching vibrations of C=O bond (COO^-).		
1580 cm^{-1}	C=N vibration (strong stretching vibration bands are attributed to the presence of the triazine ring).	FTIR Jasco-680 spectrometer	(Rahmati & Rafiee, 2021)
1482−1468 cm^{-1}	Asymmetric vibrations of C−H bonds.	ATR-FTIR Bruker Vertex 70	(Tran et al., 2020)
~1307 cm^{-1}	C−H bending movements.		
1162 cm^{-1}	N–C stretching of the imidazolium ring.	ATR-FTIR Bruker Tensor II	(Zhang et al., 2020)
808 cm^{-1}	the out-of-plane bending motion of O–C=O	FTIR – 4100 type A, JASCO Inc.	(Naseem et al., 2022)
595 cm^{-1}	Co−O vibration.	FT-IR Bruker TENSOR27	(Liu et al., 2019)

Results and Discussion

This section of the article provides a concise overview of the characterization of Co-MOF using FTIR by various research groups within or without the composite. The purpose of including this information is to enhance the comprehension of peak definitions obtained by understanding the methodologies employed in the Materials and Methods section of different studies. Table 1 presents a comprehensive record of spectral frequencies of Co-MOF by compiling and summarizing the spectral interpretation studies conducted thus far.

According to research conducted by Chen et al., Co-MOF was prepared by mixing $Co(NO_3)_2 \cdot 6H_2O$ with a solution of 2-methylimidazole in ethanol. The mixture was then stirred for 6 hours and heated at 100°C for 24 hours. The FTIR spectrum (Figure 3) of the Co-MOF and Co-MOF/g-C_3N_4 composites with different compositions of Co-MOF was obtained using a spectrophotometer, and the spectral features were analyzed. The absorption peak at 3432 cm^{-1} in Co-MOF is due to the stretching vibration of O-H in the H_2O molecules that are adsorbed within the Co-MOF structure. Two peaks detected at 1649 and 1383 cm^{-1} represent the asymmetric and symmetric

stretching vibrations, respectively, of O=C-O that is bonded to Co. From the article, Co-MOF could act as an electron donor to promote the visible-light photoactivity of g-C_3N_4 nanosheets for CO_2 reduction. Wang et al., (2020) characterize the functional group of Co-MOF synthesized using FTIR by the simple solution method as shown in Figure 4. The FTIR spectra showed absorption bands at 3455 cm^{-1}, which corresponds to O-H stretching vibration, and at 2923 cm^{-1}, which corresponds to the C-H stretching vibration of thermoplastic polyurethane (TPU). Additionally, the spectrum showed absorption bands at 1643 cm^{-1} and 1375 cm^{-1}, which correspond to the asymmetric and symmetric stretching vibrations of the C=O bond in Co-MOF, indicating the successful synthesis of Co-MOF. As a comparison of the results of FTIR, salicylaldehyde (SA) and 4,4-Diaminodiphenyl methane (DDM) are selected to synthesize ligand (H_2L) and were used to show that Co-MOF was synthesized. For the application, Co-MOF can be used as a synergistic flame retardant in TPU due to its high thermal stability and good flame retardancy. The addition of Co-MOF to TPU significantly improved the flame retardant properties of TPU, including an increase in limiting oxygen index (LOI) and a decrease in peak heat release rate (PHRR).

The FTIR spectrum of the Co-MOF obtained from the reaction between cobalt nitrate hexahydrate and oxalic acid is presented in Figure 5. The FTIR spectra showed prominent peaks at 3432 cm^{-1}, 1651 cm^{-1}, and 1391 cm^{-1}. The peak at 3432 cm^{-1} is attributed to the O-H stretching vibration in adsorbed H_2O molecules within the Co-MOF structure. The peaks at 1651 cm^{-1} and 1391 cm^{-1} correspond to the asymmetric and symmetric stretching vibrations, respectively, of the O=C-O bonded to Co in the Co-MOF structure. The FTIR analysis provides evidence for the presence of water and organic functional groups in the Co-MOF structure. These functional groups are important for the adsorption of humic acid from water. The presence of O=C-O groups in the Co-MOF structure indicates that the material has the potential to interact with the humic acid, which contains carboxylic groups. The FTIR analysis supports the potential use of Co-MOF as an effective adsorbent for humic acid removal from water (Naseem et al., 2022).

The presence of functional groups in the synthesized Co-MOF material mixed with composites covalent organic framework (COF) based on melamine and terephthaldehyde (based on Rahmati & Rafiee, (2021)) was also determined through FTIR. Figure 6 presents the FTIR spectra of Co-MOF, COF, Co-MOF-NH_2, and Co-MOF/COF. The peak at 3432 cm^{-1} in Co-MOF corresponds to the O–H stretching vibration of adsorbed H_2O molecules in the Co-MOF structure. The two absorption peaks at 1649 and 1383 cm^{-1} indicate

the asymmetric and symmetric stretching vibrations of the O=C–O bonded to metal cobalt. The FTIR spectrum of Co-MOF/COF shows new stretching vibrations at 1575, 1501, and 1380 cm^{-1}, which arise from the C=N, C=C, and C–N bonds, respectively, indicating condensation and tautomerization.

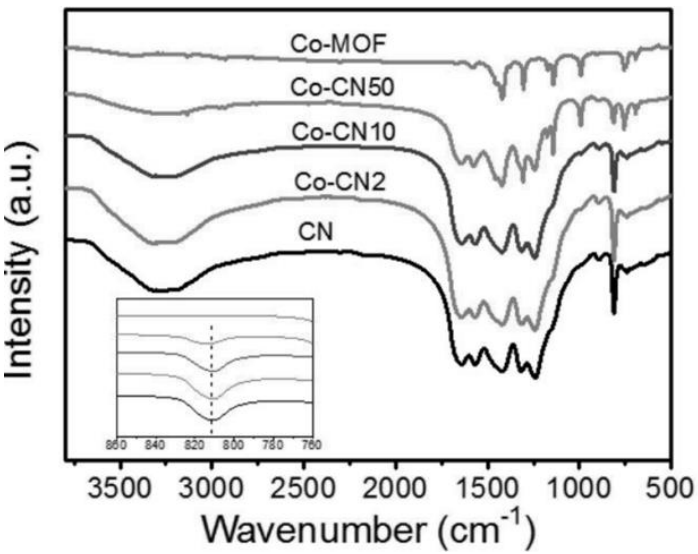

Figure 3. FTIR spectra Co-MOF. (Figures were adopted from Chen et al., 2020).

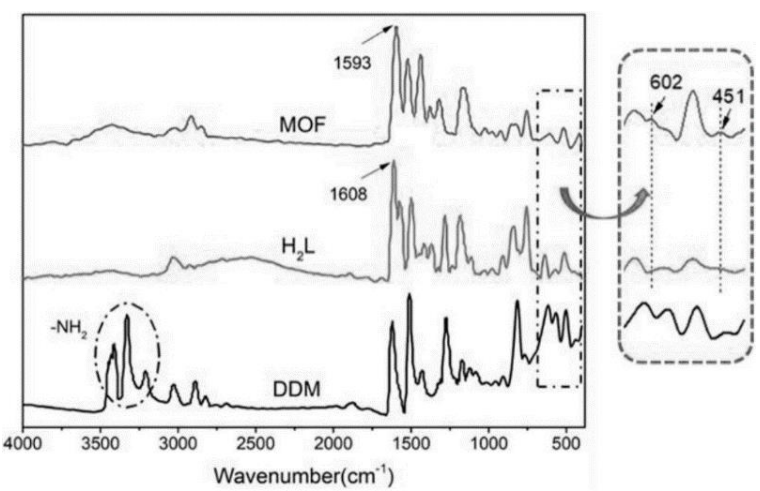

Figure 4. FTIR spectra of DDM, H_2L, and Co-MOF. (Figures were adopted from Wang et al., 2020).

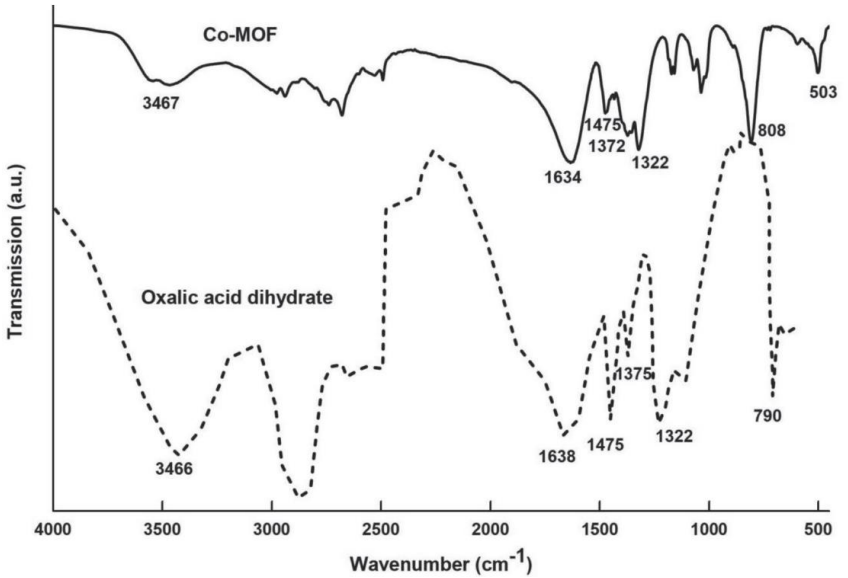

Figure 5. FTIR spectra of Co-MOF and *oxalic acid di-hydrate* (Figures were adopted from Naseem et al., 2022).

The FTIR analysis of Co-MOF is influenced by several factors that can affect the obtained results. One of the factors is the addition of other materials to the Co-MOF structure, which can result in changes in the spectral pattern. For instance, the incorporation of melamine into the COF structure in the Co-MOF/COF nanocomposite leads to strong stretching vibration bands at 1551 and 1475 cm^{-1} (C=N vibration), indicating the successful incorporation of melamine. Similarly, the functionalization of Co-MOF with ethylenediamine results in new absorption peaks at 3423 and 3247 cm^{-1}, assignable to the stretching vibrations of NH_2 groups, and at 2965 and 2914 cm^{-1}, corresponding to the stretching vibrations of C-H bonds of ethylenediamine. The presence of these additional materials in the Co-MOF structure can alter the vibrational modes of the bonds, leading to changes in the FTIR spectra. Therefore, the interpretation of the FTIR results of Co-MOF should take into account the influence of other materials that may be present in the sample (Srinivasan et al., 2020).

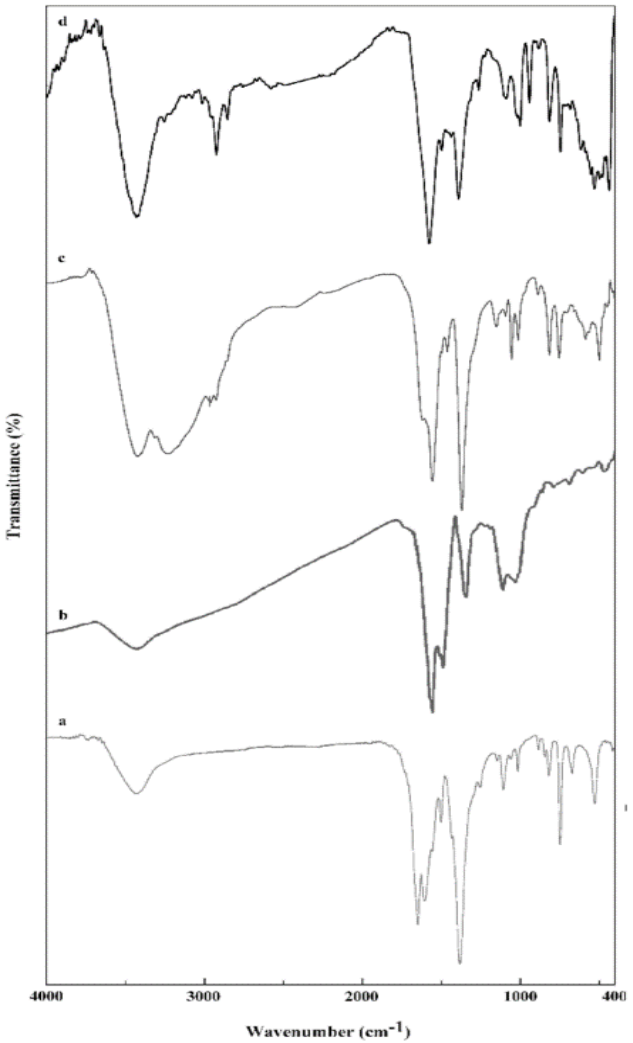

Figure 6. FTIR spectra of Co-MOF (a), COF (b), Co-MOF-NH_2 (c), and Co-MOF/COF (d) (Figures were adopted from Rahmati & Rafiee, 2021).

Strauss et al. (2019) explored the effect of incorporating TTF (tetrathiafulvalene) into Co-MOF-74 on its electrical conductivity and gas-sensing properties. The addition of TTF not only increased the electrical conductivity of the Co-MOF-74-TTF composite, but it also caused changes in the infrared (IR) spectra. Specifically, the peak at 1586 cm^{-1} (corresponding to C=C stretching in the benzene ring) shifted to lower frequencies in the

composite, indicating an interaction between TTF and the Co-MOF-74. This change in the IR spectra could provide insight into the mechanism of conductivity enhancement in the Co-MOF-74-TTF composite. The study demonstrated the potential of using TTF as a dopant to tune the properties of MOFs for various applications. Figure 7 displays a comparison of the IR spectra of Co-MOF-74 and Co-MOF-74-TTF, wherein the νC=O band appears at the typical peak of around 1700 cm^{-1}. In the range of 3000 to 3500 cm^{-1}, Co-MOF-74 exhibits the νOH stretching, which is likely due to the presence of –COOH groups and water molecules. This stretching is observed to be less intense for Co-MOF-74-TTF, indicating that the inclusion of TTF within the pores could lead to reduced water adsorption.

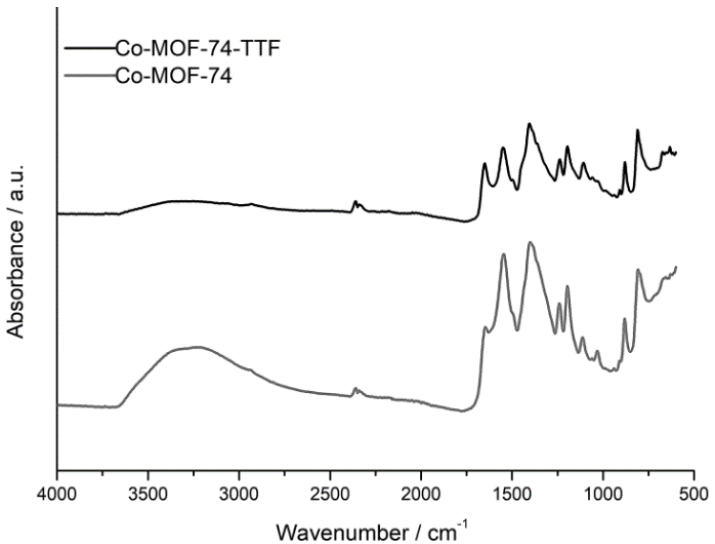

Figure 7. Co-MOF-74 IR-spectra compared to Co-MOF-74 infiltrated with TTF. (Figures were adopted from Strauss et al., 2019).

Another factor that can impact the IR spectra is temperature changes. The research of H. Jiang et al., (2016) was about characterized of Co-MOF-74 before and after the reaction by FTIR spectroscopy. The FTIR spectra showed that the stretching vibration peaks of the carboxylic groups (C=O) and hydroxyl groups (O-H) in the Co-MOF-74 structure decreased with increasing temperature, indicating that the adsorption strength of NH_3 on Co-MOF-74 was weakened by the elevated temperature. This weakening of adsorption strength caused a decrease in the catalytic activity of Co-MOF-74 at higher

temperatures. Additionally, the FTIR spectra also showed that the stretching vibration peak of NH_3 (at 1385 cm^{-1}) decreased at higher temperatures, indicating that NH_3 was desorbed from the Co-MOF-74 structure. This desorption of NH_3 from the structure at higher temperatures contributed to the decrease in the catalytic activity of Co-MOF-74.

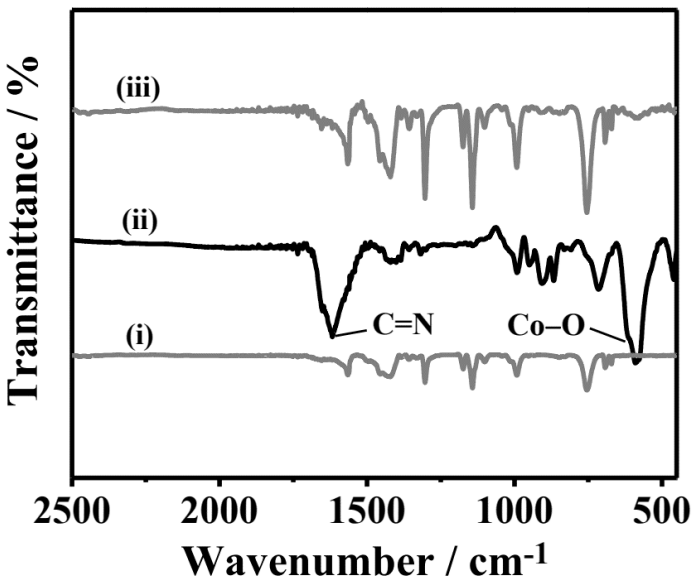

Figure 8. FTIR spectra of (i) TPN-COF, (ii) Co-MOF, and (iii) Co-MOF@TPN-COF. (Figures were from Liu et al., 2019).

Figures 8 show FTIR spectra of the Co-MOF-on-TPN-COF hybrid showed characteristic bands of both Co-MOF and TPN-COF. The peak at 1600 cm^{-1} corresponded to the stretching vibration of the aromatic ring, while the peak at 1400 cm^{-1} corresponded to the C-N stretching vibration of the TPN-COF structure. The presence of the Co-MOF was confirmed by the characteristic peaks at 1380 cm^{-1} and 1520 cm^{-1}, which corresponded to the COO- stretching vibrations. The FTIR spectra of the hybrid material were further investigated by monitoring changes in the spectra upon the addition of Ampicillin. The results showed a decrease in the peak intensity at 1600 cm^{-1}, which corresponded to the stretching vibration of the aromatic ring, indicating the interaction between the Ampicillin and the hybrid material. The observed changes in the FTIR spectra were attributed to the binding of the aptamer probe to the Ampicillin, leading to a change in the local environment of the

hybrid material and the disruption of the π-π interactions between the TPN-COF structure and the Co-MOF. This study demonstrates the potential of the Co-MOF-on-TPN-COF hybrid material as an ultrasensitive and selective platform for the electrochemical detection of antibiotics.

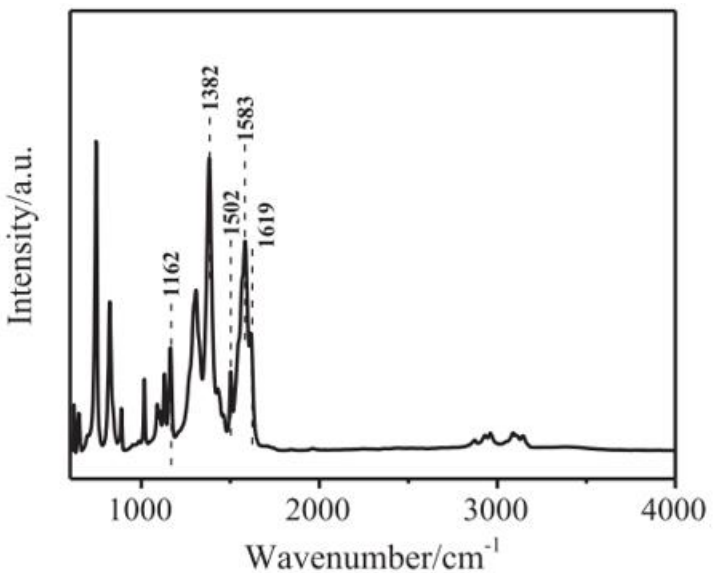

Figure 9. ATR-FTIR spectra of the Co-MOF (Figures were adopted from L. Zhang et al., 2020).

FTIR and ATR-FTIR are two methods of infrared spectroscopy. FTIR is commonly used for analyzing powdered samples by mixing them with a KBr powder matrix. On the other hand, ATR-FTIR is a surface analysis technique that does not require additional materials or holders for the samples. In addition, Co-MOF was also characterized using ATR-FTIR in a study conducted by L. Zhang et al., (2020) (Figure 9). ATR-FTIR analysis was carried out to confirm the structural properties of both Co-MOF and $Co(OH)_2$. The results showed that the peaks at 1619 cm^{-1} and 1583 cm^{-1} were due to the asymmetric stretching vibrations of υas (COO–), whereas the peaks at 1382 cm^{-1} and 1502 cm^{-1} corresponded to the symmetric stretching vibrations of υs (COO–). In addition, a peak at 1162 cm^{-1} was observed, indicating the N–C stretching of the imidazolium ring. These stretching vibrations were found to shift too much lower wavenumbers when compared with the carbonyl frequencies of the free H_2BDC ligand (υC=O = 1682 cm^{-1}), indicating the

presence of a coordinated carboxylate group. These peaks were not observed in the IR spectrum of the MOF-derived $Co(OH)_2$. Instead, a new peak was observed at 3633 cm^{-1}, which was assigned to O–H stretching vibration, and the peaks at 1441 cm^{-1}, 1071, 827, and 747 cm^{-1} corresponded to the ν3, ν1, ν2, and ν4 modes of the carbonate ion, respectively.

In summary, our review of the literature on FTIR analysis of Co-MOF materials reveals that this technique is a powerful tool for characterizing the chemical composition and structure of these materials. Our analysis of the FTIR spectra from different Co-MOF materials shows that characteristic peaks can be identified for different types of linkers, ligands, and metal centers, allowing for a detailed understanding of the material's chemistry. However, the interpretation of FTIR spectra can be complicated by factors such as sample preparation, measurement conditions, and the presence of overlapping bands. Future studies should aim to validate FTIR results using complementary techniques and to further refine the interpretation of FTIR spectra in Co-MOF materials.

Conclusion

In summary, FTIR spectroscopy is a valuable analytical technique for studying the chemical composition and structure of Co-MOF materials. The presence of a peak at around 1600 cm^{-1} is indicative of the carboxylate group in the organic ligand, while the presence of typical peaks of Co-MOF at around 595 cm^{-1} indicates the presence of Co−O vibration. The interaction of Co-MOF with other molecules can be identified through changes in absorption peaks, whether it be a shift in wavenumber, intensity change, or the appearance of a new peak. Through analysis of the literature, this chapter shows that FTIR can provide information on the types of chemical bonds and functional groups present in Co-MOF materials, as well as the effects of different synthesis and treatment conditions on the material's properties.

Disclaimer

The authors declare that there is no conflict of interest regarding the publication of this article. The authors confirmed that the paper was free of plagiarism.

References

Baudot, C., Tan, C., & Kong, J. (2010). FTIR spectroscopy as a tool for nano-material characterization. *Infrared Physics & Technology*, 53, 434–438. https://doi.org/10.1016/j.infrared.2010.09.002.

Bhadra, B. N., Ahmed, I., Lee, H. J., & Jhung, S. H. (2022). Metal-organic frameworks bearing free carboxylic acids: Preparation, modification, and applications. In *Coordination Chemistry Reviews*. https://doi.org/10.1016/j.ccr.2021.214237.

Chen, Q., Li, S., Xu, H., Wang, G., Qu, Y., Zhu, P., & Wang, D. (2020). Co-MOF as an electron donor for promoting visible-light photoactivities of g-C3N4 nanosheets for CO2 reduction. *Chinese Journal of Catalysis*, 41(3), 514–523. https://doi.org/10.1016/S1872-2067(19)63497-2.

Eid, M. M. (2021). Characterization of Nanoparticles by FTIR and FTIR-Microscopy BT - *Handbook of Consumer Nanoproducts* (S. Mallakpour & C. M. Hussain (eds.); pp. 1–30). Springer Singapore. https://doi.org/10.1007/978-981-15-6453-6_89-1.

Escobar-Barrios, V. a, Rangel-Méndez, J. R., Pérez-Aguilar, N. V, Andrade-Espinosa, G., & Dávila-Rodríguez, J. L. (2012). FTIR – An Essential Characterization Technique for Polymeric Materials. *Infrared Spectroscopy - Materials Science, Engineering and Technology*.

Hu, Y., Lin, B., He, P., Li, Y., Huang, Y., & Song, Y. (2015). Probing the Structural Stability of and Enhanced CO2 Storage in MOF MIL-68(In) under High Pressures by FTIR Spectroscopy. *Chemistry - A European Journal*. https://doi.org/10.1002/chem.201502980.

Hua, Y., Li, X., Chen, C., & Pang, H. (2019). Cobalt based metal-organic frameworks and their derivatives for electrochemical energy conversion and storage. In *Chemical Engineering Journal*. https://doi.org/10.1016/j.cej.2019.03.163.

Jiang, H., Wang, Q., Wang, H., Chen, Y., & Zhang, M. (2016). Temperature effect on the morphology and catalytic performance of Co-MOF-74 in low-temperature NH3-SCR process. *Catalysis Communications*. https://doi.org/10.1016/j.catcom.2016.03.013.

Jiang, Y., Li, C., Nguyen, X., Muzammil, S., Towers, E., Gabrielson, J., & Narhi, L. (2011). Qualification of FTIR spectroscopic method for protein secondary structural analysis. *Journal of Pharmaceutical Sciences*, 100(11), 4631–4641. https://doi.org/10.1002/jps.22686.

Jiao, L., Seow, J. Y. R., Skinner, W. S., Wang, Z. U., & Jiang, H. L. (2019). Metal–organic frameworks: Structures and functional applications. In *Materials Today*. https://doi.org/10.1016/j.mattod.2018.10.038.

Khan, S. A., Khan, S. B., Khan, L. U., Farooq, A., Akhtar, K., & Asiri, A. M. (2018). Fourier transform infrared spectroscopy: Fundamentals and application in functional groups and nanomaterials characterization. In *Handbook of Materials Characterization*. https://doi.org/10.1007/978-3-319-92955-2_9.

Liu, X., Hu, M., Wang, M., Song, Y., Zhou, N., He, L., & Zhang, Z. (2019). Novel nanoarchitecture of Co-MOF-on-TPN-COF hybrid: Ultralowly sensitive bioplatform of electrochemical aptasensor toward ampicillin. *Biosensors and Bioelectronics*, 123, 59–68. https://doi.org/10.1016/j.bios.2018.09.089.

Mengist, W., Soromessa, T., & Legese, G. (2020). Method for conducting systematic literature review and meta-analysis for environmental science research. *MethodsX*. https://doi.org/10.1016/j.mex.2019.100777.

Mohamed, M. A., Jaafar, J., Ismail, A. F., Othman, M. H. D., & Rahman, M. A. (2017). Fourier Transform Infrared (FTIR) Spectroscopy. In *Membrane Characterization*. Elsevier B.V. https://doi.org/10.1016/B978-0-444-63776-5.00001-2.

Nandiyanto, A.B.D. (2019). Nano metal-organic framework particles (ie MIL-100 (Fe), HKUST-1 (Cu), Cu-TPA, and MOF-5 (Zn)) using a solvothermal process. *Indonesian Journal of Science and Technology*, *4*(2), 220-228. https://doi.org/10.17509/ijost.v4i2.18178

Nandiyanto, A.B.D., Oktiani, R., and Ragadhita, R. (2019). How to read and interpret FTIR spectroscope of organic material. *Indonesian Journal of Science and Technology*, *4*(1), 97-118. https://doi.org/10.17509/ijost.v4i1.15806

Nandiyanto, A.B.D., Ragadhita, R., and Fiandini, M. (2023). Interpretation of Fourier Transform Infrared Spectra (FTIR): A practical approach in the polymer/plastic thermal decomposition. *Indonesian Journal of Science and Technology*, *8*(1), 113-126. https://doi.org/10.17509/ijost.v8i1.53297

Naseem, S., Aslam, Z., Abbas, A., Sumbal, S., Ali, R., & Usman, M. (2022). Synthesis and Application of Cobalt-based Metal-organic Framework for Adsorption of Humic Acid from Water. *Chemical and Biochemical Engineering Quarterly*, 36(1), 39–50. https://doi.org/10.15255/CABEQ.2021.1960.

Nordin, N.A.H.M., Ismail, A.F., Racha, S.M., Cheer, N.B., Bilad, M.R., Putra, Z.A., and Wirzal, M.D.H. (2018). Limitation in fabricating PSf/ZIF-8 hollow fiber membrane for CO2/CH4 Separation. *Indonesian Journal of Science and Technology*, *3*(2), 138-149. https://doi.org/10.17509/ijost.v3i2.12757

Obinna, E.N. (2022). Physicochemical properties of human hair using Fourier Transform Infra-Red (FTIR) and Scanning Electron Microscope (SEM). *ASEAN Journal for Science and Engineering in Materials*, *1*(2), 71-74.

Ovchinnikov, O. V, Evtukhova, A. V, Kondratenko, T. S., Smirnov, M. S., Khokhlov, V. Y., & Erina, O. V. (2016). Manifestation of intermolecular interactions in FTIR spectra of methylene blue molecules. *Vibrational Spectroscopy*, 86, 181–189. https://doi.org/https://doi.org/10.1016/j.vibspec.2016.06.016.

Pettinari, C., Marchetti, F., Mosca, N., Tosi, G., & Drozdov, A. (2017). Application of metal − organic frameworks. In *Polymer International*. https://doi.org/10.1002/pi.5315.

Rahmati, E., & Rafiee, Z. (2021). Synthesis of Co-MOF/COF nanocomposite: application as a powerful and recoverable catalyst in the Knoevenagel reaction. *Journal of Porous Materials*, 28(1), 19–27. https://doi.org/10.1007/s10934-020-00965-2.

Rakipov, I. T., Petrov, A. A., Akhmadiyarov, A. A., Khachatrian, A. A., & Varfolomeev, M. A. (2022). FTIR spectral study of intermolecular interactions of C=O groups of amides in solution. *Journal of Molecular Liquids*, 354, 118838. https://doi.org/https://doi.org/10.1016/j.molliq.2022.118838.

Ren, J., Huang, Y., Zhu, H., Zhang, B., Zhu, H., Shen, S., Tan, G., Wu, F., He, H., Lan, S., Xia, X., & Liu, Q. (2020). Recent progress on MOF-derived carbon materials for energy storage. In *Carbon Energy*. https://doi.org/10.1002/cey2.44.

Rosas-Casarez, C. A., Arredondo-Rea, S. P., Gómez-Soberón, J. M., Alamaral-Sánchez, J. L., CorralHiguera, R., Chinchillas-Chinchillas, M. J., & Acuña-Agüero, O. H. (2014). Experimental study of XRD, FTIR and TGA techniques in geopolymeric materials. *International Journal of Advances in Computer Science & Its Applications*.

Sahoo, M. K., Samantara, A. K., & Behera, J. N. (2020). In Situ Transformed Cobalt Metal–Organic Framework Electrocatalysts for the Electrochemical Oxygen Evolution Reaction. *Inorganic Chemistry*, 59(17), 12252–12262. https://doi.org/10.1021/acs.inorgchem.0c01300.

Sargazi, G., Afzali, D., Ghafainazari, A., & Saravani, H. (2014). Rapid Synthesis of Cobalt Metal Organic Framework. *Journal of Inorganic and Organometallic Polymers and Materials*, 24(4), 786–790. https://doi.org/10.1007/s10904-014-0042-z.

Sargazi, G., Afzali, D., Ghafarinazari, A., & Saravani, H. (2014). Rapid Synthesis of Cobalt Metal Organic Framework. *Journal of Inorganic and Organometallic Polymers and Materials*, 24, 786–790. https://doi.org/10.1007/s10904-014-0042-z.

Shabanian, M., Hajibeygi, M., & Raeisi, A. (2020). FTIR characterization of layered double hydroxides and modified layered double hydroxides. In *Layered Double Hydroxide Polymer Nanocomposites.* https://doi.org/10.1016/b978-0-08-101903-0.00002-7.

Shidiq, A.P.A. (2023). Bibliometric analysis of nano metal-organic frameworks synthesis research in medical science using VOSviewer. *ASEAN Journal of Science and Engineering*, *3*(1), 31-38. https://doi.org/10.17509/ajse.v3i1.43345

Śmiechowski, M. (2021). The influence of intermolecular correlations on the infrared spectrum of liquid dimethyl sulfoxide. *Spectrochimica Acta Part A: Molecular and Biomolecular Spectroscopy*, 260, 119869. https://doi.org/https://doi.org/10.1016/j.saa.2021.119869.

Srinivasan, R., Elaiyappillai, E., Nixon, E. J., Sharmila Lydia, I., & Johnson, P. M. (2020). Enhanced electrochemical behaviour of Co-MOF/PANI composite electrode for supercapacitors. *Inorganica Chimica Acta*. https://doi.org/10.1016/j.ica.2019.119393.

Strauss, I., Mundstock, A., Treger, M., Lange, K., Hwang, S., Chmelik, C., Rusch, P., Bigall, N. C., Pichler, T., Shiozawa, H., & Caro, J. (2019). Metal-Organic Framework Co-MOF-74-Based Host-Guest Composites for Resistive Gas Sensing. *ACS Applied Materials and Interfaces*. https://doi.org/10.1021/acsami.8b22002.

Sukamto, S., and Rahmat, A. (2023). Evaluation of FTIR, macro and micronutrients of compost from black soldier fly residual: In context of its use as fertilizer. *ASEAN Journal of Science and Engineering*, *3*(1), 21-30. https://doi.org/10.17509/ajse.v3i1.42798

Tatulian, S. A. (2019). FTIR Analysis of Proteins and Protein-Membrane Interactions. *Methods in Molecular Biology* (Clifton, N.J.), 2003, 281–325. https://doi.org/10.1007/978-1-4939-9512-7_13.

Tran, Y. B. N., Nguyen, P. T. K., Luong, Q. T., & Nguyen, K. D. (2020). Series of M-MOF-184 (M = Mg, Co, Ni, Zn, Cu, Fe) Metal-Organic Frameworks for Catalysis Cycloaddition of CO2. *Inorganic Chemistry*. https://doi.org/10.1021/acs.inorgchem.0c02807.

Wang, H., Qiao, H., Guo, J., Sun, J., Li, H., Zhang, S., & Gu, X. (2020). Preparation of cobalt-based metal organic framework and its application as synergistic flame

retardant in thermoplastic polyurethane (TPU). *Composites Part B: Engineering*. https://doi.org/10.1016/j.compositesb.2019.107498.

Wu, M. X., & Yang, Y. W. (2017). Metal–Organic Framework (MOF)-Based Drug/Cargo Delivery and Cancer Therapy. In *Advanced Materials.* https://doi.org/10.1002/adma.201606134.

Xiao, X., Zou, L., Pang, H., & Xu, Q. (2020). Synthesis of micro/nanoscaled metal-organic frameworks and their direct electrochemical applications. In *Chemical Society Reviews*. https://doi.org/10.1039/c7cs00614d.

Zhang, H., Li, J., Li, Z., Song, Y., Zhu, S., Wang, J., Sun, Y., Zhang, X., & Lin, B. (2022). Influence of Co-MOF morphological modulation on its electrochemical performance. *Journal of Physics and Chemistry of Solids.* https://doi.org/10.1016/j.jpcs.2021.110336.

Zhang, L., Wang, N., Cao, P., Lin, M., Xu, L., & Ma, H. (2020). Electrochemical non-enzymatic glucose sensor using ionic liquid incorporated cobalt-based metal-organic framework. *Microchemical Journal*. https://doi.org/10.1016/j.microc.2020.105343.

Zheng, S., Li, X., Yan, B., Hu, Q., Xu, Y., Xiao, X., Xue, H., & Pang, H. (2017). Transition-Metal (Fe, Co, Ni) Based Metal-Organic Frameworks for Electrochemical Energy Storage. In *Advanced Energy Materials*. https://doi.org/10.1002/aenm.201602733.

Zhou, H. C., Long, J. R., & Yaghi, O. M. (2012). Introduction to metal-organic frameworks. In *Chemical Reviews.* https://doi.org/10.1021/cr300014x.

Chapter 5

The Structural Characterization of Cobalt Metal Organic Framework-74 (Co-MOF-74) Using a Scanning Electron Microscope (SEM)

Brigitta Stacia Maharani
and Asep Bayu Dani Nandiyanto*
Department of Chemistry Education, Indonesian University of Education,
Bandung, West Java, Indonesia

Abstract

This chapter aims to explain how to characterize the structure of the organic metal cobalt framework-74 (Co-MOF-74) material using scanning electron microscopy (SEM). The method used in this research is Systematic Literature Review (SLR). The results of the study explain that the Scanning Electron Microscope method is very effective and useful in characterizing the structure of the Co-MOF-74 material due to its success in accurately determining the morphology, size, and agglomeration of the Co-MOF-74 material. Most of the morphological shapes of the Co-MOF-74 material are spherical and hexagonal. This research is useful to produce the best Co-MOF-74 material design for future research through structural characterization information using SEM.

Keyword: SEM, Co-MOF-74, structure characterization, SLR

* Corresponding Author's Email: nandiyanto@upi.edu.

In: Advances in Materials Science Research. Volume 65
Editor: Maryann C. Wythers
ISBN: 979-8-89113-090-6

Introduction

Metal-Organic Framework (MOF) is a unique crystalline material made of a metal center and organic ligands. MOF is one of the popular subjects that has been well-studied and reviewed (Nandiyanto, 2019; Shidiq, 2023; Nordin et al., 2018). MOF also has a distinctive crystal structure, a large surface area, and varied catalytic activity, so it has been widely used as a heterogeneous catalyst (Huang et al., 2018; Zhao et al., 2014; Zhou et al., 2019). MOF can be separated easily and reused in catalytic reactions because of its polymeric nature and organic-inorganic hybrid arrangement in its structure (Sun et al., 2017). In addition, the morphology, size, and surface of MOF crystals have a significant impact on their catalytic properties and applications (Khan & Shahid, 2022). MOF crystal size and morphology have been controlled by various techniques to date, including composition tuning, process parameter management, and coordination modulation which have succeeded in producing unique structures with attractive features (Dang et al., 2017; Li et al., 2018). However, until now the synthesis of MOF with simple techniques has been very difficult because of the varied MOF structures and other factors that influence them.

MOF-74 is a type of MOF material that contains 2,5-dihydroxytereph-thalic acid as an organic ligand and various transition metals as nodes. This material has been widely used as a heterogeneous catalyst because of its large surface area, stable structure, and many unsaturated metal sites (Ruano et al., 2015). Several experiments have been carried out before to make MOF-74, for example, MOF-74 which is shaped like a flower, has the highest ability as a catalyst (Zhang et al., 2022).

The Co(II) ion in Co-MOF-74, also called CPO-27-Co, is linked together by a 2,5-dioxido-1,4-benzenedcarboxylate linker (Co2(dobdc)) (Dietzel et al., 2005). According to the absorption test using in-situ IR microscopy detection, the crystal structure (trigonal space group 148, R-3) is characterized by linear micropores (1.1 nm) with a hexagonal cross-section parallel to the c axis of the crystal (Chmelik et al., 2014). The Co(II) ion is penta-coordinated by the linker, and its sixth coordination site (usually controlled by a water molecule) is exposed to the interior of the pore channel. Concerning host-guest interactions, Co-MOF-74 is a very interesting system because of its structural characteristics, which include catalysis (Valvekens et al., 2014), gas adsorption (Dietzel et al., 2009; Strauss et al., 2018), and gas sensing (Strauss et al., 2019). The channel also allows for water-mediated proton conduction (Hwang et al., 2018).

Electron microscopy (EM) is a technique that can be used to characterize the structural properties of Co-MOF-74, such as Scanning Electron Microscope (SEM). SEM is a tool used to analyze the morphological characteristics and ultrastructural analysis of various materials (Klang et al., 2012). In EM, the interaction of a material with an electron beam produces an electron micrograph, which is then converted to an image. Many variables, such as the energy of electrons, the density of the material, the atomic number of the element, and the topography of the material's surface, can affect this interaction. Various forms of electrons, such as secondary electrons and backscattered electrons, are usually generated by the interaction of electrons in the atoms of the material, which can be elastic or non-elastic. Scattering of the electron beam over the surface of the sample will cause SEM to create an image of the surface (Suga et al., 2014).

Several scientists have characterized the structure of Co-MOF-74 using different types of SEM tools. Co-MOF-74 with a hexagonal spherical morphology and crystal sizes reaching micrometers has attracted the attention of researchers recently (Gong et al., 2020; Javed et al., 2020; Jodłowski et al., 2020; Strauss et al., 2018). The researchers varied the temperature conditions to activate the Co-MOF-74 crystals (Liang et al., 2021) or the solvent mix when synthesizing these crystals (C. Huang et al., 2020). These findings will be discussed further in this article.

Unfortunately, more thorough data collection has not been carried out regarding the determination of the Co-MOF-74 structure using SEM instrumentation. The systematic literature review (SLR) of several articles will be used further to explain the structure determination of Co-MOF-74 using SEM in this chapter. This discussion will provide an in-depth analysis of the establishment of the Co-MOF-74 structure over the previous five years.

Literature Review

Co-MOF-74

The Co(II) ion in Co-MOF-74, also called CPO-27-Co, is linked together by the 2,5-dioxido-1,4-benzenedcarboxylate linker (Co2(dobdc)) shown in Figure 1 (Dietzel et al., 2005). According to the absorption test using in-situ IR microscopy detection, the crystal structure (trigonal space group 148, R-3) is characterized by linear micropores (1.1 nm) with a hexagonal cross-section parallel to the c axis of the crystal (Chmelik et al., 2014). The Co(II) ion is

penta-coordinated by the linker, and its sixth coordination site (usually controlled by a water molecule) is exposed to the interior of the pore channel.

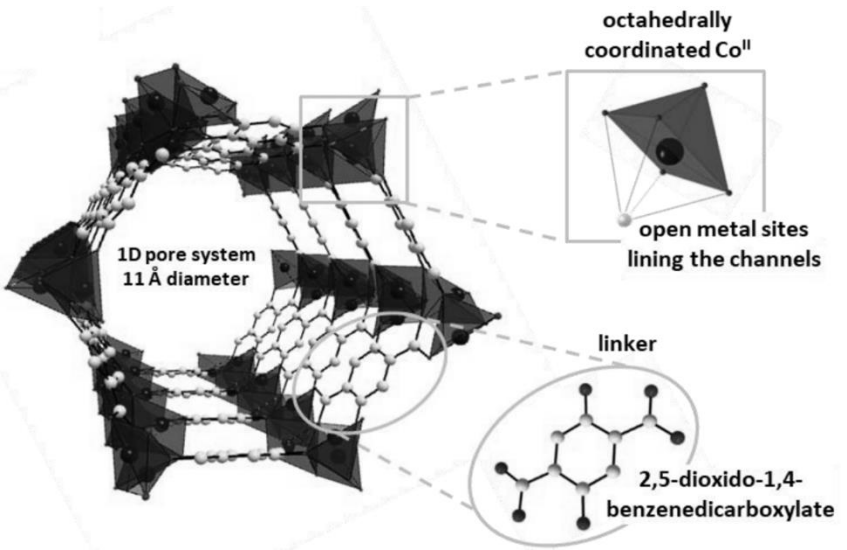

Figure 1. The crystal structure of Co-MOF-74, Co(II) is octahedrally coordinated with exposed metal sites lining the inside of the pore, and the organic linker 2,5-dioxido-1,4-benzenedcarboxylate (Figure adapted from (Strauss et al., 2018).

SEM (Scanning Electron Microscopy)

In general, there are two types of microscopes: optical microscopes and electron microscopes, or what is commonly called a Scanning Electron Microscope (SEM). Optical microscopes have been invented in the last two centuries. However, SEM has different characteristics and features from OM (Abdullah & Mohammed, 2019), which are described in Table 1.

The concept of SEM dates to the thirteenth century, when the electron microscope was first introduced in 1933 by two physicists named Ruska and Knoll. The equipment is called a Transmitted-Electron Microscope (TEM) with a magnification that is greater than an optical microscope (Savage et al., 2018). In 1938, Von Ardenne added a scanning coil to TEM resulting in a new system, namely the Scanning Transmission Electron Microscope (STEM) with a voltage of (23 kV) at a magnification (8000x) and a resolution (50-100 nm). Since then, the system has been called the SEM system (Goldstein et al.,

2003). Zworykin, Hillier, and Snyder presented a description of the new SEM system in 1942. At this stage, the three scientists used the role of secondary electron emission to create topographical contrasts that were easy to identify (Taha et al., 2022).

Table 1. The difference between OM and SEM

	OM	SEM
Working Principle	Light	Electron Emission
Number of Lenses	One lens	Two magnetic lenses
Lens magnification	400 – 1000x	300.000x
Objects	In the form of living cells or inanimate matter (color adjusts the object)	In the form of dead material only (object color is black and white)
Cost Analysis	Affordable Relatively	Expensive Relatively

In 1952, Oatley, Smith, and McMullan developed an electrostatic SEM lens using a voltage (40 kV) that produced a two-dimensional scanning system. O. Wells also devised a new stereoscopic pair in 1953 to examine the third dimension in micrographs. Pease also built the SEM V system using three magnetic lenses in 1963. After that, the SEM system continued to be developed and recorded in history until it reached a commercially usable state in 1968 (Goldstein et al., 2003). During 1991-1993, Danilatos researched the effect of the environment on the specimens studied. The latest evolution of SEM is to digitally produce images that are displayed on the computers used today.

SEM is a versatile, sophisticated instrument that is usually used to observe material surface phenomena. The sample is shot with high-energy electrons, and the ejected electrons are analyzed. The results can be obtained in the form of information about the topography, morphology, composition, orientation, crystallography, etc., of a material. SEM is considered a leading tool capable of achieving high-quality images of material even at a 1 nm scale (Ahmed & Jackson, 2014).

The SEM source will generate electrons that pass through the anode. The source will be focused by a series of magnetic lenses on a nano-sized spot, as shown in Figure 2a. The interaction of the beam with the sample surface is shown in Figure 2b to produce secondary electrons, back-scattered electrons, Auger electrons, x-rays, and heat. The small diameter raster beam allows full capture of electrons on the sample surface. Secondary electrons are low-energy electrons that are ejected from the sample by inelastic scattering of

high-energy electrons. These low-energy electrons are located close to the sample (nanometers), which allows it to produce an image of the sample surface morphology, which will be captured by the detector. The resulting interaction will release photons that will be directed to the photomultiplier tube device. In this way, a 2D distribution of electrons is created that matches the morphology of the sample. Meanwhile, backscattered electrons will produce crystallographic images through the projection of Kikuchi lines (, 2012).

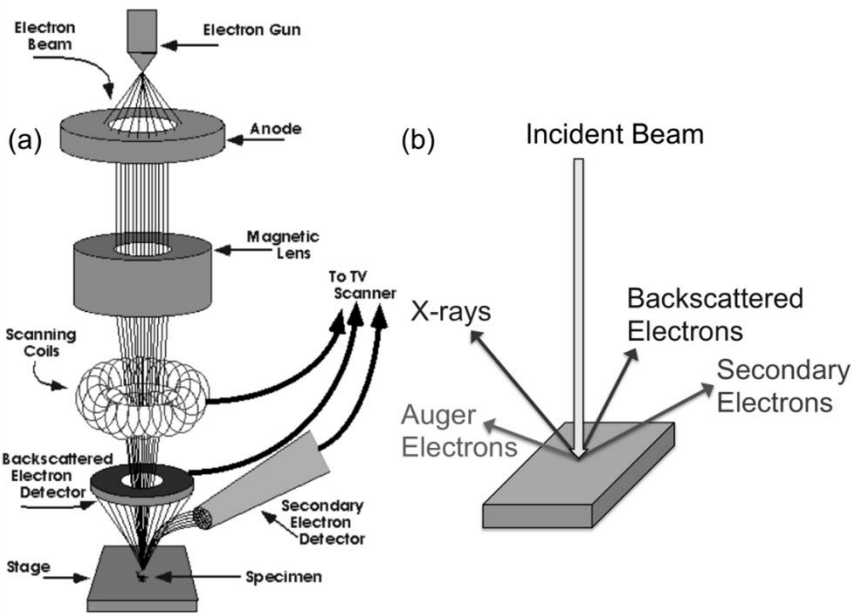

Figure 2. SEM tool scheme (a) and sample-beam interaction in SEM (b) (Walock, 2012).

Method

The characterization of the structure of Co-MOF-74 using SEM in this study is reviewed through the Systematic Literature Review (SLR) method. The SLR method is a method that critically identifies and assesses relevant research. This method will collect and analyze data from these studies. The goal of the SLR is to identify all empirical evidence that fits the relevant criteria of an article that has been predetermined to answer a particular

research question or hypothesis. By using an explicit and systematic method when reviewing articles and all available evidence, bias can be minimized, thereby providing reliable findings for making conclusions and decisions (Lame, 2019).

Reviews of this journal article were searched using the Google Scholar page using several keywords such as SEM, Co-MOF, characterization, and electron microscopy. Articles that have been found have several requirements to be used in this review article, which are described as follows:

1. Articles must contain information about pure Co-MOF-74 without any dopants or other composites.
2. The article must display the results of SEM images and analysis of the Co-MOF material.
3. Articles must contain information regarding the structure and morphology of the Co-MOF.

Articles that meet the standards will be selected and displayed in Table 2. The quality of the journal is generated by publishers based on the Scimago Journal Rank (SJR).

Results and Discussion

In this section, the state-of-the-art for SEM is presented, which is used to characterize the structure of Co-MOF-74. Table 3 displays and summarizes some of the SEM parameters used in the characterization of Co-MOF-74.

Huang et al., (2020) characterized the morphology of Co-MOF-74, which was synthesized using the solvothermal method with several modifications. He made six modifications to the Co-MOF-74 crystal that had been synthesized using DMF solvent added to water. The six types of modifications of Co-MOF-74 have different percentages of water in the DMF solvent. Figure 3a is a Co-MOF-74 crystal that is inserted into the DMF solvent alone without the addition of water. The resulting low crystallinity and aggregate form spherical crystals. The particle size of these crystals is close to 170 µm. Figure 3b shows the addition of water to the DMF solvent as much as 10 vol% which produces a different crystal morphology than before. The resulting crystals change shape like a flower and the crystallinity becomes longer and thinner. Meanwhile, the crystal size decreased to 150µm.

Table 2. List of article selection results

No.	Year	Title	Publisher's Journal	Quality	Reference
1.	2020	Controllable synthesis of Co-MOF-74 catalysts and their application in catalytic oxidation of toluene	Journal of Solid-State Chemistry	Q2	(Huang et al., 2020)
2.	2020	Humidity-Mediated Anisotropic Proton Conductivity through the 1D Channels of Co-MOF-74	MDPI Nanomaterials	Q1	(Javed et al., 2020)
3.	2021	The activation of Co-MOF-74 with open metal sites and their corresponding CO/N2 adsorptive separation performance	Microporous and Mesoporous Materials, Elsevier	Q1	(Liang et al., 2021)
4.	2018	On the interaction of guest molecules with Co-MOF-74: A Vis/NIR and Raman approach	Angewandte Chemie International Edition	Q1	(Strauss et al., 2018)
5.	2020	*In situ deposition* of M(M=Zn; Ni; Co)-MOF-74 over structured carriers for cyclohexene oxidation - Spectroscopic and microscopic characterisation	Microporous and Mesoporous Materials, Elsevier	Q1	(Jodłowski et al., 2020)
6.	2020	High-performance supercapacitor based on MOF derived porous NiCo2O4 nanoparticle	Science China Technological Science	Q1	(Gong et al., 2020)

Table 3. Summary of structural characterization of Co-MOF-74 using SEM

SEM Model	Condition	Parameter	Co-MOF-74 Morphology	Co-MOF-74 Particle Size	References
Hitachi S-3400N II	30 kV, vacuum	Morphologies and sizes distribution from different solvent	Hexagonal Spherical	(a): 170 µm (b): 150 µm (c) & (d): 70-150 µm (e): 150 µm (f): 20 µm	(Huang et al., 2020)
JEOL JSM-6700F NT	2 kV, 10 µA	Morphologies and sizes	Hexagonal Spherical	Length: 550µm, width: 100 µm	(Javed et al., 2020)
TM3000	vacuum	Morphologies in different temperature	Hexagonal Spherical	-	(Liang et al., 2021)
-	-	Morphologies and sizes	Hexagonal Spherical	Long axis: 100-200µm Short axis: 20 µm	(Strauss et al., 2018)
Nova Nano SEM 300 FEI	-	Morphologies and sizes	Hexagonal Spherical	< 20µm	(Jodłowski et al., 2020)
SUPRA-55 SAPHIRE	-	Morphologies	Hexagonal Spherical	Length: 5-b µm Width: 1,3 µm	(Gong et al., 2020)

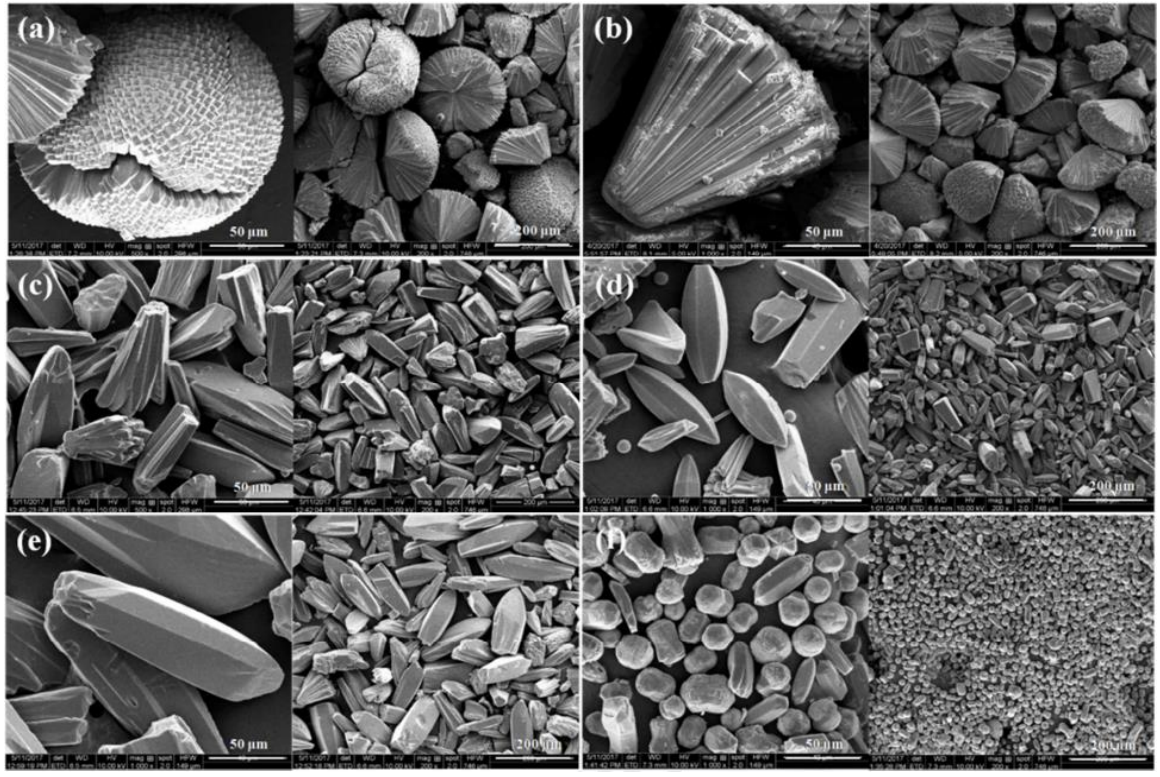

Figure 3. SEM results of Co-MOF-74 synthesized through different ratios of water-solvent mixtures in DMF. (a) 0 vol%, (b) 10 vol%, (c) 20 vol%, (d) 30 col%, (e) 50 vol%, (f) 60 vol% (Image adapted from (C. Huang et al., 2020)).

Furthermore, Figure 3c shows the addition of 20 vol% water to the DMF solvent. The flower-like crystal length decreased to in the range of 70-150 µm. However, the degree of aggregation decreases, and the size of the crystallites increases with an increasing proportion of water in the solvent. The shape of the crystals will change very clearly when the water content is increased at 30 and 50 vol% periodically, as shown in Figures 3d and 3e. In some cases, the crystals that aggregated originally turned into scattered crystals with a spindle shape, and the size of the crystals increased as the portion of water added increased as well. However, the morphology and size of the crystals changed again when the water content reached 60 vol%, and most of the particles became single spherical crystals with an average size of 20 µm (Fig. 3f). It can be seen that the DMF:H2O solvent has an important role in the formation of morphology and crystal size.

The crystal size and morphology of Co-MOF-74 have also been characterized by Javed et al., (2020) as shown in Figure 4. In this study, Co-MOF-74 crystals were prepared using the precipitation method. In this study, Co-MOF-74 crystals were dissolved using a DMF:H2O:EtOH solvent mixture with a ratio of 1:1:1. SEM results produce spherical single crystals. The crystalline particle size is about 550 µm long and about 100 µm wide.

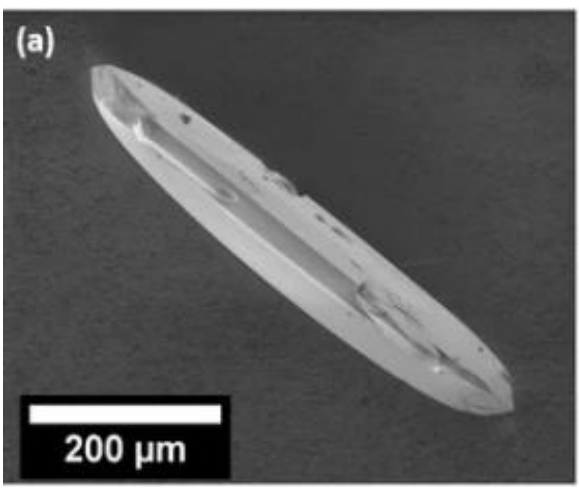

Figure 4. SEM results of Co-MOF-74 crystals (Image adapted from (Javed et al., 2020)).

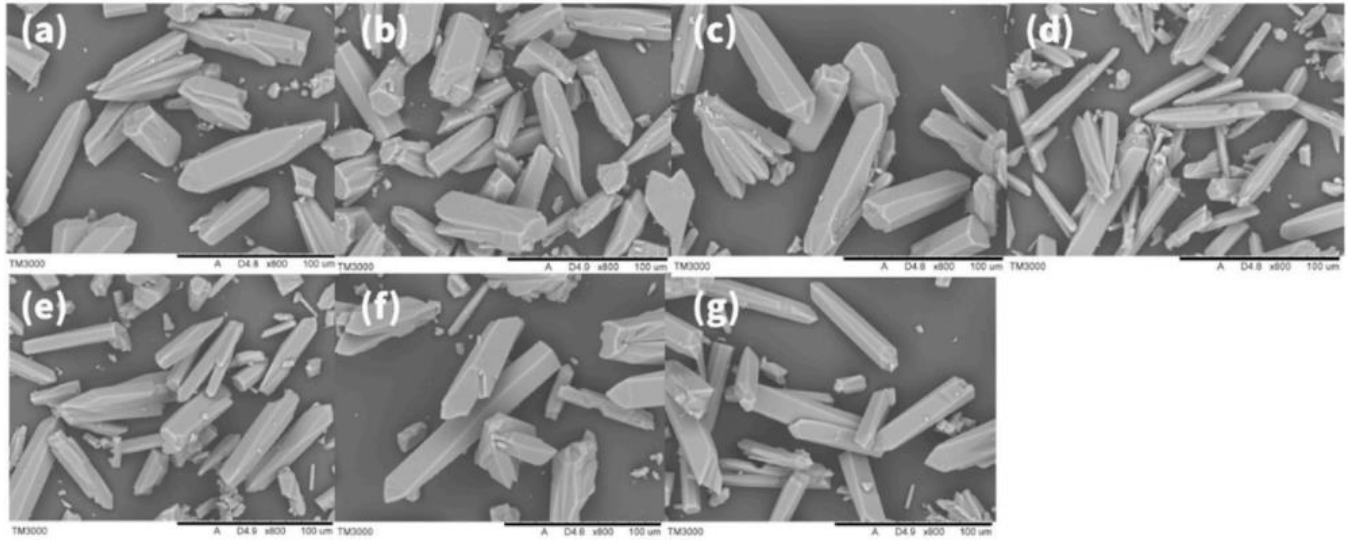

Figure 5. SEM results of Co-MOF-74 samples under different conditions (a) synthesized, activated at (b) 50, (c) 100, (d) 150, (e) 200, (f) 250, (g)) 300°C under vacuum conditions (Figure adapted from (Liang et al., 2021)).

Liang et al., (2021) have characterized Co-MOF-74 samples under different temperature conditions. In this study, Co-MOF-74 crystals underwent several modifications by being activated at different temperatures. Figure 5 shows the SEM images obtained from the synthesis results. From the seven images, the resulting crystals are relatively uniform, which shows that the crystals are very stable even when given different conditions. In addition, the thermal stability of Co-MOF-74 is also carried out in free air. Co-MOF exhibits relatively strong stability up to 150°C (Figure 5a–5d).

The SEM results of the Co-MOF-74 crystal showing pores schematically are shown in Figure 6 (Strauss et al., 2018). According to previous studies, this Co-MOF-74 crystal will have a one-dimensional pore structure with a pore size of around 1.1-1.2 nm which is shaped like a honeycomb. The results show the presence of Co-MOF-74 crystals in various hexagonal spherical rods measuring 100-200 μm (length) and 20 μm (width) which are presented in Figure 6a. Meanwhile, Figure 6b shows that the one-dimensional pores are parallel to the long axis of the Co-MOF-74 crystal, as described in previous IR microscopy studies (Chmelik et al., 2014; Dietzel et al., 2009).

Jodlowski et al., (2020) have succeeded in synthesizing and characterizing the crystal structure of Co-MOF-74. This study used a DMF:H2O solvent mixture of 20:1. The results show that the Co-MOF-74 crystals have a thickness lower than 20μm in every single crystal formed (Figure 7). This can be caused by the growth of MOF perpendicular to the surface of the support. Thus, the crystals tend to fill the free space between crystals rather than continuing the growth of crystals from existing crystals. The morphology of Co-MOF-74 forms a more regular hexagonal.

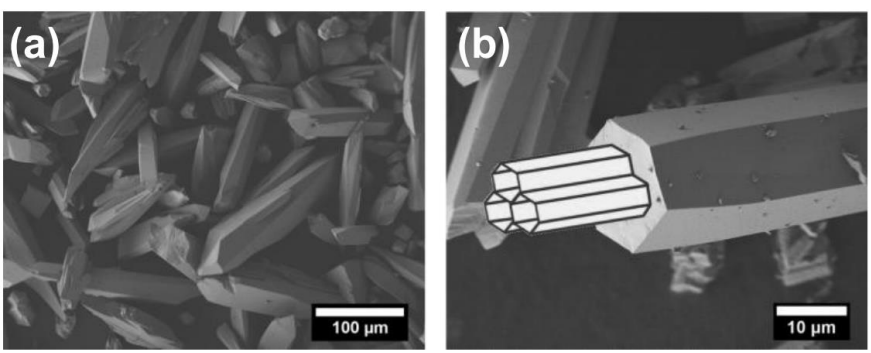

Figure 6. (a,b) SEM results of Co-MOF-74 crystals showing pores schematically (Image adapted from (Strauss et al., 2018)).

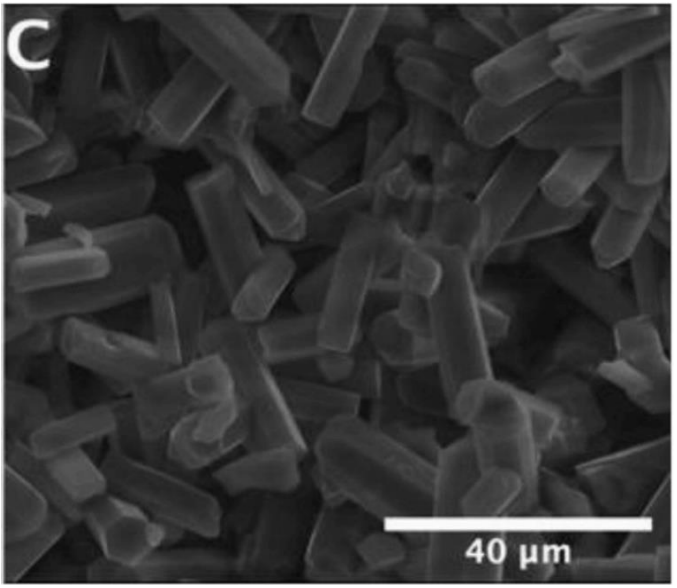

Figure 7. Co-MOF-74 SEM results at 2000x magnification (Image adapted from (Jodłowski et al., 2020)).

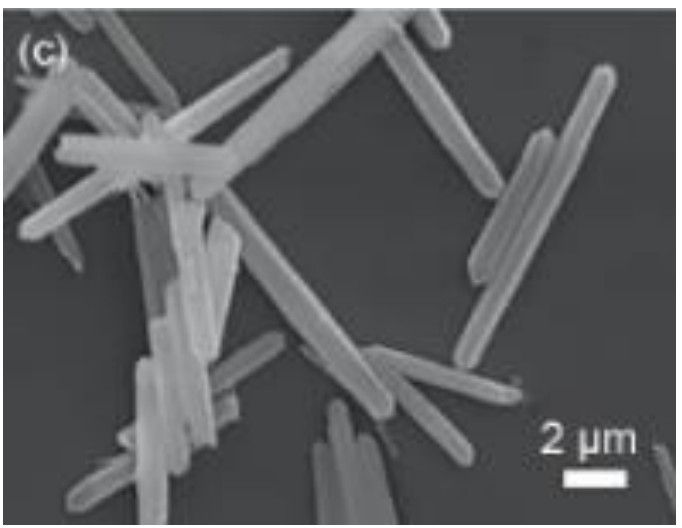

Figure 8. SEM results of Co-MOF-74 crystals (Image adapted from (Gong et al., 2020)).

Gong et al., (2020) successfully synthesized and characterized the crystal structure and morphology of Co-MOF-74 using SEM. They synthesized Co-MOF-74 crystals using a DMF:H2O:EtOH solvent mixture of 1:1:1, as previously done. When MOF-74 has been added by Co2+, the crystal morphology is in the form of a fine spherical spindle with a length of 900 nm and a width of 6-12 μm, as shown in Figure 8. When a Co atom binds to MOF-74, it will increase the length of the crystal and decrease the width of the crystal, which was considered a result consistent with previous studies (Chen et al., 2015; Grant Glover et al., 2011).

Conclusion

Based on the results of searches and investigations from researched literature studies, characterization of the Co-MOF structure using Scanning Electron Microscopy is considered effective and very useful in analyzing the structure and morphology of Co-MOF so that the design criteria for Co-MOF applications can be better designed. In this study, the structure and morphology of Co-MOF have a spherical and hexagonal shape. Meanwhile, the crystalline properties and crystal size of Co-MOF can be determined from the SEM photos that have been produced.

References

Abdullah, A., & Mohammed, A. (2019). Scanning Electron Microscopy (SEM): A Review. *Proceedings of 2018 International Conference on Hydraulics and Pneumatics - HERVEX, 2018*, 77–85.

Ahmed, W., & Jackson, M. J. (2014). Emerging nanotechnologies for manufacturing. In *Emerging Nanotechnologies for Manufacturing*. William Andrew. https://doi.org/10.1016/B978-0-323-28990-0.00018-X.

Chen, S., Xue, M., Li, Y., Pan, Y., Zhu, L., & Qiu, S. (2015). Rational design and synthesis of NixCo3-xO4 nanoparticles derived from multivariate MOF-74 for supercapacitors. *Journal of Materials Chemistry A*, *3*(40), 20145–20152. https://doi.org/10.1039/c5ta02557e.

Chmelik, C., Mundstock, A., Dietzel, P. D. C., & Caro, J. (2014). Idiosyncrasies of Co2(dhtp): In situ-annealing by methanol. *Microporous and Mesoporous Materials*, *183*, 117–123. https://doi.org/10.1016/j.micromeso.2013.09.002.

Dang, S., Zhu, Q. L., & Xu, Q. (2017). Nanomaterials derived from metal-organic frameworks. *Nature Reviews Materials*, *3*(1), 1–14. https://doi.org/10.1038/natrevmats.2017.75.

Dietzel, P. D. C., Besikiotis, V., & Blom, R. (2009). Application of metal-organic frameworks with coordinatively unsaturated metal sites in storage and separation of methane and carbon dioxide. *Journal of Materials Chemistry*, *19*(39), 7362–7370. https://doi.org/10.1039/b911242a.

Dietzel, P. D. C., Morita, Y., Blom, R., & Fjellvåg, H. (2005). An in situ high-temperature single-crystal investigation of a dehydrated metal-organic framework compound and field-induced magnetization of one-dimensional metal-oxygen chains. *Angewandte Chemie - International Edition*, *44*(39), 6354–6358. https://doi.org/10.1002/anie.200501508.

Goldstein, J. I., Newbury, D. E., Echlin, P., Joy, D. C., Lyman, C. E., Lifshin, E., Sawyer, L., & Michael, J. R. (2003). Special Topics in Scanning Electron Microscopy. *Scanning Electron Microscopy and X-Ray Microanalysis*, 195–270. https://doi.org/10.1007/978-1-4615-0215-9_5.

Gong, L. T., Xu, M., Ma, R. P., Han, Y. P., Xu, H. B., & Shi, G. (2020). High-performance supercapacitor based on MOF derived porous NiCo2O4 nanoparticle. *Science China Technological Sciences*, *63*(8), 1470–1477. https://doi.org/10.1007/s11431-020-1658-7.

Grant Glover, T., Peterson, G. W., Schindler, B. J., Britt, D., & Yaghi, O. (2011). MOF-74 building unit has a direct impact on toxic gas adsorption. *Chemical Engineering Science*, *66*(2), 163–170. https://doi.org/10.1016/j.ces.2010.10.002.

Huang, C., Gu, X., Su, X., Xu, Z., Liu, R., & Zhu, H. (2020). Controllable synthesis of Co-MOF-74 catalysts and their application in catalytic oxidation of toluene. *Journal of Solid State Chemistry*, *289*, 121497. https://doi.org/10.1016/j.jssc.2020.121497.

Huang, D., Wu, X., Tian, J., Wang, X., Zhou, Z., & Li, D. (2018). Assembling of a novel 3D Ag(I)-MOFs with mixed ligands tactics: Syntheses, crystal structure and catalytic degradation of nitrophenol. *Chinese Chemical Letters*, *29*(6), 845–848. https://doi.org/10.1016/j.cclet.2017.09.043.

Hwang, S., Lee, E. J., Song, D., & Jeong, N. C. (2018). High Proton Mobility with High Directionality in Isolated Channels of MOF-74. *ACS Applied Materials and Interfaces*, *10*(41), 35354–35660. https://doi.org/10.1021/acsami.8b11816.

Javed, A., Strauss, I., Bunzen, H., Caro, J., & Tiemann, M. (2020). Humidity-mediated anisotropic proton conductivity through the 1d channels of co-mof-74. *Nanomaterials*, *10*(7), 1–9. https://doi.org/10.3390/nano10071263.

Jodłowski, P. J., Kurowski, G., Dymek, K., Jędrzejczyk, R. J., Jeleń, P., Kuterasiński, Gancarczyk, A., Węgrzynowicz, A., Sawoszczuk, T., & Sitarz, M. (2020). In situ deposition of M(M=Zn; Ni; Co)-MOF-74 over structured carriers for cyclohexene oxidation - Spectroscopic and microscopic characterisation. *Microporous and Mesoporous Materials*, *303*, 110249. https://doi.org/10.1016/j.micromeso.2020.110249.

Khan, M. S., & Shahid, M. (2022). Synthesis of metal-organic frameworks (MOFs): Routes to various MOF topologies, morphologies, and composites. In *Electrochemical Applications of Metal-Organic Frameworks: Advances and Future Potential* (pp. 17–35). Elsevier. https://doi.org/10.1016/B978-0-323-90784-2.00007-1.

Klang, V., Matsko, N. B., Valenta, C., & Hofer, F. (2012). Electron microscopy of nanoemulsions: An essential tool for characterisation and stability assessment. *Micron*, *43*(2–3), 85–103. https://doi.org/10.1016/j.micron.2011.07.014.

Lame, G. (2019). Systematic literature reviews: An introduction. *Proceedings of the International Conference on Engineering Design, ICED*, *2019-August*(1), 1633–1642. https://doi.org/10.1017/dsi.2019.169.

Li, X., Zhang, J., Han, Y., Zhu, M., Shang, S., & Li, W. (2018). MOF-derived various morphologies of N-doped carbon composites for acetylene hydrochlorination. *Journal of Materials Science*, *53*(7), 4913–4926. https://doi.org/10.1007/s10853-017-1951-3.

Liang, X., Wang, P., Li, C., Yuan, M., Shi, Q., & Dong, J. (2021). The activation of Co-MOF-74 with open metal sites and their corresponding CO/N2 adsorptive separation performance. *Microporous and Mesoporous Materials*, *320*, 111109. https://doi.org/10.1016/j.micromeso.2021.111109.

Nandiyanto, A.B.D. (2019). Nano metal-organic framework particles (ie MIL-100 (Fe), HKUST-1 (Cu), Cu-TPA, and MOF-5 (Zn)) using a solvothermal process. *Indonesian Journal of Science and Technology*, *4*(2), 220-228. https://doi.org/10.17509/ijost.v4i2.18178

Nordin, N.A.H.M., Ismail, A.F., Racha, S.M., Cheer, N.B., Bilad, M.R., Putra, Z.A., and Wirzal, M.D.H. (2018). Limitation in fabricating PSf/ZIF-8 hollow fiber membrane for CO2/CH4 Separation. *Indonesian Journal of Science and Technology*, *3*(2), 138-149. https://doi.org/10.17509/ijost.v3i2.12757

Ruano, D., Díaz-García, M., Alfayate, A., & Sánchez-Sánchez, M. (2015). Nanocrystalline M-MOF-74 as heterogeneous catalysts in the oxidation of cyclohexene: Correlation of the activity and redox potential. *ChemCatChem*, *7*(4), 674–681. https://doi.org/10.1002/cctc.201402927.

Savage, J. C., Picard, K., González-Ibáñez, F., & Tremblay, M. É. (2018). A brief history of microglial ultrastructure: Distinctive features, phenotypes, and functions discovered over the past 60 years by electron microscopy. *Frontiers in Immunology*, *9*(APR), 803. https://doi.org/10.3389/fimmu.2018.00803.

Shidiq, A.P.A. (2023). Bibliometric analysis of nano metal-organic frameworks synthesis research in medical science using VOSviewer. *ASEAN Journal of Science and Engineering*, *3*(1), 31-38. https://doi.org/10.17509/ajse.v3i1.43345

Strauss, I., Mundstock, A., Hinrichs, D., Himstedt, R., Knebel, A., Reinhardt, C., Dorfs, D., & Caro, J. (2018). The Interaction of Guest Molecules with Co-MOF-74: A Vis/NIR and Raman Approach. *Angewandte Chemie - International Edition*, *57*(25), 7434–7439. https://doi.org/10.1002/anie.201801966.

Strauss, I., Mundstock, A., Treger, M., Lange, K., Hwang, S., Chmelik, C., Rusch, P., Bigall, N. C., Pichler, T., Shiozawa, H., & Caro, J. (2019). Metal-Organic Framework Co-MOF-74-Based Host-Guest Composites for Resistive Gas Sensing. *ACS Applied Materials and Interfaces*, *11*(15), 14175–14181. https://doi.org/10.1021/acsami.8b22002.

Suga, M., Asahina, S., Sakuda, Y., Kazumori, H., Nishiyama, H., Nokuo, T., Alfredsson, V., Kjellman, T., Stevens, S. M., Cho, H. S., Cho, M., Han, L., Che, S., Anderson, M. W., Schüth, F., Deng, H., Yaghi, O. M., Liu, Z., Jeong, H. Y., Stein, A., Sakamoto, K., Ryoo, R., Terasaki, O. (2014). Recent progress in scanning electron microscopy

for the characterization of fine structural details of nano materials. *Progress in Solid State Chemistry*, *42*(1–2), 1–21. https://doi.org/10.1016/j.progsolidstchem.2014.02.001.

Sun, Q., Liu, M., Li, K., Han, Y., Zuo, Y., Chai, F., Song, C., Zhang, G., & Guo, X. (2017). Synthesis of Fe/M (M = Mn, Co, Ni) bimetallic metal organic frameworks and their catalytic activity for phenol degradation under mild conditions. *Inorganic Chemistry Frontiers*, *4*(1), 144–153. https://doi.org/10.1039/c6qi00441e.

Taha, J. H., Electron, S., Electrons, S., Lens, C., & Obaid, S. A. (2022). Review of Scanning Transmission of High Voltage Electron Microscope. *Eurasian Journal of Physics, Chemistry and Mathematics*, *13*(December), 20–27.

Valvekens, P., Vandichel, M., Waroquier, M., Van Speybroeck, V., & De Vos, D. (2014). Metal-dioxidoterephthalate MOFs of the MOF-74 type: Microporous basic catalysts with well-defined active sites. *Journal of Catalysis*, *317*, 1–10. https://doi.org/10.1016/j.jcat.2014.06.006.

Walock, M. (2012). Nanocomposite coatings based on quaternary metalnitrogen. In *University of Alabama at Birmingham* (p. 189). Paris, ENSAM.

Zhang, X., Pan, H., Jia, Y., Zhang, Y., Jiang, Z., Li, C., Li, X., Bao, L., Ma, R., & Wang, K. (2022). Flower-like MOF-74 nanocomposites directed by selenylation towards high-efficient oxygen evolution. *Journal of Colloid and Interface Science*, *623*, 552–560. https://doi.org/10.1016/j.jcis.2022.04.181.

Zhao, M., Ou, S., & Wu, C. De. (2014). Porous metal-organic frameworks for heterogeneous biomimetic catalysis. *Accounts of Chemical Research*, *47*(4), 1199–1207. https://doi.org/10.1021/ar400265x.

Zhou, W., Huang, D. D., Wu, Y. P., Zhao, J., Wu, T., Zhang, J., Li, D. S., Sun, C., Feng, P., & Bu, X. (2019). Stable Hierarchical Bimetal–Organic Nanostructures as HighPerformance Electrocatalysts for the Oxygen Evolution Reaction. *Angewandte Chemie - International Edition*, *58*(13), 4227–4231. https://doi.org/10.1002/anie.201813634.

Chapter 6

The Thermal Characterization of Pure and Modified Co-MOF-74 (Mn, TTF, NDHPI, and Ni) Using a Thermogravimetric Analysis (TGA)

Gabriela Chelvina Santiuly Girsang and Asep Bayu Dani Nandiyanto*

Departemen Pendidikan Kimia, Universitas Pendidikan, Jawa Barat, Indonesia

Abstract

This chapter aimed to provide an in-depth explanation of the thermal characterization of pure and modified Co-MOF-74 materials (Mn, TTF, NDHPI, and Ni) using Thermogravimetric Analysis (TGA). The analysis was carried out using Systematic Literature Study (SLR) method with six Q1-Q2 journal articles that are relevant to the topic. According to the study's findings, TGA is highly useful for examining the thermal characteristic profile of both pure and modified Co-MOF-74. The presence and quantity of additional materials inserted into the MOF framework can be determined via TGA. TGA analysis is highly helpful for figuring out the temperatures at which materials' constituent parts degrade as well as researching thermal phenomena including solvent evaporation, the breakdown of MOF or ligand structures, and metal oxides formation. In general, the mass reduction in the resulting TGA Co-MOF-74 occurs in two stages: solvent evaporation and decomposition of the MOF/ligand structure. The atmospheric circumstances employed in the TGA analysis, such as the atmospheric

* Corresponding Author's Email: nandiyanto@upi.edu.

In: Advances in Materials Science Research. Volume 65
Editor: Maryann C. Wythers
ISBN: 979-8-89113-090-6

conditions of N_2 and air, have an impact on the TGA profile as well. The findings of this study are anticipated to serve as a basis for information in the development of modified Co-MOF-74.

Keywords: Co-MOF-74, pure, modified, thermal characterization, TGA

Introduction

Metal-organic frameworks (MOFs) are materials with a wide range of applications ranging from separation, storage, catalysts, adsorbents, and electrode materials. MOF is one of the popular subjects that has been well-studied and reviewed (Nandiyanto, 2019; Shidiq, 2023; Nordin et al., 2018). One of the MOF derivatives, namely MOF-74, is a material with a honeycomb structure with a pore size of about 1.2 nm which is formed by a combination of divalent ions and 2,5-dihydroxyterephthalic acid (Xie et al., 2020a). This chapter specifically discusses MOF-74 which is synthesized using the divalent Co ion (Co-MOF-74).

Several studies have shown promising applications of Co-MOF-74 for CO/CO_2 separation materials, solid phase extraction, gas detection, solvent-free aerobic oxidation, and supercapacitors (Evans et al., 2020; Mendiola-Alvarez et al., 2020; Pliekhov et al., 2018; Strauss et al., 2018; Xie et al., 2020b; Young et al., 2018). In fact, in some cases, organic and inorganic additive elements such as Mn, TTF, NDHPI, and Ni are added to the Co-MOF-74 network to improve the performance of the Co-MOF-74 material for certain functions. In each of these applications, the framework or network between MOF, Co, ligands, and additive elements is expected to be stable and difficult to decompose under extreme conditions such as high temperatures. Therefore, the thermal characterization of the Co-MOF-74 material is a crucial step in determining the scope of application of the Co-MOF-74 material.

The thermal characteristics of Co-MOF-74 can be analyzed using a Thermogravimetric Analysis instrument (TGA). TGA is a method of thermal analysis to determine mass degradation along with temperature variations (Ghodke et al., 2021). In TGA, the mass of the sample is measured over time with a uniform change in temperature. TGA can provide physical and chemical information about a material by evaluating changes in mass due to heat treatment. In modern chemical engineering, researchers apply TGA to obtain conversions, kinetics, and mechanisms for each process with changes in mass using isothermal, non-isothermal, and quasi-isothermal methods

(Saadatkhah et al., 2020). In TGA, the mass of the sample decreases as the sample decomposes, volatile compounds evaporate, or the oxidation state decreases. Meanwhile, in a reactive environment, such as an air environment (O_2), samples containing transition metals can experience an increase due to the reaction of metals with air (Coker et al., 2012).

Several studies have reported physical and chemical phenomena related to the thermal characteristics of Co-MOF-74, including solvent evaporation, oxide formation, decomposition of MOF structures, and decomposition of organic ligands (Evans et al., 2020; Strauss et al., 2018; Young et al., 2018). However, data collection for determining the thermal characteristics of Co-MOF-74 using the TGA method has not been carried out in a more comprehensive and in-depth manner. Therefore, in this chapter, the thermal characterization of modified Co-MOF-74 using TGA will be discussed further through Systematic Literature Studies (SLR) of several journal articles. This study contains a comprehensive and in-depth study of the thermal characterization of pure and modified Co-MOF-74 from 2018-2022 using 6 journal articles Q1-Q2.

Literature Review

Co-MOF-74

Co-MOF-74, also known as CPO-27-Co, is a MOF material with 5 oxygen atoms originating from the 2,5-dihydroxyterephthalic acid (H_4DOBDC) ligand in the coordination area of each Co^{2+} ion with the sixth coordination position occupied by a guest molecule (Dietzel et al., 2010; Strauss et al., 2018). Upon activation, the coordinated guest molecule disengages, so that the Co^{2+} central site has an open coordination position (Liang et al., 2021).

The structure and building blocks of Co-MOF-74 are shown in *Figure 1*. Each atom coordinates with 3 oxygen atoms from carboxylates and 2 oxygen atoms from hydroxyl groups (Xie et al., 2020b). Meanwhile, the sixth metal Co atom binds to a hydrogen peroxide molecule or a solvent molecule. Water and solvent molecules can be easily removed by heating and vacuum. This process opens the active site on Co-MOF-74. Thus, it is often referred to as the activation process. Generally, water and solvent removal treatments are carried out when Co-MOF-74 is to be used as a catalyst (Jiang et al., 2016).

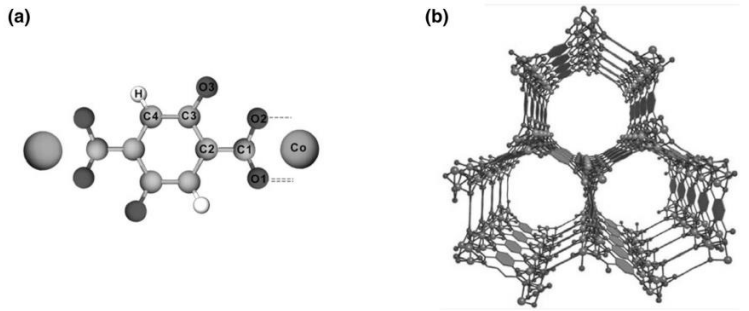

Figure 1. Building block (a) and framework structure (b) from Co-MOF-74. (Figure was adopted from Sladekova et al., 2021).

Thermogravimetric Analysis (TGA)

Thermogravimetric analysis (TGA) is an analytical technique used to determine the thermal stability of a material and its volatile component fractions by monitoring the weight change that occurs when the sample is heated at a constant rate (Rajisha et al., 2011). At TGA, samples can be analyzed at a constantly decreasing temperature or isothermal temperature.

TGA is a low-cost quantitative and qualitative analysis technique that requires a small sample. However, TGA is a destructive analysis (the sample cannot be reused after analysis) and the results of the analysis may be inaccurate due to the presence of volatile components in the sample (Mansfield et al., 2010). Common applications of TGA include (Nasrollahzadeh et al., 2019):

1) material characterization through analysis of decomposition characteristic patterns,
2) study of degradation mechanisms and reaction kinetics,
3) determination of the organic content in the sample,
4) determination of inorganic content in the sample,

which may be useful for corroborating material structure predictions or simply for chemical analysis.

Generally, TGA is used to study thermal (physical and chemical) phenomena such as absorption, adsorption, desorption, evaporation,

sublimation, decomposition, oxidation, and reduction (Loganathan, Valapa, et al., 2017). TGA can also be used to identify the presence of molecules that are present in very small amounts because the decreasing mass curve of the sample is very sensitive. Factors that can affect changes in mass in TGA analysis are (1) sample mass and volume, (2) sample form, (3) shape and nature of the sample container, (4) type of TGA analysis atmosphere, (5) atmospheric pressure at the chamber, and (6) heating and cooling rates.

Figure 2 shows the schematic diagram of the TGA instrument. The thermal balance is an important unit of the TGA instrument (*Figure 3;* Loganathan, Ravi, et al., 2017). The thermal balance is composed of an electronic microbalance, sample container, furnace, temperature programmer, and recorder. The thermal balance consists of clamps that serve to hold the arms of the microbalance. After the clamp is released, the balance will return to the zero position. To avoid zero offsets, the thermobalance cannot be moved while it is holding the microbalance arm. The thermal balance is usually left for 15-20 minutes after the sample is placed. In the TGA curve, the y-axis is the percentage of mass loss and the x-axis is the temperature (or time, and most of the time the direct heating rate) (Lozano-Peral et al., 2020).

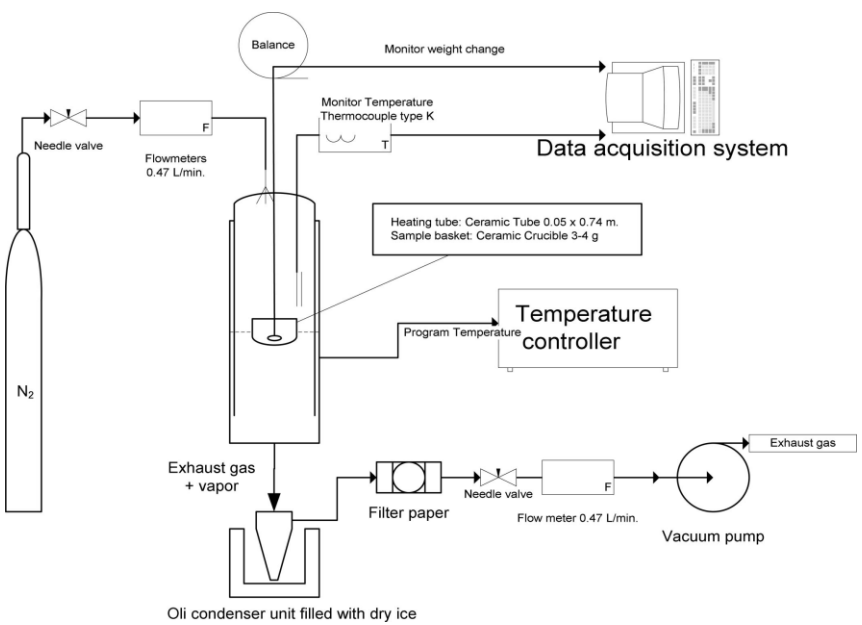

Figure 2. Schematic diagram of a TGA instrument (Figure was adopted from Unapumnuk et al., 2012).

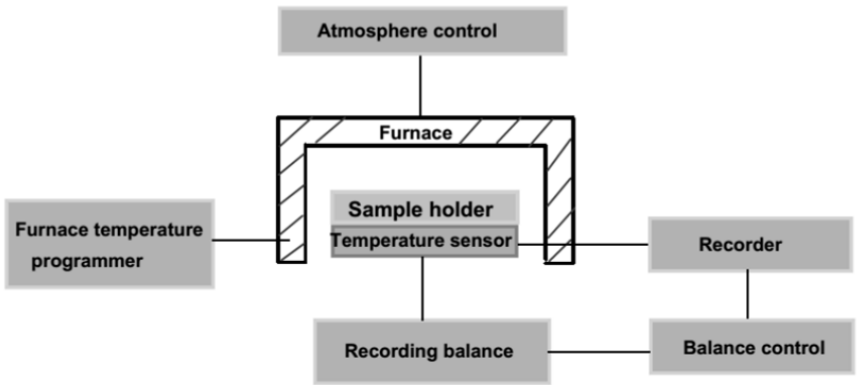

Figure 3. Schematic diagram of the thermobalance on the TGA unit (figure was adopted from Loganathan et al., 2017).

Method

In this study, the thermal characterization of pure and modified Co-MOF-74 using the TGA instrument was studied using the Systematic Literature Review (SLR) method. SLR is a research method for identifying and critically assessing relevant research and for collecting and analyzing data. SLR aims to identify all appropriate empirical evidence to test certain hypotheses and/or develop new theories. In addition, SLR can be used in evaluating the validity and quality of existing findings to reveal weaknesses, inconsistencies, and contradictions (Xiao & Watson, 2019). Detailed information for how to search documents for SLR is reported elsewhere (Azizah et al., 2021; Al Husaeni et al., 2022).

Journal articles analyzed in this study were searched using Google Scholar with publication years ranging from 2018 to 2022. The keywords used included Co-MOF-74, modification, materials, composite, and TGA. Articles are selected based on the relevance of the journal article title to the topic. The article must contain information on the thermal characterization of pure Co-MOF-74 or Co-MOF-74 modified by some additives. Six articles that met the criteria were selected and presented in *Table 1*.

Table 1. List of articles studied in this study

No	Publication Year	Title	TGA Profile	Product Applications	Journal Quality	Reference
1	2020	Optimisation of Cu+ impregnation of MOF-74 to improve CO/N_2 and CO/CO_2 separations	Pure Co-MOF-74	CO/N_2 and CO/CO_2 separations	Q1	(Evans et al., 2020)
2	2020	Magnetic porous carbons derived from cobalt (ii)-based metal–organic frameworks for the solid-phase extraction of sulfonamides	Pure Co-MOF-74	Solid phase extraction for sulfonamides	Q1	(Mendiola-Alvarez et al., 2020)
3	2019	MOF-74-M (M = Mn, Co, Ni, Zn, MnCo, MnNi, and MnZn) for Low-Temperature NH_3-SCR and In Situ DRIFTS Study Reaction Mechanism	Modified Co-MOF-74 with Mn	In situ reaction	Q1	(Xie et al., 2020b)
4	2019	Metal–Organic Framework Co-MOF-74-Based Host–7Guest Composites for Resistive Gas Sensing	Modified Co-MOF-74 with tetrahiafulvalene (TTF)	Gas detection	Q1	(Strauss et al., 2019)
5	2018	The Co-MOF-74 modified with N,N′Dihydroxypyromellitimide for selective, solvent free aerobic oxidation of toluene	Modified Co-MOF-74 with N,N′-Dihydroxypyromellitimide (NDHPI)	Free solvent aerobic oxidation for toluene	Q2	(Pliekhov et al., 2018)
6	2018	One-Step Synthetic Strategy of Hybrid Materials from Bimetallic Metal–Organic Frameworks for Supercapacitor Applications	Modified Co-MOF-74 with Ni	Supercapacitor	Q1	(Young et al., 2018)

Results and Discussion

TGA Profile of Pure Co-MOF-74

Evans et al. (2020) investigated the relationship between the temperature of reduction activation and the thermal decomposition of Co-MOF-74. The thermogravimetric analysis showed that the activation temperature and reduction temperature did not damage the structure of Co-MOF-74. The gravimetric curves show solvent release at < 350 °C, thermal decomposition at 350-400 °C, and solvent decomposition at ~550 °C (*Figure 4*).

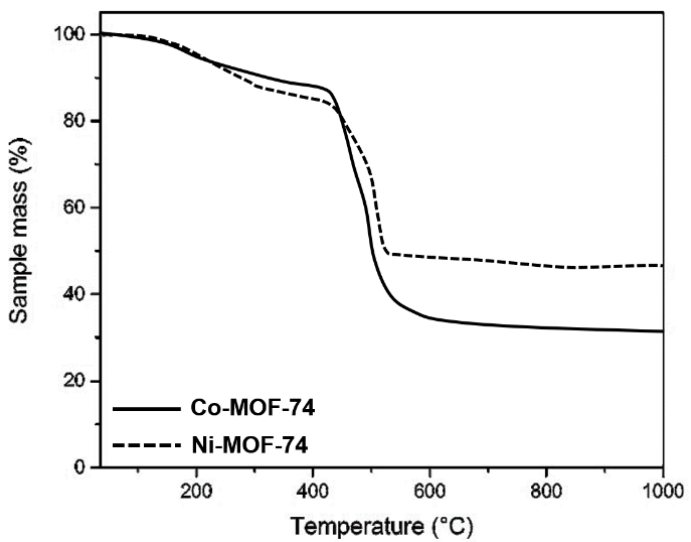

Figure 4. TG curves of Ni-MOF-74 and Co-MOF-74 under an N_2 atmosphere (Figure was adopted from Evans et al., 2020).

Mendiola-Alvarez et al. (2020) investigated the degradation of Co-MOF analyzed using TGA (*Figure 5*). The first stage of mass loss (< 200 °C) was caused by the removal of the solvent adsorbed on the sample. The disintegration of the MOF structure led to the second step of mass loss for Co-MOF-74 at about 300 °C. After a temperature of 800 °C, the mass of the sample is relatively stable.

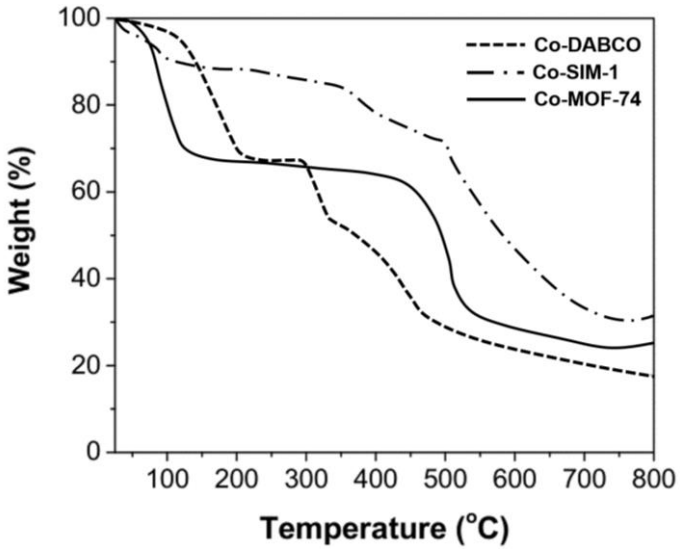

Figure 5. TGA curves of Co-SIM-1, Co-MOF-74, and Co-DABCO (Figure was adopted from Mendiola-Alvarez et al., 2020).

TGA Profile of Modified Co-MOF-74

Modification with Mn

To ensure the catalyst was not destroyed in the SCR reaction gas, thermogravimetric tests were carried out under atmospheric air conditions to determine the activation temperature and decomposition temperature of the catalyst. The mass reduction in the MOF-74-Co catalyst was more drastic compared to the mass reduction in the MOF-74 catalyst with a combination of Co and Mn (MOF-74-Mn-Co). Three stages of mass change were observed in the temperature range of 0-600 °C, with details as follows.

i. First stage: desorption of H_2O and CH_3OH at around 120 °C
ii. Second step: removal of DMF around 225 °C, except for sample MOF-74-Zn
iii. Third stage: collapse or damage to the MOF structure at around 275 °C, except for the MOF-74-Zn sample

Based on these data, the temperature selection in the second stage can be used to remove H_2O, CH_3OH, dan DMF in the activation stage. The selection

of the activation temperature is crucial for ensuring that the catalyst has been fully activated and that the structure of the catalyst has not been damaged.

In addition, the thermal stability of the samples under N_2 and air atmospheric conditions was also studied. The sample TGA curve under N_2 was comparable to that in an atmosphere of air. The main difference found is the mass drop temperature. The catalyst has better thermal stability in the N_2 atmosphere compared to the air atmosphere.

Modification with Tetrahiafulvalene (TTF)

Figure 6 shows the TGA of Co-MOF-74 and Co-MOF-74-TTF under the N_2 atmosphere. Results are normalized at 100 °C. The TGA of empty Co-MOF-74 (without TTF) at air conditions showed a mass reduction of 26.4% at 100 °C associated with adsorbed water. The Co-MOF-74-TTF sample has a lower water content compared to MOF without TTF (5.7% mass reduction). This also shows the success of TTF in filling MOF pores.

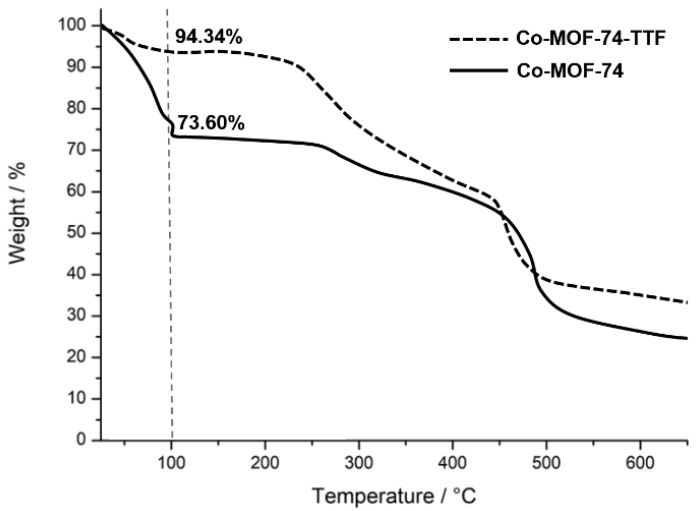

Figure 6. TG curves of Co-MOF-74 and Co-MOF-74-TTF (Figure was adopted from Strauss et al., 2018).

The TGA curve results from Co-MOF-74-TTF was in between the TGA results from Co-MOF-74 and pure TTF. Based on the TGA, the TTF that was successfully incorporated into the Co-MOF-74 network was approximately 16%wt.

Modification with N,N'-Dihydroxypyromellitimide (NDHPI)

Figure 7 compares the TGA profiles of the Co-MOF-74 and Co-MOF-74@NDHPI samples. The first mass loss (22%) at 30-150 °C was due to moisture loss. The second mass loss started at 250°C where the Co-MOF-74 structure was damaged and the organic linker underwent decomposition. Modification with NDHPI increased the maximum decomposition temperature of the ligand from 290 °C to 315 °C. This is because NDHPI has a high decomposition temperature of 320 °C. The TGA results show that the number of NDHPIs that have successfully entered the Co-MOF-74 network is 5%.

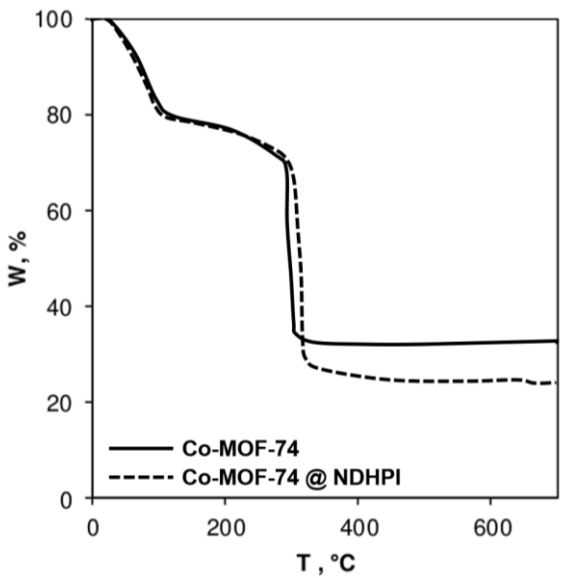

Figure 7. TGA curves of Co-MOF-74 and Co-MOF-74@NDHPI (Figure was adopted from Pliekhov et al., 2018).

Modification with Ni

The thermal decomposition of NiCo-MOF-74 and Co-MOF-74 was studied using TGA in N_2 atmosphere and air as shown in *Figure 8.* In the N_2 atmosphere, the TGA profiles of NiCo-MOF-74 and Co-MOF-74 showed a decrease in mass through two stages.

i. The first stage (25-200 °C) indicates evaporation of the solvent.
ii. The second stage (280-500 °C) shows the decomposition of MOF-74.

The curves are further shown to be stable after 800 °C, indicating no loss of mass due to decomposition or phase transformation.

In the air atmosphere, mass loss also takes place in two stages. The first stage occurred due to solvent evaporation. The second step at 200-350 °C can be associated with the decomposition of the network/framework to form metal oxides. Based on the TGA results, NiCo-MOF-74 and Co-MOF-74 can be heated at 800 °C under atmospheric N_2 conditions to obtain hybrid materials.

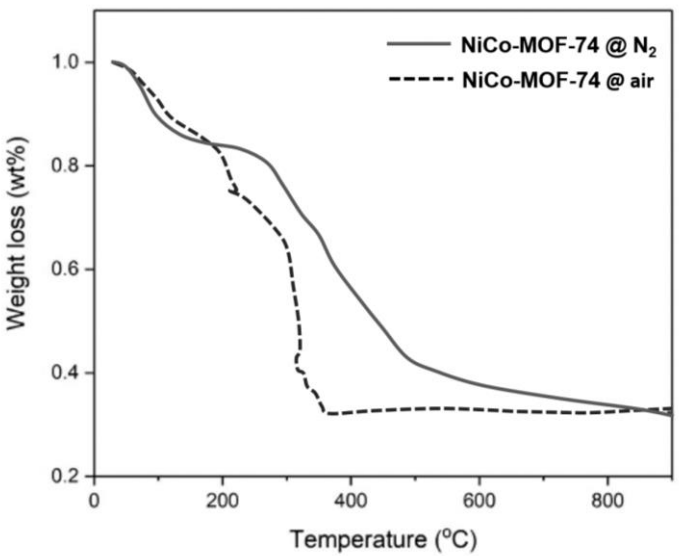

Figure 8. NiCo-MOF-74 TGA curve under N_2 and air atmospheric conditions (Figure was adopted from Young et al., 2018).

Based on the literature that has been described, *Table 2* shows a summary of the TGA profile findings summary of pure and modified Co-MOF-74. Atmospheric conditions such as N_2 and air can affect the results of the TGA profile of Co-MOF-74. In addition, the additive material in the Co-MOF-74 matrix can affect the thermal decomposition of MOF and the thermal stability of the material.

Table 2. TGA profile findings summary of pure and modified Co-MOF-74

Findings	TGA Profiles					
	Evans et al., 2020	Mendiola-Alvarez et al., 2020	Xie et al., 2020b	Strauss et al., 2019	Pliekhov et al., 2018	Young et al., 2018
Co-MOF-74 Type	Pure	Pure	Modified with Mn	Modified with TTF	Modified with NDHPI	Modified with Ni
Atmospheric condition	N2	N2	N2 and air	Air	Air	N2 and air
Solvent evaporation (°C)	< 350	< 200	225 @ air 325 @ N2	-	-	25-200 @ N2 100-200 @ air
Solvent evaporation(°C)	~550	-	-	-	-	-
MOF structure decomposition (°C)	-	300	275 @ air 550 @ N2	-	250	280-500 @ N2 200-350 @ air
Water evaporation (°C)	-	-	-	100 150-350	30-150	-
NDHPI decomposition (°C)	-	-	-	-	315	-
Metal oxides decomposition (°C)`	-	-	-	-	-	200-350 @ air
Mass stabilization (°C)	600	800	320 @ air 600 @ N2	700	400	850

Conclusion

TGA is an effective technique for analyzing the thermal profile of pure and modified Co-MOF-74. TGA can show the amount and presence of additive materials incorporated into the MOF framework. TGA analysis is used to determine the degradation temperature of components in materials and to study thermal phenomena (evaporation of solvents, decomposition of MOF or ligand structures, and formation of metal oxides). Atmospheric conditions, for example, N_2 and air, can significantly affect the thermal profile of Co-MOF-74. The results of this study were expected to be used as a basis for information in the development of modified Co-MOF-74.

References

Azizah, N.N., Maryanti, R., and Nandiyanto, A.B.D. (2021). How to search and manage references with a specific referencing style using google scholar: From step-by-step processing for users to the practical examples in the referencing education. *Indonesian Journal of Multidiciplinary Research*, *1*(2), 267-294. https://doi.org/10.17509/ijomr.v1i2.37694.

Al Husaeni, D.F., and Nandiyanto, A.B.D. (2022). Bibliometric using VOSviewer with publish or perish (using google scholar data): From step-by-step processing for users to the practical examples in the analysis of digital learning articles in pre and post covid-19 pandemic. *ASEAN Journal of Science and Engineering*, *2*(1), 19-46. https://doi.org/10.17509/ajse.v2i1.37368.

Coker, E. N., Ohlhausen, J. A., Ambrosini, A., & Miller, J. E. (2012). Oxygen transport and isotopic exchange in iron oxide/YSZ thermochemically-active materials via splitting of C(18O)2 at high temperature studied by thermogravimetric analysis and secondary ion mass spectrometry. *Journal of Materials Chemistry*, *22*(14), 6726–6732. https://doi.org/10.1039/C2JM15324F.

Dietzel, P. D. C., Georgiev, P. A., Eckert, J., Blom, R., Strässle, T., & Unruh, T. (2010). Interaction of hydrogen with accessible metal sites in the metal-organic frameworks M2(dhtp) (CPO-27-M; M = Ni, Co, Mg). *Chemical Communications*, *46*(27), 4962–4964. https://doi.org/10.1039/c0cc00091d.

Evans, A., Cummings, M., Decarolis, D., Gianolio, D., Shahid, S., Law, G., Attfield, M., Law, D., & Petit, C. (2020). Optimisation of Cu + impregnation of MOF-74 to improve CO/N 2 and CO/CO 2 separations. *RSC Advances*, *10*(9), 5152–5162. https://doi.org/10.1039/C9RA10115B.

Ghodke, S. A., Maheshwari, U., Gupta, S., Sonawane, S. H., & Bhanvase, B. A. (2021). Nanomaterials for adsorption of pollutants and heavy metals: Introduction, mechanism, and challenges. *Handbook of Nanomaterials for Wastewater Treatment:*

Fundamentals and Scale up Issues, 343–366. https://doi.org/10.1016/B978-0-12-821496-1.00032-5.

Jiang, H., Wang, Q., Wang, H., Chen, Y., & Zhang, M. (2016). Temperature effect on the morphology and catalytic performance of Co-MOF-74 in low-temperature NH3-SCR process. *Catalysis Communications*, *80*, 24–27. https://doi.org/10.1016/J.CATCOM.2016.03.013.

Liang, X., Wang, P., Li, C., Yuan, M., Shi, Q., & Dong, J. (2021). The activation of Co-MOF-74 with open metal sites and their corresponding CO/N2 adsorptive separation performance. *Microporous and Mesoporous Materials*, *320*, 111109. https://doi.org/10.1016/j.micromeso.2021.111109.

Loganathan, S., Ravi, V., Mishra, R. K., Babu Valapa, R., Mishra, R., Pugazhenthi, G., & Thomas, S. (2017). Thermogravimetric analysis for characterization of nanomaterials. Elsevier. https://doi.org/10.1016/B978-0-323-46139-9.12001-8.

Loganathan, S., Valapa, R. B., Mishra, R. K., Pugazhenthi, G., & Thomas, S. (2017). Chapter 4 - Thermogravimetric Analysis for Characterization of Nanomaterials. In S. Thomas, R. Thomas, A. K. Zachariah, & R. K. B. T.-T. and R. M. T. for N. C. Mishra (Eds.), *Micro and Nano Technologies* (pp. 67–108). Elsevier. https://doi.org/ https://doi.org/10.1016/B978-0-323-46139-9.00004-9.

Lozano-Peral, D., Arango-Díaz, A., Martín-de-las-Heras, S., & Rubio, L. (2020). Thermogravimetric analysis of teeth for forensic purposes. *Journal of Thermal Analysis and Calorimetry*, *139*(2), 1121–1129. https://doi.org/10.1007/S10973-019-08441-Z.

Mansfield, E., Kar, A., chemistry, S. H.-A. and bioanalytical, & 2010, undefined. (2010). *Applications of TGA in quality control of SWCNTs*. Springer, *396*(3), 1071–1077. https://doi.org/10.1007/s00216-009-3319-2.

Mendiola-Alvarez, S. Y., Turnes Palomino, G., Guzmán-Mar, J., Hernández-Ramírez, A., Hinojosa-Reyes, L., & Palomino Cabello, C. (2020). Magnetic porous carbons derived from cobalt(II)-based metal–organic frameworks for the solid-phase extraction of sulfonamides. *Dalton Transactions*, *49*(26), 8959–8966. https://doi.org/ 10.1039/D0DT01215G.

Nandiyanto, A.B.D. (2019). Nano metal-organic framework particles (ie MIL-100 (Fe), HKUST-1 (Cu), Cu-TPA, and MOF-5 (Zn)) using a solvothermal process. *Indonesian Journal of Science and Technology*, *4*(2), 220-228. https://doi.org/10.17509/ijost.v4i2.18178.

Nasrollahzadeh, M., Atarod, M., Sajjadi, M., Sajadi, S. M., & Issaabadi, Z. (2019). Plant-Mediated Green Synthesis of Nanostructures: Mechanisms, Characterization, and Applications. *Interface Science and Technology*, *28*, 199–322. https://doi.org/10.1016/B978-0-12-813586-0.00006-7.

Nordin, N.A.H.M., Ismail, A.F., Racha, S.M., Cheer, N.B., Bilad, M.R., Putra, Z.A., and Wirzal, M.D.H. (2018). Limitation in fabricating PSf/ZIF-8 hollow fiber membrane for CO2/CH4 Separation. *Indonesian Journal of Science and Technology*, *3*(2), 138-149. https://doi.org/10.17509/ijost.v3i2.12757.

Pliekhov, O., Pliekhova, O., Lavrenčič Štangar, U., & Zabukovec Logar, N. (2018). The Co-MOF-74 modified with N,N′-Dihydroxypyromellitimide for selective, solvent free

aerobic oxidation of toluene. *Catalysis Communications*, *110*, 88–92. https://doi.org/10.1016/J.CATCOM.2018.03.021.

Rajisha, K. R., Deepa, B., Pothan, L. A., & Thomas, S. (2011). Thermomechanical and spectroscopic characterization of natural fibre composites. In N. E. B. T.-I. E. of N. F. C. for M. P. Zafeiropoulos (Ed.), *Interface Engineering of Natural Fibre Composites for Maximum Performance* (pp. 241–274). Woodhead Publishing. https://doi.org/10.1533/9780857092281.2.241.

Saadatkhah, N., Carillo Garcia, A., Ackermann, S., Leclerc, P., Latifi, M., Samih, S., Patience, G. S., & Chaouki, J. (2020). Experimental methods in chemical engineering: Thermogravimetric analysis—TGA. *The Canadian Journal of Chemical Engineering*, *98*(1), 34–43. https://doi.org/10.1002/CJCE.23673.

Shidiq, A.P.A. (2023). Bibliometric analysis of nano metal-organic frameworks synthesis research in medical science using VOSviewer. *ASEAN Journal of Science and Engineering*, *3*(1), 31-38. https://doi.org/10.17509/ajse.v3i1.43345.

Sladekova, K., Campbell, C., Grant, C., Fletcher, A. J., Gomes, J. R. B., & Jorge, M. (2021). Correction to: The effect of atomic point charges on adsorption isotherms of CO2 and water in metal organic frameworks (Adsorption, (2020), 26, 5, (663-685), 10.1007/s10450-019-00187-2). *Adsorption*, *27*(6), 995–1000. https://doi.org/10.1007/s10450-021-00301-3.

Strauss, I., Mundstock, A., Hinrichs, D., Himstedt, R., Knebel, A., Reinhardt, C., Dorfs, D., & Caro, J. (2018). The Interaction of Guest Molecules with Co-MOF-74: A Vis/NIR and Raman Approach. *Angewandte Chemie - International Edition*, *57*(25), 7434–7439. https://doi.org/10.1002/anie.201801966.

Strauss, I., Mundstock, A., Treger, M., Lange, K., Hwang, S., Chmelik, C., Rusch, P., Bigall, N. C., Pichler, T., Shiozawa, H., & Caro, J. (2019). Metal-Organic Framework Co-MOF-74-Based Host-Guest Composites for Resistive Gas Sensing. *ACS Applied Materials and Interfaces*, *11*(15), 14175–14181. https://doi.org/10.1021/ACSAMI.8B22002/ASSET/IMAGES/LARGE/AM-2018-22002A_0006.JPEG.

Unapumnuk, K., Keener, T. C., Lu, M., & Khang, S. J. (2012). *Pyrolysis Behavior of Tire-Derived Fuels at Different Temperatures and Heating Rates*. Http://Dx.Doi.Org/10.1080/10473289.2006.10464481, *56*(5), 618–627. https://doi.org/10.1080/10473289.2006.10464481.

Xiao, Y., & Watson, M. (2019). Guidance on conducting a systematic literature review. *Journal of Planning Education and Research*, *39*(1), 93–112.

Xie, S., Qin, Q., Liu, H., Jin, L., Wei, X., Liu, J., Liu, X., Yao, Y., Dong, L., & Li, B. (2020a). MOF-74-M (M = Mn, Co, Ni, Zn, MnCo, MnNI, and MnZn) for low-temperature NH3-SCR and in situ Drifts study reaction mechanism. *ACS Applied Materials and Interfaces*, *12*(43), 48476–48485. https://doi.org/10.1021/acsami.0c11035.

Xie, S., Qin, Q., Liu, H., Jin, L., Wei, X., Liu, J., Liu, X., Yao, Y., Dong, L., & Li, B. (2020b). MOF-74-M (M = Mn, Co, Ni, Zn, MnCo, MnNI, and MnZn) for low-temperature NH3-SCR and in situ Drifts study reaction mechanism. *ACS Applied Materials and Interfaces*, *12*(43), 48476–48485. https://doi.org/10.1021/ACSAMI.0C11035/SUPPL_FILE/AM0C11035_SI_001.PDF.

Young, C., Kim, J., Kaneti, Y. V., & Yamauchi, Y. (2018). One-Step Synthetic Strategy of Hybrid Materials from Bimetallic Metal-Organic Frameworks for Supercapacitor Applications. *ACS Applied Energy Materials*, *1*(5), 2007–2015. https://doi.org/10.1021/ACSAEM.8B00103/SUPPL_FILE/AE8B00103_SI_001.PDF.

Chapter 7

The Structural Characterization of Co-MOF Using a Transmission Electron Microscope

Silvia Widiyanti
Risti Ragadhita
and Asep Bayu Dani Nandiyanto*
Department of Chemistry Education, Universitas Pendidikan Indonesia
Jl. Dr. Setiabudi, Bandung, Jawa Barat, Indonesia

Abstract

This chapter aims to provide an in-depth explanation of how to characterize the structure of currently prepared Co-MOF materials using a Transmission Electron Microscope (TEM). The study method used is a Systematic Literature Study (SLR). From the study results, TEM electron microscopy methods are known to be very effective and very useful for characterizing the structure of Co-MOF materials because of their successfulness in accurately determining the morphology and size of Co-MOF materials. Most of the morphological forms of pure Co-MOF are polyhedron and rodlike shapes. Determination of this structure is useful. Thus, the design criteria for the application of Co-MOF can be better designed. In the future, the results of this study are expected to be used as a basis for information on the structural characterization of Co-MOF using TEM.

Keywords: Co-MOF, structural characterization, TEM

* Corresponding Author's Emails: nandiyanto@upi.edu; asep.nandiyanto@gmail.com.

In: Advances in Materials Science Research. Volume 65
Editor: Maryann C. Wythers
ISBN: 979-8-89113-090-6

Introduction

Metal-Organic Framework (MOF) is a unique crystalline material made of a metal center and organic ligands. MOF is one of the popular subjects that has been well-studied and reviewed (Nandiyanto, 2019; Shidiq, 2023; Nordin et al., 2018). Co-MOF material is a type of material consisting of a cobalt metal framework coordinated with organic molecules, which are usually referred to as ligands. This material has an orderly crystal structure and has small pores in it. Thus, it can be used for various applications, such as gas absorption and catalysis (Ren et al., 2023).

Co-MOF can be used as a catalyst in various chemical reactions, such as hydrogenation, dehydrogenation, oxidation, and transformation of other organic compounds (Guo et al., 2023). In addition, the adaptable pore structure of the MOF allows for the development of more efficient and selective catalysts. Co-MOF can also be used as gas storage. The pore structure of Co-MOF can be adapted to capture gases such as hydrogen, carbon dioxide, methane, etc. This makes Co-MOF a promising choice in gas storage applications (Thanasamy et al., 2023).

Co-MOF can be used as a base material for the manufacture of sensors which are highly sensitive to various compounds, including gases, chemicals and heavy metals (Manjula et al., 2023). For example, Co-MOF can be used for the detection of mercury compounds in water or air. Co-MOF also shows potential as a battery electrode, because its porous structure can increase the surface area available for electrochemical reactions. On the whole, Co-MOF offers a variety of promising applications in various fields and continues to be an interesting research subject for scientists (Shi et al., 2023).

The crystal form of Co-MOF varies depending on the type of organic molecule used in its synthesis. Several forms of Co-MOF crystals include hexagonal prism crystal forms, cubic crystal forms, tube crystal forms, and rhombic dodecahedron crystals. To find out the structural form of Co-MOF, structural characterization was carried out using several instrumentations, especially the Scanning Electron Microscope (SEM) and Transmission Electron Microscope (TEM) (Klang et al., 2012; Fan et al., 2019). TEM will produce a two-dimensional projected image of the sample resulting from the electron beam that penetrates the sample (Rehn et al., 2018; Suga et al., 2014; Susi et al., 2019).

Judging from its various uses, Co-MOF is an interesting material to study and develop further. However, discussions regarding the characterization of the Co-MOF structure in a comprehensive manner are still rare. Thus, it is

important to study the characterization of the Co-MOF structure, especially using TEM instrumentation.

Literature Reviews

Transmission Electron Microscopy

TEM is an electron microscopy technique that uses electrons as a light source that passes through a material and projects an image on a fluorescent screen or camera sensor. This technique is often used for material characterization, because of its ability to produce material images at the nanometer to sub-angstrom scales (Tang & Yang, 2017).

TEM is one of the most important and powerful electron microscopy techniques used in materials characterization and materials science. This technique was first developed in 1931 by Ernst Ruska and Max Knoll in Germany (Zhou et al., 2023).

Ruska and Knoll built the first electron microscope by using a needle-shaped electrode to produce a source of electrons and an electromagnetic lens to focus the electrons. At first, these microscopes could only achieve a resolution of about 50 nm, but with developments in technology and improvements in instrument design, the resolution can increase to about 0.1 nm or even less (Zhou et al., 2023).

In 1933, Ruska succeeded in producing the first drawing of a metal sample using TEM, and the technique has developed rapidly since then. In 1940, James Hillier and Albert Prebus from the United States introduced the concept of dual magnetic lenses to increase image resolution. Later in the 1950s, electron diffraction techniques were integrated into instruments, enabling direct measurements of crystal structure and material composition (Tang & Yang, 2017).

Until now, TEM techniques continue to be used in a variety of applications in the fields of materials, environmental science, biology, and others. This technique has enabled scientists to study the internal structure and properties of materials at very high levels of resolution, thereby enabling the development of more advanced and efficient technologies. Electron microscope also has been used for understanding the morphology of the material, specifically its size (Yolanda & Nandiyanto, 2022).

TEM is a material characterization technique that uses electrons as a radiation source. This technique is usually used to study the structure and properties of materials on an atomic and molecular scale (Rostamabadi et al., 2020).

In TEM, electrons are passed through a thin sample so they can penetrate and produce an electron diffraction pattern. This electron diffraction pattern is then used to determine the crystal structure of the sample (Grimley & LeBeau, 2019).

In addition, TEM can also be used to measure the energy spectrum of electrons emitted or absorbed by a sample. This spectrum can provide information about the electronic structure of the sample, including bond energies and valence energies (Grimley & LeBeau, 2019).

Other techniques frequently used in TEM are low-energy electron spectroscopy (EELS) and photoelectron spectroscopy (XPS). EELS allows the measurement of the energy spectrum of electrons absorbed by the sample, while XPS allows the measurement of the energy spectrum of electrons emitted by the sample (Grimley & LeBeau, 2019).

In this series, TEM makes it possible to study the crystal structure, electronic properties, and surface chemistry of materials. However, TEM is different from XRD that focuses only directly on the diffraction of crystal structure (Fatimah et al., 2022). TEM analyzes on the morphology of crystal. Therefore, this technique is very useful in materials research and development, including in the fields of electronics, energy, and catalysis (Grimley & LeBeau, 2019).

Following are the steps in material characterization using TEM:

1. Sample preparation. The sample to be analyzed must be carefully prepared to ensure good image quality. The sample to be observed is usually very thin (less than 100 nm) and is prepared by slicing or thinning techniques. The sample is then placed on a TEM grid made of metal or carbon (Zhao & Liu, 2022)
2. Electron injection. Electrons are obtained from an electron tube, then accelerated and focused on the sample. The electrons then pass through the sample and spread elastically or inelastically within it. This process produces lots of secondary electrons and backscattered electrons, which will form the image of the sample (Zhao & Liu, 2022)
3. Image analysis. The images produced by TEM can show various material characteristics, such as morphology, crystal structure, and

compositional distribution. Several analysis techniques that can be performed on TEM images are:

- Electron Diffraction (Electron Diffraction): A technique used to identify the crystal structure of a sample, through analysis of electron diffraction by the crystal lattice (Smith et al., 2023).
- Energy Dispersive Spectroscopy (EDS): A technique used to analyze the distribution of chemical elements in a sample, by analyzing the energy spectrum produced by electrons interacting with the sample (Smith et al., 2023).
- EELS: A technique used to analyze the energy spectrum of electrons that lose energy when interacting with a sample (Smith et al., 2023).

TEM and SEM are two electron microscopy techniques used for material characterization. Although both use electrons to form images, their working principle, equipment, and output are very different (Inkson, 2016).

TEM uses electrons to penetrate a sample, similar to the way X-rays penetrate objects. Electrons passing through the sample form a 2D image on a fluorescent screen or CCD sensor. With this technique, we can see the internal structure and microstructure of materials on the nanometer to angstrom scale, with very high resolution. The advantage of TEM is the ability to obtain information about the distribution of chemical composition and crystallography of materials directly (Inkson, 2016).

Meanwhile, SEM uses electrons to scan the sample surface and map the surface topography and morphology. SEM beams electrons to the sample to form a 3D image of the surface. This technique has a lower resolution than TEM but can be used to examine larger samples and provides information about the shape, size, and distribution of grains on the surface of the sample. In addition, SEM can also provide information about the chemical composition of surfaces using X-ray energy dispersive detectors (Inkson, 2016; Williams, 2008).

In selecting the appropriate technique for material characterization, it is important to consider the information to be obtained, the sample size to be observed, and the scale of resolution required. If you want to see the internal structure and microstructure of materials on the nanometer to angstrom scale, then TEM is a more appropriate choice. However, if you want to map the shape, size, and distribution of the grains on the surface of the sample, then SEM can be a more appropriate choice (Grimley & LeBeau, 2019).

TEM instrumentation consists of several main parts as shown in Figure 1, namely the electron source, electromagnetic lens system, detection system, and image processing software (Tang & Yang, 2017).

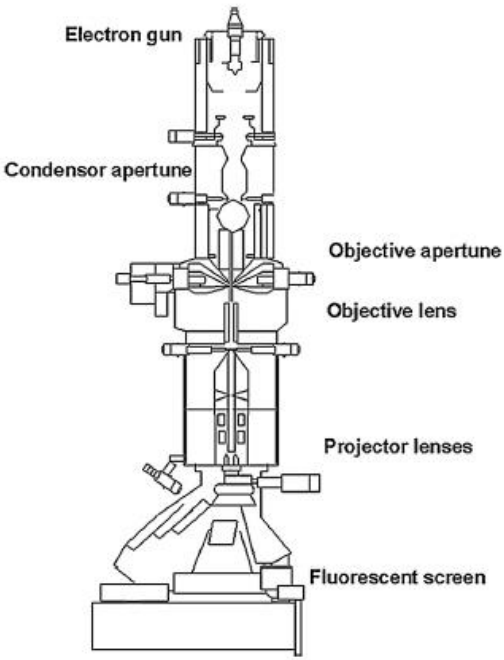

Figure 1. Instrumentation of TEM image, adopted from Tang & Yang (2017).

Electron Source The electron source in TEM usually uses a tungsten filament or LaB6 (lanthanum hexaboride) as the electron source. This electron source is placed at the top of the instrument column and is equipped with a heating system to generate electrons which are directed to the sample. The electron source also has a current and voltage regulating system to produce electrons with the desired energy (Tang & Yang, 2017).

Electromagnetic Lens System The electromagnetic lens system in TEM consists of a series of electromagnetic lenses that are used to focus and accelerate electrons before they reach the sample. Electromagnetic lenses usually consist of a condenser lens and an objective lens. The condenser lens is used to focus electrons on the sample, while the objective lens is used to focus electrons that have passed through the sample so that high-resolution images can be produced. There are also other electromagnetic lenses such as

aperture lenses and magnifying lenses which are used to control the number of electrons passing through the sample (Tang & Yang, 2017).

Detection System The detection system in TEM is used to collect electrons that have passed through the sample and form an image. There are two types of detection systems commonly used in TEM, namely photographic film systems and digital camera systems. In a photographic film system, electrons passing through the sample will produce an image on the photographic film, whereas, in a digital camera system, electrons passing through the sample will produce an electronic signal which is then converted into a digital image (Tang & Yang, 2017).

Image Processing Software After the image has been captured by the detection system, image processing software is used to process and analyze the image. This software is usually equipped with features such as contrast adjustment, noise reduction, image positioning, and advanced image analysis such as particle measurement, diffraction pattern analysis, and identification of crystal structures (Tang & Yang, 2017).

In addition to the main components above, the TEM instrument is also equipped with various supporting components such as a vacuum control system to avoid contamination, a temperature control device to control the sample temperature, an alignment control device to adjust the sample position, and an electromagnetic lens. All of these components work together to produce very detailed drawings and information about the structure and properties of the material being examined (Tang & Yang, 2017).

Co-MOF

The Co-MOF structure, as shown in Figure 2, consists of a cobalt atom bonded to an organic ligand molecule via a coordinate bond. This structure forms an ordered crystal framework, and tiny pores form within it between the ligand molecules. The pore size can be adjusted by changing the size of the ligand molecule used (Singh et al., 2021).

The advantage of the Co-MOF material is that its pores are very small. Thus, it can absorb large amounts of gas molecules. This makes Co-MOF especially useful for applications such as gas storage and purification. In addition, Co-MOF can also be used as a catalyst in chemical reactions, because it can effectively catalyze chemical reactions (Shi et al., 2023). However, Co-MOF materials also have some drawbacks. One of them is its low stability in an acidic or alkaline environment, so it needs special handling to maintain its

stability. In addition, the process of making Co-MOF also requires quite a lot of time and costs (Shi et al., 2023).

In further research, the addition of other elements into the Co-MOF structure such as other metals or non-metal atoms, can improve its properties and performance. Thus, it can be applied in a wider variety of applications (Singh et al., 2021).

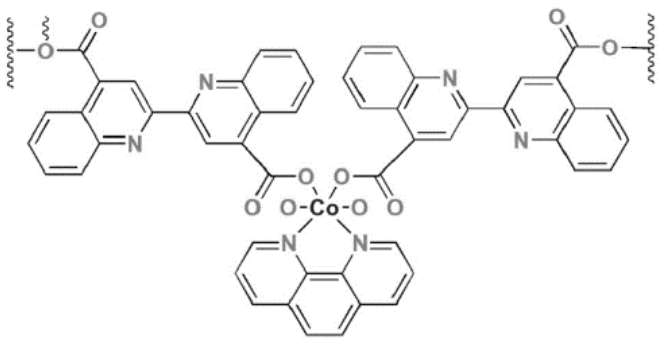

Figure 2. Co-MOF structure. Figure was adopted from Singh et al. (2021).

Methods

The structural characterization of Co-MOF using TEM in this study was investigated through a Systematic Literature Review (SLR) method. SLR is a research method and process for identifying and critically assessing relevant research, as well as for collecting and analyzing data from that research. The purpose of the SLR is to identify all the empirical evidence that fits the pre-determined inclusion criteria to answer a particular research question or hypothesis. By using explicit and systematic methods when reviewing articles and all available evidence, bias can be minimized, thereby providing reliable findings from which conclusions can be drawn and decisions made (Snyder, 2019).

The journal articles reviewed in this study were searched through various search media and journal publications such as Google Scholar, Science Direct, Springer, and MDPI. The keywords used to browse these articles include Co-MOF structural characterization TEM, electron microscopy, TEM of Co-MOF, and Co-MOF structural characterization.

The articles being searched were selected according to the following criteria.

1. Articles must contain information related to pure Co-MOF without any kind of dopants or composites.
2. The article contains information regarding the structure of Co-MOF.

Results and Discussion

Singh et al. (2021) has synthesized three heteroleptic Co(II)-MOFs ie catena-[(diaqua-(μ2 -bqdc- κO,O)-(phen- κN,N)-cobalt (II)] (1), {[Co(pa)(4,4'-bipy)(H_2O) (CH_3OH)] DMF} n (2), and [Co(ia)(bpe)0.5(H_2O)] n (3), (H2bqdc = 2,2-biquinoline-4,4'-dicarboxylic acid, phen = 1,10-phenanthroline), (H_2pa = pamoic acid) (H_2ia = ita- conic acid, bpe = 1,2- bi(4-pyridyl)ethane). As shown in Figure 3, Among Co(II)-MOFs, 1 displays small-sized crystals in the entire morphology of material along with pores visible in the TEM image (measuring scale 200 nm). sharp contrast, the entire morphology of 2 exhibits elongated rectangular-shaped nanocrystals assuming multiple crystallographic orientations in TEM images Interestingly, 3 comprises uniformly organized porous morphology like silica in its TEM image.

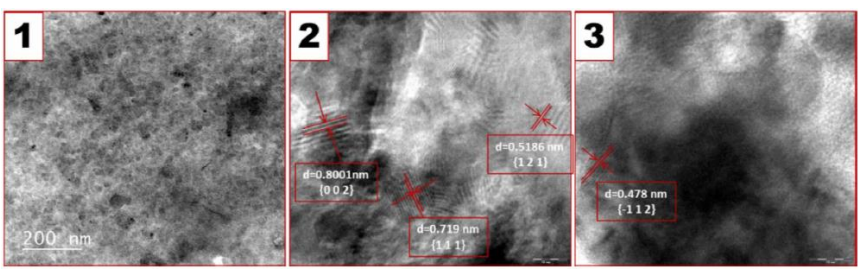

Figure 3. TEM image of Co-MOF. The image was adopted from Singh et al. (2021).

Xie et al. (2022) synthesized Co MOFs. Briefly, 0.582 g of $Co(NO_3)_2 \cdot 6H_2O$ was dissolved in 40 mL of dimethylformamide (DMF) containing 20 mL ethanol. Then, 0.344 g of 2,5-Thiophenedicarboxylic acid (Tdc) and 0.312 g of 4,4′ -bipyridine (Bpy) were added to this mixture by continuously agitating for 60 min. After that, the mixture was placed in a Teflon liner, which was heated at 105°C for 72 h. And then cooling down to room temperature, the mixture was centrifuged (6500 rpm), and washed with ethanol. Finally, the

product obtained was dried in a vacuum oven at 45°C for 12 h. The result as shown in Figure 4 that the synthesized Co-MOFs nanocomposite was a rodlike structure with a diameter of about 500 nm (Xie et al., 2022).

Shi et al. (2023) synthesized Co-MOF with 765 mg 2-methylimidazole and 582 mg $Co(NO_3)_2 \cdot 6H_2O$ powders were dissolved into 25 mL anhydrous methanol, respectively. After then, the as-resulted 2- methylimidazole solution was rapidly injected into $Co(NO_3)_2 \cdot 6H_2O$ solution with continuous stirring for 5 minutes. After that, the mixture was kept still at room temperature for 24 hours. At last, the suspension was treated by filtration, washing, and drying at 60°C. As shown in Figure 5 the pristine ZIF-67 exhibited a typical polyhedral shape with a size of about 500 nm.

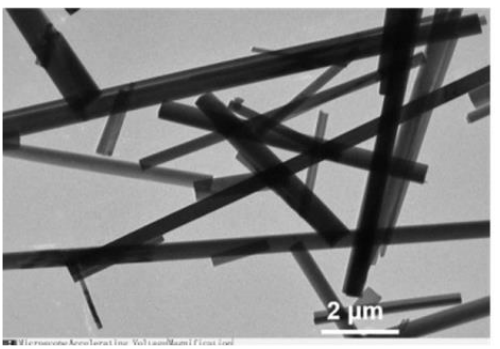

Figure 4. Co-MOF morphology, adopted from Xie et al. (2022).

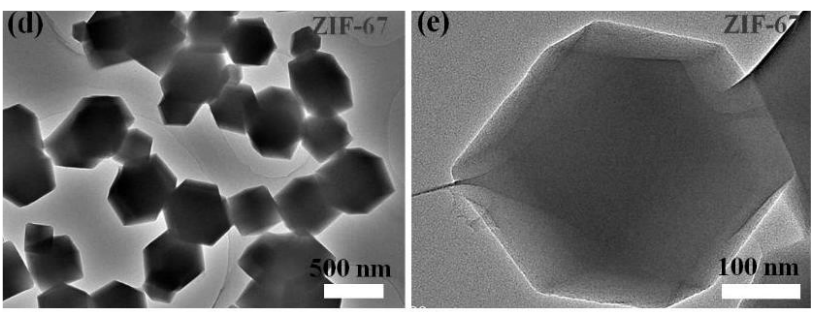

Figure 5. Co-MOF Morphology, adopted from Shi et al. (2023).

Ren et al. (2023) synthesized Co-MOF by carrying out 182.48 mg of cobalt nitrate hexahydrate and 205.00 mg of 2-methylimidazole were dissolved in 5 mL of anhydrous methanol to form a transparent pink solution (solution A) and a colorless solution (solution B), respectively. Solution A was

then added to solution B in a dropwise manner and ultrasonicated for 30 min. After centrifugation, the precipitate is washed with methanol and dried to obtain 3D ZIF-67 crystals. The obtained 3D ZIF-67 was dispersed in 5 mL of anhydrous methanol, mixed with another solution A, transferred to a 20-mL Teflon stainless steel autoclave, and stored at 120°C for 60 min. Finally, the product was centrifuged, washed with anhydrous methanol, and dried to obtain yellow Co-MOF nanosheets. The result as Figure 6 showed that 3D ZIF-67 has a regular dodecahedron structure with a diameter of 1 μm.

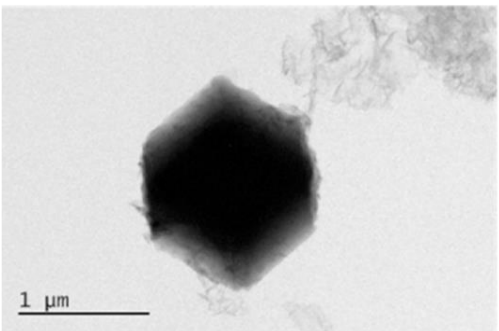

Figure 6. Co-MOF morphology from Ren et al. (2023).

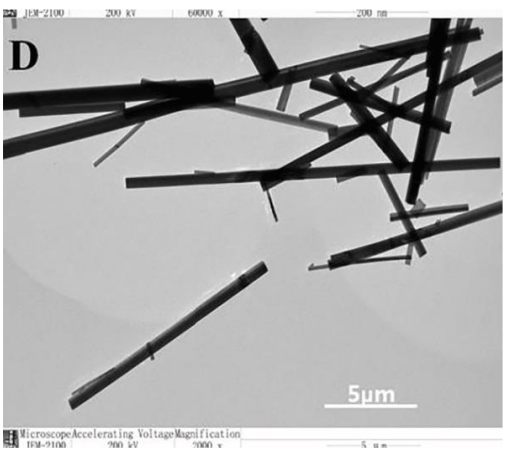

Figure 7. Co-MOF morphology. Image was adopted from Guan et al. (2023).

Guan et al. (2023) synthesized Co-MOFs by carrying out $Co(NO_3)_2 \cdot 6H_2O$ (0.582 g) that was dissolved in DMF-water (V/V = 1:1, 20 mL) and mixed solvent system. Then, Tdc (0.344 g) and Bpy (0.312 g) were added to

the above solution under stirring for 1 h. Subsequently, the mixtures were put into an autoclave lined with Teflon and allowed to react at 105°C for 72 h. After cooling to room temperature, the mixtures were filtered, washed three times with ethanol, and dried overnight in a vacuum at 40°C. The results in Figure 7 showed that the synthesized Co-MOFs are rod-shaped 1D nanostructures with a diameter of 300 nm.

Conclusion

This study showed that TEM is indeed effective and very useful to characterize Co-MOF especially to know the structure and shape of Co-MOF. We can conclude that Co-MOF has varied shapes from porous, rectangular, polyhedron, and dodecahedron to rodlike shapes. With a range of sizes from 0.3-1 μm.

Disclaimer

The authors declare that there is no conflict of interest regarding the publication of this article. The authors confirmed that the paper was free of plagiarism.

References

Fatimah, S., Ragadhita, R., Al Husaeni, D.F., and Nandiyanto, A.B.D. (2022). How to calculate crystallite size from x-ray diffraction (XRD) using scherrer method. *ASEAN Journal of Science and Engineering*, *2*(1), 65-76. https://doi.org/10.17509/ajse.v2i1.37647.

Grimley, ED, & LeBeau, JM (2019). Transmission Electron Microscopy (STEM and TEM). In *Ferroelectricity in Doped Hafnium Oxide: Materials, Properties and Devices* (pp. 317–340). Elsevier. https://doi.org/10.1016/B978-0-08-102430-0.00015-2.

Guan, Y., Si, P.-B., Yang, T., Wu, Y., Yang, Y.-H., & Hu, R. (2023). A novel method for detection of ochratoxin A in foods—Co-MOFs based dual signal ratiometric electrochemical aptamer sensor coupled with DNA walker. *Food Chemistry*, *403*, 134316. https://doi.org/10.1016/j.foodchem.2022.134316.

Guo, H., Lu, X., He, J., Zhang, H., Zhang, H., Dong, Y., Zhou, D., & Xia, Q. (2023). Co-MOF nanosheet supported on ZSM-5 with an improved catalytic activity for air

epoxidation of olefins. *Materials Chemistry and Physics, 294,* 127001. https://doi.org/10.1016/j.matchemphys.2022.127001.

Inkson, BJ (2016). Scanning electron microscopy (SEM) and transmission electron microscopy (TEM) for materials characterization. In *Materials Characterization Using Nondestructive Evaluation (NDE) Methods* (pp. 17–43). Elsevier. https://doi.org/10.1016/B978-0-08-100040-3.00002-X.

Manjula, N., Pulikkutty, S., & Chen, S.-M. (2023). Simple synthesis of MOF-derived Zn, Co electrocatalyst for sensitive detection of digoxin in urine samples. *Colloids and Surfaces A: Physicochemical and Engineering Aspects, 660,* 130830. https://doi.org/10.1016/j.colsurfa.2022.130830.

Nandiyanto, A.B.D. (2019). Nano metal-organic framework particles (ie MIL-100 (Fe), HKUST-1 (Cu), Cu-TPA, and MOF-5 (Zn)) using a solvothermal process. *Indonesian Journal of Science and Technology*, *4*(2), 220-228. https://doi.org/10.17509/ijost.v4i2.18178

Nordin, N.A.H.M., Ismail, A.F., Racha, S.M., Cheer, N.B., Bilad, M.R., Putra, Z.A., and Wirzal, M.D.H. (2018). Limitation in fabricating PSf/ZIF-8 hollow fiber membrane for CO2/CH4 Separation. *Indonesian Journal of Science and Technology*, *3*(2), 138-149. https://doi.org/10.17509/ijost.v3i2.12757

Ren, M., Zhang, Y., Yu, L., Qu, L., Li, Z., & Zhang, L. (2023). A Co-based MOF as a nanozyme with enhanced oxidase-like activity for highly sensitive and selective colorimetric differentiation of aminophenol isomers. *Talanta, 255,* 124219. https://doi.org/10.1016/j.talanta.2022.124219.

Rostabadi, H., Falsafi, SR, & Jafari, SM (2020). Transmission electron microscopy (TEM) of nanoencapsulated food ingredients. In *Characterization of Nanoencapsulated Food Ingredients* (pp. 53–82). Elsevier. https://doi.org/10.1016/B978-0-12-815667-4.00002-X.

Shi, S., Cao, G., Chen, Y., Huang, J., Tang, Y., Jiang, J., Gan, T., Wan, C., & Wu, C. (2023). Facile synthesis of core-shell Co-MOF with hierarchical porosity for enhanced electrochemical detection of furaltadone in aquaculture water. *Analytica Chimica Acta,* 341296. https://doi.org/10.1016/j.aca.2023.341296.

Shidiq, A.P.A. (2023). Bibliometric analysis of nano metal-organic frameworks synthesis research in medical science using VOSviewer. *ASEAN Journal of Science and Engineering*, *3*(1), 31-38. https://doi.org/10.17509/ajse.v3i1.43345

Singh, D., Raj, KK, Azad, UP, & Pandey, R. (2021). In situ transformed three heteroleptic Co(II)-MOFs as potential electrocatalysts for the electrochemical oxygen evolution reaction. *Electrochimica Acta, 395,* 139117. https://doi.org/10.1016/j.electacta.2021.139117.

Smith, J., Wang, S., Eldred, TB, DellaRova, C., & Gao, W. (2023). Characterization of nanomaterials dynamics with transmission electron microscope. In *Encyclopedia of Nanomaterials* (pp. 123–145). Elsevier. https://doi.org/10.1016/B978-0-12-822425-0.00049-X.

Tang, CY, & Yang, Z. (2017). Transmission Electron Microscopy (TEM). In *Membrane Characterization* (pp. 145–159). Elsevier. https://doi.org/10.1016/B978-0-444-63776-5.00008-5.

Thangasamy, P., He, R., Randriamahazaka, H., Chen, X., Zhang, Y., Luo, H., Wang, H., & Zhou, M. (2023). Collectively exhaustive electrochemical hydrogen evolution reaction of polymorphic cobalt selenides derived from organic surfactants modified Co-MOFs. *Applied Catalysis B: Environmental*, *325*, 122367. https://doi.org/10.1016/j.apcatb.2023.122367.

Williams, DF (2008). On the mechanisms of biocompatibility. *Biomaterials*, *29* (20), 2941–2953. https://doi.org/10.1016/j.biomaterials.2008.04.023.

Xie, F.-T., Li, Y.-L., Guan, Y., Liu, J.-W., Yang, T., Mao, G.-J., Wu, Y., Yang, Y.-H., & Hu, R. (2022). Ultrasensitive dual-signal electrochemical ratiometric aptasensor based on Co-MOFs with intrinsic self-calibration property for Mucin 1. *Analytica Chimica Acta*, *1225*, 340219. https://doi.org/10.1016/j.aca.2022.340219.

Yolanda, Y.D., and Nandiyanto, A.B.D. (2022). How to read and calculate diameter size from electron microscopy images. *ASEAN Journal of Science and Engineering Education*, *2*(1), 11-36. https://doi.org/10.17509/ajsee.v2i1.35203

Zhao, J., & Liu, X. (2022). Electron microscopic methods (TEM, SEM and energy dispersion spectroscopy). In *Reference Module in Earth Systems and Environmental Sciences* (p. B9780128229743000000). Elsevier. https://doi.org/10.1016/B978-0-12-822974-3.00013-6.

Zhou, W., Ikuhara, YH, Zheng, Z., Wang, K., Cao, B., & Chen, J. (2023). Transmission electron microscopy (TEM) studies of functional nanomaterials. In *Modeling, Characterization, and Production of Nanomaterials* (pp. 467–512). Elsevier. https://doi.org/10.1016/B978-0-12-819905-3.00017-8.

Chapter 8

Phase States and Surface Electrical Activity of the Low-Temperature Synthesized Fine $PbZr_{0.52}Ti_{0.48}O_3$ Powders

O. A. Bunina*
M. A. Bunin†
Yu. A. Kuprina
V. G. Smotrakov
V. A. Chichkanov
and V. P. Sakhnenko
Research Institute of Physics, Southern Federal University, Rostov-on-Don, Russia

Abstract

A high performance of $PbZr_{1-x}T_{ix}O_3$ (PZT) solid solutions at $x = 0.45 - 0.50$ at the morphotropic boundary is still the target indicator for newly developed environmentally friendly ferroelectric materials. However, despite their wide application, the physical nature of the properties of some PZT compositions between the tetragonal and rhombohedral phases still remains unclear. In addition, in some cases, the method for obtaining this material predetermines its characteristics. The low-temperature synthesis using a special precursor was applied to obtain the PZT morphotropic finely dispersed powders in an equilibrium state with a partial ordering. These powders were obtained by single-stage low-

* Corresponding Author's Email: obunina@gmail.com.
† Corresponding Author's Email: bunin.m.a@gmail.com.

In: Advances in Materials Science Research. Volume 65
Editor: Maryann C. Wythers
ISBN: 979-8-89113-090-6

temperature firing of precursors at $T = 650°C$ and 700°C in a uniform equilibrium state without intermediate phases. The synthesis regimes are chosen in accordance with the order-disorder phase transition temperatures calculated within the framework of the elastic cation-anion bond model, that assumes the participation of diffusion processes and the ordering possibility. X-ray phase studies confidently confirmed the previously undescribed properties of the powders studied by us: a tetragonal structure with the lattice parameters ratio $c/a < 1$ and a ferroelectric phase transition to the cubic phase at $T = 300°C$. Obtained in the same way, but by annealing at $T = 800°C$, the nanopowder had $c/a > 1$, traditional for PZT, and a phase transition temperature of 350°C. The purity, stoichiometry and resistance to thermal cycling up to $T = 1200°C$ of the newly obtained PZT phase were confirmed. The piezoelectric activity and ferroelectric properties of these powders surface have been confirmed by the piezoresponse force microscopy and Kelvin probe force microscopy. It is shown that the unusual aforementioned characteristics of PZT powders are not related to the particle size. Our assumptions on the influence of the partial ordering in the B-sublattice on the properties of the unusual T1 phase and the possibility of the partial ordering in the B-sublattice are confirmed.

Keywords: oxides of the perovskite family (OPF), PZT solid solution, morphotropic phase boundary, phase state, x-ray diffraction, scanning probe microscopy, atomic ordering

Introduction

Lead zirconate-titanate $PbZr_{1-x}Ti_xO_3$ (PZT) solid solutions are known due to their high-value and practically important ferroelectric-piezo-characteristics (Cheng et al.,2010), which ensure their wide application in electronics, acoustics, and piezotechnics. This is especially true for the compositions near the morphotropic phase boundary between the tetragonal and rhombohedral phases ($x = 0.45 - 0.50$). It is noteworthy that the method to prepare makes it possible to control the properties and phase composition of PZT. For example, the characteristics of materials obtained by "bulk"-like methods (solid state reactions, simple ceramic route, single crystals manufacturing) may differ both from "sol-gel"-like nanoparticles and from "film"-like coatings. The reasons for the differences are not always completely clear, and this circumstance does not reduce interest in possibilities of application of the aforementioned methods. Hence,

studies on the PZT morphotropic region continue, testifying to the complexity and diversity of its properties and the physical reasons that determine them (Schonau et al., 2007; Frantti et al., 2002; Panda, 2017; Ohno et al., 2007), and reviews attract interest.

Upon obtaining of a new material, it is desirable to control its characteristics with the least effort/cost, preferring variations in technological modes of manufacturing, rather than the chemical composition. The present chapter is devoted to the method based on using the solid-phase synthesis to obtain morphotropic finely dispersed PZT powders and to study their properties. To understand the relationship between the composition of morphotropic PZT and their macroscopic physical properties, it is necessary to obtain single-phase compositions in an equilibrium state and to analyze their phase states. Thus, we mainly consider this method, and almost do not touch on others, including the preparation of films. In addition, far beyond the scope of this work, a detailed review on the relationship between preparation methods and material properties is given.

The most traditional method for obtaining PZT solid solutions is based on solid-phase reactions involving simple oxides (PbO, TiO_2 and ZrO_2). Samples are synthesized by traditional methods at $800-900^{\circ}C$ and then sintered at temperatures $T > 1200^{\circ}C$ (Eremkin et al., 2012; Lee et al., 1999; Okazaki, 1976) or sintered once at a high temperature (Cordero et al., 2008; Necira et al., 2012; Hammer and Hoffmann, 1998). There is a known method for obtaining $PbZr_{1-x}Ti_xO_3$ from phases being rich in $PbTiO_3$ and Zr, far from the morphotropic boundary, where the final product is obtained as a result of a sequence of simple phase reactions of mixed oxides (Hammer and Hoffmann, 1998; Jaffe and Cook, 1971; Chandratreya et al., 1981). In this sequence of reactions, the Ti atom is incorporated into the already formed perovskite lattice with an excess of Zr. In this method, it is not possible to achieve the desired maximum single-phase state and a uniformity of the final product, even with the maximum homogeneity of the charge. Hence, the disadvantage of this path is the inhomogeneity on the microlevel, that leads to variations in the piezoelectric properties (Panda, 2017). In some cases, homogenization is achieved only during subsequent sintering above $1000^{\circ}C$ (Eremkin et al., 2012).

The synthesis from simple oxides without the formation of intermediate phases becomes possible by a mechanoactivation (Lee et al., 1999). This method requires annealing at a high temperature ($T = 1000-1200^{\circ}C$), which is accompanied by a significant loss of lead above $1000^{\circ}C$ (Necira et al., 2012; Jaffe and Cook, 1971; Okazaki, 1976). In order to avoid the lead deficiency

in the final product (in the target material), a mixture with an excess of PbO is often used, which is to be evaporated during firing. Without careful control over the sintering atmosphere, the grain boundaries of the obtained ceramics are enriched in PbO (Hammer and Hoffmann, 1998). When firing below 1000°C, the evaporation of lead oxide is insignificant (Necira et al., 2012; Jaffe and Cook, 1971; Okazaki, 1976), which justifies the expediency of lowering the synthesis temperature.

An alternative method to perform the synthesis of PZT from simple oxides is the B-site precursor method based on the reaction from PbO and lead-free-precursor $Zr_{1-x}Ti_xO_2$ (Eremkin et al., 2012; Matsuo et al., 1965; Tashiro et al., 1989) as follows:

$$Zr_{1-x}Ti_xO_2 + PbO \rightarrow PbZr_{1-x}Ti_xO_3. \quad (1)$$

In this case, the formation of the PZT phase occurs directly, without the formation of any intermediate phases, including $PbTiO_3$, and also avoiding the Zr gradient in the reaction zone. This method provides favorable conditions for chemically homogeneous solid solutions of PZT in an equilibrium state. A study on these solid solutions is of particular interest because of the possibility of creating an equilibrium phase state. The implementation of the one-stage method (1) can make it possible to obtain a material with unusual crystallographic characteristics. There is a report on the use of this synthesis method to obtain ceramics based on PZT (Robert et al., 2001).

The structure of the OPF lattice of the $AB'_{0.5}B''_{0.5}O_3$ composition allows different degrees of structural ordering, which significantly affects the ferroelectric-piezo-characteristics (Setter and Cross, 1980; Chu, Setter and Tagantsev, 1993; Sakhnenko and Ter-Oganessian, 2018; Sakhnenko et al., 1972; Vasala and Karppinen, 2015). The ordered alternation of two sorts of B-cations favors the emergence of polar systems of atomic displacements in the A- and O-sublattices. Depending on the technological conditions of the preparation, some of them can exist in an ordered state, disordered state (Setter and Cross, 1980; Chu, Setter and Tagantsev, 1993; Vasala and Karppinen, 2015), or in a state with an intermediate degree of the structural order. This makes it possible to control the macroscopic properties of the material through it structural ordering. A well-known example is a significant difference in dielectric permittivities of $PbSc_{0.5}Ta_{0.5}O_3$ ceramics with different degrees of order (Setter and Cross, 1980; Chu, Setter and Tagantsev, 1993). In some cases [$PbIn_{0.5}Nb_{0.5}O_3$ (Ohwada et al., 2008; Bokov, Rayevsky, 1989) and $PbSc_{0.5}Nb_{0.5}O_3$ (Bokov,

Rayevsky, 1989; Zhu et al., 2008)], it can be controlled by varying technological parameters. In principle, such an ordering in the B-sublattice can be formed in morphotropic PZT solid solutions near binary perovskite 1:1 ($PbZr_{0.5}Ti_{0.5}O_3$), but the description of the ordered state of these compositions is not yet found in the literature.

The possible ordering in the B-sublattice of PZT in the morphotropic region was modeled in (Hayn, 2013) by combining the results of the *ab-initio* Density Functional theory (DFT) and Monte Carlo (MC) calculations. The thermodynamically equilibrium structure was presented as a mixture of several preferred structural motifs with a little difference in formation energies between them. The size of ordered local polar regions, that may be formed at on almost zero diffusion of B-cations, was considered to be too small. In a case of probabilistic overcoming of entropy, the preferential ordering in these structures is possible even at low temperatures. This does not correspond to the common practice of sintering PZT ceramics with subsequent rapid cooling to the temperature region of the stable ferroelectric phase (Hayn, 2013; Kingon Clark, 1983). At commonly used high temperatures, this technology does not provide an advantage of any particular configuration, which deliberately destroys the possibility of ordering, instead of stimulating diffusion (Hayn, 2013). Calculations predicted the formation temperature of chaotic alloys above 2000 K. This value is "outside the stability region of cubic perovskite" and means that $PbZr_{0.5}Ti_{0.5}O_3$ - is to be in an always ordered state (Hayn, 2013).

So far, these predictions have not been verified experimentally, at least for commonly used synthesis methods, including film technologies. There are two possible reasons for lack of descriptions of the ordered state in the PZT solid solution system. Firstly, when synthesized from simple oxides, a nonequilibrium state is formed therein. Secondly, high annealing temperatures are applied that exceed the temperature of the ordering state existence. Perhaps, a new way to prepare the material or a specific application of one of the known methods is needed. There is a need for a technology for obtaining morphotropic PZT solid solutions, which can provide a phase equilibrium in the resulting material and lower the synthesis temperature. Such methods are described by (Matsuo et al., 1965 and Hayn, 2013), but in order to use these methods, it is important to know an estimate of a possible value of the ordering temperature T_{od} of cations in the B-sublattice. This can be obtained in two ways: the first way is based on first-principles calculation, and the second way is based on a simpler semi-empirical model. In the latter, the temperature T_{od} of the order-disorder phase transition

is estimated in terms of the cation-anion elastic bond model (Sakhnenko and Ter-Oganessian, 2018; Sakhnenko et al., 1972). For a large number of representative perovskite compounds, this approach gives a plausible estimate of T_{od} and, therefore, we apply it to PZT.

The aim of our research is to obtain the most probable (equilibrium) phase, which has the possibility of some ordering in the B-sublattice. For this, the possible values of T_{od} were estimated, and then, at various low sintering temperatures, a one-stage low-temperature synthesis was performed according to (1) without intermediate phases from the lead-free precursor $Zr_{0.52}Ti_{0.48}O_2$ and PbO. Nanopowders of the morphotropic $PbZr_{0.52}Ti_{0.48}O_3$ solid solution were obtained, and their crystal structure and electrical/piezoactivity were studied.

The present chapter is organized as follows: in Section 2, the thermodynamic description of the ordering of cations in the B-sublattice is used to calculate the dependence of the temperature T_{od} on the degree of the structural ordering s for the tetragonal solid solution with the $PbZr_{0.52}Ti_{0.48}O_3$ composition. This result was used in the synthesis procedure described in Section 3. Section 4 consists of several parts as follows: crystallographic characteristics of obtained materials were determined by X-ray diffraction methods (XRD), and the stoichiometry, temperature stability, phase purity, and homogeneity of these material were confirmed (Section 4.1). Scanning probe microscopy (SPM) methods were used to confirm the electrical activity (Section 4.3). That result made it possible to refine the lattice structure by XRD methods (Section 4.4) and to study the temperature phase transition (Section 4.5). Then, the possibility of the influence of the particle size on the phase transition temperature was verified (Section 4.6).

Order-disorder Phase Transition in 1:1 Binary Perovskites $AB'_{0.5}B''_{0.5}O_3$

The distribution of cations in 1:1 binary perovskites $AB'_{0.5}B''_{0.5}O_3$ is described by the parameter of the degree of structural order:

$$s = \left| \frac{N_{B'} - N_{B''}}{N_{tot}/2} \right|, \tag{2}$$

which values can vary from 0 for a completely disordered state to 1 for an ordered state. In Eq.(2) $N_{B'}$ and $N_{B''}$ are the number of atoms in the B′- and

B″-sublattices, each of which consists of N_{tot} / 2 sites. To consider the ordering of cations in B-sublattices, the model of cation-anion elastic bonds is used (Cordero et al., 2008; Necira et al., 2012). It is assumed that above, the order-disorder phase transition temperature T_{od}, only a disordered state can exist, and below T_{od}, an ordered state can arise due to diffusion processes. This yields the relation for the maximum achievable due to diffusion processes for the value of s at $T<T_{od}$:

$$KT \ln \frac{1+s}{1-s} = 3(k_{B'} + k_{B''})u^2 s, \tag{3}$$

where K is the Boltzmann constant, $k_{B'}$ and $k_{B''}$ are the stiffness coefficients of unstrained B′-O and B″-O, and u is the displacement of oxygen from the centrosymmetric position in the ordered state.

For the $Fm3m$ space group, which describes the cubic phase of binary perovskite, the oxygen atoms are located in the Wyckoff position 24e (x; 0; 0). For a disordered state, the average B′-O and B″-O distances are the same and correspond to the oxygen coordinate $x = 1/4$. In the ordered state, the difference in the lengths and stiffnesses of the unstrained B′-O and B″-O bonds leads to a shift of oxygen to the (1/4+u; 0; 0) position. Since this displacement is related to ordering, it exists in all phases, including the cubic one.

For the perovskite structure a good approximation for the stiffness coefficients of B-O bonds is $k_B = n_B\gamma$, where n_B is the B-cation valence value, and γ is a constant (Sakhnenko and Ter-Oganessian, 2018; Sakhnenko et al., 1972). When generalizing the data on the bulk modulus and lattice parameters for a number of known ABO_3 perovskites, the value of γ was estimated to be 70 N/m (Sakhnenko and Ter-Oganessian, 2018).

According to (3), the degree of order, which is maximally achievable as a result of the order-disorder phase transition, vanishes at $T \geqslant T_{od}$, i.e., $s = 0$, and increases upon cooling, reaching 1:

$$T_{od} = \frac{3(k_{B'} + k_{B''})u^2}{2K}. \tag{4}$$

The calculation of T_{od} values for many $AB'_{0.5}B''_{0.5}O_3$ binary perovskites (Sakhnenko and Ter-Oganessian, 2018) showed good agreement with their structural characteristics. An important general conclusion follows from work by (Sakhnenko and Ter-Oganessian, 2018): compounds, for which the T_{od} values are too high (i. e. technologically unachievable), are in an ordered state,

compounds with T_{od} much lower than the synthesis temperature are disordered in any way of their preparation. For compounds with technologically achievable T_{od}, the degree of order s can be controlled.

The proposed approach to the implementation of the sintering process is based on the assumption that $T_{od} > T_C$. In this case, there is no reason to believe that the diffusion of B-cations is equal to zero (as in work by Hayn, 2013), and the problem of explaining the formation of local polar ordered regions is removed. In practice, this means that ordering due to diffusion processes can be obtained by prolonged firing at lower (compared to commonly used) temperatures. The possibility of forming ordered structures will make it possible to test models of preferred structural motifs from (Hayn, 2013) or propose and discuss new ones.

To calculate the value of T_{od} from (4), the u^2 values of the squared oxygen displacements for the ordered PZT phase are required. They were obtained by refining high resolution neutron data for both isotropic and anisotropic displacement models in the cubic phase (Zhang et al., 2011). Because this estimate is based on a model, the actual order-disorder transition temperature may differ slightly from the predicted temperature.

Figure 1 shows the dependence of the maximum degree of ordering s on the reduced temperature (T/T_{od}) plotted according to (4) for the tetragonal $PbZr_{0.52}Ti_{0.48}O_3$ solid solution. The obtained value of $T_{od} = 913$ K (640°C) is approximately equal to the lowest synthesis temperature for this composition (Tashiro et al., 1989), however much lower than the known published estimates, which reach 2000 K [according to (Hayn, 2013)].At room temperature, samples synthesized below T_{od} should be in a highly ordered state when measured (as for $s > 0.95$ in Fig. 1). However, according to the assumption, ordering is possible only due to the diffusion of B-cations, which is "kinetically hindered" and practically absent at $T < T_C$ (Erhart, Albe, 2007; Islam, 2000). If this is a case, then the degree of order achieved in synthesis at a sufficiently low temperature cannot be higher than that provided by the diffusion mechanism at the same temperature. Then just these values of s will be revealed by room-temperature measurements.

These considerations substantiate the possibility of obtaining the ordered state of $PbZr_{0.53}Ti_{0.47}O_3$ during the synthesis at temperatures below those usually used at the synthesis of PZT Section 2. For this, the long-term synthesis from a lead-free precursor according to the procedure described in book by (Jaffe and Cook, 1971), and in work by (Sakhnenko and Ter-Oganessian, 2018)

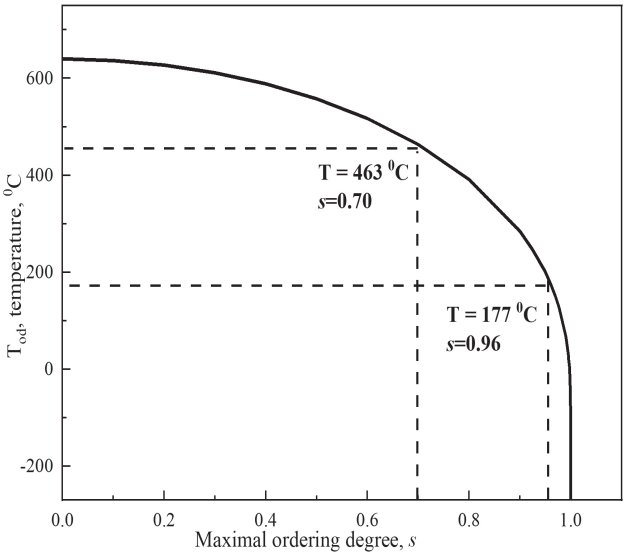

Figure 1. Dependence of the ordering temperature T_{od} on maximum ordering degree s for $PbZr_{0.52}Ti_{0.48}O_3$.

is suitable to a largest extent. Previously, pure perovskite $PbZr_{0.53}Ti_{0.47}O_3$ powder was obtained by (Eremkin et al., 2012; Lee et al., 1999 ; Okazaki, 1976; Matsuo et al., 1965; Tashiro et al., 1989) from $Zr_{0.53}Ti_{0.47}O_2$ and PbO by single firing at 650°C (Tashiro et al., 1989); however, a detailed XRD study of the resulting phase was not performed.

Experimental

$PbZr_{0.52}Ti_{0.48}O_3$ powders were prepared by single firing at various temperatures from the range of T=650-800°C. The annealing temperature and time values we are used to designate the samples: for example, PZT 650-4 is obtained by firing at 650°C for 4 hours.

Synthesis was performed according to the methodology (Eremkin et al., 2012; Lee et al., 1999 ; Okazaki, 1976; Matsuo et al., 1965; Tashiro et al., 1989) from the extra "pure" grade PbO and "pure" grade fine $Zr_{0.52}Ti_{0.48}O_2$ powder lead-free precursor, synthesized by hydrothermal technique at Ural Plant

of Chemical Reagent:

$$PbO + Zr_{0.52}Ti_{0.48}O_2 \rightarrow PbZr_{0.52}Ti_{0.48}O_3. \quad (5)$$

Raw materials were weighted in accordance with the $PbZr_{0.52}Ti_{0.48}O_3$ stoichiometry, and then water-mixed in a ball mill for 48 h. After drying, the mixture was briquetted and synthesized by single firing in a closed platinum crucible at $T = 600 - 800$°C. According to work by (Necira et al., 2012; Jaffe and Cook, 1971; Okazaki, 1976), below 1000°C, the evaporation of lead oxide is negligible, and therefore, firing at this temperatures is carried out under normal conditions, as a rule. Nevertheless, a PbO-enriched atmosphere was created. For this, tablets were placed in the crucible onto a PbO powder bed and covered with a massive PbO plate.

The phase composition of the samples and data for the analysis of XRD profiles were obtained by the powder method on a Rigaku Ultima IV diffractometer with filtered Cu-K radiation and a standard powder sample holder. Temperature studies were performed on an Anton Paar 1000 temperature attachment with a temperature stability of at least ±0.5°C on a DRON 7 diffractometer with filtered Co$K\alpha$ radiation. In the UltimaIV and DRON-7 diffractometers, a β-filter was used on the scattering side of the X-ray source without a monochromator.

Results and Discussion

Crystallographic characteristics were determined and the stoichiometry and single-phase nature of the powders synthesized in Section 3 were proved. Section 4.1 is devoted to this proof. Section 4.2 is devoted to the *in-situ* synthesis. SPM methods are applied to verify the presence of electrical activity and ferroelectric properties in Section 4.3. After that, it became possible to refine the structure and estimate the ordering in Section 4.4. In Section 4.5, the polymorphic phase transition is studied, and reasons for differences between the ordinary T phase and the newly obtained T1 phase with an unusual unit-cell parameter ratio (tetragonality) $c/a < 1$ are discussed. The influence of the size effect on the obtained results is estimated in Section 4.6.

Crystallographic Properties

The X-ray diffraction patterns of the obtained samples do not have superstructural reflections (Fig. 2). This indicates that, starting from the synthesis temper-

ature of 650°C, samples with the perovskite structure are formed without any impurity phases. Samples synthesized at lower temperatures contain traces of raw materials. A similar result was described in (Tashiro et al., 1989) when obtaining a similar $PbZr_{0.53}Ti_{0.47}O_3$ composition from PbO and $Zr_{0.53}Ti_{0.47}O_2$ raw materials (SAKAIChem. Co., ZT0-5347).

The full powder diffraction pattern of the PZT 650-4 sample corresponds to the tetragonal symmetry of the reduced perovskite cell. The inset in Fig. 2 shows the profiles of its characteristic reflections (100) and (200). Also, in accordance with the rules for splitting reflections for a tetragonal unit-cell, reflections (111) are single, and (h00) are split into two components {(h00)T + (0h0)T} and (00h)T with an intensity ratio of 2:1. The weaker component (00h) corresponds to the larger Bragg angle; therefore, the tetragonal unit cell parameter c is smaller than the parameter a. Such a ratio $c/a < 1$ has not been previously described in the $PbZr_xTi_{1-x}O_3$ system. This new phase with an unusual tetragonality $c/a < 1$ is denoted as T1. In this case, the commonly detected tetragonal phase, denoted as T, is characterized by a unit-cell elongated along the polar axis, for which $c/a > 1$ (Zhang et al., 2011; Noheda et al., 1999; Noheda et al., 2000; JCPDS 33-784).

The structure of the PZT 650-4 sample obtained under the conditions described by (Vasala and Karppinen, 2015) corresponds to an ideal perovskite. To analyze what happens about the crystallographic characteristics of $PbZr_{0.52}Ti_{0.48}O_3$ with a change in the temperature and duration of a single firing, samples were synthesized at 700°C and 800°C. At these temperatures, long exposures are used, since diffusion processes are necessary for the formation of an equilibrium state (Section 2), which requires a considerable time. They contribute to obtaining an ordered state in binary perovskites. For example, ordered $Pb(Sc_{0.5}Ta_{0.5})O_3$ ceramic was obtained by (Chu, Setter and Tagantsev, 1993) at sintering at 950°C for 110 h.

Powder XRD data shows that all samples belong to the tetragonal perovskite phase and do not contain impurities. According to the X-ray phase analysis (XPA) reflection profiles obtained at room temperature, the $PbZr_{0.52}Ti_{0.48}O_3$ composition can be formed in one of two different structural states, depending on the firing temperature. Phase T1 with the "inverse" tetragonality $c/a < 1$ is obtained after a single long firing at 650°C and 700°C for 100, 200, 300 and 400 h. A single firing at 800°C for 100 h (PZT 800-100) leads to the formation of the well-known tetragonal T phase with $c/a > 1$. In the inset to Figure 2 compares the (h00) reflections for the PZT 650-4 and PZT 800-100 samples are

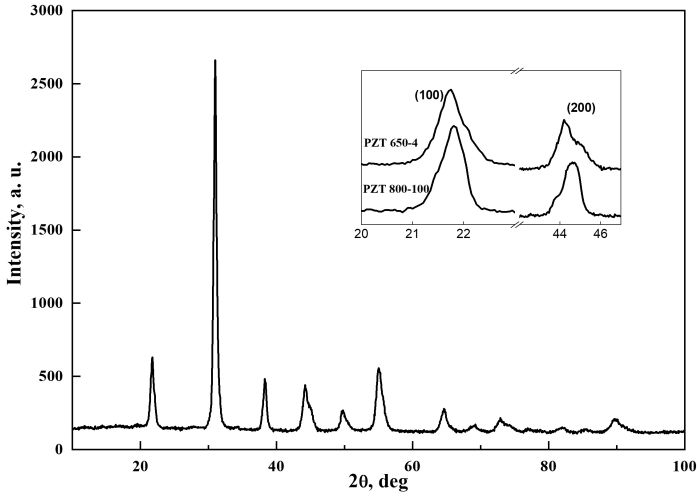

Figure 2. The full XRD powder pattern of PZT 650-4 sample. The inset contains the reflections $\{h00\}$ for samples PZT 650-4 (T1) and PZT 800-100 (T) for comparison.

given for comparison.

In-situ Synthesis

In the XRD study on the $PbZr_{0.52}Ti_{0.48}O_3$ sintering process, the powder mixture was heated at a rate of 10 deg/min. Full-scale data recording began at $T = 650°C$ (from the *ex-situ* powder diffraction data, this value was considered the minimum temperature for the formation of the pure perovskite phase). Hereafter results were obtained during the isothermal exposure. To minimize the registration time, scanning was carried out with a step of 0.04 deg and an exposure time of 1 *s*; temperature attachment Anton Paar-1000 with filtered Co$K\alpha$ radiation.

X-ray diffraction patterns of the *in-situ* process obtained after a 15-min exposure at 650°C showed the presence of only a pure perovskite phase without any impurity phases. The data obtained during a 4-h isothermal exposure consistently showed the presence of pure cubic perovskite, without a noticeable change in the shape of the reflection profiles (Fig. 3). The XRD pattern of the

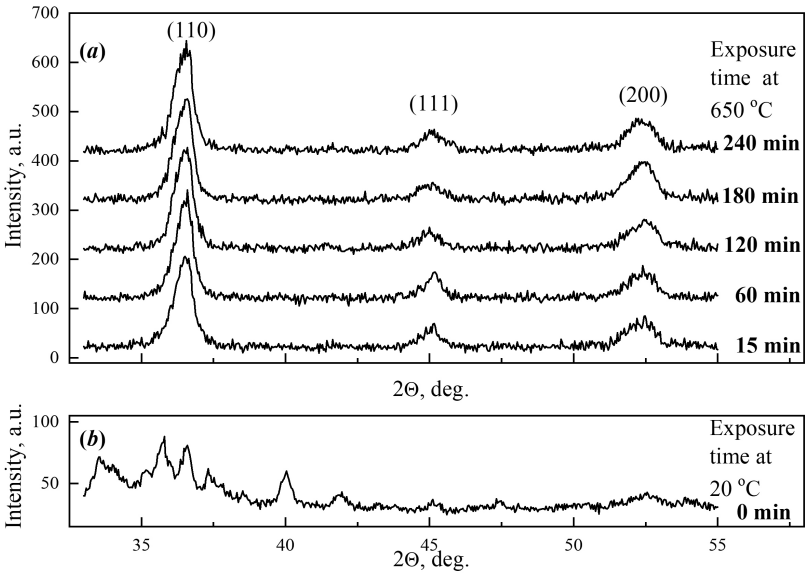

Figure 3. XRD powder patterns of $PbZr_{0.52}Ti_{0.48}O_3$: (a) *in-situ* data, recorded during exposure at 650°C; (b) initial components mixture at 20°C.

obtained sample showed the presence of the tetragonal T1 phase with tetragonality $c/a < 1$ at room temperature.

To analyze the temperature stability of the sample synthesized *in-situ*, two heat treatment cycles were carried out. Firstly, the sample was heated up to 700°C without removing it from the Anton Paar chamber and kept at this temperature for 2 h. Then, after cooling, the sample was annealed *ex-situ* for 1 h at 1200°C in a layer of PbO powder. Secondly, after cooling, the sample was *ex-situ* annealed for 1 h at 1200°C in a PbO powder bed. Both XRD patterns at room temperature, obtained after the first and second annealing stages, are almost identical to those shown in Figs. 2 for the PZT 650-4 sample. This indicates the stability of the T1 phase with respect to the heat treatment up to 1200°C.

Electrical Activity of the Sample Surface

To be able to further refine the lattice structure of the nanodisperse powders synthesized in Section 3, it is necessary to verify their electrical activity. Taking into account the small particle sizes, the methods of the scanning probe microscopy (SPM) were applied. Usually they are used to study surface properties, but they are quite suitable for powders like those studied by us. During measurements, the surface of the sample should retain the characteristics of the initial material as fully as possible and be dense enough so that the particles do not stick to the SPM probe. Since the heat treatment is undesirable, a special technique was developed: the synthesized powder was mixed with a 5% Nafion solution for 4 h until a homogeneous emulsion was obtained, which was then applied as a monolayer on a conductive substrate pre-treated with a 0.001% Nafion solution (for a better adhesion), and then dried for 24 h in a desiccator. The resulting layers completely retained the properties of the original material and met the requirements of SPM measurements. However, due to the inevitable adhesion of particles, the appearance of larger fragments was possible. Therefore, at first, the conformity of the studied surface objects with the source material was checked. To evaluate the presence (or absence) of foreign inclusions, the homogeneity of morphology was studied. Only then the results of measurements of the electrical potential and piezoresponse can be related to the electrical activity of the synthesized powders. Finally, the possibility of electrical switching of the samples was verified.

Relief, piezoelectric response (PR) and surface electrical potential were measured on the Veeco Multimode VS SPM. MESP probe with $k \approx 3.6$ N·m^{-1}, resonant frequency $f_0 = 63.69$ kHz. The results are presented in Figs. $4-6$ and in Table 1. The Ag layer served as the conducting substrate. The electrical potential was measured by non-contact force microscopy with a Kelvin probe (SKPM), the height of the probe above the surface was 40 nm. Then, without changing the probe (MESP is suitable for both methods), the amplitude and phase of the PR were measured at a frequency f_{ac} in a vicinity of the contact resonance frequency. This choice of the f_{ac} value ensured the highest response amplitude and made enabled us to avoid an attachment of particles weakly bound to the sample surface to the SPM probe. In addition, the analysis of the PR phase image contrast can provide information on the direction of the polarization vector (Proksch and Kalinin, 2015). Surface relief images were recorded simultaneously with the electrical characteristics of the surface.

Morphology. The histograms of surface particle size distribution and the results of roughness measurements are shown in Fig. 4 and in Table 1. Surface roughness values are as follows: $\sim 30-40$ nm for PZT 700-100, $\sim 40-50$ nm for PZT 650-4 and $\sim 180-220$ nm for PZT 800-100.

Table 1. The surface roughness of the T1 sample: R_a (arithmetic) and R_q (quadratic) for the entire scan area (10 x 10 μm^2) and for a smaller area ($\sim 10-15\%$ of the entire scan). The data were averaged over several measurements

	The entire scan area		The smaller part of the scan area	
Sample	R_a, nm	R_q, nm	R_a, nm	R_q, nm
PZT 700-100	264	330	31	40
PZT 650-4	190	231	41	53
PZT 800-100	321	408	181	222

Figure 4(a) shows the histograms of the height distribution of the sample surface for the entire scanned area (bottom) and for three surface areas 1, 2, and 3 marked with a white rectangle in Fig. 4(a), 4(b), 4(c). These rectangles have the same area and contain both small and large particles. All the histograms in Fig. 4(a) have the form of a wide distribution with the main maximum near $\sim$400 nm (for the 1st, 3rd regions and for the entire scan) and a noticeable contribution of particles $\sim 30-70$ nm in size. [For the 2nd region, the distribution in Fig. 4(a) looks narrower, which is due to the features of the larger particle surface, Fig. 4(c)]. The shapes of all the histograms do not have fundamental or sharp differences and are generally similar. This evidences in favor of the homogeneity of the surface characteristics of the samples.

On all the histograms shown in Fig. 4(a), the contribution from the region corresponding to small particles (less than $\sim$100 nm) is noticeable. The larger the proportion of fine particles, the clearer and wider the maximum(s) on the histogram in Fig. 4(a). So, in region 1, the distribution of particles up to $\sim$100 nm in size is almost flat; for region 2, there is a maximum between $\sim 30-50$ nm; and for region 3, a maximum in the region of $\sim 30-40-70$ nm. These values are consistent with the particle sizes estimated above from the roughness data in Table 1. For larger particles, the histograms in Fig. 4(a) have pronounced

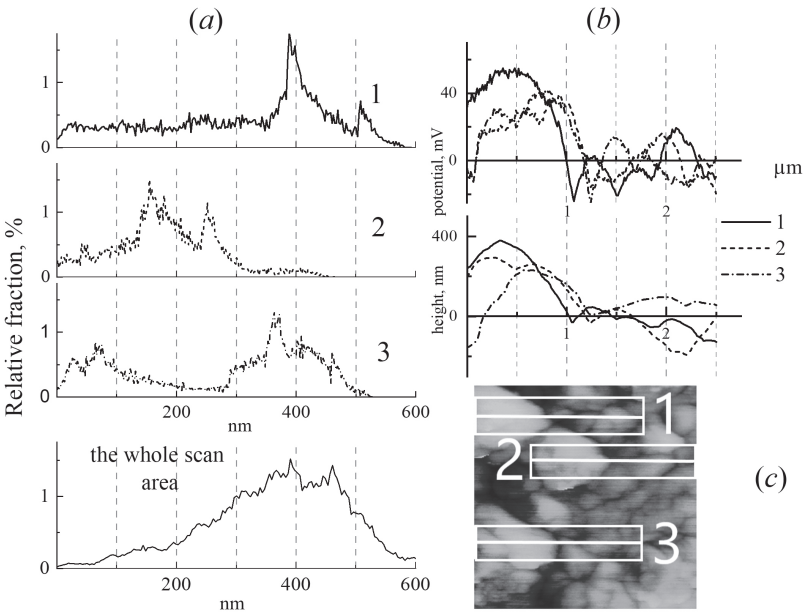

Figure 4. Characteristics of relief and electrical potential of surface areas 3.3 x 3.3 μm^2 of sample PZT 650-4. (a) Histograms of sample surface height distribution. The upper plots (numbered 1, 2, and 3) correspond to the sections along midline inside the rectangular areas in Fig. 4(c) with the same numbers. (b) Electrical potential (top) and relief (bottom) along the thick white lines drawn through the midpoints of regions 1, 2, and 3 in Fig. 4(c). (c). The height image.

maxima, the width of which is most likely due to the coalescence of small particles into larger ones.

Electric potential. Figure 4(b) shows cross-sections of the potential images (top three curves) and relief (three bottom curves) along the midline of the rectangular areas depicted in Fig. 4(c), shown as a thick white line in Fig. 4(c). Large particles [their size apparently corresponds to the main maximum in the histograms in Fig. 4(a)] have an electrical potential with a maximum value of $\sim 30-60$ mV, see Fig. 4(b). The size of such particles is less than $\sim$0.9$-$1.1 μm. For them, the shape of the cross sections of the potential [Fig. 4(a)] and the distribution of the surface relief [Fig. 4(b)] correlate with each other. The elec-

trical potential of larger particles [from ∼1.1 to 3 μm in Fig. 4(b), on the right side of the rectangles in Fig. 4(c)] varies from ∼ 1 mV to 10 mV; its sign may change. It is possible that such particles are formed by smaller ones, with a size of ∼ $(30-70)$ nm. When sticking together, they form larger ones, the electrical potential of which is several tens of millivolts, which corresponds to the value mentioned above. In general, potential measurements confirm the presence of charged particles on the sample surface. There are no sharp in homogeneities in the potential distribution, which may indicate lack of foreign inclusions.

Piezoresponse. The piezoelectric activity of the surface of PZT 650-4 powder particles was verified by comparing the simultaneously recorded PR amplitude, PR phase, and relief (Fig. 5). To avoid any occasion, the scan size (10 x 10 μm^2) is chosen larger than for the charged regions in Fig.4. The comparison was carried out for sections drawn through three typical sections of the PR phase image [highlighted by thick white lines in Figure 5(a)]. The phase/amplitude signal values of the 1st, 2nd, and 3rd sections differ strongly (Fig. 5). In addition, the graphs of the upper row in Fig. 5 clearly show changes in the sign of the PR phase near ∼1 μm (for the 1st region) and between 1 and 2 μm (for the 2nd region). Such changes are completely analogous to those discussed by (Proksch and Kalinin, 2015), which explained the opposite signs in the phase contrast PR for oppositely directed polarization vectors of electrical domains on a rough surface, when the frequency f_{ac} approached to the contact resonance value. Hence, it can be assumed that the 1st and 2nd sections correspond to piezoelectrically active areas, and the 3rd section (without a response) is to be considered as a background. All this testifies to the piezoelectric activity of the sample, surface from PZT 650-4 particles and the presence of regions with oppositely directed polarization vectors, i.e., electric domains. The conclusion on the piezoelectric activity can also be drawn from the amplitude dependences of PR (see graphs of the middle row in Fig. 5). Their changes are located near the same points as for the PR phase (see graphs of the upper row in Fig. 5), despite their more complex shape and the presence of a larger background.

Evidence for PR activity was obtained by the contact PR method. Hence, it is necessary to make sure that this result is not occasional. Figure 5 (a)−(c) shows the PR phase images obtained at different frequencies f_{ac}. These images confirm the piezoelectric activity of the same surface areas 1, 2 and 3 in Fig. 5. Moreover, at a frequency $f_{ac} = 13$ kHz, the contrast is increased: the boundaries of small (with a size of ∼ 10^{-8}m) electrically active fragments on the sample surface are more clearly defined. This frequency dependence reminds that was

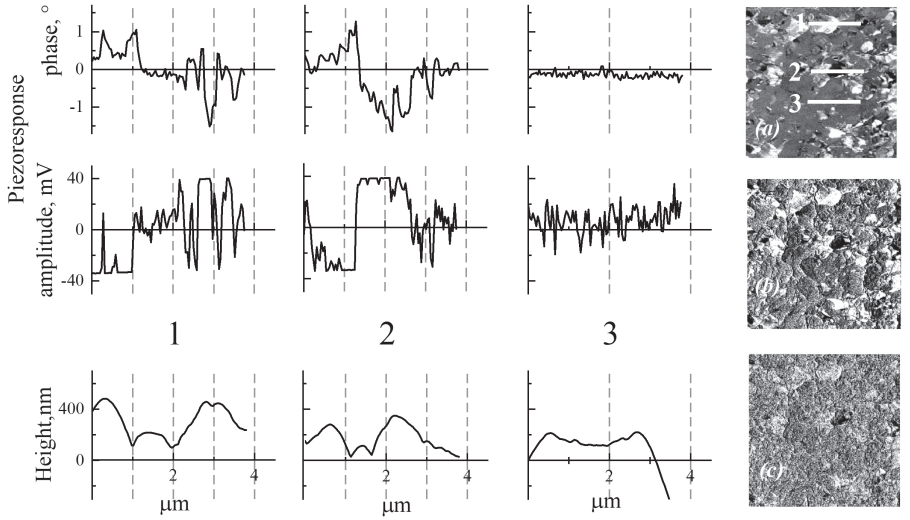

Figure 5. Comparison of the piezoresponse and surface topography of the PZT 650-4 sample for the same area of 10 x 10 μm^2 at different frequencies f_{ac}: 400 kHz (a), 13 kHz (b), and 8 kHz (c). Characteristics are presented as sections along white lines 1, 2, 3, the position of which on the surface is shown in the image (a) and not shown for (b) and (c) to make the difference in image contrast more noticeable for different frequencies. Columns 1, 2 and 3 are sections of the image (on the right) at the corresponding f_{ac} value for the PR (top row-phase, middle row-amplitude) and surface height (bottom row).

observed previously and should be typical for a piezoactive material. (Bo et al., 2010; Bunin et al., 2016; Bunin et al., 2015; Vasudevan et al., 2017).

Finally, the surface topography (see bottom row plots in Figure 5) does not correlate with changes in the PR phase or PR amplitude (see top and middle row plots in Figure 5). In this case, the PR amplitude depends linearly on the V_{ac} amplitude. These features, as well as the above consideration of piezoelectric activity, confirm the piezoelectric nature of the electromechanical response of the sample surface prepared from PZT 650-4 powder particles.

Testing the initial synthesis components for their possible piezoelectric activity gave a negative result. SPM measurements did not show the presence of particles, or areas that would differ strongly in their properties.

Switching. The possibility of the electrical switching in the PZT 650-4 was tested using PFM under the same experimental conditions. The result is shown in fig. 6. The nature of the switching depends on the magnitude and polarity of the bias: at 10 V, a change in the polarity of the bias reverses almost the entire contrast of the surface image (see the upper part of Fig. 6), and at 2 V, as the switching affects only part of it (see the lower part of Fig. 6). A similar situation was observed for the hysteresis dependence of the polarization on the external field in a thick $Pb(Zr_{0.3}Ti_{0.7})O_3$ film (Bdikin et al., 2008). As the histograms in Fig. 6 show, the values of the PR amplitudes are localized in two fairly narrow ranges corresponding to multidirectional displacements of the surface. This confirms the piezoelectric properties of the PZT 650-4 sample, in which a large displacement switches almost the entire surface by 180°, and a smaller one switches only part of it, and in general, SPM measurements indicate the ferroelectric nature of the behavior of the PZT 650-4 sample.

Verification by SPM methods confirmed the electrical activity and possibility of ferroelectric properties of the PZT 650-4 fine powder. This establish the approach to the treatment of the structure refinement for the T1 phase. The homogeneity and lack of sharp anomalies in the SPM morphology data and electrical activity favor our assumption on the single-phase sample proposed in Section 4.1.

Structure Refinement

For binary perovskites $AB'_{0.5}B''_{0.5}O_3$, the structural ordering parameter s in (2) can be obtained from p being the probability that B-atoms occupy the 4a-position of the space group $Fm3m$ (Stenger et al., 1979):

$$s = 2p - 1. \tag{6}$$

The parameter p refers to refined structural parameters and is determined by the XRD method. For binary perovskites 1:1, it is sufficient to set p values in the range of $0.5 \leq p \leq 1$, because from the point of view of the crystal lattice structure, the lattice arranging of B′ atoms with $p = 0$ (1) is similar to that at $p = 1$ (0) for B″ atoms. Therefore, we will further assume that $p = 0.5$ for the completely disordered structure $AB'_{0.5}B''_{0.5}O_3$ and $p = 1$ for the completely ordered

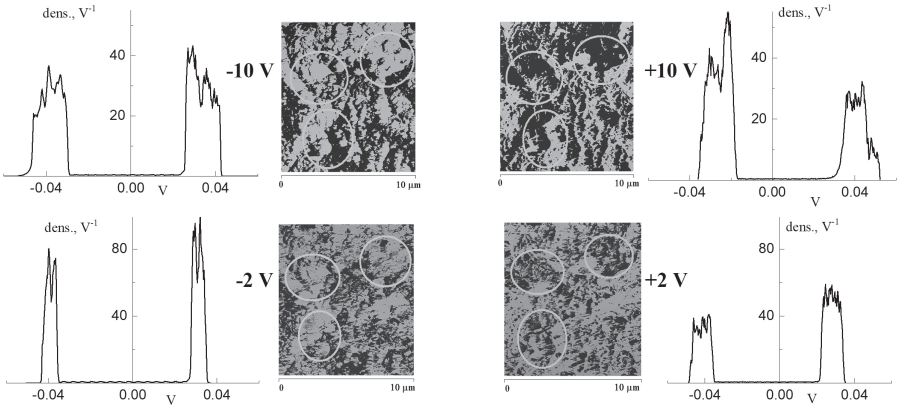

Figure 6. PR images of 10 x 10 μm^2 scans of the PZT 650-4 sample surface at biases $V_{dc} = \pm 2$ V and ± 10 V, and their amplitude distribution histograms (located on the left/right in the corresponding PR image). Some representative areas are marked with ovals for convenient comparison of their PR contrast dependence on the bias polarity. PR values are in mV (20 mV corresponds to 1 nm in height).

structure. The experimental accuracy of determining p in the structure refinement procedure depends on the intensities of superstructural reflections due to the ordering of atoms. For $PbZr_{0.5}Ti_{0.5}O_3$, the calculated intensities of these XRD reflections are small even for the case of a completely ordered structure with $s = 1$.

The cationic stoichiometry and lattice parameters of all obtained $PbZr_{0.52}Ti_{0.48}O_3$ powders were determined by the full-size Rietveld method. A consequence of the possible ordering of B-cations in the T1 phase sample should be a change in it symmetry with a doubling of the reduced perovskite cell and the appearance of XRD superstructural reflections. However, due to the approximately equal values of the scattering coefficients of titanium and zirconium, their intensities turn out to be too low even with complete ordering at $s = 1$. Therefore, for the Rietveld analysis, a reduced ABO_3 perovskite cell with polar group $P4mm$ was used, with atomic coordinates $z = 0$ and 0.5 as the initial

approximation for all the atoms.

XRD precise powder data for Rietveld analysis were collected on a Rigaku Ultima IV diffractometer, with filtered Cu$K\alpha$ radiation and with θ-2θ scanning in the range of $2\theta = 10^\circ - 100^\circ$. The structure was refined using the PowderCell software (Kraus, Nolze 1996). The reflections were fitted to the pseudo-Voigt function of the peak shape with refinement coefficients U, V and W of the Cagli-oti function:

$$H = U\tan^2\theta + V\tan\theta + W. \tag{7}$$

The lattice parameters, atomic filling and displacement factors z for cations, and isotropic thermal factors B for all atoms we refined.

As a result, it was found that the samples of the T1 phase obtained by the synthesis method (5) are single-phase. This is confirmed by our comparison to the simulation results under two different assumptions: (1) a single-phase system model, in which it is assumed that the sample consists only of a pure T1 phase, and (2) a two-phase system model, in which the sample is formed by the T + A phase (ordinary tetragonal T and another one labeled A).

A comparative analysis of the (200) reflection splitting for the tetragonal phase of these models is shown in Fig.7. The single-phase model enables us to consistently explain the observed ratios of the intensities of the components of the key XRD reflections. On the contrary, to explain them in the two-phase T + A model, it is necessary to assume that the sample contains at least 50% of the additional phase A. This can be, for example, a monoclinic phase (see the example of the formation of the z (200) reflection profile in the two-phase model in Fig.7, where the additional phase is designated by M). In addition, in this case it is necessary to explain the ratio of intensities characteristic of the T1 phase, which is possible only with a specific combination of the lattice parameters of the T and A phases. However in this case, with a change in the external influence (for example, temperature), the lattice parameters of the A and T phases will begin to change independently of each other, which will affect the integral shape of the reflection. Such an effect is not exclude and was found earlier in field studies (Medvecky et al., 2007). Therefore, we verified this possibility in special measurements, which did not reveal significant changes in the XRD profile for any of the reflections in the entire temperature range under consideration. In general, the two-phase model requires the simultaneous fulfillment of several conditions and is not confirmed by experimental verification. This means that the single-phase model is correct, and the unusual "inverse" tetragonality $c < a$

is a feature of a new low-temperature- synthesized T1 phase.

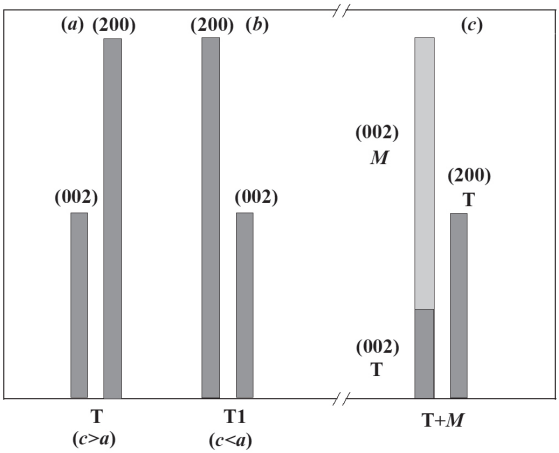

Figure 7. Splitting of reflections (200) in the tetragonal phase. (a) Phase T with $c > a$; (b) Phase T1 with $c < a$. (c) Artifitial superposition of the tetragonal T and monoclinic M phases during the formation of a pattern similar to that shown for the T1 phase.

The material composition, calculated from the refined coefficients of crystallographic sites occupation by Pb, Ti, and Zr atoms, coincides with the nominal value within the experimental error. The tetragonality $c/a < 1$, determined from the shape of the main reflections, is reliably confirmed by the good convergence of the full XRD pattern.

The refined crystallographic data for all synthesized $PbZr_{0.52}Ti_{0.48}O_3$ powders are summarized in Table 2. For all the samples, the refinement was carried out in the same route, and the obtained reliability factors R_p did not exceed 6%.

The neutron and X-ray diffraction data (Frantti et al., 2002) were used to plot the dependence of the unit-cell volume on the zirconium concentration x in $PbZr_xTi_{1-x}O_3$ solid solutions. For the zirconium atomic molar concentration range $0 < x < 0.8$, the volume V(in $Å^3$) of the formed ABO_3 unit cell is described by the following linear function:

$$V = 8.75x + 63.05. \tag{8}$$

Relation (8) was tested on experimental data on the lattice structure of $PbZr_xTi_{1-x}O_3$ solid solutions with $x = 0.40 - 0.50$ (Panda, 2017; Noheda et al., 1999; Noheda et al., 2000; JCPDS 33-784; Medvecky et al., 2007). For them, the value of the average discrepancy between the nominal and calculated composition did not exceed 4%. Then the calculation was performed for the $PbZr_{0.52}Ti_{0.48}O_3$ powders obtained by us of phase T1. It gave a concentration of zirconium from 0.50 to 0.52 (Table 2), which confirmed their stoichiometry and phase purity.

Table 2. Lattice parameters of $PbZr_{0.52}Ti_{0.48}O_3$ powders calculated according to the linear law (Frantti et al., 2002). x is the atomic molar concentration of zirconium.

Sample	Phase	a, Å	c, Å	c/a	V, Å^3	$\sqrt[3]{V}$, Å	x
650-4	T1	4.091	4.037	0.987	67.54	4.072	0.52
700-100	T1	4.088	4.042	0.989	67.57	4.073	0.51
700-200	T1	4.086	4.043	0.990	67.48	4.071	0.51
700-300	T1	4.086	4.043	0.989	67.51	4.072	0.51
700-400	T1	4.085	4.041	0.989	67.41	4.070	0.50
800-100	T	4.068	4.119	1.013	68.16	4.085	0.58

Polymorphic Phase Transition

The polymorphic phase transitions in $PbZr_{0.52}Ti_{0.48}O_3$ powders have been studied by XPA. Changes in the lattice parameters were recorded in the temperature range from $20 - 500$°C. XRD patterns of all the samples were obtained in the same mode: cooling from 500°C in steps of 10°C and holding for 15 min at each point before the next measurement. To measure the temperature dependence of the phase composition upon cooling from the paraelectric phase, the (110), (111), and (220) reflections were selected from the XPA data.

Methodology. At first, XRD-powder patterns were registered at room temperature. Then the sample was heated in the diffractometer chamber to $T = 500$°C (significantly higher than the Curie temperature) and hold at this temperature for 1 h. After such exposure in the cubic phase, the XRD data were measured in the cooling mode. Then, after 7 days of the exposure at room temperature, the measurement procedure was repeated. Within the experimental

error, the results of the two measurements coincided.

The temperature dependences of the lattice parameters of the T1 phase samples are practically the same. For all of them, in the temperature range of $300 - 500°C$, the existence of a pure cubic perovskite phase was established. At 300°C, the asymmetric broadening of the reflections (h00) indicates a transition to a tetragonal phase with the tetragonality $c/a < 1$. These distinct changes in the profiles of the (111) and (200) reflections are shown for samples PZT 650-4 [Fig. 8(a)] and PZT 800-100 [Fig. 8(b)]. The difference in the c/a ratio in the low-temperature T and T1 phases is clearly shown. When the PZT 650-4 sample is cooled to $T \approx 300°C$, a noticeable splitting of the (200) reflection is observed, which is characteristic of the ratio $c/a < 1$. Above $T = 300°C$, there are no splitting and broadening of the XRD reflections. It is important that there is no splitting even at $T = 350°C$, which is known to be the transition temperature for $PbZr_{0.52}Ti_{0.48}O_3$ (Tashiro et al., 1989; Noheda et al., 1999), Fig. 8(a). On the contrary, for the PZT 800-100 sample, the splitting of the (200) reflection, which is characteristic for the tetragonality $c/a > 1$, appears at $T = 350°C$, Figs. 3 and 8(b).

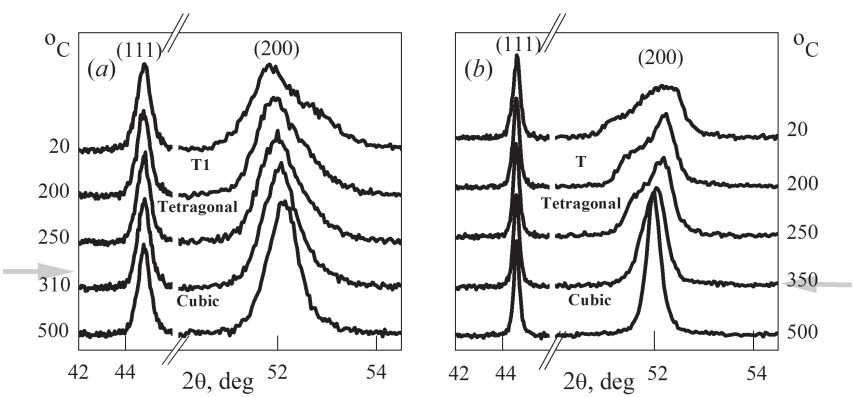

Figure 8. Temperature changes in the XRD reflections shape: (a) PZT 650-4 and (b) PZT 800-100 samples. The gray arrows mark the transition temperature from the cubic phase to the tetragonal one.

Temperature dependences of the lattice parameters a and c of the PZT 650-4 powder in Figs. 9(a) are similar for all samples of the T1 phase. All these dependences confirm the transition to the tetragonal phase at $T = 300°C$ and

the absence of anomalies at the phase transition temperature at 350°C. Similar dependences for the PZT 800-100 sample shown in Fig.9(b) demonstrate tetragonal-to-cubic phase transition just for 350°C.

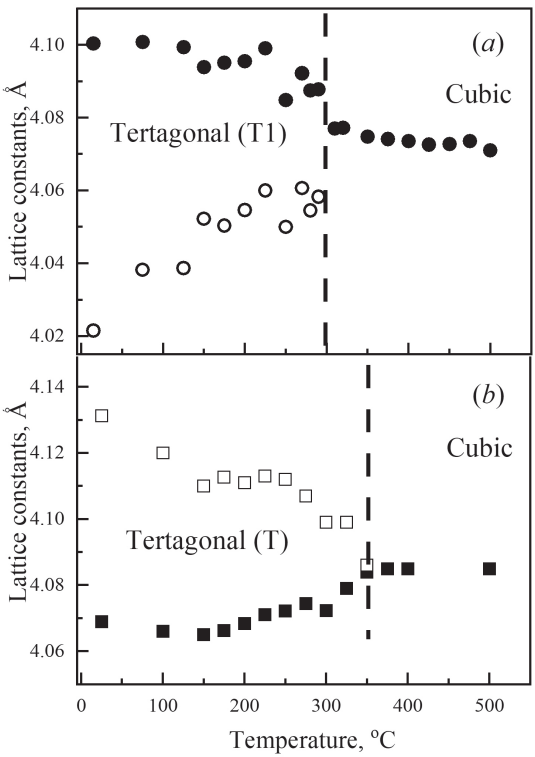

Figure 9. Temperature dependence of lattice parameters: (a) PZT 650-4 and (b) PZT 800-100 samples. In the tetragonal phase, open and closed symbols denote the *a* and *c* lattice parameters, respectively.

In Sections 4.1, 4.4 and 4.5 the stoichiometry and single-phase purity of the samples were proved, which were confirmed by the SPM data (Section 4.3). Now the reasons for the difference between the T and T1 phases are possible to consider. Our ideas on the ordering of B-cations in the PZT 650-4 and PZT 700-100 samples are best suited for this. Such an assumption is confirmed by

the data from various works: a decrease in the temperature of the maximum permittivity for $PbSc_{0.5}Nb_{0.5}O_3$ with an increase in the degree of ordering in (Zhu et al., 2008), extrapolation of the inverse temperature dependence of the permittivity for cubic $PbSc_{0.5}Ta_{0.5}O_3$ (Chu, Setter and Tagantsev, 1993). The latter also indicates a decrease in the ferroelectric instability temperature in the ordered compound.

The calculated temperature value $T_{od} = 640°C$ was obtained for PZT in Section 2. The range of experimental values $650 < T_{od} <\sim (750-800)°C$ was estimated from the T1 and T phases synthesis temperatures. In this range, the degree of ordering is the highest possible with $s = 0.4-0.6$ calculated according to (3) and (4).This explains lack of superstructural reflections in the XRD patterns of the T1 phase samples. Because of the approximately equal values of the scattering coefficients of Ti and Zr (they scatter in antiphase), the intensities of the XRD superstructural reflections are low even in highly ordered PZT compositions. In addition, the s values are quite low, and the polycrystalline powder is not completely homogeneous. This significantly complicates the detection of the ordered phase by other experimental methods.

Size/Strain Analysis

Another possible reason for the decrease in the phase transition temperature may be the size effect. This is to be verified, since our results of SPM measurements (Section 4.3) confirmed the low-size of the powder particles under study. For $PbZr_xTi_{1-x}O_3$ solid solutions, the critical particle size D_C, below which T_C decreases, is $25-50$ nm (Ohno et al., 2007; Wang et al., 2018; Ishikawa et al., 1998; Ohno et al., 2002). We use the XRD data to estimate the particle size D for the T and T1 phases of our samples.

In the conventional Williamson−Hall method, the dependence of the Bragg reflection width on the average size of the coherent diffraction region (i.e., on the particle size D) and microstrain ε is written by the linear equation as follows:

$$\beta\cos\theta = k\lambda/D + 4\varepsilon\sin\theta. \tag{9}$$

where D is the mean size of coherently diffraction region (particle size); β (in rad) is the FWHM width of the Bragg reflection; $\lambda = 0.154051$ nm is the wavelength of Cu$K\alpha_1$ radiation; $\varepsilon = \Delta d/d$ is the mean uniform lattice distortion (microstrain) and $k = 0.9$ is Scherer factor for spherical particles. The intercept and slope of the linear dependence (9) graph determine the values of D and ε.

Williamson−Hall plots for all PZT samples are shown in Fig. 10(a). Silicon standard corrected values β (Rigaku Corporation) are obtained from Rietwed analysis. It turned out that they are well described by a linear dependence, without differences between the graphs for the T and T1 phases. The calculated values of the particle size D and microstrains ε are given in Table. 3 and in fig. 10b.

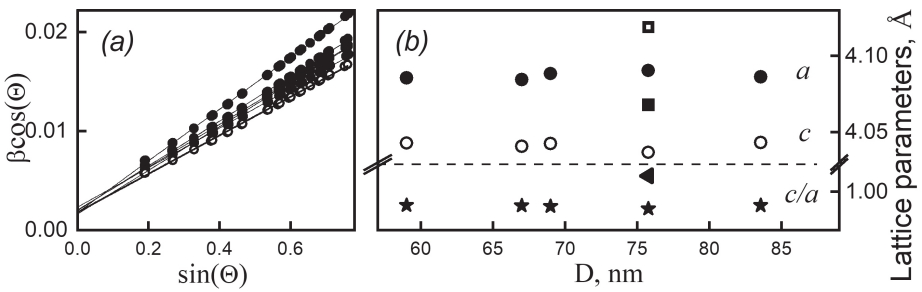

Figure 10. (a) Williamson−Hall plots for the $PbZr_{0.52}Ti_{0.48}O_3$ powders. Linear fits for all plots are shown by solid lines. (b) Lattice parameters and tetragonality values vs crystalline size D for the T1 phase (closed symbols) and T phase (open symbols) for $PbZr_{0.52}Ti_{0.48}O_3$ samples listed in Table 3. Open square − for PZT 800-100, stars − for set of the PZT 700 samples, triangle correspond to conventional phase of the PZT. Circles and square symbols corresponds to designations in Figure 9.

Table 3. Particle size D and microstrain $\varepsilon = \Delta d/d$.

Sample	Phase	D, nm	ε
PZT 650-4	T1	76	0.0065
PZT 700-100	T1	69	0.0056
PZT 700-200	T1	59	0.0050
PZT 700-300	T1	84	0.0055
PZT700-400	T1	67	0.0054
PZT 800-100	T	76	0.0049

For all the samples studied by us, the determined parameters vary within the interval of $D = 59 - 84$ nm. This means that, they exceed the estimated value of the critical grain size $40 - 50$ nm. Moreover, the D value for the T phase sample

(75 nm) is not the end point of the D interval, but approximately corresponds to its middle. So, for all the T1 phase samples, the lattice parameters and its ratio c/a are almost independent on the particle size D [Fig.10(b)].Therefore, the crystallite sizes for these samples are far from critical, and this is consistent with the value of $D_C = 40 - 50$ nm obtained by (Ohno et al., 2007; Wang et al., 2018; Ishikawa et al., 1998; Ohno et al., 2002). The results of this section clearly demonstrate that the unusual crystallographic characteristics of the T1 phase are not related to the size effect.

Conclusion

To study and understand structural features of compositions from the morphotropic region, it is necessary to obtain samples in an equilibrium state. This requires low-temperature the synthesis using special precursors, and not from simple oxides. The use of this approach enabled us to obtain finely dispersed PZT powders in the equilibrium state with partial ordering.

$PbZr_{0.52}Ti_{0.48}O_3$ nanopowders were obtained by low-temperature single-stage firing from PbO and $Zr_{0.52}Ti_{0.48}O_2$ precursors. The synthesis temperatures were estimated in terms of the elastic cation-anion bond model , which assumes the necessity for diffusion to form a sufficiently significant ordering. This is favored by the long annealing times used in the work. The advantage of the single-stage synthesis method to obtain $PbZr_{0.52}Ti_{0.48}O_3$ is the formation of the most possible homogeneous equilibrium state, as in works by (Eremkin et al., 2012; Matsuo et al., 1965; Tashiro et al., 1989).

The synthesis proceeded without the formation of any intermediate phases, including $PbTiO_3$ and Zr-enriched phases being significantly far from the target composition, is in agreement with the results by (Hammer and Hoffmann, 1998; Jaffe and Cook, 1971; Chandratreya et al., 1981; Eremkin et al., 2012; Matsuo et al., 1965; Hayn, 2013). Despite lack of the lead evaporation at $650 - 800°C$ (Necira et al., 2012; Jaffe and Cook, 1971; Okazaki, 1976), the synthesis was carried out in a closed crucible in an atmosphere of PbO vapor. Samples obtained in this way do not contain lead vacancies or areas of lead excess.

The phase purity, stoichiometry, and tetragonal lattice symmetry of the samples were confirmed by presize powder XRD studies, including *in-situ* synthesis, temperature studies of XRD reflection changes, and Rietveld refinement.

It has been established that, depending on the firing temperature, $PbZr_{0.52}Ti_{0.48}O_3$ samples can be obtained in one of the two different structural

states:

- A single firing at 800°C (PZT 800-100) produces a well-documented tetragonal phase T with tetragonality $c/a > 1$ and a tetragonal-cubic phase transition temperature $T_C = 350$°C;
- Samples synthesized at 650 and 700°C (PZT 650-4 and PZT 700-100) had unusual properties:
  - At room temperature, they are in the tetragonal phase T1 with the unusual tetragonality $c/a < 1$;
  - At $T_C = 300$°C, they transform into the cubic phase.

To the best of our knowledge, such a phase in the PZT system has not been previously described.

The electrical activity of the surface of samples in the T1 phase samples was confirmed by Kelvin probe force microscopy and PR force microscopy. The possibility of switching is shown, which confirms the possibility of ferroelectric properties for samples of this phase. These data allowed its structure refinement.

The unusual properties of the T1 phase can be due to the ordering of B-cations, which is favored by the synthesis conditions determined from the elastic cation-anion bond model. This result is in agreement with the studies on other similar OPFs: $PbSc_{0.5}Nb_{0.5}O_3$, $PbSc_{0.5}Ta_{0.5}O_3$ (Chu, Setter and Tagantsev, 1993; Zhu et al, 2008; Stenger et al, 1979).

Acknowledgment

The authors are very grateful to Prof. V.Yu.Topolov for his interest in the work and valuable comments significantly improved the text.

Author's Contributions

OB and MB – the whole chapter text; $T_{od}(s)$ evaluation (Sect.2), OB – samples properties from XRD data analysis (Sect. 4.1, 4.2, 4.4, 4.5, 4.6); MB – SPM experiment and data analysis (Sect.4.3) ; KYuA – XRD data, XPA, *in-situ* analysis (Sect. 4.1, 4.2, 4.5), specimens preparation (Sect. 4.3); SVG – PZT powders obtaining process (Sect.4.2); ChVA – the manuscript preparation; discussion on the PZT ordering (Sect. 2); SVP – the basic idea, chapter text, theoretical basis for Sect.2.

Conflict of Interest

Authors have no conflict of interests.

Funding

The study was financially supported by the Ministry of Science and Higher Education of the Russian Federation (State task in the field of scientific activity 2023) № GZ0110/23-08-IF.

References

Bdikin IK, Kholkin AL, Morozovska AN, Svechnikov SV, Kim S-H, Kalinin SV. Domain dynamics in piezoresponse force spectroscopy: Quantitative deconvolution and hysteresis loop fine structure. *Appl.Phys.Lett.* (2008) 92(18): 182909(3) . doi:10.1063/1.2919792.

Bo H, Kan Y, Lu X, Peng S, Wang X, Liu Y, Cai W, Xue R, Zhu J. Influence of the feedback parameters on ferroelectric domain imaging with piezoresponse force microscopy. *Review of Scientific Instruments* (2010) 81(4): 043704(8). doi:10.1063/1.3387342.

Bokov AA, Rayevsky IP. Compositional ordering in ferroelectrics with diffuse phase transition. *Ferroelectrics* (1989) 90: 125-133. doi:10.1080/00150198908211280.

Bunin MA, Rybyanets AN, Fedorovskiy AE, Sukhomlinov DI, Bunina OA. Frequency dependence in the piezoresponse force microscopy of dense piezoceramics, *Bulletin of the Russian Academy of Sciences: Physics* (2016) 80: 1396-1398. doi:10.3103/S1062873816090057.

Bunin MA, Rybyanets AN, Naumenko AA, Sukhomlinov DI, Fedorovskiy AE. Piezoelectric response from porous ferroelectric ceramics at low drive voltage. *Ferroelectrics* (2015) 475: 96-103. doi:10.1080/00150193.2015.995531.

Chandratreya SS, Fulrath RM, Pask JA. Reaction Mechanisms in the Formation of PZT Solid Solution. *J. Am. Ceram. Soc.* (1981) 64: 422-425. doi:10.1111/j.1151-2916.1981.tb09883.x.

Chu F, Setter N, Tagantsev AK. The spontaneous relaxor-ferroelectric transition of $Pb(Sc_{0.5}Ta_{0.5})O_3$. *J. Appl. Phys.* (1993) 74: 5129-5134. doi:10.1063/1.354300.

Cordero F, Craciun F, Galassi C. Anelastic and dielectric study of the phase transformations of $PbZr_{1-x}Ti_xO_3$ around the morphotropic phase boundary. *J. Phys. Chem. Solids* (2008) 69(9): 2172-2176. doi:10.1016/j.jpcs.2008.03.025.

Eremkin VV, Marakhovsky MA, Panich AE, Smotrakov VG. 2012. "Low-temperature sintering of rigid PZT piezoceramics." Paper presented at the *International Scientific and Technical Conference*, Moscow, December 21-24 (in Russian).

Erhart P, Albe K. Thermodynamics of mono- and di-vacancies in barium titanate. *J. Appl. Phys.* (2007) 102(8): 084111(9). doi:10.1063/1.280101.

Frantti J, Ivanov S, Eriksson S, Rundlof H, Lantto V. Lappalainen J, Kakihana M. Phase transitions of $Pb(Zr_xTi_{1-x})O_3$ ceramics. *Phys. Rev. B* (2002) 66: 064108 (15). doi:10.1103/PhysRevB.66.064108.

Hammer M, Hoffmann MJ. Sintering Model for Mixed-Oxide-Derived Lead Zirconate Titanate Ceramics, *J. Am. Ceram. Soc.* (1998) 81(12): 3277-3284. doi:10.1111/j.1151-2916.1998.tb02768.x.

Hayn S. 2013. *"First-principles calculations on the structural and thermodynamic stability of* $(Na_{1/2}Bi_{1/2}Ba)TiO_3$ *and* $Pb(Zr,Ti)O_3$*."* PhD diss., Technishe Universitat Darmstadt.

Ishikawa K, Yoshikawa K, Okada N. Size effect on the ferroelectric phase transition in $PbTiO_3$ ultrafine particles. *Phys. Rev. B* (1988) 37(10): 5852-5855. doi:10.1103/PhysRevB.37.5852.

Islam MS. Ionic transport in ABO(3) perovskite oxides: a computer modelling tour. *J. Mater. Chem.* (2000) 10: 1027-1038. doi:10.1039/A908425H.

Jaffe B, Cook WR, Jaffe H. 1971. *Piezoelectric ceramics*. Academic Press. London/New York.

JCPDS file № 14-31.

JCPDS file № 33-784.

Kingon A, Clark B. Sintering of PZT Ceramics: I, Atmosphere Control. *J.Am. Ceram. Soc.* (1983) 66: 253-256. doi:10.1111/j.1151-2916.1983.tb15708.x.

Kraus W, Nolze G. POWDER CELL-A Program for the Representation and Manipulation of Crystal Structure and Calculation of the Resulting X-Ray Powder Pattern. *J. Appl. Cryst.* (1996) 29(3): 301-303. doi:10.1107/S0021889895014920.

Kungl H, Theissmann R, Knapp M, Baehtz C, Fuess H, Wagner S, Fett T, Hoffmann MJ. Estimation of strain from piezoelectric effect and domain switching in morphotropic PZT by combined analysis of macroscopic strain measurements and synchrotron X-ray data. *Acta Materialia* (2007) 55: 1849-1861. doi:10.1016/j.actamat.2006.10.046.

Lee SE, Xue JM, Wan DM, Wang J. Effects of mechanical activation on the sintering and dielectric properties of oxide-derived PZT. *Acta Materialia* (1999) 47: 2633 -2639. doi:10.1016/S1359-6454(99)00141-X.

Matsuo Y, Sasaki H. Formation of Lead Zirconate-Lead Titanate Solid Solutions. *J. Am. Ceram. Soc.* (1965) 48: 289-291. doi:10.1111/J.1151-2916.1965.TB14743.X.

Medvecky L, Kmecova M, Saksl K. Study of $PbZr_{0.53}Ti_{0.47}O_3$ solid solution formation by interaction of perovskite phases. *Journal of the European Ceramic Society* (2007) 27(4): 2031-2037. doi:10.1016/j.jeurceramsoc.2006.05.100.

Necira Z, Boutarfaia A, Abba M, Abdessalem N. Synthesis of PZT powder by conventional method at various conditions. *EPJ Web of Conferences* (2012) 29: 00038 (7). doi:10.1051/epjconf 201/22900038.

Noheda B, Cox DE, Shirane G, Gonzalo JA, Cross LE, Park S-E. A monoclinic ferroelectric phase in the $PbZr_{1-x}Ti_xO_3$ solid solution. *Appl. Phys. Lett.* (1999) 74: 2059-2061. doi:10.48550/arXiv.cond-mat/9903007.

Noheda B, Gonzalo JA, Cross LE, Guo R, Park S-E, Cox DE, and Shirane G. Tetragonal-to-monoclinic phase transition in a ferroelectric perovskite: The structure of $PbZr_{0.52}Ti_{0.48}O_3$. *Phys. Rev. B* (2000) 61: 8678-8689. doi:10.1103/PhysRevB.61.8687.

Ohno T, Mori T, Suzuki H, Fu DS, Wunderlich W, Takahashi M, Ishikawa K. Size effect for lead zirconate titanate nanopowders with $Pb(Zr_{0.3}Ti_{0.7})O_3$ composition. *Jpn. J. Appl. Phys.* (2002) 41(11): 6985-6988. doi:10.1143/JJAP.41.6985.

Ohno T, Suzuki D, Ishikawa K, Suzuki H. Size effect for lead zirconate titanate nano-particles with PZT(40/60) composition. *Advanced Powder Technol.* (2007) 18(5): 579-589. doi:10.1163/156855207782146607.

Ohwada K, Hirota K, Terauchi H, Fukuda T, Tsutsui S, Baron AQR, Mizuki J, Ohwa H, Yasuda N. Intrinsic ferroelectric instability in $Pb(In_{1/2}Nb_{1/2})O_3$ revealed by changing B-site randomness: Inelastic x-ray scattering study., *Phys. Rev. B* (2008) 77: 094136(8). doi: 10.1103/PhysRevB.77.094136.

Okazaki K. trans. 1976. *Ceramic engineering for ferroelectrics*. (Gakkenska Co.Tokio,1969). Energy Publishing Office. Moscow.

Panda PK. 2017. "Piezoceramic Materials and Devices for Aerospace Applications." In *Aerospace materials and material technologies* v.1, edited by Eswara Prasad N. Wanhill RJH , 501-518. Singapore: Springer Science+Business Media. doi:10.1007/978-981-10-2134-3.

Proksch R, Kalinin S. 2015. "Piezoresponse Force Microscopy with Asylum Research AFMs" *Asylum Research Application Note* 10: 1-27.

Robert G, Maeder MD, Damjanovic D, Setter N. Synthesis of lead nickel niobate-lead zirconate titanate solid solutions by a B-site precursor method. *J. Am. Ceram. Soc.* (2001) 84: 2869-2872. doi:10.1111/j.1151-2916.2001.tb01107.x.

Sakhnenko VP, Fesenko EG, Shuvaev AT, Shuvaeva ET, Geguzina GA. Interatomic distances in oxides with the perovskite structure. *Sov. Phys. Crystallogr.* (1972) 17 316-322.

Sakhnenko VP, Ter-Oganessian NV. Theory of B-cation order-disorder transitions. *Acta Cryst. B* (2018) 74: 264-273. doi:10.1107/S205252061800392X.

Schonau KA, Knapp M, Kungl H. Hoffmann MJ, Fuess H. In situ synchrotron diffraction investigation of morphotropic $PbZr_{1-x}Ti_xO_3$ under an applied electric field. *Phys. Rev. B* (2007) 76(14): 144112 (12). doi:10.1103/PhysRevB.76.144112.

Setter N, Cross LE. The role of B-site cation disorder in diffuse phase transition behavior of perovskite ferroelectrics. *J. Appl. Phys.* (1980) 51: 4356-4360. doi:10.1063/1.328296.

Stenger CGF, Scholten FL, Burggraaf AJ. Ordering and diffuse peasetrpnsitions in $Pb(Sc_{0.5}Ta_{0.5})O_3$ ceramics. *Solid State Communications* (1979) 32(11): 989-992. doi:10.1016/0038-1098(79)90812-3.

Tashiro S, Kotani Y, Fukai K, Igarashi H. Fabrication of PZT Ceramics from $Zr_{0.53}Ti_{0.47}0_2$ Solid Solution. *Jap. J. Appl. Phys.* (1989) 28(2): 80-82. doi:10.7567/JJAPS.28S2.80.

Vasala S, Karppinen M. $A_2B'B''O_6$ perovskites: A review. *Progress in Solid State Chem.* (2015) 43: 1-36. doi:10.1016/j.progsolidstchem.2014.08.001.

Vasudevan RK, Balke N, Maksymovych P, Jesse S, Kalinin SV. Ferroelectric or non-ferroelectric: Why so many materials exhibit "ferroelectricity" on the nanoscale. *Applied Physics Reviews* (2017) 4(2): 021302(47). doi:10.1063/1.4979015.

Wang X, Yan Y, Shimada T, Wang J, Kitamura T. Ferroelectric critical size and vortex domain structures of $PbTiO_3$ nanodots: A density functional theory study. *J. Appl. Phys.* (2018) 123(11): 114101(14). doi:10.1063/1.5013049.

Yang Y, Wang Y, Meng H. Study on $Pb(Mg_{1/3}Ta_{2/3})O_3$-$Pb(Mn_{1/3}Sb_{2/3})O_3$-$Pb(Zr_xTi_{1-x})O_3$ high power piezoelectric ceramics near the morphotropic phase boundary. *J. Alloys and Comp.* (2010) 508(2): 364-369. doi:10.1016/j.jallcom.2010.08.026.

Zhang N, Yokota H, Glazer AM, Thomas PA. The not so simple cubic structure of $PbZr_{1-x}Ti_xO_3$ (PZT): complex local structural effects in perovskites. *Acta Cryst. B* (2011) 67: 461-46. doi:10.1107/S010876811103936X.

Zhu M, Chen C, Tang J, Hou Y, Wang H, Yan H, Zhang W, Chen J, Zhang W. Effects of ordering degree on the dielectric and ferroelectric behaviors of relaxor ferroelectric $Pb(Sc_{1/2}Nb_{1/2})O_3$ ceramics. *J. Appl. Phys.* (2008) 103(8): 084124(9). doi:10.1063/1.2909283.

Contents of Earlier Volumes

Advanced in Materials Science Research. Volume 64

Advanced in Materials Science Research. Volume 62

Advanced in Materials Science Research. Volume 61

Index

E

F

H

I

M

N

O

P

S

T

X

Z

VOLUME

65

Maryann C. Wythers

EDITOR

ADVANCES IN Materials Science Research

nova
science publishers

www.novapublishers.com

ISBN-13: 979-8-89113-112-5